ProQuest LLC.
789 East Eisenhower Parkway
P.O. Box 1346
Ann Arbor, MI 48106 – 1346

THE DESIGN AND APPLICATION OF POLYMERIC MATERIALS IN A NOVEL LIGHT MODULATED ACCELEROMETER

by

Paul J. Grassham B.Sc.(Hons)

A thesis submitted in partial fulfilment of the requirements of the Council for National Academic Awards for the degree of Doctor of Philosophy

Sponsoring Establishment:

School of Engineering
Sheffield City Polytechnic
Pond Street
Sheffield
S1 1WB

June 1992

Preface

All work reported in this thesis was carried out at Sheffield City Polytechnic during the period October 1988 to March 1992.

The candidate has not, during the period of registration for the CNAA degree of Ph.D, been a registered candidate for any other CNAA award or for any University degree.

The results presented in the thesis are, to the best of my knowledge, original except where reference and acknowledgement has been made to other authors. No part of this thesis has been submitted for a degree at any other University or College.

The following courses were attended during the work:-

(1) "Numerical Methods and Programming", Part of Module 2 of the M.Sc in Metallurgical Process Management, October 1988 - February 1989, Sheffield City Polytechnic.

(2) "Analytical Scanning Electron Microscopy for Scientists and Engineers", Short Course held at Sheffield City Polytechnic, April - June 1990.

P.J. Grassham
June 1992

"The finding and manipulation of fringes in a Michelson interferometer is often regarded as one of the classically difficult and frustrating excercises in optics".

J. Dyson

Acknowledgements

The author would like to take this opportunity to express his appreciation to a number of people for their contribution over the duration of this research programme.

Firstly to the Science and Engineering Research Council for their financial support which enabled the completion of this research.

I express my gratitude to Dr David Clegg for taking over the responsibility of Director of Studies in January 1990 and also for his help and guidance during the period since especially during the writing of this thesis.

Thanks are also due to the technical staff in the School of Engineering, especially Mr Roy Gunson, Mr Peter Haythorne, Mr Paul Slingsby, Mr Roger Tindle and to Mr Richard Wilkinson.

A special voice of thanks is paid to Mrs Michelle Smith for numerous helpful discussions and for allowing me to take over part of her laboratory. Also many thanks to Dr Steve Bradbury for proof reading this thesis and for his useful comments.

Much gratitude is also due to BASF Plastics, Bayer UK Ltd, Ciba-Geigy Plastics, ICI Chemicals & Polymers Ltd and Wardle Storeys Ltd for supplying the test materials and associated information used in this research.

Finally, I would like to pay tribute to Sally for her undying patience, support and sheer endurance during many trying times. Also to my friends for their constant encouragement with special thanks to Peter and Vikki.

The Design and Application of Polymeric Materials in a Novel Light Modulated Accelerometer

Paul J Grassham

Abstract

A novel accelerometer based on light modulation has been designed and a prototype device manufactured. The device utilises the change in refractive index brought about by stress induced by the applied vibration. A detailed mathematical analysis of several feasible sensing designs has been performed to aid the design process.

A mathematical model has been developed to assess the performance characteristics of the light modulated accelerometer the results of which were also used as a design tool.

The prototype accelerometer was tested, from 1 g to 50 g between frequencies of 25 Hz to 2000 Hz, on a vibration system under three modulation schemes. The acceleration response of the device was seen to be linear over the testing range whilst the frequency response dropped off initially and levelled off at approximately 1 kHz.

An experimental accelerometer was also assembled on the vibration table so that various materials could easily be tested without having to undergo precise machining. The acceleration and frequency responses showed similar behaviour to those obtained with the prototype accelerometer. However, the actual response levels varied with each material.

To aid in the development of the accelerometer the stress-optic and thermo-optic coefficients have been determined for a range of polymeric materials.

The stress optic coefficient was determined for polycarbonate, polymethyl methacrylate, polvinyl chloride and araldite epoxy resin using a circular polariscope and two interferometer configurations up to the yield stress of the materials tested. Each material showed a constant coefficient over the testing range. The results obtained using each technique were in good agreement with each other and the limited literature data available.

The thermal variation of refractive index was also determined for the same materials. The Abbé refractometer was used for the determination between 5 and 140°C using five wavelength sources and two interferometer configurations using a HeNe laser from -50°C to approximately 30° above the glass transition temperatures.

The change in index was found to be linear over the temperature range tested. However, at the glass transition temperature a change in gradient was observed with each material.

Two simple mathematical relationships were used to predict the thermo-optic coefficient. These gave values reasonably close to those obtained in experiment.

Contents

1 Introduction

With the technological advances made over the past twenty five years, with regard to both lasers and optical fibres, optical measurement techniques in industry have become more common place. The laser provides coherent light in extremely narrow and highly collimated beams whilst the optical fibre provides a versatile light guide and also a means of light modulation.

The laser is now seen in domestic equipment such as audio and visual disc players. The optical fibre is common in remote visual inspection, telecommunication truck systems and local area networks. Both the laser and the optical fibre are closely related to electronics technology and are members of a range of opto-electronic components being developed and improved [1].

Early workers in the development of optical fibre cables realised the sensitivity to external influences and sought ways to minimise such effects. It was soon realised that this sensitivity could be used as the basis of various sensing devices.

Over the past fifteen years there has been a plethora of optical sensing devices designed and reported in the literature. These devices have been classified in the way in which the optical fibre is utilised: extrinsic sensors where the optical cable merely acts as a light guiding medium and intrinsic devices where the fibre itself is the sensitive element [2]. Optical methods have been useful and offer much promise of further development because light can be generated in a number of ways and can be conveniently modified by other physical phenomena [1-5].

Many of the engineering applications of such sensors are likely to rely on the inherent advantages of optical sensors over more conventional electrically based sensors ie.

freedom from electromagnetic interference, safety in hazardous environments, high electrical isolation enabling their use for high voltage applications, for data collection from points at electrical potential and may be used for distributed sensors of extreme length due to low losses achievable in optical fibres [6]. However, it is unlikely that sophisticated and expensive fibre optic systems that can be made to operate in the laboratory will stand up to the harsh environment of the process industries [7]. Therefore, relatively simple optical sensors with fibre optic links are required [8].

Vibration analysis is used to monitor the behaviour of a wide range of machines, systems and installations in a wide variety of environments. Conventional devices, be they mechanical, electro-mechanical or piezoelectric, cannot function where there is high electrical voltage, where there is high electromagnetic interference, in the presence of flammable or explosive fluids/gases and in marine environments.

To date, the optical vibration sensing devices designed and tested have employed mechanical systems which have displayed poor performance characteristics compared to those more conventional devices listed above. Hence, the aim of this programme of research was to design and manufacture a solid state light modulated accelerometer utilising the change in refractive index in polymeric materials brought about by the applied vibration.

However, very little literature data exists on the variation of refractive index induced by various environmental conditions and that information available has been somewhat contradictory. Michel et al [9] has shown that for three polymeric glasses the refractive index exhibits a linear relationship with temperature between the various transition points which occur in these materials. Work carried out by Waxler et al [10], however, did not substantiate these findings. No data has been found on the variation of index

with stress for these materials. As a consequence, a fundamental part of the research programme has been involved with the determination of these parameters.

Another important aspect has been to study the factors affecting the stress and thermo-optic coefficients in order to develop a greater understanding of their relation to material structure. This knowledge could then enable the prediction of the coefficients which would be of use in this research work, and generally, as a material selection tool, cutting down on time consuming investigatory methods.

A prototype accelerometer has been designed and manufactured using a polymeric sensing element. Some considerable time has been spent in the design of the sensing element. A mathematical model has been developed in order to predict the performance of the device and has also been used as a optimisation tool in the design of the prototype device.

2 Electromagnetic Theory and the Optical Fibre

2.1 Maxwell's Equations

The programme of work undertaken set out to discover the relation between the optical behaviour of dielectric materials and their composition and structure.

Therefore, it is of fundamental importance to understand the laws which govern the propagation of light in dielectric media.

These laws are a culmination of the work carried out in the early part of the 19th century by Oersted, Ampere and others. The field concept, introduced by Faraday, was not generally used until Maxwell showed that all electric and magnetic phenomenon could be described by only four equations involving electric and magnetic fields.

These equations, referred to as the theory of electromagnetism, are known as Maxwell's equations and have been reported in detail in many texts [11-15]. It is customary to write them in differential vector notation, thus

$$\nabla \cdot D = \rho \qquad \nabla \times E = -\frac{\partial B}{\partial t}$$

$$\nabla \cdot B = 0 \qquad \nabla \times H = J + \frac{\partial D}{\partial t} \qquad 2.1$$

The dynamic response of the atoms and molecules in the propagation medium is taken into account through what are called the constitutive relations. Assuming the relations to be independent of time or space, they are written as

$$D = \epsilon E \tag{2.2}$$

where ϵ is the dielectric constant

$$J = \sigma E \tag{2.3}$$

where σ is the conductivity, and

$$B = \mu H \tag{2.4}$$

where μ is the permeability

The constants ϵ, σ and μ contain the description of the material to which the equations are applied.

From Maxwell's equations, it can be shown that light is a transverse electromagnetic wave which travels through space at the speed of light c. It can also be shown that the oscillating electric and magnetic fields in an electromagnetic wave are perpendicular to each other and the direction of propagation.

2.2 Modes in an Optical Fibre

For a detailed understanding of the propagation of light in an optical fibre, it is necessary to solve Maxwell's equations subject to the cylindrical boundary conditions of the fibre. This has been carried out in detail by several workers [16-20].

The mathematics describing this situation are very complex and their analysis is beyond the scope of this thesis. Therefore only a general outline will be given along with the

practical implications.

By solving Maxwell's equations for the given boundary conditions, the exact characteristic equation or eigenfunction can be determined. The solutions or eigenvalues represent the propagation modes of this structure.

As an example of the complexity, the characteristic equation for a step index fibre is

$$\left[\frac{\epsilon_1}{\epsilon_2}\frac{a\gamma^2}{\kappa}\frac{J_\nu'(\kappa a)}{J_\nu(\kappa a)}+j\gamma a\frac{H_\nu^{(1)'}(j\gamma a)}{H_\nu^{(1)}(j\gamma a)}\right]\left[\frac{a\gamma^2 J_\nu'(\kappa a)}{\kappa J_\nu(\kappa a)}+j\gamma a\frac{H_\nu^{(1)'}(j\gamma a)}{H_\nu^{(1)}(j\gamma a)}\right] - \left[\nu\left(\frac{\epsilon_1}{\epsilon_2}-1\right)\frac{\beta k_2}{\kappa^2}\right]^2 \quad 2.5$$

where

k = radial wave number
k_0 = free space propagation coefficient
γ = a + $j\beta$, the longitudinal propagation coefficient
a = fibre radius
ν = order of Bessel function J and Hankel function H

A solution is obtained when a β value satisfying the equation is found corresponding to a given set of ϵ, k_0, a and ν. Each solution is referred to as a mode of the fibre waveguide.

For a round fibre, several mode types propagate with each mode assuming a unique distribution with radial and circumferential variations.

TE (transverse electric) modes exist where the electric field vector is normal to the direction of propagation and similarly for the magnetic field vector, the TM (transverse magnetic) modes. Using the ray approach to optical fibres the TE and TM modes correspond to meridional rays.

Hybrid modes which are denoted as $HE_{\nu\mu}$ and $EH_{\nu\mu}$ modes have both longitudinal

electric and magnetic field components present. The modes are designated by ν and μ, where ν is the order of the Bessel and Hankel functions and μ is the n^{th} root of the Bessel function $J_\nu(ka)$. These hybrid modes correspond to skew rays.

The theory is simplified by the assumption that the difference in index between the core and cladding materials is very small. This results in considerable mathematical simplification and very great simplification in the description of the mode fields, since it leads to the linearly polarised ($LP_{\nu\mu}$) field notation developed by Gloge [21]. In this case, ν is the azimuthal mode number and is used to give half the number of light points in each concentric light ring. The radial mode number μ is used to give the number of concentric light rings of the mode. The first ten modes of an optical waveguide are shown in figure 2.1 [22]. The fundamental mode is called LP_{01} and the next higher mode, LP_{11}. Using the ray approach, the order of a mode is dependent on the angle the ray makes with the core-cladding interface. The higher the angle the ray makes with the interface, the higher the mode number.

2.3 Mode Coupling

Figure 2.2 shows the field pattern of several low order modes in a planar dielectric slab waveguide. The order of the mode is equal to the number of field maxima across the guide and is also related to the angle made with the plane of the waveguide. The steeper the angle, the higher the order of the mode.

It is evident from this figure that the electric field of the guided modes are not completely confined to the core, but, instead, extend partially into the cladding. For low order modes the fields are tightly concentrated near the centre of the slab with little penetration into the cladding, whereas the fields of the higher order modes are

distributed more toward the edges and penetrate further into the cladding.

Further solutions of Maxwell's equations for the same boundary conditions reveals the existence of radiation modes that are not trapped in the core. The radiation field basically results from the optical power that is outside the fibre acceptance angle being refracted out of the core. This results in the appearance of cladding modes since some of this radiation is trapped due to the finite radius of the cladding.

As the light propagates along the fibre, mode coupling occurs between the cladding modes and the higher order core modes. A diffusion of power back and forth between the modes occurs which generally leads to a loss in power from the core modes. In practice, the cladding modes will be suppressed by a lossy coating which covers the fibre or they will scatter out of the fibre after travelling a certain distance because of roughness on the cladding surface.

A third type of mode that is present in an optical fibre is called a leaky mode. Leaky modes are only partially confined to the core region and attenuate by continuously radiating their power out of the core as they propagate along the fibre. This power radiation out of the waveguide is essentially based upon the upper and lower bounds that the boundary conditions for the solutions of Maxwell's equations impose on the propagation constant β.

2.4 Mode Cut-Off

A mode is cut off when its field in the cladding ceases to be evanescent and is detached from the guide, that is, the field in the cladding does not decay. The rate of decay of the field in the cladding is determined by the value of the constant γ. For large values of γ, the field is tightly concentrated inside and close to the core. With decreasing

values of γ, the field reaches out into the cladding, and for $\gamma = 0$ the field detaches itself from the guide.

An important parameter connected with the cut-off condition is the normalised frequency V (also known as the V number) and is defined by

$$V = k_c a = \frac{2\pi a}{\lambda_0}\sqrt{n_1^2 - n_2^2} \qquad 2.6$$

The cut-off parameters for all modes are obtained for a given order ν and corresponding root μ from Bessel functions. Figure 2.3 shows the allowed regions for various modes plotted against the V number for a step index fibre.

It can be seen therefore that for $V < 2.405$ that only one mode can propagate, this being the fundamental mode LP_{01} (HE_{11}). Using equation 2.6 enables the conditions for a single mode fibre to be determined.

2.5 Optical Waveguide Profiles

The term refractive index profile is used to describe the radial change of the refractive index from the axis of the fibre in the core glass toward the cladding glass. The propagation of the modes in an optical fibre depends on the shape of this refractive index profile.

The two main types are the step index profile and the graded index profile. These are shown schematically in figure 2.4. The number of modes N guided in the core glass is dependent on the normalised frequency V and also the refractive index profile [23] by the following equations.

For step index profile

$$N \approx \frac{V^2}{2} \qquad 2.7$$

and for a graded index profile

$$N \approx \frac{V^2}{4} \qquad 2.8$$

2.5.1 Step Index Profile

2.5.1.1 Multimode Fibre

Typical dimensions of a multimode step index fibre as shown in figure 2.4(a) are:

Core diameter 2a	100 μm
Cladding diameter D	140 μm
Core refractive index n_1	1.48
Cladding refractive index n_2	1.46

Light can only enter the fibre within a specific acceptance angle θ which is given by

$$\sin \theta = \sqrt{n_1^2 - n_2^2} \qquad 2.9$$

With the above parameters, the acceptance angle is approximately 14°.

In this type of waveguide, light is guided by many modes (thousands). Each mode travels a different distance and therefore arrives at different times at the end of the fibre. The distortion caused by the delay in time is called modal dispersion and causes a pulse of light to broaden in time.

This is bad for optical transmission as it reduces the transmission speed and transmission bandwidth.

This modal dispersion can be eliminated by operating the fibre under single mode conditions.

2.5.1.2 Single Mode Fibres

As already seen, in order to have just the one mode propagating, the normalised frequency V must be less than 2.405 (figure 2.3). This limits the size of the core for a given set of conditions. Typical dimensions for a single mode fibre are:

Mode field diameter 2w	10 μm
Cladding diameter D	125 μm
Core refractive index n_1	1.46
Refractive index difference Δ	0.003 = 3%
Acceptance angle	6.5°

So the core diameter and the acceptance angle are much smaller than in the case of a multimode fibre (figure 2.4(b)) which increases the difficulty in launching light into the fibre.

2.5.2 Graded Index Profile

The undesirable feature of step index multimode fibres is the modal dispersion. This can be greatly reduced by using a refractive index profile such that the refractive index of the core diminishes parabolically from a maximum n_1 at the fibre axis to n_2 at the cladding.

Typical dimensions of a graded index fibre:

Core diameter 2a	50 μm
Cladding diameter D	125 μm
Maximum core refractive index n_1	1.46
Refractive index difference Δ	0.01
Acceptance angle	12°

Due to the continuous change in refractive index, the rays are refracted continuously and their direction of propagation is changed (figure 2.4(c)). The rays oscillating around the fibre axis will still travel a longer path than the light ray along the axis, however, due to the lower refractive index these rays will travel faster which evens out the time delay.

3 Fibre Optic Sensors

3.1 Historical Development

The use of light in communication is not a new idea. In Agamemnon, the play by Aescylus written in the 5th century BC, the author writes that the news of Troy's downfall was passed on by fire signals via a long chain of relay stations from Asia Minor to Argos [24]. In 1790, Claude Chappe built an optical telegraph system which comprised of a chain of towers with moveable signalling arms. Using this system, information was transmitted 423 km from Paris to Strasbourg within six minutes [25].

Alexander Graham Bell developed the photophone in 1880 whereby voice signals could be transmitted by means of light [26]. However, this idea did not find practical application owing to the detrimental effect that the weather and visibility had on the quality of transmission.

Some ten years before Bell's invention, John Tyndall suggested a solution to the problems of transmission when he demonstrated that light could be guided in a stream of water [27]. The light was guided due to total internal reflection, the principle of which is applicable to todays optical fibres.

Following the work by Bell and Tyndall, it took until 1934 for a patent to be issued for an optical telephone system. The system designed by Joseph French described how voice signals could be transmitted by an optical cable network [28]. The cables, which were to be made of solid glass rods or some other material, were to have a low attenuation coefficient at the operating wavelength.

The technical realization of this concept was not achieved until 1958 when Schawlow

and Townes developed the laser, the first being successfully operated by Maiman in 1960 [29]. In 1962 it was recognized that laser could be manufactured from semiconductor materials and at the same time semiconductor photodiodes were developed which could be used as the receiver.

The final piece in the jigsaw, the optical cable came some time later.

Kao and Hockham [30] suggested in 1966 that glass fibres be used for light guidance. However, these fibres would have to show attenuation values of not more than 20 dB/km to be able to construct useful transmission systems and in 1965 optical waveguides still exhibited attenuations of the order 1000 dB/km.

The major breakthrough came in 1970 when step index fibres having attenuation values less than 20 dB/km at 633 nm were manufactured by Kapron et al [31] at Corning Glass Works. By 1972, optical fibres with graded index profiles achieved 4 dB/km.

Today, attenuation values of 0.2 dB/km at 1550nm are achieved in single mode fibres and the performance of the transmitters and receivers has also improved appreciably.

With the advent of low loss optical fibres, early workers became aware of the high sensitivity of fibres to external perturbations and sought ways to minimise these effects. An alternative approach was suggested by some workers who proposed exploiting the sensitivity of the fibres to develop a range of fibre optic sensors.

3.2 Introduction to Fibre Optic Sensors

Over recent years there has been a great of interest in the design and development of fibre optic sensors for scientific and industrial applications which has been due to the advances made in fibre optics technology for telecommunications and data transmission since the late 1960's. As a result a vast amount of work has taken place on the development of fibre optic cables, connectors, fusion splicers, sources, detectors and test equipment which has greatly increased availability and has brought about a considerable reduction in costs. The advantages of optical sensors over more conventional electricity based sensors are:

1 Freedom from electromagnetic interference (EMI)

2 Safety in hazardous (explosive vapour) environments

3 High electric isolation

4 Passive operation ie. no power required at remote sensing point

5 May be used for distributed sensors over long distances because of low losses achievable in optical transmission fibres

6 Can be made compatible with optically based data transmission systems

Optical sensors may be divided into two distinct classes. Firstly, those in which the optical fibre is itself the sensing medium (continuous or intrinsic sensors) and secondly, those which are optical in nature but make use of the optical fibre as a light guiding medium to and from the sensor (point or extrinsic sensors). Optical sensors may also be classified in the way the physical variable to be measured modulates the light. Light may be modulated by intensity, phase, polarisation, wavelength and spectral distribution. Sensors based on each of the modulation techniques mentioned are discussed below.

3.3 Intensity Modulated sensors

Designs based on intensity modulated sensors account for approximately half of all device designs published owing to the simplicity and potentially low cost of the technique. However optical sources are all prone to intensity drift with ageing and so a reference channel is needed.

The various designs published are reported in detail in this section.

3.3.1 Microbending Sensors

The microbend sensor capitalises on a phenomenon which is a source of loss in the telecommunications industry. Slight perturbations at the core cladding interface of the optical fibre known as microbends cause the light in the core to be coupled into the cladding and hence lost through radiation. Microbending loss is a significant design consideration in system applications of low loss optical fibres or loss modulation transducers.

Gambling et al [32] conducted a theoretical study of the transition and pure bend loss which can arise in a single mode fibre containing random bends. As a result, a modified mode coupling theory was produced which could be applied to general problems connected with curved fibres and has been used to predict transition losses.

Using this modified mode coupling theory, Gambling calculated that the loss induced at a transition between straight and curved sections of fibre and it was found that the radiated power was oscillatory at the beginning of the bend, which implies the existence of an exchange of power between the HE_{11} mode and the radiation modes. This relates to work carried out by Miyagi & Yip [33] and Gambling et al [34].

In an attempt to improve the stability and reproducibility of microbend devices, Lipscombe et al [35] performed a study of the effect of a single microbend on a single mode fibre. The experimental study showed the occurrence of oscillations in the output of a single mode fibre undergoing microbending as Gambling had proved theoretically.

In studying the effects of microbending on optical transmission for communication, Gloge [36] and Marcuse [37] have shown that random bends in the axis of the fibre need not be of large amplitude to cause significant losses in fibre transmission.

Gardner [38] obtained qualitative data on microbending loss by winding fibres under controlled tension onto a drum whose surface was not perfectly smooth. The tension forced the fibre to partially conform to the surface roughness resulting in random bending of the fibre axis which caused a measurable increase in the optical loss.

From his experiments, Gardner showed that by coating the fibre in a compliant medium, DuPont's Elvax 265, led to a reduction in the magnitude of the microbending loss. It was also demonstrated that the value of the numerical aperture had a considerable effect on the microbend loss.

Many workers have built and tested prototype sensors based on microbending.

In order to determine the potential sensitivity of a loss modulation transducer, Fields et al [39] investigated the simple bending loss transducer shown in figure 3.1. The transducer consisted of two mating ridge plates placed around a multimode step index silica fibre one of which was illuminated by a He-Ne laser, 632 nm wavelength. The upper plate was subjected to a load which produced a quasi sinusoidal distortion of the fibre. Figure 3.2 shows the transmission of the transducer as a function of the applied force. Note that attenuation increases with launch angle which is in accordance with

mode coupling theory ie. bound modes of high mode number (high launch angle) are more easily converted into radiation modes.

Fields et al calculated the minimum detectable pressure variation to be 1.3×10^{-4} Pa which is equal to that calculated by Bucaro et al [40] for an ideal fibre interferometric sensor.

Fields et al [41-42] took this further and developed a fibre optic hydrophone. The device is illustrated in figure 3.3. A multimode step index fibre passes between a pair of mating ridge plates containing ten periods of wavelength $\Lambda = 2$ mm. The experimental arrangement is shown in figure 3.4. The minimum detectable pressure for this device was 95 dB (re 1 μPa) and occurs at approximately 1.1 kHz. This low figure is due to the resonance of the structure reflecting its unsophisticated acoustic design.

Lagakos et al [43-44] built and tested a prototype fibre optic displacement sensor. The sensor configuration is shown in figure 3.5 with the experimental set up in figure 3.6. The cladding modes were stripped immediately prior to the sensing section. Microbending, induced by displacement, introduced mode coupling causing a significant increase in the light power in the cladding modes. The dark background made the cladding modes more sensitive to detection than the core modes.

Davis et al [45] showed that this dark field microbend modulated sensor (DFMM) arrangement could be employed in a fibre optic sensor array configuration employing time division multiplexing. The sensor array consisted of 25 channels extending over a distance of approximately 550 metres. The separation between channels was 22 metres corresponding to a 220 nanosecond difference in optical time of flight. A 200 nanosecond pulse of laser light was injected into the source fibre and as a result a

sequence of pulses was coupled into the sensor bus by the DFMM sensor cladding tap. This sequence of pulses, modulated by the signal, propagated to the photodetector.

An array such as this could be used to obtain data from a number of sensors deployed over a large area.

Harmer [46] described the construction and performance of a strain gauge based on microbending loss in an optical fibre and showed that sensitivity could be achieved with a reasonable environmental performance.

Another paper by Harmer [47] described a novel form of fibre optic refractometer where the critical angle of light at the probe liquid interface could be varied and controlled by introducing alternating bends in a multimode fibre. The refractometer was adapted for measurement of battery charge state in lead acid batteries. The probe tip consisted of a polystyrene fibre with three microbends. Ends of the fibre were epoxied into a red light emitting diode and photodetector. Temperature compensation was made possible by the use of a double probe using a polystyrene and glass fibre.

3.3.2 Reflective Sensors

In 1967 Kissinger [48] took out a U.S. patent on a fibre optic proximity probe using the guiding properties of optical fibres to give intensity modulation relating to the distance between the tip of a fibre probe and a reflecting target (figure 3.7).

Menadier et al [49], Lagace et al [50] and Frank [51] have all published designs based on this principle.

By using adjacent pairs of optical fibres, one transmitting and one receiving an optical signal, the distance to a reflecting surface can be measured by detecting the amount of light reflected. When the sending and receiving elements are in contact with the surface, no light is reflected to the receiving element. As the distance between the two increases, the cone of light from the transmitting element illuminates an increasingly larger area on the work surface. In effect, this area becomes the source of a secondary cone of light which in turn increasingly illuminates the receiving element. The relationship between surface displacement and receiver illumination remains essentially linear until the entire surface of the receiving element is illuminated by the reflected light at which point the curve reaches its peak. This is illustrated in figure 3.8. As the distance increases beyond this point, the illumination of the receiver decreases in approximately inverse proportion to the square of the distance.

Through the use of a large number of fibres, the fotonic sensor achieved the first claimed practical application of this principle.

Many designs based on this principle have been reported for use in fibre optic medical transducers [52-60].

Matsumoto et al [59] constructed the catheter tip transducer shown in figure 3.9. The bundle of fibres in the catheter are divided into two parts. One part is used for pressure measurement and the other for measurement of oxygen saturation. The pressure measuring optical fibres consist of two sections; one for transmitting light and the other for receiving light signals.

A metal tip containing the side hole was incorporated at the end of the catheter. The side hole was covered with a pressure sensitive watertight membrane, beneath which is a cantilever plate which moves with the pressure sensitive membrane. The end of the cantilever has a reflector which is parallel to the cross section of the fibre bundle. Any pressure on the membrane will press down the cantilever plate whereupon the reflector will change its position and angle with respect to the cross section of the fibre bundle. This change in position alters the amount of light which is reflected back through the outlet fibre and which is detected by the photoelectric transducer element. The output voltage of the element is thus proportional to the applied pressure.

The ratio of the area of inlet to outlet was chosen as one to ten in order to optimise the ratio of the signal component to the stationary component of reflected light from the outlet fibre and hence avoid saturating the photosensitive transducer.

Figure 3.10 shows relationship between the reflected intensity and the reflector deflection for different distances in an experimental model.

The primary disadvantage of these types of optical pressure sensors lies in their inherent environmental sensitivity. Because these devices measure absolute intensity, the output signal will be affected by intensity loss resulting from source intensity fluctuations and fibre microbend losses. Furthermore, pressure sensing schemes that measure the

distance to the diaphragm will be strongly affected by changes in this distance resulting from environmental effects such as vibration and thermal expansion.

In order to minimise these environmental sensitivity problems, Lawson and Tekippe [60] designed a pressure transducer that relied on diaphragm curvature rather than diaphragm displacement. The diaphragm deflection is derived from the ratio of light received by the collection fibres to that from the inside collection fibres. Because of this 'ratioing' procedure, this sensing technique automatically compensates for variation in the source intensity, for losses in the input fibres and for variations in the reflectivity of the diaphragm surface.

Furthermore, since the pressure determination depends on the diaphragm curvature instead of the distance between the fibres and the diaphragm, this technique is not affected by temperature or vibration effects that cause a displacement of the fibre bundle relative to the diaphragm. The system was also made to operate in a linear fashion. When the pressure differential across the diaphragm is zero the diaphragm will be flat and an equal amount of light will be reflected to the inside and outside fibres. With positive pressure the diaphragm will be concave and more light will be reflected to the outside collection fibres. With negative pressure the converse will be the case.

A miniaturised prototype reflectance sensor suitable for in-vivo medical applications was constructed and tested. The output signal, $Ln(I_{out}/I_{in})$ was recorded as a function of gauge pressure and was observed to be linear. The dynamic range was calculated to be 115 dB.

Although the size and pressure range of this prototype was engineered for in-vivo medical applications, the sensing technique has potential applicability in a variety of

military and commercial areas in which small size and environmental insensitivity are desired.

The reflection from a moving cantilever beam is the basis of a device developed commercially by ASEA Ltd [61] and now manufactured by Takaoka [62]. The sensing principle is shown in figure 3.11. The sensor is located at the end of a single strand optical fibre and is excited by light from a near infra-red LED which is transmitted from the instrument. Two optical signals of differing wavelengths return through the same fibre; one is a measurement signal, the other a reference. The measurement signal is generated by the effect that light collimated in a graded index lens is reflected in a cantilever beam which is deflected by acceleration. The light is then focused back towards the fibre, but due to the angular deflection of the collimated light beam, the focal point has been moved and the intensity of the light that returns in the fibre is modulated by acceleration. The reference signal makes it possible to compensate for losses in fibres and connectors and is generated from a neodymium doped glass inside the sensor by means of photoluminescence. This device, being mechanical in nature, has a very narrow frequency response of the order of 10-1000 Hz compared to existing piezo-ceramic transducers, 10 Hz - 30 kHz.

3.3.3 Moiré Fringe

High precision optical displacement sensors with sub micron resolution have been used in hostile environments in the machine tool industry since the mid 1950's [63].

If two optical gratings, consisting of alternate parallel strips of clear and opaque materials of equal width, are overlaid, light will either be transmitted or obstructed depending on whether or not the clear areas coincide. If the lines on one grating are aligned at a small angle relative to those on the other then the loci of their intersections will be visible as dark moiré fringes running approximately at right angles to the grating lines.

Translation of one grating over the other in a direction perpendicular to its rulings causes these fringes to move in a direction perpendicular to this movement. If a collimated light source is used to illuminate an area of the overlaid gratings and a photoelectric device is positioned to detect the transmitted light then a periodic electrical signal is produced as the gratings are translated, its periodicity corresponding with a grating movement of one grating period.

The measurement accuracy of the system is fundamentally limited only by the precision with which the gratings have been ruled.

The potential offered by moiré fringes for use with optical fibres as a universal process control displacement sensor was recognised by Jones and Spooncer [64] who initially foresaw their use in incremental, fringe counting applications as a way of overcoming the need for referencing which exists in analogue intensity modulated systems. However long term semi-static measurements such as those encounted in process control applications do not lend themselves to incremental sensing because of the danger of a

loss of datum caused by noise pick up or power supply interruptions. Recent work by Jones and Spooncer [65-68] has been aimed at producing an absolute moiré fringe displacement sensor by using two gratings with their lines parallel, as an optical shutter.

Sayce [69] suggests that gratings with spatial frequencies of less than 25 lines/mm can be considered as being purely mechanical in their action whereas finer gratings become increasingly dominated by diffraction effects.

In an amplitude modulated system effects other than changes in the measurand such as variations in emission from the light source or in fibre attenuation may alter the light level.

Compensation may be provided (at a cost) if a reference light signal is installed but the problem can be avoided if amplitude measurement is replaced by moiré fringe counting.

Murray [70] has described experimental pressure and temperature sensors using gratings.

In work carried out by Jones et al [71] infra red (IR) light (820nm) from a light emitting diode (LED) was coupled into a 300μm diameter core step index fibre, with a numerical aperture of 0.48 approximately 1m long (maximum launch power 70mW), led to the modulator and returned via a second similar link to a PIN photodiode operated at zero bias to reduce noise.

The sensor, shown in figure 3.12, consisting of two parallel gratings about 5mm x 10mm is interposed between the sapphire spheres. One grating is fixed relative to the input fibre and the other mounted on a pair of spring flexures to ensure parallel motion

and to provide a restoring force, is traversed across the fixed grating in a direction perpendicular to the grating lines. The typical output/displacement characteristics of the modulator, I(x), are shown in figure 3.13 for two different bar/space ratios.

Both the 1:1 and 7:3 gratings showed good linearity with a new serrisoidal profile but the 7:3 grating showed higher sensitivity and better modulation depth and extinction ratio. As the grating pitch reduces, the characteristic changes from the serrisoidal shape to an almost sinusoidal profile at 25 lines/mm, with reduced linearity range and modulation depth.

In other work carried out by Jones and Spooncer [64], gratings were used which have a line spacing of 4μm. For each grating cycle the output rose to 14mV and fell to 7mV and fringes could be counted visually. Identification of both the peaks and the troughs of the cycle gave a resolution of 2μm. Initial results were encouraging with fringe counts of 100 in either direction corresponding precisely with a 0.4mm micrometer movement.

The moiré fringe modulator is a good prospect for development as an accurate measuring instrument. It has adequate resolution and a digital output which does not suffer from the problems of amplitude measurement. It has relatively low attenuation and a linear output displacement characteristic. It can still however only give an absolute output which limits its usefulness. An absolute form of output must be developed before moiré fringe modulation can be considered for use as an optical transducer in a process plant.

In a paper by Spillman [72], a multimode fibre optic hydrophone is described which is based on the schlieren technique. A schematic of the device is shown in figure 3.14.

Light from one multimode fibre is collimated by a gradient index microlens and passed through an opposed grating structure after which it is focussed down onto an output fibre by a second microlens. The opposed grating structure is coupled to 2 flexible diaphragms which are attached to the top and bottom of the hydrophone housing. Deflection of the diaphragms by ac pressure changes causes relative motion of the two gratings and thereby modulating the amount of light coupled between input and output fibres.

The minimum detectable displacement for this device was calculated as 3.4E-03Å and the total insertion loss of the device was 18dB and dynamic range of 125dB.

3.3.4 Optical wedge amplitude modulator

An optical wedge is a variable optical attenuator which may be straight or circular. It is normally graded so that the attenuation varies logarithmically with translational or angular displacement. The principle is shown in figure 3.15. The wedge used in trials by Jones and Spooncer [71] was of a translational form.

The configuration forms a simple optical displacement transducer in which the logarithm of the output voltage is proportional to input displacement. It also has advantages in that

1 the light beam geometry is unchanged by the displacement modulation so that the system is independent of variations in light intensity across the beam

2 the diameter of the light beam is sufficiently large (3mm) to average minor irregularities in the optical transmission of the wedge and to limit the effects of vibration

Displacement output characteristics of the modulator were measured at various light levels corresponding to optical powers launched into the system of between 12.5mW and 140mW. Traverses over a distance of 10mm at each light level gave characteristics which were almost logarithmically linear; maximum deviation from linearity was 0.1mm. The gradient of the characteristics equivalent to the sensitivity of the system varied by approximately $\pm 3\%$.

Additional wedges could be combined to give even greater sensitivity, but increased sensitivity coupled with better repeatability can be obtained using parallel grating structures.

Similar devices have been used in high sensitivity fibre optic hydrophones [72-73].

3.3.5 Moving Ball Lenses

This technique offers a high opto-mechanical sensitivity and the principle is illustrated in figure 3.16. The light of the transmitting fibre, intensity I_0, is focused by a ball lens onto the faces of two receiving fibres. A displacement of the ball lens, in the plane containing the receiving fibres, changes the distribution of the light into those fibres and it has been shown by Dotsch et al [74] that the log of the ratio I_1/I_2 exhibits a linear dependence on the displacement of the lens.

One advantage of sensors utilising this principle is that the ratio of light intensity in the two receiving fibres is independent of the primary intensity and is therefore immune to the usual drift problem associated with intensity modulated sensors.

Dotsch et al [74] demonstrated the possible use of the moving lens arrangement in optical switches, differential pressure sensors and in particular temperature sensing applications. A temperature sensor was produced the output (the ratio I_1/I_2) of which showed a linear response over the 20 - 90°C temperature range.

3.3.6 Frustrated Total Internal Reflection

The mechanism of frustrated internal reflection (FTIR) may be exploited to produce modulation of light passing through an optical fibre as shown in figure 3.17 [75]. The two fibre ends are polished at an angle to the fibre axis large enough to cause TIR for all modes propagating in the fibre. By bringing the two fibre ends sufficiently near to one another a large fraction of light power can be coupled between the two fibres. Modulating the gap thickness x between the two fibres causes the amount of light power coupled between the fibres to be modulated. Spillman et al [75] developed a computer

program to model the sensitivity of the structure shown in figure 3.17 as a function of vertical displacement.

Figure 3.18 shows the results of this model. It can be seen that changing the fibre gap by a small fraction of a wavelength of light produces a large change in relative intensity of the transmitted light from one fibre to the other. The optical sensitivity increases as r approaches 90°.

An experimental sensor based on FTIR was constructed as shown in figure 3.19. Fibres with an 85mm diameter, NA = 0.2 were used and were cut at 76°. Light from a He-Ne laser was used.

Although the constructed device was less sensitive than theoretical predictions, its performance is substantially better than any other multimode fibre optic hydrophone reported to date.

3.3.7 Level Sensors

In 1954 Geake [77] described an optical dipstick - a probe using the critical internal reflection of light to detect a liquid surface. The basic arrangement is shown in figure 3.20. If a transparent rod has as 90° conical or bevelled end, light travelling down the rod will be totally internally reflected twice and will pass straight back up the rod - provided that the tip of the rod is dry; if it is wet then the light leaves the rod at the tip and does not return up the rod. Plastics such as perspex, polystyrene or polycarbonate are usually satisfactory as gauge materials while in solvents, glass, pyrex or quartz may be used.

Hood and Oldham [78] and Baumbick and Alexander [79] have described a different

type of gauge element which uses a single U shaped rod; the rod acts as a light pipe when dry but light leaves it at the bend when it is wet. These arrangements do not discriminate between liquids. However, Geake [80] describes a possible arrangement which operates within a restricted range of refractive index and is able to detect the interface between two specific liquids. This is required in processes where a tank contains two immiscible liquids and one wishes to know the level of the lower one.

3.3.8 Switching

A very high percentage of monitoring concerns switching at prescribed values of the measurands. Thus for example, process plants and aircraft contain numerous microswitches and valves and it is not surprising therefore that manufacturers now produce switches of one form or another.

Control or alarm switches for the common physical variable utilise a basic mechanical sensing mechanism which operates an electrical microswitch at a predetermined set point.

The optical microswitch with fibre links can be employed in all applications where a standard electrical microswitch is currently used and a typical arrangement using an opaque shutter is shown in figure 3.21 [81]. In the off state there is a low light transmission to provide continuous check of the integrity of the complete optical loop.

3.4 Phase Modulated Sensors

3.4.1 Mach Zehnder Interferometer

Tveten et al [82] and Miles et al [83] have reported details of a simplified device employed to demonstrate the principle of operation of a fibre optic accelerometer. The accelerometer consisted of a mass suspended between two fibres or a mass suspended from a single fibre as shown in figure 3.22. When the device is accelerated in the indicated direction, a strain $\delta L/L$ is introduced in the supporting fibres proportional to the acceleration a.

The measurement of the small change in optical path induced in the fibre was accomplished using an all fibre Mach Zehnder interferometer. The accelerometer exhibited detection sensitivity of less than 1 μg with excellent linearity as a function of acceleration. Any practical device based on this principle would require the inertial mass to be constrained to eliminate lateral movement.

Davis et al [84] have also tested similar devices.

A fibre optic accelerometer which incorporates two right circular cylinders wrapped with separate single mode optical fibres has been tested by Furlong et al [85]. The cylinders are affixed on opposite ends in their housing structure. When one cylinder experiences an acceleration induced radial reduction, the other undergoes a radial expansion of the same amount. This configuration has two main advantages. Firstly, the sensitivity is increased by a factor of two when the phase information is processed differentially and secondly, effects of lateral acceleration are cancelled out. Furlong et al report that this device displays excellent frequency response and linearity characteristics.

Bucaro et al [86] have demonstrated the feasibility of employing acousto optic interactions in an optical fibre to produce a sensitive acoustic detector. The experimental configuration is shown in figure 3.23. The technique utilises the phase modulation of an optical beam in a submerged optical fibre coil by sound waves propagating in a fluid. Analysis of the results indicated that the sensitivity of the technique compares well with that of the best available hydrophone.

Devices based on Mach Zehnder interferometer have also been used to measure magnetic fields [87-88] and pressure [89].

The possibility of detecting weak magnetic fields by the magnetostrictive perturbation of optical fibres was proposed by Yariv and Windsor [90]. The basic principle of operation is associated with the measurement of the longitudinal strain induced in the optical fibre by a magnetostrictive jacket.

The magnetostrictive materials used by Jones et al [87] were all amorphous metals. They were either in the form of a jacket sputtered onto the cladding of the fibre for approximately 50 mm of its length or metallic glass ribbons to which the bared fibre was bonded. Results were obtained for various configurations of magnetostrictive jacket.

Initial investigations by Dandridge et al [88] attempted to evaluate the sensitivity of fibre optic magnetic sensors for fields in the range from 10^{-5} Oe to 10 Oe for time varying signals ranging from 100 Hz to 10 kHz. Figure 3.24 illustrates the linearity of the sensor response against the applied field.

3.4.2 Michelson Interferometer

An alternative interferometer configuration is the Michelson which is similar to the Mach Zehnder. The advantage in this case is that only a single fibre direction coupler is required and consequently the theoretical fringe visibility is unity. Another advantage is in remote sensing where only a single fibre is needed between the source and sensor.

Parmigiani [91] has reported high sensitivity vibration measurements by Michelson polarising interferometer with an optical fibre probe. The smallest detected velocity of vibration was 30.1 μm/s over a frequency range of 1-400 Hz. The feasibility of the technique had been reported earlier by Ueha et al [92].

A multimode fibre Michelson interferometer has been demonstrated by Imai et al [93] where bulk optic components were used and sensing was carried out using an external mirror. Kashap & Nayar [94] reported an all-fibre Michelson interferometer to measure acoustic signals. This consisted of a single mode fibre directional coupler with mirrors formed on the cleaved ends of both fibres on the same side of the coupler. The results indicated a similar performance to that of a Mach Zehnder interferometer.

3.4.3 Sagnac Interferometer

An optical device capable of detecting the rotation of a securely coupled reference system was first demonstrated by Sagnac in 1913 [95]. The device is a ring interferometer in which light beams propagate in opposite directions over the same closed path.

Bukhman et al [96] described a method of measuring rotation velocities in a fibre optic ring interferometer which was able to measure velocities of rotation as low as 0.3 degrees per second.

Goldstein and Goss [97] constructed and tested a single axis rotation sensor utilising a 200 metre single mode fibre in a 30 centimetre diameter coil. Figure 3.25 shows a schematic diagram of the sensor system. The output of silicon detectors viewed two complementary interference patterns electronically differenced to obtain a rotation dependent signal. The response was linear over a rotation range of 10^{-4} to 10^{-1} rads/second.

Udd has described a series of fibre optic acoustic sensors based on the Sagnac effect. Details were also given on how the sensitivity of the system could be optimised [98].

3.4.4 Fabry Perot Interferometer

Sensors which can be interrogated by the use of colour offer some progress towards a true digital system. One approach to using colour is to consider the Fabry Perot white light interferometer [99] as a general purpose displacement sensor for use in physical measurement. When addressed by a broadband source, multiple reflections between the two lightly silvered mirror surfaces results in a number of transmission fringes in the output spectrum. The position of these fringes is a unique representation of the mirror spacing. A changing physical parameter, for example temperature or pressure, can be translated into mirror displacement and hence a shift in the transmission fringes.

Cox and Jones [100] investigated a temperature sensor, based on Fabry Perot interferometry, as shown in figure 3.26. The main problems associated with this device was the alignment of the mirrored surfaces which led to a loss is fringe sharpness. Initial results were promising.

Kist and Drope [101] have also investigated a Fabry Perot resonator for use as a

temperature sensor and also an optical spectrum analyzer.

The main problem with conventional flat Fabry Perot interferometers for use in sensing applications has been their vulnerability to mechanically induced misalignment. Jackson et al [102] have reported that this problem does not arise with Confocal Fabry Perot interferometers.

3.5 Polarisation Modulation

The photoelastic effect was discovered by Sir David Brewster in 1816 who found that under the application of mechanical stress normally transparent isotropic materials became optically anisotropic. The phenomenon is known as birefringence because the refractive index of the materials, and hence, the velocity of light within them varies with the plane of polarisation.

If a photoelastic material is stressed and set between two crossed polaroids, the plane polarised incident light falling normally onto the material is split into two components polarised at right angles to each other. These are transmitted through the material with different velocities so that on emergence there is a phase difference between them which is proportional to the difference in principle stresses. These two waves on passing through the second polaroid or analyzer are both resolved into a plane parallel to the axis of the analyzer and therefore interfere because of the phase difference.

In a monochromatic system, destructive interference will occur extinguishing the light when the delay between the two waves is equivalent to an integral number of wavelengths.

Variations in light polarisation are difficult to interpret in optical fibre transducers since the fibre is often itself inherently birefringent and this birefringence varies with time [103]. However, sensors which rely on detecting polarisation can be built.

Magnetic field measurement for current monitoring of high voltage power lines has been made by wrapping a single mode fibre coil around the transmission cable [104-109].

Faraday rotation simply produces a polarisation rotation in the fibre proportional to the magnetic field produced by the wire. For a typical system, using ten turns of monomode fibre it is found that the polarisation rotation is 3.3×10^{-3} degrees per ampere. Polarimeters with a resolution of 0.1 degrees are readily available giving a current resolution of 30 A.

Papp and Harms [105-106] and Aulich et al [107] found measurement accuracy to be 0.24% in the current range 50 - 1200 A and the signal to noise ratio to be 85dB at 1000 A. Reduction of the high birefringence due to intrinsic stresses in the fibre is important. Single mode fibres with low birefringence are sought for this device but it has been pointed out that highly birefringent fibres can be used by twisting the fibre to suppress the birefringence [110]. Fibres made by spinning the preform during pulling should be valuable for this application [111].

In the polarimeter [112] light of a known polarisation is launched into a single mode fibre which is attached to a piece of magnetostrictive material. Typically the fibre is wound around and bonded to a nickel cylinder. An analysing polariser is arranged at the other end of the fibre such that in the zero field condition no light reaches the detector behind it. Application of a magnetic field strains the fibre bonded to the stretcher and the consequent induced birefringence modifies the state of polarisation of light at the output of the fibre and results in a signal at the detector.

Shibata [113] considered using the electrooptic effect of certain crystals to be suitable for measuring voltage or electric field of high voltage machines and several sensors have been developed. In these sensors $LiNbO_3$, $Bi_{12}SiO_{20}$ [114] and $Bi_4Ge_3O_{12}$ have been used as electro-optic crystals.

Figure 3.27 shows the make-up of the sensor. To prevent the modal noise, an LED is used as the light source and light is propagated in the optical fibre to reach the probe. The current of the LED is kept constant and the intensity of the light incident on the probe is approximately constant too.

Figure 3.28 shows the probe. In this sensor the light is propagated along <110> direction of $Bi_4Ge_3O_{12}$ crystals and the electric field is applied along the $<\bar{1}10>$ direction, that is, the sensor is formed in transverse mode of modulation.

The measured temperature dependence of this sensor is $\pm 0.5\%$ between -15 and 60°C. This result implies that the sensor has very high accuracy and it is considered that the electrooptic coeffecient has no dependence in this temperature range.

The sensitivity of this sensor depends on the angle between its probe and the electric field.

Hamasaki et al [115] reported the development of an optical sensor for the measurement of high electric field intensity (OPSEF) using the characteristic electro-optical effect of single crystal of $Bi_{12}SiO_{20}$. One of the most outstanding features of this system is that the temperature dependency of the OPSEF is better than $\pm 3\%$ in the temperature range from -15 to 70°C.

Figure 3.29 shows the basic structure. $Bi_{12}SiO_{20}$ shows optical activity as well as an electro-optic effect. The electro-optic coefficient is 4.35×10^{-12} cm/V. The optical activity is 10.5°/mm which means that the linearly polarised beam is rotated 10.5° when no electric field is applied.

A sensitive single fibre acoustic sensor has been constructed [116] by securing single

mode fibre to the diaphragm of an optical cavity. The acoustic pressure induced a birefringence in the fibre and alters the state of polarisation of the light.

The first working model of the polarisation hydrophone is shown schematically in figure 3.30. The acoustic cavity cosists of an aluminium housing that supports aluminium diaphragms (2.54cm x 15.2cm x 0.16cm) on opposing sides. Half cylinders are attached to each end of the cavity to provide support for the optical fibre windings. Sixteen turns of bare single mode fibre are wound lengthwise over the centres of the diaphragms and secured in place with optical cement. The unit contained a Helmholtz tube that connects the acoustic cavity to a reservoir sealed with a compliant rubber cap. The tube allowed fluid to pass slowly in and out of the cavity thereby eliminating low frequency response and compensating for changes in hydrostatic pressure. The hydrophone included opposing acoustic diaphragms in order to eliminate acceleration effects. The sensitivity to longitudinal accelerations was negligible because both polarisation states of the fibre were equally affected.

The working model of the single fibre polarisation hydrophone was demonstrated and was shown to be capable of detecting acoustic pressures as low as 33 dB, have a linear dynamic range of at least 88 dB and exhibit a sensitivity comparable to that of a Mach Zehnder interferometer.

The development of an optical pressure sensor in which pressure acts directly to stress the photoelastic material without any intervening mechanism such as a diaphragm follows logically and a photoelastic pressure sensor with no moving parts has been built by Jones and Spooncer [117].

Figure 3.31 shows the initial design for such a sensor.

Light transmission through the system was determined as a function of the applied pressure measured by a sub standard pressure gauge.

Spillman and McMahon [118] also showed that the photoelastic effect can be used to detect stress as illustrated in figure 3.32.

The paper by Spillman and McMahon [118] described the theory behind photoelastic fibre optic sensors and detailed the fabrication, testing and performance of such a sensor.

Polarisation sensors have been limited by inherent fibre characteristics (stress induced birefringence, non circularity of core) but with new fabrication techniques emerging and a better understanding of polarisation effects in fibres, this should lead to improved devices and more varied applications.

3.6 Wavelength Modulation

The intensity referencing requirement of intensity modulators may be avoided using a digital system and sensors which can be stimulated by the use of colour, lead towards a true digital sensor.

In 1982, Dakin [119] was granted a US patent for a transducer which converted angular displacement into a wavelength change. This device made use of a grating monochromator and is shown in figure 3.33. Angular displacement could be determined over a range of 40° which was useful but of limited application.

However, Hutley et al [120] applied the same principle to measure linear displacement by utilising the properties of the Fresnel zone plate. The focal length of a zone plate is inversely proportional to wavelength. The device is shown in figure 3.34 and the output of the system was found to be linear with respect to displacement.

A practical vibration sensor for stator coil measurements in an electric generator has been developed using two coloured filters in a shutter arrangement with two matched LED sources. The output was linear over a 400mm range [121].

Many temperature sensors have been devised with wavelength dependent effects. The band edge of semiconductors (eg. GaAs, CdS, Se) shift strongly with temperature and are situated at convenient wavelengths for the use of LED sources, but are limited to moderate temperatures. Coloured filter glasses contain coloidal suspensions of semiconductors in glass and exhibit sharp cut offs with temperature shifts of 0.1 to 0.5 nm/°C. Monitoring the absorption at a single wavelength converts this to an amplitude measurement with a resolution of 2°C in a temperature range 20 to 200°C [122]. A similar concept has been used in a fibre probe with a Europium doped core [79]. The

absorption is monitored by two LED's at 610 and 940 nm giving an accuracy of 2°C in the range 0 to 400°C. However long term drifts equivalent to an error of 6°C or more occur due to wavelength shifts in the LED light emission.

One device uses a Fabry Perot cavity with an air gap which varies with temperature [123]. This is achieved by mounting up a small metal expansion sleeve between two glass plates or lenses. The first order interference peak has a wavelength shift of 36 nm/°C and is read by a scanned wavelength source to give a resolution of better than 1°C in a 100°C range.

Chemical reactions have many wavelength related effects. A good example is a device which has existed for many years, a fibre optic medical probe for in vivo oximetry [124]. The oxygen concentration in the blood is determined by monitoring the absorption of oxygen saturated haemoglobin near its peak absorption (660 nm) and normalising for the absorption of unsaturated haemoglobin at a wavelength where the two absorptions are equal (805 nm).

One form of wavelength modulation is simply Doppler shift which may be produced by, for instance, backscatter from moving particles at the end of the fibre. This forms the basis of the fibre optic anenometer [109] which requires the use of a coherent source.

A more general form of wavelength modulation may occur when incoherent light is transmitted along a large core fibre to phosphorescent material. Light emitted from the phosphor may be at a different wavelength. The wavelength and/or intensity of the return light will be a function of the parameter to be measured and hence remote monitoring may be performed. Clearly much depends on the stability of both the light source and the phosphor.

One example of such a system is the fluoroptic temperature sensor now available as a commercial product. A rare earth phosphor is illuminated by white light along a short (a few metres) length of large core optical fibre. The light exites the phosphor which emits a number of lines. Two of these lines are selected using the filters in the receiver (figure 3.35). The ratio of the intensities of the chosen lines which are at 540 and 630 nm is a single valued function of the temperature of the phosphor. Thus by measuring this ratio, an exact measure of the temperature - which is independent of the light intensity - may be made. Resolution of 0.1°C over the range -50 to 250°C is possible. The instrument is in practice rather complex requiring calibration during thermal stabilisation since the sensitivities of even matched photodetectors do not track at two different wavelengths as temperature varies.

The device is well suited to medical applications - for instance monitoring tissue temperature - due to its small size and rapid response time.

It is evident that many optical phenomena produce wavelength changes as a function of physical variables and that spectroscopy has always been one of the most accurate optical measurement techniques for precision, resolution and dynamic range. Thus wavelength scanned systems offer the potential for very high performance systems at the expense of increased sophistication in the instrumentation. However few practical systems have been constructed and the sources of error (eg wavelength shifts in light sources, wavelength dependent transmission variations) have not yet been fully evaluated.

Successful implementation of wavelength modulated sensors depends on the development of a cheap, good resolution spectrometer such as a CCD or photodiode square matrix detector array.

3.7 Spectral Distribution

There has been very little information published in the literature on sensors based upon spectral distribution modulation. Culshaw [103] in a review of optical fibre transducers discussed spectral distribution transducers briefly.

Spectral distribution modulation is very similar to that of wavelength modulation described above. A distinction may be made by taking as an example radiation from a black body. This radiation varies fairly slowly with temperature but optical fibre probes may be used to monitor the variations. One well known form is the optical fibre pyrometer, which simply uses a fibre to guide the light from a hot zone to the instrument, a normal pyrometer with slightly different optical components.

Another example is to use the radiation itself as the signal to an electronic pyrometer. The pyrometer may take many forms but its function is one of spectral analysis. In the case of a black body temperature probe for use at 200°C, it is possible to use the spectral filtering properties of a photodiode.

4 The Optical Properties of Materials

4.1 Refractive Index

When light propagates through a dielectric material, it travels with a velocity v. Since the dielectric is optically more dense than free space, v is less than c, the speed of light in a vacuum. From Maxwell's equations, it can be shown that v is related to c by the equation

$$\frac{c}{v} = \sqrt{\frac{\epsilon\mu}{\epsilon_0\mu_0}} \qquad 4.1$$

where

ϵ/ϵ_0 permittivity of material/free space

μ/μ_0 permeability of material/free space

This ratio is more commonly referred to as the refractive index, n.

4.2 Snell's Law

In 1621, Willebrord Snell related experimentally the angle of incidence α and the angle of refraction β to the refractive indices between two media

$$n_1 \sin\alpha = n_2 \sin\beta \qquad 4.2$$

This equation is generally quoted for the case when light travels from air (n = 1) into a medium n. The equation therefore becomes

$$\frac{\sin\alpha}{\sin\beta} = n \qquad 4.3$$

4.3 Fresnel's Equations

When a beam of light impinges on the surface of a transparent medium, the light is not only transmitted via the refracted ray but some is reflected. The intensity of the reflected beam relative to the intensity of the incident beam depends on the angle of incidence α and the angle of refraction β and is given by Fresnel's equation.

$$\frac{I_r}{I_0} = \frac{1}{2}\left[\frac{\sin^2(\alpha-\beta)}{\sin^2(\alpha+\beta)} + \frac{\tan^2(\alpha-\beta)}{\tan^2(\alpha+\beta)}\right] \qquad 4.4$$

This equation is illustrated graphically in figure 4.1. From this it can be seen that even when the light is incident normally, approximately 5% is reflected.

4.4 Dispersion and The Lorentz Theory

When a beam of white light is incident upon a material of index n at an angle α, the beam is split into different coloured rays each one having its own particular angle of refraction β. From this, it is apparent that the refractive index of the material is dependent on the wavelength of the light. The effect is known as dispersion and is illustrated graphically in figure 4.2.

The simple classical model of Lorentz gives an adequate qualitative picture of the phenomenon of dispersion. This section describes the physical basis of the model and quotes equations derived from it. Full accounts are given by Seitz [125] and Ditchburn [126].

The model pictures the material as consisting of electrons bound to equilibrium positions by linear forces ie. if an electron is displaced from its equilibrium position by

a distance y it experiences a force Ky acting to restore it to that position. It is assumed that each electron is also subjected to a damping force which is proportional to its velocity dy/dt. If the electrons are subjected to the alternating electric field of a light wave of amplitude E they vibrate in response to the field. The equation of motion of each electron is therefore

$$m\frac{d^2y}{dt^2} + 2\pi m\gamma\frac{dy}{dt} + Ky + eE_0e^{2\pi ivt} = 0 \qquad 4.5$$

where v is the frequency of the light wave e and m are respectively the electronic charge and mass and γ is the damping constant. The solution of the equation is

$$y = \frac{-(e/4\pi^2m)E_0e^{(2\pi vt-\phi)}}{\sqrt{(\nu_0^2-\nu^2)^2+\gamma^2\nu^2}} \qquad 4.6$$

where

$$\nu_0 = \sqrt{\frac{K}{4\pi^2m}} \qquad 4.7$$

and

$$\phi = \tan^{-1}\left(\frac{\gamma\nu}{\nu_0^2-\nu^2}\right) \qquad 4.8$$

Thus the electron displacement varies periodically, the phase differing by ϕ from that of the light wave. ν_0 is the natural frequency of oscillation of the electron. The dielectric constant ε of a material containing n_0 such electrons per unit volume is given by

$$\epsilon = 1+4\pi\alpha = 1+\frac{(n_0e^2/m\pi)(\nu_0^2-\nu^2)}{(\nu_0^2-\nu^2)^2+\gamma^2\nu^2} \qquad 4.9$$

and the absorption coefficient η by

$$\eta = \left(\frac{2n_0e^2}{mc}\right)\left(\frac{\gamma\nu^2}{(\nu_0^2-\nu^2)^2+\gamma^2\nu^2}\right) \qquad 4.10$$

where c is the velocity of light in vacuo. The variations of α and η are shown in figure 4.3. The region of frequencies which is of interest when considering the dispersion properties of optical glasses is that to the left of the absorption maximum ie. on the long wavelength side of the absorption band. At wavelengths well removed from the band η is low and $(\nu_0^2-\nu^2)$ is large compared with $\gamma^2\nu^2$. The equation for ε then simplifies to

$$\epsilon = 1+\frac{n_0e^2/m\pi}{\nu_0^2-\nu^2} = n^2 \qquad 4.11$$

Thus the refractive index increases as the absorption band is approached. This is shown in figure 4.2 for a number of crystalline alkali halides all of which have strong absorption bands in the ultra-violet. The nearer the band is to the visible part of the spectrum the more marked is the dispersion.

The variation of refractive index of transparent materials is more complicated than given by equation 4.11 due to the Lorentz theory being an over simplification and due to the fact that any real material has more than one strong absorption band.

4.5 Molecular Polarisability

The density change resulting from a thermal or mechanical stress is accompanied by some change in molecular or atomic polarisability. The most comprehensive theory is due to Mueller [127-128] who considers the following factors involved in change of refractive index of a solid under applied stress:

1 change of density
2 change of the Lorentz-Lorenz field
3 change of the coulomb field
4 change in the intrinsic polarisabilities of the atoms

Mueller was the first investigator to recognize the importance of the last factor. The theory has been applied so far only to cubic crystals and isotropic solids because in these cases the symmetry is such that the coulomb field can be taken to be zero. Under hydrostatic pressure the symmetry is unchanged and the coulomb field remains zero but the Lorentz-Lorenz field may change because of the change in density.

There are two principal theoretical relationships relating the index and density, the Lorentz-Lorenz,

$$\frac{n^2-1}{n^2+1}\left(\frac{1}{\rho}\right) = \alpha_1 \qquad 4.12$$

and the Drude

$$\frac{n^2-1}{\rho} = \alpha_2 \qquad 4.13$$

where ρ is the density and α_1, α_2 are the respective polarisabilities.

In deriving the Lorentz-Lorenz equation the local field has been accounted for through

the theoretical value $4\pi P/3$ where P is the polarisation of the medium and the change in local field with density is accounted for in the equation. The change in the local field has been ignored in the Drude equation. Krishnan and Roy [129] have shown the equivalence of the Lorentz-Lorenz and Drude equations in expressing the frequency dependence of the refractive index and have shown that the Drude expression accounts for the local field by incorporating its effect into the value of the fundamental absorption frequency. However equation 4.13 is a simplified version of the generalised Drude equation and is valid only at a single frequency. When written in the form of equation 4.13 it is implied that the change in the local field with density has been ignored.

If α_1 and α_2 are constant, equation 4.12 and 4.13 may be differentiated to obtain the change of index with density. This was first done by Pockels [130] who obtained the expressions

$$\rho\frac{\partial n}{\partial \rho} = \frac{(n^2-1)(n^2+2)}{6n} \qquad 4.14$$

$$\rho\frac{\partial n}{\partial \rho} = \frac{n^2-1}{2n} \qquad 4.15$$

corresponding to the Lorentz-Lorenz and Drude formulations respectively.

The partial derivatives are used to indicate that there may be change in atomic polarisability which is neglected. Mueller [127-128] introduced the strain polarisability parameter λ_0 to evaluate the change in polarisability by means of the relationship

$$\rho\frac{dn}{d\rho} = (1-\lambda_0)\rho\frac{\partial n}{\partial \rho} \qquad 4.16$$

4.6 The Change in Refractive Index with Pressure, dn/dP

Many transparent amorphous materials that are optically isotropic when unstressed become optically anisotropic and display characteristics similar to crystals when subject to stress. Whilst the loads are maintained, these effects persist and disappear when the load is removed. Sir David Brewster was the first to observe this phenomena, known as temporary double refraction, in 1816. This physical behaviour is the basis of photoelasticity.

At each point in a loaded body there are three mutually perpendicular planes which are free of shear stress. These planes are defined as principal planes and the normal stresses acting on them are known as the principal stresses.

In general, the three principal stresses at a point have different magnitudes. A geometric representation that provides an insight into the nature of the state of stress at a point is known as the stress ellipsoid. Each radius of this ellipsoid represents the magnitude of the resultant stress on some plane through the point.

The optical anisotropy which develops as a result of the stress can also be represented by an ellipsoid known as the index ellipsoid. The semi-axes of the index ellipsoid represent the principal indices of refraction of the material at that point as shown in figure 4.4. For a material which is optically anisotropic the three principal indices of refraction are equal and the index ellipsoid becomes a sphere. Hence, the refractive index is the same in all directions. The relationship between the two quantities is known as the stress optic law.

The theory which relates changes in indices of refraction of a material exhibiting temporary double refraction to the state of stress in the material is due to Maxwell who

reported the phenomenon in 1853 [131]. Maxwell noted that the changes in indices of refraction were linearly proportional to the loads (thus to stress or strain for linearly elastic materials). The relationships are

$$n_1 - n_0 = C_1\sigma_1 + C_2(\sigma_2+\sigma_3)$$

$$n_2 - n_0 = C_1\sigma_2 + C_2(\sigma_3+\sigma_1) \qquad 4.17$$

$$n_3 - n_0 = C_1\sigma_3 + C_2(\sigma_1+\sigma_2)$$

where

σ_1, σ_2, σ_3 are the principal stresses at a point, n_0 is the refractive index when the material is unstressed, n_1, n_2, n_3 are the refractive indices of the material in the stressed state associated with the principal stress directions (principal refractive indices) and C_1, C_2 are the stress optic coefficients.

These equations are the fundamental relationships between stress and optical effect and are known as the stress optic law. These equations indicate that the complete state of stress at a point can be determined by measuring the three principal indices of refraction and establishing the directions of the three principal optical axes.

These measurements are extremely difficult to make in three dimensions and practical application has been limited to cases of plane stress.

The change of refractive index with hydrostatic pressure has been investigated [130,132-133] in order to yield information on the index change with density. This is of importance in elucidating thermo-optic theory because of the change in volume with temperature [134].

The relation between index of refraction and density is also of importance because of the effect of atomic interactions on the atomic polarisabilities.

For transparent solids, values of $\rho dn/d\rho$ have been obtained by calculation from photoelastic constants [135]. For crystals as well as glasses, values of $\rho dn/d\rho$ so calculated have been found to be less than the corresponding values calculated on theoretical grounds ie. from the Lorentz-Lorenz and the Drude relationships.

For glasses, data on $\rho dn/d\rho$ have been obtained by Ritland [136].

Waxler and Weir [130] measured the refractive index change with hydrostatic pressure between 1 bar and 1 kbar for several materials. The experimental method used has been described in detail [132]. Briefly, a plate of the test specimen is immersed in liquid in a pressure vessel equipped with glass windows. Hydrostatic pressure is generated by compressing the liquid and the number of fringes passing a reference line was determined visually.

The quantity $\rho\partial n/\partial\rho$ was calculated according to the relationship

$$\rho\frac{\partial n}{\partial \rho} = \left(\frac{1}{B}\right)\left(\frac{dn}{dP}\right) \qquad 4.18$$

where B is the compressibility. Using the Drude equation as Ramachandran had done [134], Waxler [132] went on to calculate the strain polarisability constant and found for each material that was tested λ_0 had a positive value.

The change in index resulting from applied hydrostatic pressure on cubic crystals and glasses is attributed to two opposing effects.

(1) Increase in N, the number of scattering centres per unit volume, which always produces an increase, and

(2) A contraction of the electronic cloud which affords a decrease in atomic polarisability and the refractive index.

For MgO, diamond and ZnS, this second effect outweighs the first and these crystals exhibit negative values of $\rho\partial n/\partial\rho$ [137].

Feldman et al [138] measured the shift in Twyman Green and Fizeau fringes as a function of applied uniaxial and hydrostatic stress for transparent materials so that the photo-elastic and elastic constants could be calculated. Uniaxial loading was achieved by the use of the stressing frame illustrated in figure 4.5.

Vedam et al [139] determined the variation of refractive index of vitreous silica with hydrostatic pressure to 7 kbars from the shift of localised interference fringes across a specimen kept in an optical pressure bomb.

Kastner [140] has reported the pressure dependence of the refractive index of several amorphous chalcogenide semiconductors. It was found that dn/dP was positive for materials containing group VI elements in lone pair semiconductors.

4.7 The Change in Refractive Index with Temperature, dn/dT

The change in refractive index with temperature, referred to as the thermo-optic coefficient, has assumed greater practical importance with the advent of the laser due to the thermal self focusing of laser beams [141-142]. This data is also of interest due to the relevance to the theory of molecular scattering in solids [143]. Investigations of the thermo-optic coefficient was reviewed by Baak [144].

Waxler et al [132] evaluated the thermo-optic coefficient of five laser glasses over a wide temperature range by use of an interferometric method [145]. Both positive and negative changes in index were observed.

Data on the refractive index of fused silica at low temperatures, which were required in the design of optical systems for space applications was investigated by Waxler and Cleek [146]. They used the interference method employed by Austin and Pierce [147] to determine the index of commercial fused silica at 10 wavelengths between -200 and 20 °C.

For solid dielectrics, including glasses, it is frequently assumed that dn/dT depends directly upon the temperature induced change in density ρ, but not on temperature itself. In fact

$$\frac{dn}{dT} = \left(\frac{\partial n}{\partial T}\right)_{\rho} + \left(\frac{\partial n}{\partial \rho}\right)_{T}\left(\frac{\partial \rho}{\partial T}\right) \qquad 4.19$$

or

$$\frac{dn}{dT} = \left(\frac{\partial n}{\partial T}\right)_{\rho} - \left(\rho\frac{\partial n}{\partial \rho}\right)_{T}(\beta) \qquad 4.20$$

where β is the coefficient of volume expansion. For most substances, the first term in the above equation is much smaller than the second and dn/dT is essentially equivalent to the second term. It has been found in an earlier study that for three glasses, $(\partial n/\partial T)_\rho$ was much smaller than expected [130].

Waxler and Cleek [133] have measured the effect of temperature on the refractive index for a range of oxide glasses.

Direct experimental data on $\rho dn/d\rho$ are required to understand thermo-optic properties. Values of dn/dT have been measured for many solids and it is known that the sign may be positive or negative. For most crystals dn/dT is found to be negative but in the case of diamond, MgO and ZnS the reverse is true [134]. Most optical glasses exhibit a minimum in the n-T curve somewhat below room temperature so that above room temperature dn/dT is positive but at some lower temperature the sign reverses [148]. Any attempt to explain such a complex thermo-optic behaviour must require an understanding of the $\rho dn/d\rho$ effect because thermal dilation is an important contributing factor to the value of dn/dT.

Starting with the Drude equation, Ramachandran [134] has shown that dn/dT consists of three independent contributions which he labelled P, Q and R.

P is dependent only on change of density and arises from the change in the number of scattering centres.

$$P = -\beta\left(\frac{n^2-1}{2n}\right) \qquad 4.21$$

Q denotes the change in polarizability caused by change in density and R represents the change in polarizability arising from temperature change alone.

$$Q = -\beta\left[\rho\frac{\partial n}{\partial \rho} - \frac{n^2-1}{2n}\right] \qquad 4.22$$

$$R = \frac{dn}{dT} + \gamma\rho\frac{\partial n}{\partial \rho} \qquad 4.23$$

For the five glasses that Waxler studied [133], P, Q and R were calculated.

P was always negative reflecting the lessening in the number of scattering centres with rise in temperature. Values of P and Q for fused silica are very small because of the very small coefficient of thermal expansion. It was seen that R is positive and is significantly larger than Q in all cases indicating that the change in polarisability is largely dependent solely on temperature change. This is not true for crystals where R may be of either sign and is always smaller than Q [149].

Polarizability is the fundamental optical property and in comparing the thermo-optic properties of different materials, it is necessary to compare values of Λ_0, γ, and τ_0, where

$$\tau_0 = \frac{1}{\alpha}\left(\frac{\partial \alpha}{\partial T}\right)_\rho \qquad 4.24$$

is the temperature coefficient of polarizability. Ramachandran has shown that the change in polarisability with temperature can be written as

$$\alpha_T = \alpha_0[1+\Lambda_0\gamma T+\tau_0 T] \qquad 4.25$$

and that

$$\frac{dn}{dT} = \frac{n^2-1}{2n}[-\gamma+\Lambda_0\gamma+\tau_0] \qquad 4.26$$

Calculations of Λ_0 and τ_0 for the glasses were made according to the equations

$$\Lambda_0 = -\frac{Q}{P} \quad and \quad \tau_0 = -\frac{R\gamma}{P} \qquad 4.27$$

In the case of cubic crystals studied, Ramachandran noted that τ_0 is much smaller than $\Lambda_0\gamma$ indicating that the change in polarisability, due to the pure temperature effect is much smaller than that due to a change in the lattice parameter. For the five glasses studied by Waxler and Cleek, the relative importance of the two contributions is reversed.

For the glass systems studied by Waxler, it is apparent that the polarisability is essentially dependent upon the temperature change at constant density. This distinctive property of glasses is brought out from measurements on change in refractive index caused by changes of pressure and temperature although it had been inferred by Ramachandran from a study restricted to thermo-optic data alone over an extended temperature range [148].

Primak and Post [150] have attributed this great dependence of polarizability to the strained bond configuration of the oxygen ions in the glasses. Ramachandran has

inferred that this effect is associated with a band edge shift of the ultraviolet frequencies toward lower energy with increase of temperature that is also essentially independent of change in lattice parameter [149]. This idea of Ramachandran has been extended by more recent studies [151-152]. Apparently the lack of long range order and the random molecular structure in glass induces a broadening of the exitonic levels and a tail on the ultraviolet absorption edge, which varies exponentially with energy [151].

Feldman [153] measured the change of refractive index with temperature of infrared laser window materials using two methods. In the first method, the refractive index was measured by a minimum deviation technique at two temperatures. This was accomplished thermostatically altering the room temperature by 10°C. This technique limits the determination of dn/dT at room temperature. The second method for obtaining dn/dT was an interferometric method capable of greater precision than the first but is limited to discrete wavelengths. It involves the observation of a shift in Fizeau interference fringes, formed from reflections off the surfaces of an optical specimen polished plane parallel, as a function of temperature. The change of refractive index as function of temperature is given by the formula

$$\Delta n = \left(\frac{\Delta N\lambda}{2t_0} - n_0\frac{\Delta t}{t_0}\right)\left(1+\frac{\Delta t}{t_0}\right)^{-1} \qquad 4.28$$

where n_0 is the room temperature refractive index, ΔN is the fringe count as a function of temperature, t_0 is the specimen thickness and Δt is the specimen thickness change as a function of temperature calculated from thermal expansion measurements.

Over more recent years, transparent plastic materials have come into wide use in the

fabrication of optical components [154]. In order to make use of these materials, designers require basic optical and material parameters such as the refractive index and the thermo-optic coefficient.

Using the same interferometric technique as Feldman, Waxler et al [10] determined the thermo-optic coefficient of Plexiglass 55, a methyl methacrylate polymer, and Lexan, a polycarbonate. The resulting values were fitted to a third degree polynomial in T. The thermo-optic coefficient as a function of temperature is shown for both materials in figure 4.6. It was noted that dn/dT for both plastics was determined predominantly by the change in density which is characteristic of most single crystals.

A study of the temperature dependence of the refractive index of polymers, in addition to its considerable practical importance for the thermo-optics of laser media [155], is of scientific interest in connection with the possibility of a direct observation of the kinetics of relaxation transformations [156]. Figure 4.7 shows the temperature dependence of the different acrylic polymers investigated in the region 288-373K. The temperature coefficient of refractive index exhibits essentially no spectral dependence for any of the polymers tested.

These relationships and the features of the temperature dependence of acrylic polymers can be explained by the relaxation states of amorphous polymers [157] and the general theory of dispersion [158].

Cariou et al [159] have shown that the variation of the refractive index of some polymers versus temperature is essentially due to the variation of density. From the Lorentz-Lorenz relation, the function $(n^2+2)/(n^2-1)$ appears perfectly linear in the various temperature ranges where no phase changes occur. The slope of the

representative curve exactly follows the thermal expansion coefficient which keeps a constant value in each temperature range.

Cariou et al measured the refractive index of commercial samples of PMMA and polycarbonate between about -100°C and 150°C using the minimum deviation of a prism. For determination of the minimum deviation, the prism was set inside a Dewar built in the lab and position on the stage of a goniometer which permitted the measurement of angles with a precision of 1 sec.

The index was measured on both heating and cooling cycles and no difference was found in experimental points This meant that the temperature evolution was slow enough to make any transformation almost reversible.

The results of Waxler et al [10], as shown in figure 4.6, were determined between -160 and 60°C. They obtained irregular but continuous curves which do not evidence any systematic change in their behaviour which may be related to a phase transition. Nevertheless, in the temperature range studied, at about -30 °C polymethyl methacrylate undergoes the so called β transition which is attributed to the beginning of the rotation of lateral chains of methacrylate radicals. A relevant discontinuity of the coefficient of thermal expansion has been observed for polymethyl methacrylate's various tacticities [160]. The experimental values determined by Waxler et al generally follow the variation that Cariou et al had obtained but without presenting the discontinuities which correspond to the various phase changes. This discrepancy may be due to the large temperature steps used in Waxler's measurements.

A number of studies have been devoted to direct measurement of specific volume variations versus temperature for polymers. It has been shown, for polymethyl

methacrylate and polystyrene for example, that their specific volume varies linearly with temperature [161] except where phase changes occur. This behaviour of polymers is quite common and their coefficient of volume expansion only varies by steps at any phase change and remains nearly constant between each one. Such experiments constitute good experimental means to characterize the temperature of the transitions in the polymers and their variations with various parameters (molecular weight, tacticity, thermal treatments etc.). Experimental techniques that have been generally performed [163-164] are difficult to use and involve the sample being immersed in a liquid which may interact with the specimen and which also restricts the range of measurement.

Using the same technique as Cariou, Michel et al [9] measured the thermal variation of refractive index of polymethyl methacrylate, polystyrene and poly(4-methyl-1-pentene) over the temperature range -120 to 150°C.

In each case, the refractive index decreased linearly with temperature. However, discontinuities were observed at which point the gradient of the line changed abruptly (figure 4.8). These discontinuities appeared at certain transition points which occur in the individual polymers. With the three materials tested, a discontinuity was observed at the glass transition temperature. The β transition was also observed in polymethyl methacrylate.

The results suggest that the refractive index depends only on the material density. This is also highlighted by the change in the gradient of the data points of the various changes which generally occur in these materials. Thus the thermal expansion coefficient may be directly deduced from the index measurements by performing this technique.

5 The Design of a Vibration Measuring System

Before a light modulated vibration system could be designed it was necessary to establish a specification in order to achieve the desired features and operating parameters. The aims of the device were as follows:

1 To enable remote measurement ie. incorporate fibre optic links to transfer the measurement information from the measuring point to the source/detector;

2 To employ phase or intensity modulation;

3 To utilize the change in refractive index developed in some materials with the application of stress;

4 To be operational up to approximately 30 kHz

5 To be of similar size/weight to existing piezoelectric accelerometers and

6 To be compatible with existing tooling operations to aid in the manufacture.

Having established the specification, the design process could begin and is detailed in this section. First of all, the principal of accelerometer operation is described. The various light sources available are then discussed along with the possible ways in which the light may be coupled into and out of a fibre optic cable. The design process of the accelerometer itself is then considered from the sensing element and seismic mass to the accelerometer case and the optical connectors. Finally, the choice of detector is discussed.

A mathematical model has been developed to predict the performance characteristics of the transducer which would enable comparison with the performance of the prototype.

5.1 Vibration Measuring Instruments

There are several vibration measuring devices which are commercially available. Examples include devices based on capacitance, eddy currents, piezoresistance, potentiometric, rotational and strain gauges. However, the transducer which, nowadays, is more or less universally used for vibration measurements is the piezoelectric accelerometer. This is discussed in detail below.

5.1.1. The Piezoelectric Accelerometer

The piezoelectric accelerometer exhibits better all round characteristics than any other type of vibration transducer. It has very wide frequency and dynamic ranges with good linearity throughout the ranges. It is relatively robust and reliable so that its characteristics remain stable over a long period of time.

Additionally, the piezoelectric accelerometer is self generating, so that it doesn't need a power supply. There are no moving parts to wear out and its acceleration proportional output can be integrated to give velocity and displacement proportional signals.

The heart of the piezoelectric accelerometer is the slice of piezoelectric material, usually an artificially polarised ferroelectric ceramic. When it is mechanically stressed, either in tension, compression or shear, it generates an electrical charge across its pole faces which is proportional to the applied force.

5.1.2. Mathematical Analysis of Accelerometer Operation.

In practical accelerometer designs, the piezoelectric element is arranged so that when the assembly is vibrated the mass applies a force to the element which is proportional to the vibratory acceleration.

A simplified model of the accelerometer is shown in figure 5.1.The equation of motion of such a system can be described by

$$m\ddot{x} = -c(\dot{x}-\dot{y}) - k(x-y) \tag{5.1}$$

If the relative distance between the seismic mass and the vibration surface is denoted by z ie. z = x - y then

$$m\ddot{z} + c\dot{z} + kz = -m\ddot{y} \tag{5.2}$$

If the force motion is described by

$$y = Y \sin\omega_f^2 \tag{5.3}$$

then

$$m\ddot{z} + c\dot{z} + kz = m\omega_f^2 Y \sin\omega_f t \tag{5.4}$$

The solution to this non-homogenous linear second order differential equation is a steady state oscillation of the same frequency ω as that of the excitation and can be given by

$$z = Z \sin(\omega_f t + \phi) \tag{5.5}$$

where Z is the amplitude of the oscillation and ϕ is the phase of the displacement with respect to the exciting force. The amplitude and phase in the above equation are found by substituting Eq.5.5 into the differential Eq.5.4. Solving, it can be shown that

$$Z = \frac{m\omega_f^2 Y}{\sqrt{(k-m\omega_f^2) + (c\omega_f)^2}} \tag{5.6}$$

and

$$\phi = \tan^{-1} \frac{c\omega_f}{k - m\omega_f^2} \tag{5.7}$$

By dividing Eq.5.6 by k it can be shown that

$$Z = \frac{Y\left(\frac{\omega_f}{\omega_n}\right)^2}{\sqrt{\left[1 - \left(\frac{\omega_f}{\omega_n}\right)^2\right]^2 + \left[2\zeta\frac{\omega_f}{\omega_n}\right]^2}} \qquad 5.8$$

where ζ is the damping factor given by

$$\zeta = \frac{C}{C_c} \qquad 5.9$$

and C_c is the critical damping given by

$$C_c = 2m\omega_n \qquad 5.10$$

As $\omega_f/\omega_n \rightarrow 0$, the denominator of this equation approaches unity and therefore it can be shown that

$$Z = \frac{\omega_f^2 Y}{\omega_n^2} = \frac{acceleration\ of\ base}{\omega_n^2} \qquad 5.11$$

From this it can be seen that the relative displacement Z becomes proportional to the acceleration of the motion. Thus the output signal magnitude of such a device will therefore be proportional to the acceleration to which the pick-up is subjected. This analysis is valid for all seismic accelerometers and is independent of the operating principal.

Piezoelectric accelerometers are essentially underdamped and therefore the damping ratio is very low [165]. This is acceptable due to the very high natural frequency compared with accelerometers based on different transduction mechanisms.

5.1.3. Accelerometer Design

In practical accelerometer designs, the piezoelectric element is arranged so that when the assembly is vibrated the mass applies a force to the piezoelectric element which is proportional to the vibratory acceleration. This has been shown mathematically in section 5.1.2.

Two design configurations are commonly found in commercial accelerometers.

1 The compression type where the mass exerts a compressive force on the piezoelectric element and

2 The shear type where the mass exerts a shear force on the piezoelectric element.

Most manufacturers have a wide range of accelerometers. A small group of general purpose types will satisfy most needs and the remaining transducers have their characteristics slanted towards a particular application.

For example, small size accelerometers that are intended for high level or high frequency measurements and for use on delicate structures, panels etc. and weigh only 0.5 - 2 grammes.

Other special purpose types are optimised for: simultaneous measurement in three mutually perpendicular planes; high temperature; very low vibration levels; high level shocks; calibration of other accelerometers by comparison and for permanent monitoring on industrial machines.

5.1.4. Vibration Preamplifiers

The role of the vibration preamplifier is to convert the high impedance output of the accelerometer to a low impedance signal suitable for direct transmission to measuring and analyzing instrumentation.

Two types of preamplifier exist which may be used with the piezoelectric accelerometer. The charge preamplifier produces an output voltage proportional to the input charge whilst the voltage preamplifier produces an output voltage proportional to the input voltage.

Charge preamplifiers are generally used in preference to voltage preamplifiers. This is due to the fact that both very long and very short cables can be used without altering the overall sensitivity of the system. In the case of a voltage preamplifier, a change in cable length necessitates a recalibration of system sensitivity.

5.1.5. Accelerometer Performance

In order to obtain accurate vibration measurements, the piezoelectric accelerometer must be used correctly. Figure 5.2 illustrates the different extraneous inputs which may be present during vibration measurement.

The two general areas which affect accelerometer performance are environmental effects and the mounting method. Each will be dealt with briefly here.

(a) Environmental Effects

Temperature Range

Piezoelectric accelerometers are capable of measuring vibration over a wide temperature range. However, when the accelerometer is operated at temperatures other than the

reference temperature voltage and charge sensitivities will vary. Accelerometers have a maximum specified operating temperature above which the piezoelectric element begins to depolarise and cause permanent change in sensitivity. In most accelerometers this maximum temperature is around 250°C. The higher the temperature rises above this limit, the more rapid the depolarisation becomes rendering the transducer useless.

For vibration testing up to 450°C, accelerometers incorporating lead methaniobate are available.

Temperature Transients

Fluctuations in ambient temperature during vibration measurement give rise to a low frequency noise signal. This signal is due to two effects, the pyroelectric effect and non-linear thermal expansion effects.

When subject to temperature variations, piezoelectric materials become charged. In the artificially polarised ceramics used in accelerometers the charge is built up on surfaces perpendicular to the polarisation direction. Therefore in compression type accelerometers, this charge is picked up leading to erroneous results. This is avoided in shear type designs.

Owing to the different thermal expansion coefficients of the components in the transducer, the components expand and contract by varying degrees. This leads to forces being exerted on the piezoelectric element again leading to erroneous results.

Acoustic Sensitivity

Most vibrations have an acoustic output and measurements are made where there is a high sound pressure level. Modern accelerometers have been designed so that sound

pressure level does not interfere with vibration measurement.

Base Strain

Base strain, also referred to as base bending, occurs whenever an accelerometer is mounted on a vibrating structure. The accelerometer is subject to bending forces and as a result change will be measured. This effect is noticeable at lower frequencies where displacements and hence strains are large.

Humidity

The majority of commercial accelerometers are sealed by either a weld or epoxy isolating the accelerometer from effects of humidity. It is important that when used in wet or very humid conditions that the accelerometer cable and screw connector are completely sealed.

(b) Mounting Techniques

The techniques used to mount the accelerometer influence the frequency range and dynamic performance of the device. The two main methods are described.

Stud mounting is usually used for high frequency vibration measurements requiring the highest possible resonant frequency or for permanent vibration monitoring. This method gives optimum accelerometer performance and should be used whenever possible.

Wax mounting is an easy method and is used when it is undesirable to drill a mounting hole for the stud and for accelerometers that do not have a tapped hole in the base. The mounted resonance frequency is only slightly less than for stud mounting but this method can only be used at temperatures below 40°C and for accelerations less than 100 ms^{-1}.

5.1.6. Accelerometer Characteristics

The sensitivity is the first characteristic normally considered. Ideally we would like a high output level, but this has to be compromised because high sensitivity normally entails a relatively big piezoelectric assembly and consequently a relatively large heavy unit.

In normal circumstances the sensitivity is not a critical problem as modern preamplifiers are designed to accept low signals.

The mass of the accelerometers becomes important when measuring on light test objects. Additional mass can significantly alter the vibration levels and frequencies at the measuring point. As a general rule, the accelerometer mass should be no more than one tenth of the dynamic mass of the vibrating part onto which it is mounted.

When abnormally low or high acceleration levels are to be measured, the dynamic range of the accelerometer should be considered. The lower limit is not normally determined directly by the accelerometer, but by electrical noise from connecting cables and amplifier circuitry. This limit is normally as low as one hundredth of a $m.s^{-2}$ with general purpose instruments.

The upper limit is determined by the accelerometers structural strength. A typical general purpose accelerometer is linear up to 50000 to 100000 ms^{-2} which is well into the range of mechanical shocks.

The frequency range over which the accelerometer gives a true output is limited at the low frequency end in practice by two factors. The first is the low frequency cut-off of the amplifier which follows it. This is not normally a problem as the limit is usually

well below one hertz. The second is the effect of ambient temperature fluctuations to which the accelerometer is sensitive. With modern shear type accelerometers this effect is minimal allowing measurements down to below 1 Hz for normal environments.

The upper limit is determined by the resonant frequency of the mass spring system of the accelerometer itself.

With small accelerometers where the mass is small, the resonant frequency can be as high as 180 kHz but for the somewhat larger, higher output general purpose accelerometers, resonant frequencies of 20 to 30 kHz are typical.

5.2 The Design of the Transducer System

5.2.1 Transmitter Design

The common feature of all optical sensors is that they modulate an optical signal in response to a given measurand. In the design of a light modulated sensor system there are several light sources which are available. The main classes will be described briefly here.

The principle sources are:

1 the incandescent sources;

2 the light emitting diode (LED); and

3 the laser.

5.2.1.1 The Incandescent Source

Incandescent sources produce 'white' light and can be used for simple intensity modulated sensors and for excitation of phosphorus and photoluminescent material. The tungsten filament lamp is the most commonly used broadband sources.

The filament is heated by passing a current through it which radiates energy over a broad wavelength spectrum. The lifetime of commercially available sources are in the range 100-100,000 hours which is dependent on the operating current.

Incandescent sources cannot be directly modulated due to the delay between current change and lamp output change. Only the chopper can be used as a modulator as the other techniques are dependent on wavelength. This limits modulation to 20kHz.

5.2.1.2 The Light Emitting Diode (LED)

The LED is most commonly used in multimode fibre systems. The output from the LED is incoherent and cannot therefore be used for interferometric sensors. LEDs are relatively inexpensive and can be modulated directly by varying their current drive.

LEDs are made from a doped semiconductor p-n junction and when current is injected into the junction under forward bias, electron-hole recombination occurs and photons are emitted. This spontaneous recombination process is called injection luminescence. The wavelength of the emitted photons is a function of the energy gap between the semiconductor valence and conduction bands. This may be controlled by choice of semiconductor materials and dopant concentrations which has led to a wide range of wavelengths being available from 650nm in the visible part of the spectrum to 1.3μm in the infra-red.

The output spectrum of a LED is around 2% of its nominal centre wavelength giving a typical full width half maximum value of 50nm.

If used within specification, LEDs degenerate very slowly with time and are considered to have failed when the output drops to 67% of the original value for a given current. Specified lifetimes are in excess of 10^6 hours.

5.2.1.3 The Laser

There are a wide range of lasers commercially available each with various characteristics. Lasers are classified based on the medium in which the lasing action takes place. Hence, there are solid-state lasers, gas lasers, dye lasers and semiconductor lasers. Of these, the HeNe laser and semiconductor lasers have established themselves at the forefront in optical applications. Gas lasers and the injection laser diode can be

used for both multi and single mode optical fibre sensors. In multimode sensors they are used when an LED cannot provide sufficient power. Single mode sensors are interferometric and therefore require a coherent optical source which can only be provided by a laser. However where a highly coherent and stable continuous wave source is required a single mode HeNe laser is normally used. HeNe lasers generate output powers in the range 0.1 to 100mW; 5mW is usually adequate for single mode sensors at wavelength of 633 nm.

These two sources will now be reviewed in more detail.

(a) The HeNe Laser

The HeNe is commonplace in any optics laboratory to demonstrate reflection, diffraction and interference phenomena. It is used extensively in commercial applications including bar code scanners, alignment systems and holography.

Gas lasers consist of an optically resonant cavity filled with a medium which exhibits optical gain. In order for lasing to take place stimulated emission must dominate over spontaneous emission and absorption. This is achieved when the upper energy level population is greater than that of the lower level. This situation is described as population inversion and is brought about by an input of energy into the laser medium. Because the laser is made up of stimulated emission all the photons emitted have the same phase and this gives a highly coherent source.

(b) Semiconductor Lasers

Semiconductor lasers are, generally, favoured because they can be directly current driven and are cheaper than gas lasers. Semiconductor lasers, also known as injection laser diodes (ILD), like the LED, are formed from a p-n junction which emits light

when current is injected under forward bias. In fact at low injection currents the ILD behaves as an LED emitting light by spontaneous emission. However, the p-n junction of the ILD is heavily doped which means that larger currents cause a population inversion of charge carriers to occur. In this situation a spontaneously emitted photon may generate stimulated emission of another photon and if the injection current is sufficient, optical gain takes place. The p-n junction is contained in an optically resonant cavity to form a laser. At low currents the optical output is dominated by spontaneous emission and the ILD behaves like an LED with a wide spectrum. Above a threshold current, stimulated emission dominates which causes lasing and a consequential reduction in spectral width.

ILDs can either be multi or single mode devices. Single mode lasers have high spatial coherence and are therefore suitable for single mode interferometric sensors. For multimode systems where coherence is not relevant, the high launch powers of the ILD can make it an attractive device.

5.2.1.4. Conclusions

The device to be designed in this research programme was to utilise phase modulation. Therefore, a coherent source is a prime requisite and therefore eliminates both incandescant sources and LEDs. Planning ahead, it would make good sense to incorporate both the light source and processing electronics in a single unit. Consequently a semiconductor laser would seem appropriate given the relatively bulky nature and added expence of HeNe lasers. Both these factors would be of importance if such a light modulated accelerometer is to gain market acceptance. However, at the onset of the project a HeNe was available and was, therefore, to be used in the initial development of the device.

5.2.2 Light Coupling

To incorporate optical fibres into an optical circuit various coupling arrangements are available which are detailed below.

5.2.2.1 The Gradient Index Lens

Gradient index (GRIN) lenses offer the simplest method of collimating a laser beam. A gradient index lens is a cylinder of glass whose refractive index varies radially. In conventional lenses imaging is a result of discrete refractions occurring at the boundaries of homogenous media of different refractive index. By using materials in which the refractive index varies in some controlled way it is possible to form images by continuous refraction.

Combining surface refraction with continuous refraction provides a number of advantages over conventional lens systems. The more notable of these are:

* correction of abberations without complex, multi-element systems of aspherics
* simplification of the geometry of lenses
* formation of real images at the lens surface

The gradient index lenses available are manufactured from SELFOC® (a registered trademark of the Nippon Sheet Glass Company) which is a radial gradient index material. These are rod lenses combining refraction at the plane end surfaces with continuous refraction within the rod. They are highly suitable for coupling the output of a diode laser into an optical fibre.

In SELFOC® material, the refractive index varies parabolically as a function of radius. The index variation may be expressed as [166]:

$$n_r = n_{00}\left(1-\frac{A}{2}r^2\right) \qquad 5.12$$

where

n_r = refractive index at a distance r from the optical axis
n_{00} = design index on the optical axis
A = a positive constant

As a result of this parabolic index variation a ray incident on the front surface follows a sinusoidal path along the rod lens. The period of this sinusoidal path is called the pitch of the lens and is an important parameter in gradient index imaging. It is given by

$$P = \frac{2\pi}{\sqrt{A}} \qquad 5.13$$

Knowing the pitch of gradient index rod material it is possible to achieve various imaging characteristics simply by varying the length of the lens. Imaging properties of common fractional pitch lens types are shown in figure 5.3.

5.2.2.2 The Coupling Sphere

Of the various techniques currently used to couple optical fibres to each other (and to diode lasers and detectors) the ball lens is the one which allows the researcher to interact with the beam in the coupling process. Using this method, spheres are arranged such that the fibre end (or input/output device) is located at the focal point of the sphere. The output of the beam is then a collimated beam. If two spheres are arranged in axial alignment with each other the beam will be transferred from one focal point to the other as is shown in figure 5.4. This is exactly analogous to a pair of thin lenses

relaying the object to the image space through a collimator/focusing lens combination. By enlarging the coupling beam, translational alignment sensitivity is reduced.

Spheres are much easier to manufacture than thin lenses in these small diameters. In the same way, they are easy to align in experimental applications. Because of their simplicity, ball lens coupling systems tend to achieve better coupling efficiencies than other methods. Using communication fibres, coupling efficiencies up to 95% (0.4dB insertion loss) have been achieved [167].

All of these spheres are coated on both hemispheres with a single layer MgF_2 antireflection coating. Because of the high index of these spheres, this results in a very effective coating with low reflectivity at the specified wavelengths.

5.2.2.3 Laser to Fibre Source Coupler

The source coupler makes use of a tilt coupling method to focus the laser beam onto the fibre which is located at the image plane of a lens system. The method is based on precision control of the angle between the laser beam and the receiver lens. The source coupler is comprised of two baseplates each having axial bore. One of the baseplates is adapted to receive a lens holder which carries a lens and a fibre. The other baseplate is attached to the laser. A resilient member, such as a rubber 'O' ring, is sandwiched between the baseplates. The screws can then be adjusted by a screwdriver to alter the angular orientation of one baseplate relative to the other. By monitoring the output of the fibre, the coupler can be adjusted until the output is optimised. The coupling arrangement is shown in figure 5.5. If the lens is tilted by an angle relative to the laser beam, the focused laser spot on the focal plane of the lens will be displaced relative to the receiver lens axis by an amount given by the equation

$z = f \tan\theta$ 5.14

where f is the focal length of the lens and θ is the tilt angle.

5.2.2.4 The Fibre Collimator

Light leaving an optical fibre diverges to a great extent leading to an obvious loss of power. The beam therefore needs to be collimated. The fibre collimator is very similar in construction to the fibre optic coupler except that no aligning is necessary. The theoretical loss of this device is reported as 0.6 dB [168].

5.2.2.5 Conclusions

Both the coupling sphere and gradient index lens can be used to couple light into and out of an optical fibre as shown. In fact the gradient index lens is usually incorporated in the commercially available 'off the shelf' couplers. However, these couplers are too bulky for use in light modulated accelerometers and custom made couplers would need to be manufactured.

5.2.3 Light Modulated Accelerometer Design

5.2.3.1 Spring Mass Element Design

The light modulated accelerometer described in this section is based on the same spring mass system detailed in section 1.1.2. In this section the actual design of the accelerometer will be described.

5.2.3.2 Sensing Element Design

The most important part of any transducer system is the sensing element itself as it is this which gives the information of the required measurand.

The design of the sensing element is of uppermost importance as it is this which inherently controls the sensitivity of the device.

The important material property of such an element is the rate at which the signal from the sensing element changes with a given measurand stimulus.

In piezo-ceramic vibration transducers, it is the magnitude of the charge developed across the sensing element which is related to the acceleration and this property is called the charge sensitivity.

In this programme of research, a vibration system is to be designed and developed using light modulation and specifically, the change in refractive index with stress. The resultant change in index is used to modulate the phase or intensity of the light beam.

In this section various designs of sensing element are considered in which a change in light path length (phase change) and a change in lateral displacement (intensity change) are brought about by a change in the refractive index.

In order to determine the relative merits of each configuration information is required on both the change of path and the change of displacement with refractive index to assist in the design process.

(a) A Simple Reflection

Consider the case of a simple reflection of a light beam through a material of refractive index n_0 and of width Y as shown in figure 5.6.

From this, it can be seen that the path, P of the light beam through the material can be given by

$$P = \frac{2Y}{\cos\beta} \qquad 5.15$$

where β is the angle of refraction, related to the angle of incidence α and the refractive index n_0 by Snell's Law

$$\beta = \arcsin\left(\frac{\sin\alpha}{n_0}\right) \qquad 5.16$$

Combining these two equations and using standard trigonometrical identities, it can be shown that

$$P = 2Y\left[1-\frac{\sin^2\alpha}{n_0^2}\right]^{-\frac{1}{2}} \qquad 5.17$$

For a small change in n_0, Δn, the corresponding change in P, ΔP is given approximately by

$$\Delta P = \frac{\partial P}{\partial n}\Delta n \qquad 5.18$$

where ∂P/∂n is the partial derivative of P with respect to n evaluated at the original value of n. Consequently, this partial derivative can be found by differentiating equation 5.17 with respect to n. Thus

$$\frac{\partial P}{\partial n} = -\frac{2Y\sin^2\alpha}{\sqrt{(n_0^2-\sin^2\alpha)^3}} \qquad 5.19$$

Therefore, for a given value of α, it can be shown that

$$\Delta P = -\frac{2Y\sin^2\alpha}{\sqrt{(n_0^2-\sin^2\alpha)^3}}\Delta n \qquad 5.20$$

which is a relationship of straight line format. The negative sign indicates that the gradient is negative. This relation is shown for various values of α in figure 5.7.

From this graph it can be seen that as the angle of incidence α increases so too does the change in path length ΔP for a given change in refractive index Δn. This is also apparent from figure 5.8 which shows the effect of the angle of incidence on the path change.

Also by inspection from figure 5.6, it can be shown that the lateral distance X can be given by

$$X = 2Y\tan\beta \qquad 5.21$$

Again by combining this equation with Snell's law, an expression for the lateral distance can be given in terms of the angle of incidence and the refractive index of the medium, ie.

$$X = 2Y\left[\frac{n_0^2}{n_0^2-\sin^2\alpha}-1\right]^{\frac{1}{2}} \qquad 5.22$$

Again using the approximation given in equation 5.18 this time for X instead of P, it can be shown that

$$\frac{\partial X}{\partial n} = -\frac{2n_0 Y \sin^2\alpha}{\sqrt{[\sin^2\alpha\ (n_0^2-\sin^2\alpha)^3]}} \qquad 5.23$$

and therefore

$$\Delta X = -\frac{2n_0 Y \sin^2\alpha}{\sqrt{[\sin^2\alpha\ (n_0^2-\sin^2\alpha)^3]}}\ \Delta n \qquad 5.24$$

Again as before, this relationship is of straight line format and is shown in figure 5.9.

(b) n Type Reflection

An n type reflection is the name given to a reflection of a light beam through a triangular prism as shown in figure 5.10. Only a symmetrical reflection will be studied here as this simplifies the mathematics somewhat and would be an aid in any future prototype manufacture.

The major parameters in this design are the light entry point x, the base length X and the angle of incidence α. From these parameters all other dimensions can be

determined.

In order for the light to travel such a path the prism angle needs to be a function of α such that

$$\delta = \frac{1}{2}\left[90-\arcsin\left(\frac{\sin\alpha}{n}\right)\right] \qquad 5.25$$

To derive an expression for the path P through the medium, the path can be split into three components and then summated.

Therefore, it can be shown that

$$1P_{1,2} = \frac{x\cos\beta_{1,2}}{\sin\left[\frac{90+\beta_1-2\beta_{1,2}}{2}\right]} \qquad 5.26$$

$$2P_{1,2} = \frac{Q\cos\beta_1}{\sin\left[\frac{90-3\beta_1+2\beta_{1,2}}{2}\right]} \qquad 5.27$$

where

$$Q = \frac{X}{2\cos\left[\frac{90-\beta_1}{2}\right]} - \frac{x\sin\left[\frac{90-\beta_1}{2}\right]}{\sin\left[\frac{90+\beta_1-2\beta_{1,2}}{2}\right]} \qquad 5.28$$

and

$$3P_{1,2} = \frac{S \sin [(90-\beta_1)/2]}{\sin [90+2\beta_1-\beta_{1,2}]} \qquad 5.29$$

where

$$S = \frac{X}{2\cos\left[\frac{90-\beta_1}{2}\right]} - \frac{Q \sin\left[\frac{90+\beta_1-2\beta_{1,2}}{2}\right]}{\sin\left[\frac{90-3\beta_1+2\beta_{1,2}}{2}\right]} \qquad 5.30$$

β_1 is the angle of refraction when $n = n_1$ and $\beta_{1,2}$ is the angle of incidence when $n = n_1$ or n_2. $P_{1,2}$ is the path when $n = n_1$ or n_2. The number preceeding the P indicates the partial component of the path.

Therefore, the change in the path length, ΔP can be summated from equations 5.26, 5.27 and 5.29. Thus

$$\Delta P = P_1 - P_2 = \sum_{A-1}^{A-3} A(P_1-P_2) \qquad 5.31$$

The equations for this configuration are more complex than for the simple case and are therefore complex to differentiate. The equations have been solved numerically by creating a spreadsheet to perform the calculations. By using this method the actual results are obtained rather than the approximations brought about by differentiation.

The effect of the angle of incidence on the path difference is shown in figure 5.11 for various entry point positions.

(c) x Type Reflection

The x type reflection is the name given to the path through a triangular prism shown in figure 5.12. The path length through the prism and hence the mathematical analysis is very similar to the n type detailed in the previous section and hence the mathematical analysis is very similar. Again the prism angle is a function of α but in this case is given by

$$\delta = \frac{1}{2}\left[90 + \arcsin\left(\frac{\sin\alpha}{n}\right)\right] \qquad 5.32$$

$$1P_{1,2} = \frac{(X-x)\sin\left[\frac{90+\beta_1}{2}\right]}{\sin\left[\frac{90-\beta_1+2\beta_{1,2}}{2}\right]} \qquad 5.33$$

$$2P_{1,2} = \frac{Q\sin[90-\beta_1]}{\sin\left[\frac{90+3\beta_1-2\beta_{1,2}}{2}\right]} \qquad 5.34$$

where

$$Q = \frac{X\sin\left[\frac{90+\beta_1}{2}\right]}{\sin[90-\beta_1]} - \frac{(X-x)\sin[90-\beta_{1,2}]}{\sin\left[\frac{90-\beta_1+2\beta_{1,2}}{2}\right]} \qquad 5.35$$

and

$$3P_{1,2} = \frac{S\sin[(90+\beta_1)/2]}{\sin[90-2\beta_1+\beta_{1,2}]} \qquad 5.36$$

where

$$S = \frac{X \sin\left[\frac{90+\beta_1}{2}\right]}{\sin\left[90-\beta_1\right]} - \frac{Q \sin\left[\frac{90-\beta_1+2\beta_{1,2}}{2}\right]}{\sin\left[\frac{90+3\beta_1-2\beta_{1,2}}{2}\right]} \qquad 5.37$$

Again these equations were solved analytically using a spreadsheet. The effect of the angle of incidence on the path change and displacement is shown in figure 5.13.

The change in path length, ΔP, can again be given by

$$\Delta P = P_1 - P_2 = \sum_{A-1}^{A-3} A(P_1-P_2) \qquad 5.38$$

(d) In Line Reflection

It has already been mentioned that piezoelectric accelerometers are self generating ie. no power is required and therefore no input cable is required. This results in just one connecting cable to transmit the vibration signal to the processing electronics.

With light modulated transducers, both an input and output are required. This leads to two connectors. The designs described earlier in this section had an angular separation between the connectors. In certain applications this may cause problems.

One solution would be to place the connectors side by side. With this in mind a different sensing element could be designed. One such design is shown in figure 5.14.

As in the earlier sections expressions have been derived for the path change and the lateral displacement. Again the path has been split into several components. The important parameters in this case are the angle of incidence, the entry point position

together with the distances Y and Z. All other dimensions may be derived from this.

$$1P_{1,2} = X_0 \tan\alpha \tag{5.39}$$

$$2P_{1,2} = \frac{X_0}{\sin(\alpha-\beta_{1,2})}\left[1-\frac{\left[\frac{X_0}{\tan(\alpha-\beta_{1,2})}-Y+X_0\tan\alpha\right]\tan(\alpha-\beta_{1,2})}{X_0}\right] \tag{5.40}$$

$$3P_{1,2} = \left[\frac{X_0}{\tan(\alpha-\beta_{1,2})}-Y+X_0\tan\alpha\right]\frac{\tan(\alpha-\beta_{1,2})\sin(45+\alpha-\beta_{1,2})}{\sin(45+\beta_1-\beta_{1,2})} \tag{5.41}$$

$$4P_{1,2} = \frac{Z_2}{\sin(45-\beta_1+\beta_{1,2})} \tag{5.42}$$

where

$$Z_2 = \left[Z-\left[\frac{X_0}{\tan(\alpha-\beta_{1,2})}-Y+X_0\tan\alpha\right]\frac{\sin(90-\alpha+\beta_{1,2})}{\sin(45+\beta_1-\beta_{1,2})}\right] \tag{5.43}$$

$$5P_{1,2} = \frac{W_2\sin(45-\alpha+\beta_1)}{\sin(90+\alpha-\beta_{1,2})} \tag{5.44}$$

where

$$W_2 = Z\tan(45+\alpha-\beta_1)-\frac{Z_2\sin(45+\beta_1-\beta_{1,2})}{\sin(45-\beta_1+\beta_{1,2})} \tag{5.45}$$

$$6P_{1,2} = \frac{(Y-V_1\tan\alpha)\sin(90-\alpha)}{\sin(90+\beta_{1,2})} \tag{5.46}$$

where

$$V_1 = \frac{Z}{\cos(45+\alpha-\beta_{1,2})} - \frac{W_2\sin(45-\beta_1+\beta_{1,2})}{\sin(90+\alpha-\beta_{1,2})} \qquad 5.47$$

$$7P_{1,2} = (V_1+H)\tan\alpha \qquad 5.48$$

where

$$H = 6P_{1,2}\sin(\alpha-\beta_{1,2}) \qquad 5.49$$

Thus the change in the path length, ΔP, is given by

$$\Delta P = P_1 - P_2 = \sum_{A-1}^{A-7} A(P_1-P_2) \qquad 5.50$$

The results from this analysis were very similar in form to those described earlier. The sensitivity was not as great as the x type configuration, however, it could be of use in the type of application where space is a prime concern.

(e) Conclusions

From the above analyses several general conclusions can be drawn.

1 The greater the angle of incidence the greater will be the path change and lateral displacement.

2 The lower the value of refractive index, the greater will be the path change and lateral displacement.

3 For n type designs, the smaller the entry point position, the greater will be the path change and lateral displacement whilst the converse is true for the x type.

5.2.3.3 Accelerometer Design

Conventional general purpose piezoelectric accelerometers are based either on a compression or shear type design and are encapsulated in a cylindrical case. To encourage market acceptance of any light modulated device produced it was decided to have a similar cylindrical case to house the components of the light modulated accelerometer. This will then be compatible with existing manufacturing set up.

For simplicity in the prototype manufacture it was decided to base the accelerometer on a compression type design. The actual dimensions of the prototype light modulated accelerometer were chosen to be of comparable size to commercially available general purpose accelerometers. Thus an internal diameter of 20 mm was chosen. The working drawing for the prototype is shown in figure 5.15.

(a) Sensing Element

A mathematical analysis of several sensing configurations has been given in section 5.2.3.1 where it was found that sensitivity was improved with larger angles of incidence. However, a limiting factor is the light power reflected at the interface. Figure 4.1 shows Fresnel's equation represented graphically ie. the effect of the angle of incidence on the percentage of light reflected. From this it can be seen that the percentage loss remains around 4% up to an incidence angle of 50 degrees. Therefore given that the path change and displacement increases with angle of incidence an incidence angle of 45 degrees was considered appropriate.

Having decided on the dimensions of the case, it was necesssary to calculate which design configuration was best suited to this accelerometer casing ie. the one giving the best sensitivity. This was acieved by calculating the dimensions of the largest possible

element for each design configuration that could be applied in the case. This is shown in figure 5.16. Using these dimensions and considering a given change in the refractive index of the medium, both the change in path length and the change in lateral displacement was calculated. The results of this analysis is given in the table 5.1.

To determine the thickness of the sensing element, the coupling arrangement had to be considered. The actual arrangement is detailed in the following section. From this, it was judged appropriate to have an element 5 mm thick. To determine the thickness of the seismic unit the model, described in section 5.2.3.4, was employed. The effect of the seismic mass thickness on the natural frequency and the maximum and minimum detectable acceleration is shown in figures 5.17 and 5.18. From this, it is easily seen that increasing the thickness of the mass reduces the resonant frequency of the device. However, this also leads to a reduction of both the minumum and maximum acceleration levels detectable. Therefore, the thickness of the seismic unit was chosen again as 5 mm.

(b) Light Input/Output Connection

Piezoelectric accelerometers are self generating ie. they require no power. An induced acceleration causes a force to act upon the piezoelectric element and the force produces a charge in the element. This charge is therefore proportional to the acceleration. Consequently only an output connection is required so that the acceleration can be analyzed.

In a light modulated accelerometer, there needs to be both an input and an output and due to the configurations considered two ports in the transducer case are required.

The transducer could be operated without any actual connection so that the light travels through the air. However, one aim of the project was to design and develop an

accelerometer which could be used for remote measurement. To do this necessitates the use of fibre optic cables. The fibre cables needed to be single mode at the operating wavelength of 632.8nm. Hence, two 2m lengths of single mode optical fibre cable (4/125μm) with SMA connectors were purchased from Spindler & Hoyer Ltd. The transducer connectors therefore had to be designed to be compatible with the SMA connectors and also house the coupling optics.

Gradient index lenses were chosen for the coupling operation due to their low coupling loss, small size and for ease of handling. The pitch of the lens was chosen to be 0.23P (see figure 5.3) to achieve a specific focusing arrangement. The working distance, d_w, for this lens at the operating wavelength is 0.15mm. This distance was incorporated into the design of the connector. The working drawing for the connector is shown in figure 5.19.

5.2.3.4. Prediction of Accelerometer Performance

Any vibrating system for which the restoring force is directly proportional to the negative of the displacement is said to exhibit simple harmonic motion. Most solid materials stretch or compress according to the equation F = kx as long as the displacement is not too great. Because of this many natural vibrations are simple harmonic or close to it.

It can be shown that

$$\frac{d^2x}{dt^2} + \frac{k}{m}x = 0 \qquad 5.51$$

which is known as the equation of motion for a simple harmonic oscillator. This equation was used earlier in section 5.1.2 applied to a spring mass system as used in piezoelectric accelerometers.

From this equation, expressions can be derived for displacement velocity and acceleration. The equation for acceleration is

$$a = -\omega^2 D \cos(\omega t+\phi) \qquad 5.52$$

where D is the amplitude of the vibration, ω is the angular frequency and ϕ the phase angle ie. the time after t=0 that the peak displacement is reached.

It can be shown that the natural frequency of such a mass/spring system is given by

$$\omega_n = \sqrt{\frac{k}{m}} \qquad 5.53$$

where k is the spring stiffness and m is the mass of the seismic unit.

The spring stiffness, of the system shown in figure 5.1, can be calculated by the expression

$$k = \frac{EA}{L} \qquad 5.54$$

where E is the Young's modulus of the material, A is the cross sectional area of the spring mass unit and L is the length.

Since an oscillating mass repeats its motion after a time equal to its period and a sine/cosine function repeats itself after every 2π radians then it can be shown that

$$\omega = \frac{2\pi}{T} = 2\pi f \qquad 5.55$$

where f is the frequency of motion.

When a spring mass assembly is vibrated the mass applies a force to the spring element which is proportional to the vibratory acceleration. Therefore, it can be written that

$$F = -m\omega^2 D \cos(\omega t+\phi) \qquad 5.56$$

where m is the mass of the seismic unit.

Consequently, the stress, S, acting on the spring is

$$S = -\frac{m\omega^2 D}{A} \cos(\omega t+\phi) \qquad 5.57$$

where A is the cross sectional area of the spring.

If an optic element is used as the spring material then the applied stress will create a change in the refractive index. The material parameter which relates the applied stress to the change in index is known as the stress optic coefficent, C. Hence, the change in refractive index is given by

$$\Delta n = -\frac{mC\omega^2 D}{A}\cos(\omega t+\phi) \qquad 5.58$$

Using the mathematical analyses, in section 5.2.3.2, for the various design configurations studied in conjuction with the equation above it is possible to determine accelerometer performance.

The two parameters usually associated with the performance of piezoelectric accelerometers are the electrical response with acceleration and the electrical response with frequency. The two ideal responses are illustrated in figure 5.20 where it can be seen that the response to acceleration increases linearly with the acceleration level. The frequency response, however, remains constant over a wide frequency range.

In the light modulated accelerometer manufactured, a polymethyl methacrylate sensing element was used in a x type configuration. Therefore inserting the material parameters into the appropriate equations the maximum and minimum detectable acceleration levels can be determined.

The minimum acceleration level that can be determined can be given by

$$a_{min} = \frac{S_{\lambda/2}\, AC}{m} \qquad 5.59$$

where

C is the stress optic coefficient
A is the cross sectional area of the sensing element
m is the mass of the seismic unit and
$S_{\lambda/2}$ is the stress required to cause a path change of $\lambda/2$

The stress required to bring about a phase change of $\lambda/2$ is obviously dependent on the design of the element along with the stress optic coefficient of the sensing material. Using the mathematical analysis in section 5.2.3.2.(c) it can be shown that the minimum acceleration level detectable is of the order of 50 000g which is a high level of acceleration.

The maximum acceleration detectable is dependent upon the compressive yield strength, S_y of the material, thus

$$a_{max} = \frac{S_y\, AC}{m} \qquad 5.60$$

Using this equation, the maximum detectable acceleration level can be shown to be of the order of 500,000 g which is far in excess of the acceleration levels such a device would be subjected to.

Therefore this analysis shows that the bright/dark interference brought about by a phase change of $\lambda/2$ cannot be used practically. However, the change in intensity due to this interference effect of two beams can still be detected with modern electronic detection equipment. Therefore,this model could be further developed to calculate the maximum and minimum detectable levels using such an intensity system.

5.2.4 Light Detectors

At the end of an optical transmission line there must be a receiving device in order to monitor the optical signal. The first element of the receiver is the photodetector. The photodetector senses the luminescent power falling upon it and converts the variation of this optical power into a corresponding varying electric current.

There is a wide range of photodetectors available each with various properties and performance characteristics. These devices are usually classified according to their detection mechanism and those commonly encountered fall into three main categories namely:

(a) photoemissive detectors;

(b) thermal detectors; and

(c) semiconductor detectors.

Details of these devices is given below.

5.2.4.1 Photoemissive detectors

The photomultiplier is the most common photoemissive device. Materials such as lithium, sodium and caesium emit electrons from their surface when illuminated by an external source of light. This phenomenon is known as photoelectric emission and is the basis of operation of photoemissive detectors such as the photomultiplier.

In the photomultiplier, electrons are emitted from the photosensitive surface when the incident photons have enough energy to free the electron from its bond and remove it from the material. This energy corresponds to the energy difference between the top of the valence band and the ionization level of the material. This, therefore, represents the

minimum energy required to remove an electron from the surface and as a consequence there is a cut-off wavelength above which no photoelectrons will be emitted. This condition is expressed as

$$W_{min} = \frac{hc}{\lambda_c} \qquad 5.61$$

where λ_c is the cut-off wavelength.

Photomultipliers normally consist of a photocathode (the light sensitive surface), a series of secondary electrodes called dynodes and a photoelectron collector known as the photoanode.

Light impinging on the photocathode ejects electrons from the surface. The electric potential between the cathode and anode accelerates the photoelectrons towards the chain of dynodes each of which is at a slightly higher potential than the one before it. As each electron strikes a dynode a number of secondary electrons are produced each of which produces further secondary electrons at successive dynodes. The overall gain can be as high as 10^6.

Unfortunately, their large size and high voltage requirements make them unsuitable for optical fibre systems.

5.2.4.2 Thermal Detectors

Unlike other detectors which respond directly to photon collisions with electrons, thermal detectors respond to the heat content of the incident radiation. On irradiation light is absorbed and the detector material increases in temperature producing a change in one or more of its electrical properties. Sensitivities tend to be lower but the devices

can normally withstand much higher irradiances.

Certain crystalline materials exhibit a phenomenon known as ferroelectricity by which the existence of an internal electric field induces a charge distribution on opposite faces of the crystal. The origin of this field arises from the small permanent electric field associated with the individual atoms or molecules which comprise the crystal. When the crystal is well below a certain temperature, the Curie temperature, the individual fields align themselves in the same direction to produce a net internal field parallel to the crystal axis. As the crystal is heated, thermal agitation of the molecules disrupts the alignment of the field and with it, the charge distribution on the crystal faces until, at the Curie temperature, alignment is totally destroyed.

Typical ferroelectric crystals such as lead zirconate form the sensitive element in pyroelectric detectors. The crystals faces are coated with a transparent material, permitting transmission of incident radiation and which also acts as electrodes. Incident radiation produces local heating which changes the surface charge in the crystal and hence alters any stored charge in the electrodes. It is this change in the stored charge which is detected as a current flow in the external circuitry. Because it is a change in stored charge which is measured, pyroelectric detectors can only be used with continuous light beams if an external beam chopper is used. The sensitivity and spectral response are dependent on the chopping frequency.

Pyroelectric detectors involve the conversion of photons to heat. Photon absorption results in a temperature change of the detector material. This gives rise to a variation in the dielectric constant which is usually measured as a capacitance change. The response of this detector is quite flat over a broad spectral band but its speed is limited

by the detector cooling rate after it has been excited. Its principal use is for detecting high speed laser pulses and it is not well suited for optical fibre systems.

5.2.4.3 Semiconductor Photodetectors

Semiconductor photodetectors are small, light, sensitive, fast and can operate with just a few bias volts and are, therefore, ideal for optical fibre systems. The two most used are the pin and avalanche photodiode.

(a) PIN Photodiode

PIN photodiodes are the most common detectors in fibre systems. The pin diode has a wide intrinsic semiconductor layer between the p and n regions. This layer has no free charges so its resistance is high, most of the diode voltage appears across it and electrical forces are strong within it.

Because the intrinsic layer is so wide, there is a high probability that incoming photons will be absorbed in it rather than in the p or n regions.

To create an electron-hole pair, an incoming photon must have enough energy to raise an electron across the band gap. This requirement leads to a cut-off wavelength.

$$\lambda = \frac{1.24}{W_g} \qquad 5.62$$

where λ is the wavelength in μm and W_g is the bandgap in electron volts.

Silicon is the most practical fibre optic detector but it cannot be used at wavelengths above 1.1μm.

(b) Avalanche Photodiode

The avalanche photodiode (APD) is a semiconductor junction detector that has internal gain, which increases its responsitivity over pin devices. In this respect the APD is similar to the photomultiplier tube and the avalanche gain is much less. This gain, however, makes the APD more sensitive than pin diodes.

Avalanche current multiplication comes about in the following way. A photon is absorbed in the depletion region, creating a free electron and a free hole. The large electrical forces in the depletion region cause these charges to accelerate, gaining kinetic energy. When fast charges collide with neutral atoms, they create additional electron-hole pairs by using part of their kinetic energy to raise electrons across the band gap. An accelerating charge can generate several new secondary charges. The secondary charges, themselves, can accelerate and create even more electron-hole pairs. This is the process of avalanche multiplication.

The accelerating forces must be strong to impart high kinetic energies and this is achieved with large reverse biases, several hundred volts in some instances. Typical avalanche responsivites range from 20 to 80 A/W.

As with nonmultiplier pin diodes, the response speed of the APD is limited by the charge carrier transit time and the RC time constant.

Avalanche photodiodes have excellent linearity over optic power levels ranging from a fraction of a nanowatt to several microwatts. If more than a microwatt is available at the receiver, an APD is usually not needed. At this power level pin diodes provide enough responsivity and sufficiently large signal to noise ratios for most applications.

5.2.4.4 Conclusions

In this research an optical detector was required for use in the materials investigation and also in the testing of the accelerometer. The requirements for such a detector was that the output should be linear with the light intensity and be able to operate at high speed.

Therefore. a high speed pin photodiode was chosen and incorporated into the circuit shown in figure 5.21.

5.2.5 Light Modulated Transducer System

A schematic diagram of a light modulated transducer system is shown in figure 5.20. The various components of the system have been described earlier. This section deals with the way in which the individual components make up such a system.

A requirement of the project was that the light modulated accelerometer was to use phase/intensity modulation and therefore a reference channel was required. Consequently, beamsplitters would have to be incorporated into the system. Ideally the reference channel should be identical to the transducer channel except that it is not subjected to the measurand. However, due to the expensive nature of optical equipment and the limited finances available, the reference channel was to be passed through air. This eliminated the necessity for an additional coupler, fibre and collimator.

The beamsplitters, coupler and collimator, supplied by Spindler & Hoyer, were incorporated into their "microbench cubes". A connector was machined so that the whole assembly fitted onto the laser.

The light modulated accelerometer designed has been described earlier and is shown in figure 5.15. The input and output optical fibres plug into the accelerometer by the use of the connectors shown in figure 5.19.

The theoretical losses for this system were calculated and this is shown in the table 5.2.

6 Experimental Procedure

The objectives of this research program were concerned with the design and development of a light modulated accelerometer. Section 5 described in detail the whole design process from the choice of light source and optical detectors to the design of the accelerometer and the fundamental component of any device, the sensing element.

The development of such a device can be split into two key areas. Firstly, the testing of the accelerometer to determine performance characteristics and secondly, the determination of certain properties for a range of materials. This second key area is extremely important as optimisation of the sensing element by the right choice of material would undoubtedly lead to an improvement in the operating performance.

This section details the experimental procedure for the testing of the accelerometer and the material property determination. No experimental facilities were readily available and therefore some considerable time was spent acquiring and setting up appropriate apparatus and devising suitable procedures.

6.1 Determination of Material Properties

For a material to be considered for application in a light modulated transducer information is required of certain material properties, the most important of which, in the transducer which has been designed, are the stress optic coefficient, the expansion of the material due to an applied stress and the compressive yield stress. Thermal properties are also of interest, as accelerometer performance could be affected, the most important being the thermo-optic coefficient, the thermal expansion and the temperature of any phase transitions.

This section describes the experimental techniques for determination of such properties.

6.1.1 Sample Preparation

6.1.1.1 General Sample Preparation

The polymeric samples were machined into parallelepipeds of various dimensions so that all angles were very close to 90°. The edges of the specimens were ground to a 60 μm paper finish.

The sensing element was machined from cast polymethyl methacrylate sheet to the dimensions shown in figure 6.1. The edges of the element, ie. those which transmit or reflect the light, were polished flat down to 1μm using standard polishing wheels.

6.1.1.2 Optical Coating

In the interferometer tests which will be described in later sections, some samples required a reflective coating in order to reflect the light. For the sensing medium, to be used within the light modulated accelerometer, a reflective coating is also necessary.

Although internal reflection occurs in both these cases a reflective coating is advantageous as it reduces light loss and results in brighter fringes. Two methods were tested as described below.

(a) Sputter Coater

The sputter coater within the School of Engineering was used to coat samples with platinum for subsequent examination using surface analysis techniques.

The sample is placed in a small chamber which is evacuated to $7x10^{-2}$ mbar. The sample is placed onto the anode and the platinum target forms the cathode. The chamber is flushed with argon at low pressure and a potential difference of approximately 2.5 kV is applied between the two electrodes.

This intense electric field ionises the argon gas forming ions which are attracted to the cathode. These ions then knock off, or sputter, platinum atoms some of which fall onto the sample producing a layer, the thickness of which is dependent on the sputtering time.

Typically, two minutes sputter at 2.5 kV, 25 mA produces a platinum overlayer of approximately 300 nm.

Test samples were sputtered for ten minutes in order to assess the coating quality. The resultant coating had a dull appearance and was not thick enough to reflect all the light. Sputtering times needed to achieve an acceptable thickness were considered impractical. Therefore, an alternative coating techniques was required.

(b) Edward's Vacuum Coating Unit

The Edward's vacuum coating unit is used for depositing carbon films onto samples to undergo analysis on a Scanning Electron Microscope (SEM). However, by fitting an appropriate attachment, coating with other materials becomes possible. This entails placing a tungsten basket between two terminals within the sample chamber. The appropriate coating material is then placed within the basket. The material chosen for use within this unit was high purity aluminium, which was thought to be a more suitable material for this type of application owing to its higher reflectivity. The operation of the coating unit was as follows.

Appropriate samples were placed on the stage of the chamber approximately six inches below the basket. A small cylinder of high purity aluminium welding rod (99.999% Al), approximately 50 mg, was placed within the basket. The glass bell jar was then placed onto the baseplate ensuring that the sealing gasket was in place and the air admit

was switched off. A schematic diagram of the vacuum system is shown in figure 6.2. On this particular unit all valves were operated using a central level on the front of the control panel. By moving the valve lever through 180 degrees in an anti-clockwise direction, the backing valve was closed and the roughing valve was opened to permit the pumping down of the chamber. The chamber was pumped down until the pressure reading on the Pirani gauge read $3x10^{-1}$ mbar. By turning the valve lever 180 degrees in a clockwise direction the roughing valve was closed and the backing valve opened. The high vacuum valve was then opened by slowly pulling the valve lever outwards and turning by 180 degrees again in a clockwise direction. This enabled a chamber pressure of the order of $1.5x10^{-5}$ mbar to be achieved, as denoted by the Penning gauge.

The low tension selector was depressed and the setting of the variable transformer was increased slowly. As the current through the basket increased, it was observed to glow and a point was reached, midway on the transformer setting, at which the aluminium was observed to commence melting. After approximately two minutes at this setting, all the aluminium had dispersed in the chamber.

To remove the samples, the pressure in the chamber was brought up to atmospheric by closing the high vacuum valve and opening the air admittance valve.

This procedure was repeated twice in order to guarantee total light reflection within the polymer samples. Placing twice as much aluminium within the sample basket led to premature failure of the tungsten baskets.

Initially, the basket needed to be descaled to remove any surface grime which could affect the quality of the resultant coating. This entailed the same procedure as above but with no samples in the chamber and an empty basket.

6.1.1.3 Differential Scanning Calorimetry (DSC) Samples

The maximum size of samples to undergo DSC analysis is determined by the aluminium crucible in which the sample sits. This restricts samples to a maximum size of 2 x 3 x 3 mm. Small samples were cut from cast sheet of polycarbonate, polymethyl methacrylate, polystyrene, polyvinyl chloride and araldite epoxy resin using a fine hacksaw and polished down to the required size on a 60 μm grade paper.

The sample was then placed inside a pre-weighed aluminium pan and lid, complete with ventilation hole, and hermetically sealed using the Mettler sealing press available. The sealed crucible was then weighed to determine the mass of the polymeric sample (10-20 mg). The sample was then ready for insertion into the DSC cell.

6.1.2 Determination of Stress Related Properties

When a stress is applied to a material certain changes occur in the material as a result. In a project of this type it is important to have a knowledge of these changes.

Of fundamental importance is a knowledge of the rate of change of refractive index with stress, the stress optic coefficient, as it is this parameter on which the sensor has been based. A knowledge of the extent of the expansion caused by the applied stress is also desirable. The materials available to be tested under stress were polycarbonate, polymethyl methacrylate, polyvinyl chloride and an epoxy resin.

When determining these parameters, it is important to consider how the stress is to be applied. In the tests described below, this was to be achieved using a compression rig fitted to a tensile testing machine. It was considered useful to observe the stresses generated in a material by such a rig and this was realised using a plane polariscope as described below.

6.1.2.1 Description of Stressing Apparatus

In the following tests the stress was applied to the material samples by placing in a compression rig fitted to a JJ Lloyd tensile testing machine. A schematic diagram of the rig is shown in figure 6.3. The directions of the resultant principal stresses generated in the samples to be tested were determined using a crossed plane polariscope.

(a) Principal Stress Determination

The polariscope is used to measure the relative retardation or phase differences produced when polarised light passes through a stressed photoelastic model.

The polariscope consists of a suitable light source and two polarisers. The first polariser

converts the natural light from the source into a field of plane polarised light into which the model is placed. The second polariser, called the analyzer, resolves the component waves emerging from the model into one plane so that the effects produced by the model can be measured from the resulting interference of the waves. Such an arrangement is known as a plane polariscope.

In the crossed plane polariscope it can be shown that the transmitted intensity can be given by

$$I = I_0 \sin^2 2\theta \sin^2 \frac{\alpha}{2} \qquad 6.1$$

where θ is the angle between the principal stress σ_1 and the polariser and α is the phase difference between the two components in the model.

From this equation it is obvious that there are two separate conditions under which extinction of the light will be obtained. One condition is that $\theta = 0$ or $90°$ which is satisfied by all points on the plate where the directions of the principal stresses are parallel to the axes of the polaroids and such points appear dark. In general these points lie on continuous curves forming a system of dark bands known as isoclinics. For any given setting of crossed polaroids a corresponding isoclinic pattern can be observed. As the crossed polaroids are rotated this pattern changes as the condition that the directions of the principal stresses and the axes of the polaroids coincide is satisfied in turn by different points within the plate.

The isoclinic pattern is independent of the wavelength of the light used, the phase difference and hence the magnitude of the applied loads and the stress optic coefficient for the material.

The second condition of this equation will be dealt with in the section 6.2.1.3 (a).

The following procedure was used in the setting up of the crossed plane polariscope to investigate the principal stresses in the compression samples. A sodium spectral lamp, used as the light source, was placed in front of the first polaroid. The analyzer was set at 90 degrees to this polaroid so that all the light was extinguished. This is shown schematically in figure 6.4.

A polymethyl methacrylate specimen, approximately 30 x 10 x 5 mm, was placed in a compression rig of a JJ Tensile testing machine and a stress imposed upon it.

A Hitachi CCTV camera was focused on the resultant isoclinic fringes and observed on a CCTV monitor. The fringes were recorded onto video tape enabling photographs to be printed out at a later date.

6.1.2.2 Determination of Stress Expansion

A knowledge of the change in thickness of the specimens with applied stress is important because the path length through an optic medium would obviously change. The change in thickness is also required for the interferometric determination of the stress optic coefficient.

To determine the expansion caused by the applied stress a front face mirrored test sample (30 x 10 x 5 mm) was inserted between the platens of the compression rig incorporated into the JJ tensile testing machine. The setting up of the tensile testing machine is described in detail in section 6.1.2.4. In this case, the slowest test speed being selected, 1mm/min.

The mirror formed the moveable mirror of the Michelson interferometer, shown

schematically in figure 6.5. The main parts consist of two highly polished plane mirrors M_1 & M_2 and two plane parallel plates of glass, G_1 & G_2. G_1 is silvered so that the light coming from the source is divided into a reflected and transmitted beam of equal intensity. G_2 is called the compensating plate and makes the path in glass of the two rays equal.

By makings both arms of the interferometer of equal length, equal size laser spots will recombine at the beamsplitter G_1 and will lead to light being extinguished when the path difference is equal to $\lambda/2$.

Thus by allowing the resultant spot to fall on a photodiode the change in the thickness of the specimen M_2 could be determined. The setting up of the Michelson interferometer was as follows.

The beam of a HeNe laser, radiating at 632.8nm, was made to impinge on the front face of the mirrored test sample at 90 degrees. This was achieved using the positioning equipment available. The components of the Michelson interferometer were then inserted and adjusted so that the two split beams were in planar alignment so that on recombination only one beam appeared.

The detector used in this case was as described in section 5.2.4.4. The output signal from the circuit was connected to the terminal panel of a data acquisition system (see section 6.3) along with the load output signal from the JJ machine.

The sampling rate used to determine the stress expansion was 1000 Hz and once the data had been logged to disk, it could be analyzed via a spreadsheet. In this research programme As-Easy-As was utilised. Using this data the maximum light intensity levels could be correlated to a change in thickness of 632.8nm and thus the expansion as a

function of stress could be determined.

6.1.2.3 Determination of Stress Optic Coefficient

(a) The Circular Polariscope

As stated in section 6.1.2.1.(a) there are two conditions where extinction of light occurs. The second condition is that $\sin^2(\alpha/2) = 0$ ie. $\alpha = 2N\pi$ radians = N cycles where N is zero or an integer. This is equivalent to a relative retardation of N wavelengths. Thus all points on a plate, at which the difference in principal stresses is such that the relative retardation produced is equal to a whole number of wavelengths, will appear dark. In general the difference in the principal stresses varies continuously within the plate so that the loci of such points are smooth curves. These are known as isochromatics and are classified in terms of their fringe order. Isochromatics representing the locus of all points at which the relative retardation is equal to one wavelength (N=1) is called the first order fringe.

Frequently, all information required can be obtained from the isochromatic fringe pattern. Therefore it is desirable to eliminate the isoclinic pattern from the isochromatic pattern. This is achieved by inserting two quarter-wave plates into the polariscope. Circularly polarised light is produced and this eliminates the directional characteristics of the light incident upon the model, on which the formation of the isoclinics depends.

The intensity of the light transmitted through the circular polariscope can be shown to be

$$I = I_0 \sin^2 \frac{\alpha}{2} \qquad 6.2$$

This is the same as the second of the conditions in the plane polariscope and hence only the isochromatic pattern is produced.

As stated previously, isochromatic fringes are loci of points of constant difference in principal stresses and are classified in terms of fringe order. A first order fringe is one in which the relative retardation between the two components is equal to one wavelength.

It can be shown that

$$\frac{N\lambda}{t} = (n_1 - n_2) \qquad 6.3$$

where λ is the wavelength of the light, t is the thickness of the sample and n_1 and n_2 are the principal refractive indices.

For the case of uniaxial stress, the stress optic law (stated in section 4.6) can be shown to be

$$n_1 - n_2 = C\sigma_1 \qquad 6.4$$

where C is the stress optic coefficient. Therefore, it can be seen that

$$\frac{N\lambda}{t} = C\sigma_1 \qquad 6.5$$

which is an equation of straight line format. The stress optic coefficient was therefore determined as follows.

The material under investigation was placed in the compression rig inserted into the

circular polariscope (see figure 6.6) and, as in the principal stress determination, a CCTV camera was focused upon the material which could be observed on a CCTV monitor.

The JJ tensile machine was set up as follows. The lower platen, upon which the sample sat, was raised up to the upper platen so that the sample just touched the upper platen. The machine was set at 20 kN load and 25:1 extension ratio. Both the load and extension gauges were set to zero both on the machine and on the chart recorder. The crosshead speed was set to the slowest possible, 1mm/minute.

The test was started and the fringe change was observed on the CCTV monitor. When a dark fringe passed through the centre of the sample, the pen on the chart recorder was displaced slightly on the extension axis for later analysis.

When the test was complete, the load, and hence the stress, at which the fringe order changed could be calculated, allowing the determination of the stress optic coefficient using equation 6.5. This procedure was carried out under both dark and bright field conditions.

(b) Fizeau Interferometry

Fizeau interferometry is based on the fringes developed from a plane parallel sided slab of material. There are two paths corresponding to reflections from the front and back surface of the slab as shown in figure 6.7. Point P will be light or dark depending on whether the optical paths (taking into account the phase change at the upper surface) differ by an odd or even number of wavelengths. Dark fringes will be present when

$$N\lambda = 2nt \qquad 6.6$$

If the material is stressed then n will change by Δn and the thickness will change by Δt.

It can be shown that the number of fringes passing a point is given by

$$\Delta N = \frac{2t\Delta n + 2n\Delta t + 2\Delta n\Delta t}{\lambda} \qquad 6.7$$

Rearranging this expression, it can be shown that

$$\Delta n = \left[\frac{\Delta N\lambda}{2t} - \frac{n\Delta t}{t}\right] \cdot \left[1+\frac{\Delta t}{t}\right]^{-1} \qquad 6.8$$

Therefore by counting the number of fringes passing a point and measuring the change in thickness upon application of the stress the change in refractive index can be evaluated. The change in thickness was determined as described in section 6.1.2.2 above.

A mirrored test specimen, approximately 30 x 10 x 5 mm was prepared as described in section 6.1. The specimen was then placed in the compression rig incorporated into the JJ tensile testing machine. The machine was then set up again as described in section 6.1.2.4.

The specimen formed the interferometer as shown in figure 6.8. The laser beam passed through the beamsplitter and was incident on the mirrored sample at 90°. The two beams generated ie. from reflection from each face, then propagated along the original path and were redirected onto the photodiode by the beamsplitter.

To reduce errors caused by natural vibrations, the interferometer was placed on an anti-vibration table.

The output from the photodiode circuit was connected to the terminal panel of the data acquisition system (see section 6.3). In order to correlate the fringe shift to the applied stress, the load reading from the JJ machine was also connected to the terminal panel.

The data acquisition software used in this case was Analog Connection (see section 6.3.2). The sampling rate, which was controlled by the software, was set to 1000 Hz. The test commenced and the change in fringe order as the load increased was observed on the graphical screen output of the software. The data was stored to disk for subsequent analysis.

(c) Michelson Interferometry

The configuration of the Michelson interferometer used to determine the stress optic coefficient was slightly different from that used in the expansion tests. In this case a test sample was inserted into one arm of the interferometer.

It can be shown that the extra optical path length as a result of the sample is equal to 2(n-1)t. If the material is stressed so that the refractive index changes by Δn and the thickness by Δt, then it can be shown that the number of fringes passing a point is given by

$$\Delta N = \frac{2t\Delta n + 2(n-1)\Delta t + 2\Delta n\Delta t}{\lambda} \qquad 6.9$$

Rearranging this expression, it can be shown that

$$\Delta n = \left[\frac{\Delta N\lambda}{2t} - \frac{(n-1)\Delta t}{t}\right]\cdot\left[1+\frac{\Delta t}{t}\right]^{-1} \qquad 6.10$$

Again the change in refractive index could be determined by measuring the number of fringes passing a point, using a photodiode, and from measurements taken on the change in thickness.

6.1.2.4 Determination of Compressive Yield Stress

For application of any material in a light modulated accelerometer one of the limiting factors in its upper frequency limit/acceleration limit is the compressive yield stress. Above this value there would be an irreversible change in sensing element shape which would seriously affect the performance characteristic of such a device. Hence, a material with a high compressive stress could be used to higher acceleration levels. Knowledge of these values for a range of materials would therefore be of use.

It was shown that the yield stress of the polymeric materials would only be reached at extremely high acceleration levels. Nevertheless, it is still a property which needs to be known in this type of application.

The compressive yield stress of polymethyl methacrylate, polycarbonate, polyvinyl chloride and an araldite epoxy resin was determined using the compression attachment to the JJ tensile testing machine (figure 6.3). Parallelepipeds 30 x 10 x 5 mm were prepared as described in section 6.1.1. The tensile testing machine was set up as follows.

The sample was placed onto the lower (moveable) platen which was raised so that it was just touching the upper (fixed) platen. The 20 kN load was selected together with a 25:1 paper to crosshead ratio. Both the load and extension gauges were brought to zero along with the pen on the chart recorder. The test was then ready to proceed.

All the materials listed were tested at two crosshead speeds, namely 1 mm/min and 50 mm/min.

The chart recorder produced a graph of load versus extension which, knowing the original dimensions of the sample, could be converted into a stress strain graph. The compressive yield stress could thus be determined simply by reading the appropriate value off the graph.

Values obtained for the compressive yield stress were expected to vary with the test speed due to the viscoelastic nature of such polymeric materials. The rate of loading would obviously vary during testing but as stated above would only become important at those very high acceleration levels indicated.

6.1.3 Determination of Thermal Properties

With regard to a light modulated accelerometer, fluctuations in temperature will give rise to various changes in the sensing element. Such changes include a change in the element dimensions, a change in the refractive index of the material and a possible change in the properties due to microstructural variations. All these factors will lead to a change in the performance characteristics of such a device.

Consequently, a knowledge of the effects that such a temperature variation has on possible materials for application in an accelerometer would be desirable. Such information could then be used to reduce the detrimental effects of temperature change by design. The materials available for these experimental tests were polycarbonate, polymethyl methacrylate, polystyrene, polyvinyl chloride and an epoxy resin.

This section describes the techniques for determination of the thermal properties along with thermal variation apparatus.

6.1.3.1 Description of Thermal Equipment

In order to determine the thermal variation of certain properties, samples need to be situated in a variable temperature environment compatible with the measuring technique.

Most of the techniques within this section utilise interferometry in the property determination. Two variable temperature environments have been used, one for temperatures between -50 and 20°C and one for temperatures between 20 and 200°C. Both these systems may be incorporated into or form the interferometer. These systems are described below.

(a) Low Temperature Environment

The apparatus used for the determination of thermal properties from -50 to 20°C is shown in figure 6.9. A small chamber which contained the sample was manufactured out of polymethyl methacrylate. This chamber contained two ports; one for the attachment of a vacuum pump to prevent condensation at low temperatures, the other to admit a thermocouple to enable temperature measurement. The top of the chamber was sealed by an optical flat and vacuum grease.

This chamber sat inside a insulation gasket which fitted into the neck of a dewar flask. Liquid nitrogen was poured into the flask to lower the temperature of the sample within the chamber. Using this apparatus, the sample could be reduced to temperatures around -50°C.

(b) High Temperature Environment

A high temperature configuration was used to vary the temperature of the sample between 20 and 200°C. This was achieved by converting a conventional dilatometer. The dilatometer was originally manufactured to measure the expansion of specially prepared metallic samples over the range 20 to 1200°C.

A new temperature controller was fitted to the furnace so that the temperature could be controlled more accurately between 0 and 400°C. In order to place the samples within the furnace a moveable platform was manufactured as shown in figure 6.10. The top of the platform coincided with the hot zone of the furnace. Four finely threaded screws were also manufactured to enable the plane of the sample to be finely adjusted to aid alignment when incorporated into a Michelson interferometer.

6.1.3.2 Determination of Thermal Expansion

Knowledge of the thermal expansion of the materials was needed for two reasons. Firstly, when applied to a light modulated accelerometer, if thermal expansion is not taken into consideration, a variation in temperature will lead to stresses building up with the material due to restriction of the casing which will result in erroneous readings. Secondly, to calculate the thermo-optic coefficient in an interferometer, the change in thickness with temperature is required.

The thermal expansion of each material was determined by incorporating the variable temperature apparatus, described in section 6.1.3.1, with one arm of a Michelson interferometer. This experimental technique was identical to that described in section 6.1.2.2 for the determination of stress expansion.

6.1.3.3 Determination of the Thermo-Optic Coefficient

(a) The Abbe Refractometer

An Abbe refractometer was used to determine the refractive index of the available materials at various temperatures, to an accuracy of $\pm 1 \times 10^{-4}$.

As the critical ray is inextricably linked to refractive index, instruments, such as the Abbe refractometer, may be calibrated to read refractive index directly.

Samples, approximately 30 x 10 x 5 mm, of each material were prepared with faces AB and BC (figure 6.11) polished flat and with corner ABC close to 90°. A small quantity of contact liquid, monobromonapthalene), having a refractive index intermediate between the specimen and the prism was used to form a thin film between the surface BC and the upper face of the instrument prism.

Light from a spectral lamp and interference filter was incident upon the sample at varying incidence angles and was refracted through the sample and the prism. At angles greater than the critical, light is unable to pass through into the prism and the critical ray forms a boundary between bright and dark areas. The light area represents the range of possible light paths through the prism. On emerging from the prism, the rays fall on a mirror where they are reflected into the field telescope of the instrument. The position of the mirror required to bring the borderline into coincidence with the telescope crosswires is indicated by a moving scale observed in the scale telescope from which the refractive index is read.

The prism box of the refractometer is fitted with nipples for circulation of fluids in order to maintain the prism and sample at known temperatures. Using water as the circulation fluid readings of refractive index can be taken between 5 and 80°C. For temperatures between 80 and 150°C polyethylene glycol 400 can be used. The refractive index of polycarbonate, polymethyl methacrylate, polystyrene, polyvinyl chloride and araldite epoxy resin were determined using five wavelength sources between 5 and 140°C. Graphs of refractive index against temperature were then plotted enabling the calculation of the thermo-optic coefficient for each material.

(b) Fizeau Interferometry

The procedure for the determination of the thermo-optic coefficient by Fizeau interferometry is exactly the same as that reported in section 6.1.2.3.(b) except that the variable temperature apparatus described in section 6.1.3.1 replaced the stressing apparatus. Again the fringe shift was monitored this time as a function of temperature.

(c) Michelson Interferometry

Again the Michelson interferometer set up used was identical to that used in the determination of the stress optic coefficient. As above, the stressing equipment was replaced by the variable temperature apparatus.

6.1.3.4 Prediction of the Thermo-Optic Coefficient

Over the past fifty years, many workers have attempted to understand the thermo-optic behaviour of a range of materials. This has been done for a variety of reasons but such work has predominantly involved crystals and inorganic glasses. As a result various theories and relationships have been developed.

To date, however, very few papers have attempted to relate these theories to polymeric materials. The prediction of the thermo-optic behaviour in materials would be useful generally, especially so in this work.

Refractive index can be regarded as a measure of optical density since the greater the index, the lower the velocity of light through the medium. It would be useful to formulate an expression for the actual density change with temperature and attempt to relate this to the change in refractive index (optical density) with temperature.

Consider a material at a temperature T_0 occupying a volume V_0 with density ρ_0. The mass of the material can be given by $m = \rho_0 V_0$.

If the temperature is increased to $T = T_1$, the change in volume can be given by

$$\Delta V = \beta V_0 \Delta T \qquad 6.10$$

where $\Delta V = V_1 - V_0$, $\Delta T = T_1 - T_0$ and β is the coefficient of volumetric thermal expansion.

At this new temperature T_1, the density is ρ_1 and the mass $m = \rho_1 V_1$. Using equation 6.10, it can be shown that

$$V_1 = V_0 + \beta V_0 \Delta T \qquad 6.11$$

Assuming constancy of mass, the resulting change in density $\Delta\rho$, corresponding to the change in volume, can be shown to be

$$\Delta\rho = \frac{m}{V_1} - \frac{m}{V_0} \qquad 6.12$$

which leads to the equation

$$\Delta\rho = \rho_0 \left[\frac{1}{1 + 3\alpha\Delta T} - 1 \right] \qquad 6.13$$

where $\beta = 3\alpha$, for isotropic materials, α being the linear thermal expansion coefficient.

Using this equation, an expression can be derived for the change in density for a unit rise in temperature, namely

$$\frac{\Delta\rho}{\Delta T} \approx 3\alpha\rho_0 \qquad 6.14$$

Using the product rule it can be seen that to derive an expression for dn/dT, an expression for $dn/d\rho$ is required. Hence,

$$\frac{dn}{dT} \approx -3\alpha\rho\frac{dn}{d\rho} \qquad 6.15$$

This is similar to a relationsip derived by Waxler et al

$$\frac{dn}{dT} = -3\alpha\rho\left(\frac{\partial n}{\partial \rho}\right)_T + \left(\frac{\partial n}{\partial T}\right)_\rho \qquad 6.16$$

Waxler et al [130] have also shown that

$$\rho\left(\frac{\partial n}{\partial \rho}\right)_T = \frac{n^3}{6}(p_{11}+2p_{12}) \qquad 6.17$$

Performing several experimental investigations, Waxler et al [10] determined p_{11} and p_{12} along with the thermo-optic coefficient. His results showed that dn/dT was mainly attributable to the first term in equation 4.19.

For both polymethyl methacrylate and polycarbonate the term $(p_{11} + 2p_{12})$ was equal to 0.834. Assuming then, that $(p_{11} + 2p_{12})$ is constant, equation 6.18 becomes

$$\frac{dn}{dT} \sim -2.682\alpha\rho\frac{n^3}{6} \qquad 6.18$$

Therefore, by using the literature data available for n, α and ρ, it is possible to calculate a value for dn/dT.

If the change in index that occurs in polymeric material is merely due to the change in density, then if it is assumed that the time taken for a light beam to propagate through a given medium remains constant, then another expression for dn/dT can be derived.

At a temperature T_1 the thickness of the material is t_1 of refractive index n_1. Therefore the time taken for a beam to pass through is n_1t/c. If the temperature is raised to T_2 the thickness becomes $t_1(1 + \alpha\Delta T)$ and the index n_2. Equating these terms gives

$$\frac{\Delta n}{\Delta T} - n\alpha \qquad 6.19$$

Again using literature data, it is possible to calculate values for dn/dT. However, the material property information that is required in the prediction, ie. n, α and ρ is usually only available at 20°C. This, therefore, limits the prediction of the thermo-optic coefficient to room temperatures.

6.1.3.5 Differential Scanning Calorimetry (DSC)

Michel et al has reported that the temperature coefficient of refractive index shows discontinuities at transition points with three polymeric samples [9].

Although the glass transition temperature and other transition temperatures of various polymers has been well documented, there is obviously a slight variation in transition temperature between samples of the same generic material. Therefore, it was important to determine the transition temperatures of the materials to be investigated in the course of this research. This was achieved using Differential Scanning Calorimetry (DSC).

A sectional view of the Mettler DSC30 measuring cell is shown in figure 6.12 and the measuring principle is as follows.

The required heating rate $\dot{T}$ is input into the Mettler TA3000 controller. The furnace temperature is then increased at such a rate that the reference pan temperature increases at the set rate $\dot{T}$. The temperature of the sample pan T_s lags behind the reference pan owing to the heat capacity of the sample. When the sample starts undergoing a phase transition its temperature falls further behind T_r (figure 6.13) at which point the heat flow to the sample increases as $Q \propto T_r - T_s$. The constant of proportionality is found

by calibrating with an indium standard. The output from the DSC is a plot of heat flow to the sample against temperature.

The samples were prepared as detailed in section 6.1.3. All analyses were carried out at a heating rate of 10°C/min over the temperature range -160 to 250°C. The output was printed on a Epson printer interfaced with the DSC and controller.

The temperature of any transitions could be evaluated with the TA3000 controller. Three temperatures were provided for each transition namely, the intersection of the regression line with the inflection tangent at each side of the transition and at the 50% transition point.

6.2 Characteristics of the Light Modulated Accelerometer Prototype

6.2.1 Determination of Losses in Transducer System

The theoretical losses, for the transducer system described in section 5.2 were calculated from manufacturers data.

When the optical components became available, the losses of each were assessed by 'plugging' the various components together and measuring the light power transmitted using a Megger Optics optical power meter. This meter was able to display a figure in dBm ie. relative to 1mW,

$$Power,\ dBm = 10 \log \frac{I_1}{1mW} \qquad 6.21$$

or alternatively dBr ie. relative to a user selected light level.

$$Power,\ dBr = 10 \log \frac{I_1}{I_0} \qquad 6.22$$

This enabled not only the absolute power through various components to be determined but also the loss through each. By measuring the actual loss through the system, it would be possible to determine where, if necessary, improvements could be made.

6.2.2 Description of Accelerometer Test Equipment

In order to determine the performance characteristics of the light modulated accelerometer prototype vibration test equipment was required. That available consisted of a Ling Dynamic Systems (LDS) control amplifier along with a LDS shaker unit. This system enabled the accelerometer to be tested at variable vibration amplitudes up to a frequency of 10 kHz. Both control dials on this unit were analogue and were not very

accurate. A disadvantage of this system was that very large accelerations could occur given the equation

$$A = -\omega^2 D_m \cos(\omega t+\phi) \qquad 6.23$$

where A is the acceleration, D_m is the maximum vibration amplitude and ω ($=2\pi f$) is the angular frequency.

It is obvious from this equation that for a constant vibration amplitude, an increase in frequency can lead to a considerable increase in the acceleration. If not take into consideration, this could cause damage of the test equipment and accelerometers.

A major improvement in this system was possible by incorporating a piezoelectric accelerometer along with a Ling Dynamic Systems (LDS) model SCO 200 servo controlled oscillator. This system constituted a complete vibration test system capable of performing numerous test functions. The servo controlled oscillator provided a sophisticated vibration test control centre enabling a 4 level vibration test programme.

Both the output of piezoelectric accelerometer and the light modulated accelerometer were displayed on an oscilloscope. The output signal from the processing electronics was recorded using the data acquisition system described in section 6.3.

For testing an accelerometer, driving the shaker sinusoidally with a constant peak acceleration is desirable as an increase in the vibration frequency should not affect the accelerometer output.

Testing of the accelerometer was performed for three modulation modes, namely intensity modulation, phase modulation and polarisation modulation.

6.2.3 Vibration Testing of Polymeric Materials

Mirrored samples of polycarbonate, polymethyl methacrylate, polyvinyl chloride and epoxy resin were prepared to 20 x 10 x 5 mm as described in section 6.1.1.

These samples were placed onto a vibration table and a small block of steel (20 g) was placed on top and clamped down as shown in figure 6.14. This formed the basis of an experimental accelerometer, based on simple reflection, and enabled various materials to be tested under a series of vibratory conditions.

Light from a HeNe laser was made to impinge on the sample surface at an angle of 45 degrees. The light beam was refracted by the sample, reflected off the mirrored rear face and refracted out of the sample so the exiting beam was at 90° to the beam entering.

The polymer sample were tested using three modulation schemes as described below.

(a) Intensity Modulation

A schematic diagram of the experimental set up used for intensity modulation configuration is shown in figure 6.15. In this laser light is incident upon the transducer at 90 degrees. The beam passes through the sensing element and field stop where it is expanded, using a diverging lens, to fill the active area of a photodiode. The output of the photodiode circuit is connected to an oscilloscope and in turn the data acquisition system.

(b) Phase Modulation

For testing under phase modulation, the light beam needs to be split into two to create a reference beam and allow interference when combined. However, for interference to

occur the two beams need to be of the same polarisation state. As stated in section 5, an unpolarised laser beam passing through a stressed plate would create an elliptically polarised beam due to the differing principal indices of refraction within the plate. If the elliptically polarised beam was combined with the unpolarised reference beam interference would not occur. Inserting a polariser in front of the first beamsplitter would enable interference to occur if the direction of polarisation was perpendicular to the principal indices of refraction. The set up is the same as above except that a polariser, two beamsplitters and a mirror have been incorporated (figure 6.16). The second beamsplitter recombines the two beams a results in interference. Again a diverging lens is incorporated to increase the fringe width relative to the photodiode.

(c) Polarisation Modulation

The apparatus used in the polarisation configuration was similar to the two arrangements described above except that two polariser and quarter wave plate units were placed either side of the accelerometer (figure 6.17).

Using the three configurations along with the vibration system, the prototype was tested at accelerations from 1g to 50g and from 25 Hz to 2 kHz. These tests then enabled the calculation of the accelerometer response against acceleration and the response against frequency.

6.2.4 Vibration Testing of Prototype Accelerometer

The prototype accelerometer that was manufactured from the drawings shown in figure 5.15 was tested under the three modulation schemes as described above. Again the device was tested at accelerations from 1 to 50g and from 25 to 2000 Hz.

6.3 Data Acquisition and Analysis

With the experimental tests conducted during the course of this research programme, a method was required to record the experimental data. One method has become commonplace with competitively priced, high powered personal computers. This involves interfacing the sensing equipment and the computer with an analogue to digital converter. The analogue to digital converter modifies the analogue input from the sensing equipment to a digital signal which the computer can read. The data may then be processed using one of the many data processing packages available. This section briefly describes both the hardware and software details.

6.3.1 Hardware Details

For the experimental tests described in sections 6.1 and 6.2, a Strawberry Tree analogue card, incorporating an analog to digital converter, was installed into one of the peripheral connector slots located inside an Opus PC5 computer. This complied with the hardware requirements of the acquisition system.

A terminal panel was connected to the analog card via two cables. All signal input connections were made to the panel which could handle a wide variety of signals and incorporated cold junction compensation for thermocouples.

This analog card was capable of acquisition speeds up to 10kHz with up to 14 bit resolution.

6.3.2 Software Details

(a) Low Acquisition Rates

For acquisition rates below 50Hz a package called Labtech Acquire was used. This enabled the various choices to be made, through the configuration program, such as the sampling frequency, the sampling time, the number of channels etc. As acquisition proceeded a graph plotted on the screen showed how events were proceeding. The data was automatically written to the hard disk as an ASCII text file. When the run was complete the data could be parsed into data format and analyzed by a spreadsheet, in this case As-Easy-As.

(b) High Acquisition Rates

In the testing of the prototype accelerometer, acquisition rates a great deal higher than 50 Hz were required. In this case, software supplied with the analogue card, called Analog Connection was used. As the board was capable of acquiring data at 10 kHz, the highest frequency to which the accelerometer could be realistically tested was of the order of 2 kHz. Again, the software could be configured to the users requirements and the data was logged into an ASCII text file. The data was processed in the same way as described above.

7 Results

The results obtained from the experimental tests are reported in this section. Where appropriate the data has been represented graphically so as to illustrate any trends and relationships.

7.1 Stress Results

7.1.1 Principal Stresses

The isoclinic fringe pattern generated in the polymethyl methacrylate specimen was recorded onto video cassette for a range of polaroid/analyzer orientations. It was then possible to produce photographs from the video image.

Figure 7.1 shows the photographs obtained for several polaroid/analyzer settings. Combinations of all these patterns gives one composite figure showing the isoclinic parameters over the entire field. The resultant composite pattern for this sample is shown in figure 7.2 and from this the direction of the principal stresses at every point in the model can be determined.

7.1.2 Stress Expansion

The expansion of each test material as a result of applied stress was determined using the Michelson interferometer. The variation of the intensity impinging on the photodiode was recorded along with the applied load.

At the points of maximum light intensity the corresponding load values were read and converted into stress. Each stress value then represented the stress necessary to increase the thickness of the sample by 632.8 nm. The resultant graph of expansion against stress, for each material tested, is shown in figure 7.3.(a)-(d). It is evident from these

graphs that the relationship between stress and expansion is essentially linear but at higher stresses a deviation from this behaviour is observed.

7.1.3 Stress Optic Coefficient

(a) Circular Polariscope

When the unstressed test samples were placed in the circular polariscope, the degree of initial birefringence could be observed. Photographs were then printed from the recorded video image. These are shown in figure 7.4 for each specimen and it can be seen that there is negligible birefringence in polymethyl methacrylate, epoxy resin and polyvinyl chloride. The polycarbonate sample displayed a small degree of birefringence. Fine isochromatic fringes could also be observed along the edges of the sample.

As the applied load to the test sample was increased the change in the isochromatic fringe order at the centre of the sample was observed and the pen on the chart recorder was marginally displaced, as can be seen from figure 7.5, in order to correlate the applied stress to the isochromatic fringe order. From this graph, the stress was determined and plotted against the parameter $N\lambda/t$. Figures 7.6.(a)-(d) shows the typical relation for each material tested. The gradient of the resultant graph, as shown by equation 6.5, is equal to the stress optic coefficient.The relationship between the stress and the parameter $N\lambda/t$ for both polycarbonate and epoxy exhibited very good linearity with the large number of experimental points obtained. Due to the low value of the stress optic coefficient, only a small number of data points were obtained with polymethyl methacrylate and polyvinylchloride as is evident in figures 7.6.(c) and (d). However, these results do show essentially linear behaviour.

The stress optic coefficient ie. the gradient of these graphs, was determined by

performing a linear regression analysis on the data points obtained. The coefficients of the analyses for each material is given in table 7.1. Also given is the fringe stress coefficient which is determined from the stress optic coefficient by the relation

$$f_\sigma = \frac{\lambda}{C} \qquad 7.1$$

The photographs shown in figures 7.7 show the isochromatic fringe pattern obtained for each material at various loads. The difference in the stress optic coefficient obtained for each material is immediately evident. Some interesting effects can also be seen. With the polycarbonate specimen, a large number of fine fringes can be seen close to both platens.

(b) Fizeau Interferometer

Using the experimental technique described in section 6.1.2.3.(b) the fringe shift as a function of applied stress could be determined. The change in index as a result of applied stress could then be calculated using equation 6.8.

The resulting graphs of refractive index against stress are shown in figures 7.8.(a)-(d). These graphs show excellent linearity and from the data the stress optic coefficient was determined. The values obtained for each material are reported in table 7.2.

(c) Michelson Interferometer

The determination of the stress-optic coefficient using the Michelson interferometer has been described in section 6.1.2.3.(c). The data is recorded and processed in the same way as that described above except that equation 6.10 is used instead of equation 6.8. This merely represents the slightly differing configurations between the two

interferometers.

Again the change in refractive index as a result of the applied stress showed good linearity as in the case above. The resultant values of stress optic coefficient are reported in table 7.3.

7.1.4 Compressive Strength

The stress strain response of each material was determined using the compression rig of the JJ Tensometer. Each material tested showed a similar response and a typical graph, for polymethyl methacrylate, is illustrated both for fast and slow tests in figure 7.9.

7.2 Thermal Results

7.2.1 Thermal Expansion

The thermal expansion of each material was determined using the method described in section 6.3.2.3. The data recorded was the same as for the stress expansion, except that temperature replaced stress, and the data was analyzed in exactly the same manner. The expansion was plotted against the temperature and are shown in figure 7.10.(a)-(e).

7.2.2 Determination of Refractive Index at 632.8 nm and 20°C

From the readings of refractive index taken using different sources, it was possible to plot the variation of refractive index with wavelength. The experimentally determined values were subsequently fitted to Cauchy's dispersion formula:

$$n = A + \frac{B}{\lambda^2} + \frac{C}{\lambda^4} \qquad 7.2$$

This fitted equation is shown for each material in figures 7.11.(a)-(e) along with the experimentally determined values. The exponents for Cauchy's equation for each material are reported in table 7.4 along with the mathematically determined values of refractive index at 632.8nm. Table 7.5 gives the experimentally determined values at each wavelength along with the value calculated using Cauchy's formula. The error in the calculated value was thought to be less than 5×10^{-4}. This data was needed for the interferometric determination of the thermo-optic coefficient.

7.2.3 Thermo-Optic Coefficient

(a) Abbe Refractometer

Using the experimental procedure described in section 6.2.3.3 readings of refractive index were taken at five different wavelengths between 5 and 130°C for polycarbonate, polystyrene, polymethyl methacrylate, polyvinyl chloride and araldite epoxy resin. Graphs of refractive index against temperature were plotted for each material. Figures 7.12 - 16 show the variation in refractive index for each material at 415.86 nm in particular and also at all five wavelengths.

It can be seen that for polystyrene, polymethyl methacrylate, polyvinyl chloride and epoxy resin that discontinuities exist in the recorded values. These discontinuities appeared in the vicinity of the glass transition temperature T_g.

A linear regression analysis was performed on each data set to determine the gradient of the line either side of the discontinuities in each case. The exponents of the regression analysis are give in table 7.6.

From figures 7.12-7.16 it can be seen that the data points fit well to a straight line indicating the linear nature between refractive index and temperature.

(b) Fizeau Interferometry

The experimental details for the fizeau interferometer have been described earlier. The data acquired using this technique gave the intensity of the light falling on the photodiode and the temperature of the sample. The intensity of the light recorded could be correlated to the number of fringes passing the photodiode over a given temperature range. The temperature at which a fringe passed the photodiode could thus be determined.

Reading off the change in thickness at this temperature from the expansion test results, calculating the refractive index at 632.8 nm using Cauchy's formula and using equation 6.8, the change in the refractive was determined. This change in refractive index could thus be plotted against the temperature change.

The resultant graph for each material is shown in figure 7.17.(a)-(e). Again a regression analysis was performed on the data points and the resultant exponents are shown in tables 7.7.

(c) Michelson Interferometry

The data acquired using the interferometer was identical to that stated above. The data analysis was also identical except that equation 6.10 was used to determine the change in index instead of equation 6.8. The change in index with temperature again showed a linear response similar to those of figure 7.17.(a)-(e). The corresponding results are again given in table 7.8.

7.2.4 Prediction of Thermo Optic Coefficient

In section 6.2.3.4 two equations were derived to predict the rate of change of refractive index with temperature.

Values of density and linear thermal expansion coefficient reported by manufacturers are given in table 7.9. The experimental determined values of thermo-optic coefficient are quoted in table 7.10 along with those predicted using the two models.

It can be seen that the two models give results which are of the same order to those values determined experimentally. The predicted values for polymethyl methacrylate are very close to those actually found. However, the predicted values for the other materials

do not agree as well.

7.2.5 Differential Scanning Calorimetry

The differential scanning calorimeter (DSC) was used to determine the transition points for each material. The unit provided a print out of the energy used over a given temperature range.

The glass transition temperature was evaluated at the 50% transition point and at the intersection of the regression line with the inflection tangent either side of the 50% transition point.

The graphs of heat flow against temperature for each material are given in figures 7.18. to 7.22 and it can be seen that a glass transition was observed for each material tested. An enlarged view of each transition region is also shown. The onset and 50% transition temperatures are reported in table 7.11.

7.3 Transducer Characteristics

7.3.1 Light Losses in Transducer System

The light losses measured for each component is shown in table 7.12. When incorporated into the system, these experimentally determined values result in system losses shown in figure 7.23. The total losses are therefore too great and need to be reduced. One way around this problem would be to use a higher powered laser but practically it is better to attempt to reduce the losses.

Following the light round the optical circuit, the first major loss is the output from the single mode fibre. Attenuation of such fibres is of the order of 5 db/km and therefore negligible in the 2 metre length of fibre used. Therefore, this was thought to be an alignment problem due to the size of the single mode core, 4μm [169]. However, after some time it was apparent that a multimode fibre coupler had been supplied instead of a single mode fibre coupler. The principal difference between the two couplers is the optical elements incorporated within them. The multimode fibre coupler focuses the beam down to a spot size of approximately 50 μm. This was obviously too large for coupling into the single mode fibre and hence excessive light losses resulted.

A replacement coupler was supplied and light losses were reduced to 5 db; still nowhere near the manufacturers reported value [168]. After consultation with the manufacturers [170], it was recommended that higher tolerance NTT-FC connectors be used with the appropriate coupler instead of the SMA connectors.

By this time, a prototype light modulated accelerometers (based on the x type configuration) had been manufactured which were compatible with the SMA connectors.

However, new FC couplers were not manufactured for two reasons. Firstly, the loss

from the accelerometer to the output fibre was high and secondly the new connector would be extremely difficult to manufacture accurately.

Due to the fine alignment procedure of the fibre optic coupler at the source end, re-design of the output connector was considered to be impractical at that stage. Light power would have to be found from elsewhere.

The beamsplitters purchased were 50:50 ratio of transmitted to reflected power and since the reference beam was to be transmitted through the air this could be changed to 90:10. This could easily be produced using the techniques described in section 6.1.1.

Taking these factors into consideration, the losses through the system would still be too high and therefore, without a higher powered laser ($\sim$20 mW) the accelerometer complete with fibre optic light guides could not be tested. Due to the unavailability of such a laser, it was decided to test the transducer with no connectors. Obviously, the testing range would be restricted owing to the size of the ports to take the beam and the actual beam diameter. However, the principle upon which the accelerometer has been based could still be tested to assess it suitability in this type of application.

7.3.2 Vibration Testing of Polymeric Materials

Polycarbonate, polymethyl methacrylate, polystyrene and polyvinyl chloride were all tested on the vibration table, described in section 6.2.2, under three modulation schemes to obtain information on the suitability of each material for application in the light modulated accelerometer. The results obtained are reported in this section. The photodetector output in each case was essentially in phase over the entire range of testing. The maximum phase difference between the piezoelectric accelerometer and the polymer was estimated to be 5° and therefore is neglected at this stage of the development programme. Of more concern was the response to acceleration and frequency.

(a) Intensity Modulation

The intensity variation with time for various acceleration levels is shown in figure 7.24.(a)-(d) for each material. It is clearly evident that as the acceleration level increases so does the intensity response, in a near linear fashion, with each material giving a different response level. The graphs in figures 7.25.(a)-(d) show the intensity response at various frequency levels where it can be seen that at higher frequency levels there is a drop off in the response.

(b) Phase Modulation

The response of the polymer to the sinusoidal input again produced a sinusoidal signal. Again the relationship between the acceleration and the output was plotted. This is shown in figure 7.26.(a)-(d) and can be seen to be essentially linear over the range tested. At higher levels a slight deviation from this linear behaviour is observed. The corresponding graph against frequency is shown where again the drop off is evident 7.27.(a)-(d).

(c) Polarisation Modulation

As in the above cases, graphs were plotted for the acceleration and frequency responses and are shown in figures 7.28.(a)-(d) and 7.29.(a)-(d) respectively. Again, it is evident that the acceleration response is essentially linear whereas that of frequency drops off initially but levels off at frequencies above approximately 1000 Hz.

7.3.3 Performance Characteristics of Prototype Accelerometer

The prototype accelerometer was tested under three modulation schemes in exactly the same manner as the polymeric materials described above. The sensing element was manufactured from polymethyl methacrylate and so similar results to those reported in section 7.3.2 were expected.

(a) Intensity Modulation

The response of the accelerometer over the range of accelerations and frequencies is shown in figure 7.30.(a) & (b). From these graphs, it can be seen the curves are very similar to those described above. However, it may be noted that the actual response level is greater in this case. This is primarily due to the design of the sensing element.

(b) Phase Modulation

Figures 7.31.(a) & (b) again show the response over the acceleration and frequency ranges tested. Again the response level is higher in this case.

(c) Polarisation Modulation

As before the acceleration and frequency responses are shown (figure 7.32.(a) & (b).

8 Discussion

A novel light modulated accelerometer has been designed utilizing the change in refractive index with stress as the transduction mechanism. The accelerometer housing has been based on the highly successful piezoelectric accelerometer which accounts for 90% of vibration monitoring applications. Particular emphasis has been placed on the design of the sensing element. Several design configurations have been considered and by calculating the path change caused by a given change in index, the best of these was selected for use. The prototype transducer manufactured has been tested on standard vibration equipment to assess its performance characteristics.

To aid in the future development of the device, information is required on specific material properties appropriate to this application. A range of experimental tests have been performed to obtain such properties as the stress and thermo-optic coefficients. Two mathematical relationships have been used to predict the thermo-optic coefficient. The prediction of this coefficient would be extremely useful in the future development of this device as an aid in the selection of materials and would also reduce the number of time consuming experimental tests. This information can thus be used as a material selection tool in order to optimize the performance characteristics of the device. The performance of the accelerometer has been modelled to see how these material properties affect the performance characteristics of the device. In this section the sources of experimental error are detailed to assess the validity of the results. The experimental results are then discussed and related to any available literature data. The whole research programme is then brought together and critically discussed to highlight the future development work which needs to be carried out.

8.1 Experimental Errors

A knowledge of the errors associated with the experimental tests carried out is extremely important in order to assess the validity of the results obtained. This section describes the sources of error in each experimental test.

8.1.1 Interferometry

Interferometric techniques were used to determine the expansion and refractive index as a function of both stress and temperature. Although the experimental configurations were slightly different in each case, there were common errors associated with them. These will be discussed briefly before proceeding to look at the errors associated specifically with the expansion and optic coefficient tests.

Even with no change in the sample under test, a shift in the fringe pattern may be observed. This effect may be explained by several factors:

(1) a change in the ambient temperature will cause a change in the refractive index of the air, through which the light propagates and hence a change in the path lengths;

(2) a change in air pressure will again cause a change in the index of the air and the associated effects;

(3) natural vibrations.

The magnitude of the first two are very small and can be assumed to be negligible. However, natural vibrations cause a visible shift in the fringe pattern which can lead to misleading results if not taken into consideration. To counteract this problem, the interferometer experiments were performed on a vibration isolation table. Thus these

possible sources of error were assumed to be insignificant.

Another source of error common to each set up was the reading of the peak intensities from the data recorded. This is dependent on the data acquisition rate compared to the rate of change. The more data points for a given change, the more representative the data will be. Consequently the acquisition rate was chosen at an appropriate level for each test.

(a) Expansion Tests

In the determination of the thermal expansion, a source of error was the expansion of part of the test unit. With the higher temperature unit, this included the expansion of the steel platform and the mirror. The low temperature cell was constructed from acrylic which has a greater expansion coefficient than both the steel and glass leading to serious errors if not accounted for.

In both these cases, these detrimental effects were eliminated by determining the expansion of the empty units. This expansion could then be deducted from the readings during the materials tests.

The uncertainty in the measurement of the stress and thermal expansion lies mainly in processing of the resultant data. Firstly the error in reading the peak intensity which is highly dependent on the data acquisition rate used. The stress at this peak intensity was read and then plotted against multiples of the laser wavelength. The stress was recorded as an electrical signal from the tensometer. This signal was then calibrated using the peak stress as read from the chart recorder. The same principle was used in the determination of thermal expansion. Taking these error sources into consideration, the uncertainty in the measurement of stress/thermal expansion was thought to be of the

order of $1x10^{-6}$m.

(b) Optic Coefficient Tests

The measurement of the stress and thermo-optic coefficients was more complex and as a result had more error involved leading to a greater uncertainty. The stress optic coefficient was calculated using equations 6.8 and 6.10 depending on the configuration of the interferometer. Hence the errors associated with each component need to be considered.

The initial thickness of the material was easily determined to an accuracy of $\pm$ 0.005 and $\pm$ 0.1 mm using a micrometer and vernier gauge respectively. The initial refractive index, however, could not be determined directly. This was achieved, as described in section 7.2.2, by plotting the refractive index at 20°C at five wavelengths determined using the Abbé refractometer and fitting these data points to formulate a Cauchy equation for each material. This equation was then used to calculate the refractive index at 632.8 nm. The error in this determination was thought to be less than $\pm$ 1 x 10^{-3}.

The other errors associated with the determination involved the measurement of the fringe shift with temperature and also the stress expansion.

The errors associated with the determination of stress/thermal expansion are given above. The measurement of the fringe shift are again the same as those described above in that the peak intensity is read along with the appropriate stress/temperature reading.

These factors lead to an error in the measurement of the change in index with stress and temperature of the order of $0.5x10^{-12}$ and $1x10^{-6}$ respectively.

8.1.2 Circular Polariscope

The movement of isochromatic fringes was observed on a video monitor. The stress level corresponding to the fringe shift was recorded on the chart recorder linked up to the tensometer. This enabled a graph of the parameter $N\lambda/t$ to be plotted against stress and so the stress optic coefficient could be determined. The fringe patterns generated within the sample were finely defined in all cases except that for polyvinyl chloride which can be seen in figure 7.7. In actual fact only the centre of each fringe band corresponds to the phase difference of N complete wavelengths and this point has to be considered when assessing the errors. Obviously the greater the number of fringes passing a point during the test the more accurate the results generated would be. This was the case with polycarbonate and araldite epoxy resin. However, with polymethyl methacrylate and polyvinyl chloride, very few fringes passed the point. The percentage error in the determination of the stress optic coefficient was thus increased.

8.1.3 Abbé Refractometer

Refractive index can be easily read to an accuracy of $\pm$ $1x10^{-4}$ using the Abbé refractometer if properly calibrated. The unit was calibrated by measuring the index of the quartz test sample at 20°C. If the unit gave the standard value, as engraved on the sample, then the unit was satisfactory. If not, the scale could be adjusted to bring it into alignment.

However, the accuracy in the determination of the index change with temperature relies on the accuracy of temperature measurement and the material under examination reaching a constant temperature.

Heating of the test sample was achieved using the circulating fluids through the

refractometer unit. Two temperature probes were utilised. One which was placed into the fluid channel, the other inserted into a small hole drilled into the sample. A slight drop in the temperature between the circulation fluid and the sample was observed.

The probes were calibrated between 0 and 100°C which enabled an accuracy in the temperature measurement of the order of $\pm$ 0.5°C. With these limits the error in the measurement of index at a given temperature was $2x10^{-4}$.

8.1.4 Differential Scanning Calorimetry (DSC)

The processing unit of the DSC cell gives an output of dissipated energy against time, as illustrated in the figures described in section 7.2.5. Various factors have an effect on the resultant trace obtained. The heating rate used has an obvious effect on the results. The slower the rate of heating the more accurate will be the transition temperature to the actual temperature.

The heating rate utilised in this work was 10°C/min. This produced a margin of error in T_g of approximately $\pm$ 2°C which was deemed accurate enough in the context which the results were to be used.

An important factor in the reliability of the results obtained from this unit was the calibration which is generally performed using an indium standard. Since the unit had been calibrated a short period before use the results obtained were considered reliable. This fact is substantiated by comparison with the literature values as shown in table 7.11.

8.1.5 Vibration Testing

In the vibration tests undertaken the output of the photodetector was connected to the terminal panel of the data acquisition system from which the data was stored onto computer for later analysis.

One extremely important factor which has to be taken into consideration when using such a system is the data acquisition rate. With a sinusoidal variation, as applied in this case, a sinusoidal output was expected. However, if the acquisition speed is badly chosen then meaningless results are obtained. The number of data points in each cycle is important to maintain the shape of the sinusoid. With only a few data points per cycle a distorted result is obtained therefore giving an inaccurate picture of the events occurring. This is the reason why with a vibration system capable of operating up to frequencies of 10 kHz, it was only possible to test the accelerometer up to 2 kHz.

Another important parameter is the resolution of the data acquisition board. In this case it was 14 bit, which correlates to a resolution of $1/2^{14}$ of the full scale ie. for a full scale of 1V the resolution is 0.06 mV.

The errors associated with the experimental tests along with the repeatability of the results are reported in Appendix A.

8.2 Stress Results

8.2.1 Stress Expansion

The expansion of polycarbonate, polymethyl methacrylate, polystyrene and polyvinyl chloride as a function of applied load was determined using a Michelson interferometer as described earlier. This information was required in order to determine the stress optic coefficient using interferometry.

Testing was restricted to stresses below the yield stress which would be the working range for a material for use in the accelerometer.

The relationship between expansion and applied stress is shown in figures 7.3.(a)-(e). As one would expect below the yield stress, the behaviour is linear over most of the testing range; a slight deviation from linearity being observed at the higher stress levels. Polycarbonate gave the greatest expansion per unit of applied stress which is accountable by the low compressive modulus of the material.

8.2.2 Stress Optic Coefficient

The stress optic coefficient is the property for which most data is required so that the accelerometer performance may be optimized. A series of tests have been performed to determine this parameter for several materials which have been considered for use in a light modulated accelerometer.

(a) Circular Polariscope

The circular polariscope has been used extensively to observe and determine the stress levels and distribution in various complex engineering components. Such data is then used in the design process as an optimization technique.

In this work, the circular polariscope has been used to enable the determination of the stress optic coefficient for polycarbonate, polymethyl methacrylate, polyvinyl chloride and araldite epoxy resin. By recording the change in the fringe order as stress was applied to the samples, under both dark and bright field conditions, it was possible to calculate the stress optic coefficient. This was achieved by plotting the parameter $N\lambda/t$ against the applied stress. Figures 7.6.(a)-(e) illustrate this relation where it can be seen to be linear. The coefficient is found by calculating the gradient. It can be noted here that in the calculation of the stress optic coefficient no account was made for the increase in thickness with applied stress. This obviously leads to a slight error in the calculated value as described in section 8.1.2.

The calculated values, determined using radiation from a sodium spectral lamp, are displayed in table 7.1. The effect of the thickness change is important as it can be seen by the adjusted values which account for the change.

In the accelerometer system which has been designed, the light source was a HeNe laser operating at a wavelength of 632.8 nm. Therefore, it was imperative to determine the stress optic coefficient at this value to assess how the stress optic coefficient varied with wavelength.

(b) Fizeau Interferometer

The experimental apparatus for the interferometric determination is described in section 6.1.2.3.(b). The fringe shift is monitored as the stress is applied which enables the stress optic coefficient to be calculated. The relationship between index and stress is illustrated in figure 7.8.(a)-(e). Again it is shown to be linear over the range tested. However the values obtained are slightly smaller than the polariscope determination

(table 7.2).

(c) Michelson Interferometer

The stress optic coefficient was also determined using the Michelson interferometer. The experimental method and data calculation are very similar to the Fizeau arrangement. Again the results obtained showed linearity over the range tested and again were slightly less in magnitude than the polariscope values.

In both interferometer configurations used, the stress optic coefficient evaluated was slightly less in magnitude than that determined using the circular polariscope. This discrepancy can be accounted for by two factors.

Firstly the change in thickness is taken into consideration in the interferometric determination whilst not in the polariscope case. If this change is considered in the polariscope values, then a reduction in the stress optic coefficient would be observed. Secondly, the interferometer determination used laser radiation of 632.8nm whilst that of the polariscope used a sodium spectral lamp. Therefore, the stress optic coefficient may decrease slightly in magnitude at increasing wavelengths.

These values compare reasonably well with the data which is reported in the literature. This can easily be seen with reference to table 7.3.

As seen from the data, the stress optic coefficient can be a positive or negative quantity which implies that the relative retardation for a material with a negative stress optic coefficient is in a perpendicular plane to that of a material with a positive coefficient. This essentially indicates which principal index exhibits the greatest change such that for a positive value of stress optic coefficient, the change in n_1, Δn_1, is greater than the

change in n_2, Δn_2. The converse is of course true for negative stress optic coefficients.

8.2.3 Stress Optic Behaviour

The accelerometer designed in the course of this research has been based on the stress optic behaviour that some materials exhibit. Therefore, to aid in the future development of the accelerometer, a knowledge of this parameter is needed for a range of materials.

Of the workers who have carried out optical tests under either hydrostatic or uniaxial stress [130,132-3] very few have reported the variation of index with stress. Consequently, the small amount of data available is restricted to those materials commonly used in photoelastic studies.

The work that has been done has either calculated either $\rho\partial n/\partial\rho$ or the photoelastic and compliance constants, p_{ij}, q_{ij}, s_{ij}, c_{ij}, in order to further understand the thermo-optic behaviour of materials.

Waxler et al [132] reported the change in index for several inorganic glasses under hydrostatic pressure up to 100 MPa. From the data reported, both positive and negative stress optic coefficients were obtained.

This change in refractive index with hydrostatic stress is attributed to a combination of two factors [132]. The stress increases the number of scattering centres per unit volume which increases the index, and there is a contraction in the electronic cloud which reduces the polarizability and hence the refractive index. The sign of the index change under these conditions depends on which of these is the overriding factor.

In this work only the absolute value of the stress-optic coefficient was determined and the results agree fairly well with previously reported values.

The magnitude and sign of the stress optic coefficient would be expected to be related to the mechanical properties and deformation behaviour of a material.

Given the values for the materials investigated, it can be seen that the actual magnitude of the stress optic coefficient can be related to the glass transition temperature, which can be regarded as a measure of the chain stiffness. The mobility of the chains at room temperature is obviously a function of the glass transition temperature. The lower the glass transition temperature the more mobile will be the chains at ambient temperatures. This can be seen by looking at polyvinyl chloride (T_g = 77°C) and polymethyl methacrylate (T_g = 116°C), both showing low stress optic coefficients. It can be argued that, although the glass transition temperature of the epoxy resin tested is very similar to that of polymethyl methacrylate, the large stress optic coefficient is due to the epoxy being a thermoset which has a degree of cross links and therefore inherent stiffness at room temperature. The polycarbonate having the highest glass transition temperature (T_g = 150°C) shows the greatest stress optic coefficient. This hypothesis is also supported by polystyrene whose stress optic coefficient is 11.6×10^{-12} /Pa [171] and glass transition temperature is 98°C.

The stress optic coefficient reported for polymethyl methacrylate, however, is negative. This then has to relate to the manner in which the material deforms under stress. One possible explanation for this is that the large side group aligns in a direction perpendicular to the applied stress giving a bigger index change in that direction than in the perpendicular.

8.2.4 Compressive Strength

The compressive strength of polycarbonate, polymethyl methacrylate, polyvinyl chloride and araldite epoxy resin was determined. This was done primarily for application in the model to predict the accelerometer performance. The results obtained showed the typical stress-strain curve, as one would expect from which the yield stress and modulus were determined.

The actual results compare reasonably well with those reported in the literature. This can be seen in figure 7.9. However, one point that has to be borne in mind is that the yield stress and modulus, as with all viscoelastic materials, are dependent upon the speed of the test. A slow speed permits more disentanglement of molecular chains and hence a lower modulus. A fast test gives insufficient time for the chains to disentangle.

8.3 Thermal Results

8.3.1 Thermal Expansion

The thermal expansion of polycarbonate, polymethyl methacrylate, polystyrene, polyvinyl chloride and araldite epoxy resin was measured, primarily to enable the interferometric determination of refractive index. This also provides information which is important in the design process so that adequate clearance can be given to prevent stresses developing in the material by restriction of the case as a result of the thermal expansion.

The relationship between the material expansion and temperature is shown in figures 7.10.(a)-(e) for each material where it can be seen to be linear over a large part of the testing range. Deviation from this behaviour is evident at high temperatures which is dependent on the material. The deviation in this behaviour occurs, as one would expect, in the region of the glass-rubber transition.

The thermal expansion coefficient calculated from this data is reported in table 8.1 along with the manufacturers data. Here, it can be seen that there is good agreement between the two sets of values.

8.3.2 Refractive index at 20°C and 632.8 nm

The refractive index of each material at 20°C and 632.8 nm, was needed to determine the change in refractive index using the HeNe laser. This was achieved by measuring the refractive index at five other wavelengths and by fitting the resultant data to Cauchy's formula.

The fitted equation is shown in figure 7.11.(a)-(e) along with the refractive index data measured at a range of wavelengths. The fitted Cauchy equation shows good agreement

with the experimental results. The differences between the fitted equation and the actual experimental results are reported in table 7.5. From the exponents of the Cauchy equation for each material, the refractive index at 632.8 nm was calculated. This value was to be used in the interferometric determination of the thermo-optic coefficient and the uncertainty in the calculation was thought to be less than $1x10^{-3}$.

8.3.3 Thermo-Optic Coefficient

The thermo-optic coefficient was determined using an Abbé refractometer and two interferometer configurations.

The Abbé refractometer is based on the critical ray and readings of refractive index are read directly from the scale.

The two interferometers, described in section 6.1, are used to determine the fringe shift as a function of temperature. Using equations 6.8 and 6.10 the change in index can be calculated. The errors associated with this determination have been discussed in section 8.1.

(a) Abbé Refractometer

The thermo-optic coefficient was determined by plotting the refractive index values read from the Abbé against the temperature and performing a linear regression analysis on the data points. The graphical results are displayed in figures 7.12 - 16 from which the change in index can be seen to be linear. The exponent for each material was calculated and reported in table 7.6. It is interesting to note that the thermo-optic coefficient remains constant over the range of wavelengths tested.

From the graphs, it is immediately evident that there is a discontinuity in each material

tested with the exception of polycarbonate. The data points to the right of the discontinuity, ie. at higher temperatures, again show linearity over the temperature range and again the thermo-optic coefficient over the range of wavelengths appears to be constant. On closer inspection, it can be seen that the discontinuity appears in the region of the glass transition temperature. This explains why polycarbonate did not show a discontinuity, the glass transition temperature being just above the testing range.

(b) Fizeau Interferometer

A description of the experimental arrangement is given in section 6.3.2.1.(b). The fringe shift was measured as a function of temperature and from the results the change in index was calculated using equation 6.8. The change in index against temperature was plotted and it is evident by reference to figures 7.17.(a)-(e) that the relationship is again linear.

As before, with the results obtained by the Abbé refractometer, the graphs produced displayed a discontinuity in the region of the glass transition temperature. Due to the higher temperature range used in this test, a change in the gradient was this time observed for polycarbonate.

(c) Michelson Interferometer

The procedure for determining the thermo-optic coefficient using the fizeau interferometer was very similar to the Michelson except that a slightly different equation was used to determine the change in index from the fringe shift.

Discontinuities were again observed in the data points. The change in the refractive index with temperature, determined using three experimental techniques, was, for each material, shown to be linear except in the region of the glass rubber transition.

This further substantiates the results obtained by Michel et al [9] and Cariou et al [159] who reported very similar results to those already seen. The gradients of each data set was also in good agreement with those reported by Michel et al. The results of Waxler [10] shown in figure 4.6 do not appear to be linear which could be a result of the small number of data points reported. In fact, if one looks more closely at the data for plexiglas, the gradient of the line appears to drop substantially at an intermediate point in the testing range. This appears to occur at approximately -20°C which is in the region of the β transition.

These results will be discussed further, in relation to the application of these materials in the accelerometer, in section 8.5.

8.3.4 Prediction of Thermo-Optic Coefficient

The experimental results obtained for the thermo-optic coefficient show good agreement with other workers [159] and therefore some degree of accuracy can be assumed. This is obviously important when testing the validity of values predicted using a mathematical model.

A predicted value of the thermo-optic coefficient was calculated for each material tested by applying the literature data available for the density ρ and the thermal expansion coefficient α to equations 6.18 and 6.19 derived in section 6.1.3.4. The results produced using these equations were reported in section 7.2.4.

From these results, some interesting observations can be made. Initially, it can be seen that both equations produce results which are of the right order. For polymethyl methacrylate, both equations produce results which are in error by -1×10^{-6} and -2×10^{-6}

which is extremely good. However the accuracy of the other predicted results was not as good when compared to the experimental values. Polycarbonate, polyvinyl chloride and araldite epoxy resin showed much greater discrepancies between the two predicted values and the those determined experimentally with polyvinyl chloride showing the largest deviation of 0.32×10^{-4}. There are several possible reasons why the results for these three materials is not as accurate as those for polymethyl methacrylate. Using equation 6.18 it was assumed that $(p_{11} + 2p_{12})$ was constant at 0.894. This is, in fact, the result obtained for polymethyl methacrylate and polycarbonate by Waxler [10]. It is, therefore, interesting to note the discrepancy for polycarbonate is much greater than that in the case of polymethyl methacrylate, the error being of the order of -0.1×10^{-4}. Also in each case the refractive index change is assumed to be due solely to the change in density brought about by the thermal expansion. However, this assumption has greater applicability to some materials over other. This assumption is obviously valid in the case of polymethyl methacrylate. The materials tested in this research are also assumed to have the properties as reported in the literature. However, the error introduced as a result of this deviation in property values is thought to be small.

Both equations include the refractive index and would therefore yield differing values of the thermo-optic coefficient over a range of wavelengths. This has been shown not to be the case in this programme of research.

Equation 6.19 is very simplistic and one would not expect accurate predictions using it. However, it gives a reasonable first approximation. The assumption that the time taken to travel through a sample remains constant with temperature is questionable.The actual situation regarding the thermo-optic coefficient is far more complex.

For a more accurate prediction, a knowledge of both p_{11} and p_{12} for each material is

required along with the change in index with temperature at constant density, $(\partial n/\partial T)\rho$.

8.3.5 Thermo-Optic Behaviour of Polymers

It has been shown in this research programme that the thermal variation of refractive index is linear except at the glass rubber transition which brings about a change in the structure of the material. At these points the gradient of the index temperature graph increases but remains linear.

These results are in good agreement with the work carried out by Michel et al [9] and Cariou et al [159]. Michel et al observed other discontinuities in the index temperature graph which have been related to other transition regions. The results of Waxler et al [10] are questionable given the small number of data points reported.

The research carried out here has shown the wavelength of light used to be independent of the thermo-optic coefficient. No other workers have reported such data to enable comparison, but given the accuracy of the results, compared to those of other workers, this is not thought to be in doubt.

The simplistic mathematical models, which assumed the thermal variation to be as a result of the density changes, were used to predict the value of the thermo-optic coefficient and gave reasonable values compared to those determined experimentally.

This highlights the fact that with the polymeric materials investigated, the change in index is predominantly due to the change with density. The increase in the thermo-optic coefficient at the glass transition temperature is again a reflection of the density change. This causes a decrease in the number of scattering centres per unit volume which produces a decrease in the refractive index [132].

This behaviour is in contrast to other materials. The thermo-optic behaviour of optical glasses has shown a minimum in the index temperature graph [135] usually below room temperature so that an increase in temperature leads to a increase in index.

This thermo-optic behaviour will be discussed in reference to the application of these materials in the light modulated accelerometer in section 8.5.

8.3.6 Differential Scanning Calorimetry (DSC)

Experimental traces of energy versus temperature were produced using the DSC unit as described in section 6.1.3.5. Each graph exhibited a glass-rubber transition which were determined using the associated processing unit.

The heating rate has an effect on the results obtained as faster heating rates displace the transition peaks to higher temperatures.

The structure of the test material under examination also affects the results. Commercial polymers can be shown to consist of the various stereoregular forms which account for the differences in the glass transition temperature. For example, commercial polymers of polymethyl methacrylate which are atactic have a glass transition temperature, T_g of approximately 104°C, whereas more syndiotactic forms undergo the transition at approximately 115°C and the isotactic form at 45°C. The polymethyl methacrylate material used in this research can, therefore, be considered to be more syndiotactic.

8.4 Transducer Characteristics

8.4.1 Light Loss

The propagation of the light beam around the optical circuit proved to be problematical with loss occurring at several points. These loss points needed to be refined to make the system workable with the equipment available.

Unfortunately, a series of events conspired to delay the assembly of ideal components, such that the transducer was tested without the fibre optic links. The performance of the accelerometer will be discussed later along with the future development of the device complete with fibre optic links.

8.4.2 Vibration Testing of Polymeric Materials

Polycarbonate, polymethyl methacrylate, polyvinyl chloride and araldite epoxy resin were tested under three modulation schemes over a range of frequency and acceleration.

The response from the photodetector for each material was sinusoidal and was observed to be in phase with the acceleration over the range tested. Given the limitations of the vibration apparatus, only the photodetector circuit was read and hence an accurate value for any phase difference over the testing range was not possible. At the lower levels of acceleration and frequency, the response was in phase with the acceleration and hence this has been assumed to be the case over the entire range.

The response of each material to various levels of acceleration are shown in figures 7.25, 7.27, 7.29 for intensity, phase and polarisation modulation respectively. In each case the photodiode response was essentially linear. The actual response levels in each case were different. The polarisation showed the largest response which was very similar to the phase response. The intensity response was very much smaller. The

intensity response was thought to be due to the variation in the surface roughness of the element rather than a change in the beam direction considered as in section 5. The phase change is due to the change in index parallel to the direction of the applied stress. The polarisation response is caused by change in index both parallel and perpendicular to the stress direction.

The corresponding frequency response times are given in figures 7.26, 7.28, 7.30. Here it can be seen that with increasing frequency there is a drop off in the response. This could be partly attributable to the reduction in the number of data points read every second. Another possible explanation is that the magnitude of the stress optic coefficient drops off with increasing frequency. The response is seen to level off at frequencies above approximately 1 kHz.

It is interesting to note the photodiode response for each material. This can be regarded as being a result of the variation in the stress optic coefficient for each material.

8.4.3. Performance Characteristics of prototype accelerometer

The sensing element incorporated into the light modulated accelerometer was manufactured from polymethyl methacrylate. Therefore, the device was expected to exhibit similar characteristics to the polymethyl methacrylate tested previously.

The result are given in figures 7.31-7.33 where it can be seen that the response is again linear over a range of accelerations. The frequency response for each modulation scheme is again observed to drop off. The photodiode response is somewhat higher than in the previous case. This is primarily due to the differing design of the element. The mathematical analysis performed in section 5 demonstrated that the x-type configuration as used in the accelerometer exhibited greater sensitivity in response to stress. These

results are encouraging for the future development of the device.

The performance characteristics of both the experimental and prototype accelerometers are reported in Appendix B for the three modulation schemes, namely intensity, phase and polarisation.

8.5 General Discussion

The ideal material for application in the light modulated accelerometer designed would be one which showed a high stress optic coefficient and no response to any other environmental conditions, such as variations in temperature.

However, such materials are unlikely to exist. The use of real materials would lead to noise when applied in a device reducing the quality and reliability of the output signal from ideal levels. The properties of a sensing material, therefore, have to be optimised to reduce these deleterious effects.

The change of refractive index with temperature was determined for five materials, the variation ranging from -1.18×10^{-4} to $1.61 \times 10^{-4}/°C$. If a sinusoidal vibration was applied to the accelerometer, the output level of the device would decrease if the ambient temperature increased. Consequently, as with piezoelectric accelerometers, the light modulated accelerometer would need to be calibrated so that the output at a given temperature would be known. The change in index of the sensing element would then be useful so that the device could be used at different temperatures. However, some optical glasses have shown dn/dT values very close to zero [132] which would be ideal in this application. These would obviously have to be investigated further to determine their other properties.

One factor which has not been dealt with is the viscoelastic nature of the polymeric materials tested. The vibration testing of these materials were carried out over short time periods and the response remained constant with time. Thus, the viscoelastic nature of the materials were not observed. It is possible that the response over long testing periods would decrease due to stress relaxation within the material. This response is

more prominent in some materials at higher temperatures. Also, a phase lag may appear, depending on the material and therefore work needs to be carried out to assess these as little data is available. The use of optical glasses may again prove beneficial as such viscoelastic behaviour would be reduced.

Unfortunately, there was not sufficient time to sort out the problems associated with the fibre optic links. These have been highlighted and given further time could be resolved. The device would then need to be tested to observe any changes in the response from the first fibreless trials. One possible source of variation would be movement of the connectors due to the applied vibration which would modulate the intensity of the returning beam.

It has, however, been mentioned that optical fibres are very sensitive to a number of parameters. For this application, one which needs to be considered is the Faraday effect. This leads to the rotation of the plane of polarisation with an electric field. This would be problematical in a phase modulated device as interference is only produced with two beams of the same polarisation. However, this effect can be negated with the use of polarisation preserving fibres.

The effect of this on polymers has not been investigated and would have to be considered along with the Kerr effect which makes isotropic materials behave like a uniaxial crystal in the presence of an electric field.

The development of a product suitable for commercial application requires a long term commitment. This research programme and has provided an excellent base for further development. The accelerometer has been designed using some optimisation techniques and the prototype has been manufactured and tested. The results obtained have been

encouraging and highlight the potential of such a device. In addition several investigatory methods have been used to determine some important material properties. A simple model has been demonstrated to yield reasonable values which is an aid in the selection of potential materials. The transducer performance has been predicted using a mathematical model which has also been used in the design process.

9 Conclusions

The research work reported in this thesis is original and represents a significant contribution to the subject area. From the results of this work several conclusions can be drawn. These have been classified into separate areas.

Accelerometer Design & Vibration Testing

1 From the experimental vibration tests performed on each material over a wide range of accelerations and frequencies, with the application of a sinusoidal vibration, the electrical response of the photodetector was also seen to be sinusoidal and in phase with the vibration.

2 The response of the each material within the experimental accelerometer was found to increase linearly with increasing acceleration over the range tested which is the response one requires of such a device.

3 The photodetector response was observed to decrease with increasing frequency up to approximately 1 kHz where the response levelled off. This response is undesirable as one requires the output to remain constant over a wide frequency range.

4 The acceleration and frequency responses of the prototype accelerometer showed the same behaviour as those of the experimental accelerometer. However an increase in output was observed which was obviously dependent on the design of the sensing element.

Material properties

1 The thermo-optic coefficients have been calculated for polycarbonate, polymethyl methacrylate, polystyrene, polyvinyl chloride and araldite epoxy resin over a wide temperature range using several wavelength sources. In each case a decrease in refractive index was observed with increasing temperature.

2 No literature data has been reported on the dispersion of the thermo-optic coefficient. This has been investigated in this work and the thermo-optic coefficient was found to be constant over the range of wavelengths tested.

3 With each material tested, a change in the magnitude of the thermo-optic coefficient was observed at certain temperatures specific to each material. These discontinuities were found to occur at the glass transition temperature in each case. This was clarified by performing a thermal analysis using differential scanning calorimetry. This clarifies the contradictory results presented in the literature.

4 The thermo-optic coefficient has been predicted using two simple mathematical models. Each model gave very similar results which compared reasonably with the values determined experimentally. This highlights the fact that with the polymeric materials investigated, the change in refractive index is predominantly due to the change with density.

5 The change in refractive index with stress was determined interferometrically for each material and for each case a decrease in index was observed.

6 The magnitude of the stress optic coefficient was determined using a polariscope which compared well with the values determined interferometrically and those

limited literature available for some of the materials tested.

7 The magnitude of the stress optic coefficient was related to the chain stiffness of the polymer via the glass transition temperature and a direct relation between the two was observed for each thermoplastic. The high value of the stress optic coefficient for araldite epoxy resin was accounted for by the inherent chain stiffness of the thermoset material.

10 Recommendations For Further Work

The prototype accelerometer designed and tested has shown promise and further development work needs to be carried out in order to develop the device into a commercial product. The work can be split into three main areas, namely, the accelerometer and testing, materials investigation and the photodetector circuit.

Accelerometer Design & Vibration Testing

1 The accelerometer needs to be tested over a prolonged period of time to investigate how the response changes with time. This is very important considering the viscoelastic behaviour of the materials used in this research. These results will thus provide information regarding the suitability of polymeric materials, which could be manufactured inexpensively, for use in the device even for short period vibration testing.

2 It would be useful to test the accelerometer over a multi-level vibration test programme to assertain whether the device has commercial suitability.

3 To use the device as a remote sensor, the fibre optic cables need to be linked to the source and detector. To achieve this requires the manufacture of FC compatible couplers to connect the accelerometer to the optical cable.

4 Once the accelerometer has been coupled with fibre optic links, the device needs to be tested on the vibration system to investigate the response compared to that reported in this thesis.

5 The major sources of loss in the system reported in this thesis need to be addressed in order to improve the efficiency. Specifically, the light propagation

through the sensing element and the coupling of the return beam into the fibre. The losses through the element may be reduced by higher tolerance polishing to fractions of a wavelength. A redesign of the return coupler may be attempted.

6 With piezoelectric accelerometers, if increased sensitivity is required, a larger device is needed. By manufacturing various size light modulated accelerometers the effect of size on sensitivity could be determined.

7 All piezoelectric accelerometers, especially those based on compression type designs have been found to be susceptible to environmental effects such as temperature variations, acoustic noise, humidity etc. Therefore, the sensitivity of the device to these parameters needs to be investigated.

8 Accelerometers based on shear type designs have shown improved tolerance to these environmental effects. Therefore, it is proposed to design a device based on shear (in conjunction with 11) and repeat the testing that was carried out in this research programme.

9 The prototype, for ease of manufacture, had a lid which was held in place with screws. It is therefore proposed to design a case based along similar lines to the piezoelectric accelerometer. This would lead to an increase in the resonant frequency and thus the operating range. Further improvement could be attained by performing a finite element analysis on the device.

Materials Investigation

10 In the long term, the accelerometer being a remote device may be required to operate at long distances ie 1km. At these distances, attenuation of the beam in the fibre becomes important. One way of reducing the attenuation is to move

towards a higher wavelength light source. There are also other advantages of moving to higher wavelengths, namely:

(a) the core diameter can be increase, still maintaining single mode characteristics, and hence reducing coupling losses;

(b) semiconductor lasers need to be used which are compact and inexpensive thus aiding market acceptance.

11 It was recommended in 8 that a device based on shear be designed. To aid in this development, the isochromatic fringe pattern generated in several shaped samples could be observed therefore permiting the optimum design to be chosen for application in a device.

12 In order to develop the model to predict the thermo-optic coefficient, it is recommended to determine both p_{11} and p_{12}. This could be achieved using interferometry.

13 It would be useful to investigate closely the phase difference between the applied oscillatory stress and the response of the material. This should be done for a range of materials.

14 The effects of both electric and magnetic fields need to be investigated for a range of materials.

15 As a consequence of the viscoelastic behaviour of polymeric materials, it would be useful to investigate the specific properties of a range of crystal and glassy materials.

16 It would be of interest to investigate the optical properties of materials produced under different conditions such as extrusion and injection moulding. This would lead to a greater understanding of the effect of microstructure on refractive index change. This knowledge would determine whether the sensing element could thus be injection moulded cheaply or have to undergo expensive machining operations.

Photodetetcor & Ancillary Equipment

17 It would be useful to write a computer program so that during vibration testing of the accelerometer, a display of the vibration along with associated information was provided.

18 For future development, a hand held box could hold the source and detector and the detctor could give information on acceleration which could be integrated to provide a velocity and displacement output.

11 References

[1] T. Ivall
Transducers, June, 32-39, 1983

[2] B.E. Jones
J. Phys. E: Sci. Instrum. Vol.18, 770-82, 1985

[3] A.L. Harmer
Measurement & Control, Vol.15, 143-51, 1982

[4] D.A. Jackson, J.D. Jones
Optica Acta, Vol.33, No.12, 1469-1503, 1986

[5] J.P. Dakin
Proc SPIE Int Soc Opt Eng, Vol.374, 172-82, 1983

[6] D.A. Jackson, J.D. Jones
Optics & Laser Technology, Vol.18, No.5, 243-52, 1986

[7] B.E. Jones
Proc Symp Optical Sensors and Optical Technology in Instrumentation, 1-15, 1981

[8] A.T. Akhmadiev, E.N. Belotserkovskii, A.L. Patlakh
Sov. J. Opt. Technol. 53 (6) 363-69, 1986

[9] P. Michel, J. Dugas, J.M. Cariou, L. Martin
J. Macromol. Sci. Phys., B25 (4), 379-94, 1986

[10] R.M. Waxler, D. Horowitz, A. Feldman
Appl. Opt. Vol.18, No.1, 101-104, 1979

[11] R.P Feynman, R.B.Leighton, M. Sands
The Feynman Lectures on Physics, Addison-Wesley, 1964

[12] R.K. Wangsness
Electromagnetic Fields, Wiley 1979

[13] R. Guenther
Modern Optics, Wiley 1990

[14] A.K. Ghatak, K. Thyagarajan
Optical Electronics, Cambridge University Press, 1989

[15] E.G. Thomas, A.J. Meadows
Maxwell's equations and their applications, Hilger 1985

[16] J. Midwinter
Optical fibres for transmission Wiley 1979

[17] A. Cherin
Introduction to Optical Fibres McGraw-Hill 1983

[18] E. Snitzer
J. Opt. Soc. Amer. 51, 491-498, 1961

[19] R. Olshansky
Rev. Mod. Phys. Vol.51, No.2, 341-367, 1979

[20] D. Gloge
Rep. Prog. Phys. Vol.42, 1777-1824, 1979

[21] D. Gloge
Appl. Opt. Vol.10, No.10, 2252-8, 1971

[22] R.H. Stolen, W.N. Leibolt
Appl. Opt. Vol. 15, No. 1, 239-43, 1976

[23] D. Gloge
Bell System Technical Journal, Vol. 52, No. 9, 1563-78, 1973

[24] J. Gower
Optical Communication Systems, Prentice-Hall 1984
[25] B.E. Jones
Proc. Conf. Design of Optical Fibre Sensors, 13-15 Sept 1988 1.1-1.19,
Brunel Centre for Manufacturing Metrology
[26] F.M. Mims
Optics News, Vol.6, No.1, 8-16, 1980
[27] J.Tyndall
Royal Inst Great Britain Proc, Vol.6, 189-99, 1870
[28] G. Mahlke, P. Gossing
Fibre Optic Cables, J. Wiley & Sons 1987
[29] T.H. Maiman
Nature, Vol.187, 493-4, 1960
[30] K.C. Kao, G.A. Hockman
Proc IEE, Vol.133, No.7, 1151-1158, 1966
[31] F.P. Kapron, D.B. Keck, R.D. Maurer
Appl. Phys. Lett. Vol.17, 423-425, 1970
[32] W.A. Gambling, H. Matsumura, C.M. Ragdale
Optical and Quantum Electronics, Vol.11, 43-59, 1979
[33] M. Miyagi, G.L. Yip
Optical and Quantum Electronics, Vol.9, 51-60, 1977
[34] W.A. Gambling, H. Matsumura, C.M. Ragdale
Electronics Letters, Vol.14, No.5, 130-132, 1978
[35] G.F. Lipscombe, S.K. Yao, C.K. Asawa
First International Conference on Optical Fibre Sensors, London,
26-28 April, 117-121, 1983
[36] D. Gloge
Appl. Opt. Vol.11, No.11, 2506-2513, 1972
[37] D. Marcuse
Bell System Technical Journal, Vol.52, No.8, 1423-1437, 1973
[38] W.B. Gardner
Bell System Technical Journal, Vol.54, No.2, 457-465, 1975
[39] J.N. Fields, C.K. Asawa, O.G. Raner, M.K. Barnoski
J. Acoust. Soc. Am., Vol.67, 816-818, 1980
[40] J.A. Bucaro, T.R. Hickman
Applied Optics, Vol.18, No.6, 938-40, 1979
[41] J.N. Fields, J.H. Cole
Applied Optics, Vol.19, No.19, 3265-67, 1980
[42] J.N. Fields, C.K. Asawa, C.P. Smith, R.J. Morrison
Advance in Cearmics Vol.2, 529-38, (Ed. B. Bendow, S. Mitra, Am. Cer. Soc.)
[43] N. Lagakos, P. Macedo, T. Litovitz, R. Mohr, R. Meister
Advance in Cearmics Vol.2, 539-44, (Ed. B. Bendow, S. Mitra, Am. Cer. Soc.)
[44] N. Lagakos, P. Macedo, T. Litovitz, R. Mohr, R. Meister
Applied Optics, Vol.20, No.2, 167-8, 1981
[45] C. Davis, T.A. Litovitz, P.B. Macedo
First International Conference on Optical Fibre Sensors, London,
26-28 April, 127-31, 1983
[46] A.L. Harmer
Colloquium on Optical Fibre Sensors, IEE Coll. Digest No. 1982/60

[47] A.L. Harmer
First International Conference on Optical Fibre Sensors, London, 26-28 April, 104-108, 1983

[48] C.D. Kissinger
U.S. Patent No. 3,327,584, 1967

[49] C. Menadier, C. Kissinger, H. Adkins
Instruments and Control Systems, Vol.40, 114-120, 1967

[50] L.J. Lagace, C.D. Kissinger
Proc. ISA 23rd Int. Instrum. Symposium, Las Vagas, 1-10, 1977

[51] W.E. Frank
U.S. Patent No. 3,919,546, 1966

[52] T.E. Hansen
Sensors and Actuators, Vol.4, 545-554, 1983

[53] L.H. Lindström
IEEE Trans Bio-Medical Engineering, BME-17, No.3, 207-219, 1970

[54] A. Ramirez, W.B. Hood, M. Polanyi, R. Wagner, N.A. Yankopoulos
J. Appl. Physiol. Vol.26, No.5, 679-683, 1969

[55] F.J. Clark, E.M. Schmidt, R.F. DeLaCroix
Proc. NEC, Vol.21, 213-216, 1965

[56] J.S. Cole, R.D. Conn
British Heart Journal, Vol.33, 463-468, 1971

[57] A. Wald, K. Post, J. Ransohoff, W. Hass, F. Epstein
Medical Instrumentation, Vol.11, No.6, 352-354, 1977

[58] K. Saito, H. Matsumoto
Digest 11th Int. Conf. Med.& Biomed.Eng. Ottawa, 690-1, 1976

[59] H. Matsumoto, M. Saegusa, K. Saito, K. Mizoi
J. Medical Eng. & Tech. Vol.2, No.5, 239-42, 1978

[60] C.M. Lawson, V.J. Tekippe
Optics Letters, Vol.8, No.5, 286-288, 1983

[61] ASEA
Product Information Brochure

[62] Takaoka
Product Information Brochure

[63] B.E. Jones, G.S. Philp
Proc SPIE Vol. 522, 184-95, 1985

[64] B.E. Jones, R.C. Spooncer
ISA/IMC Comf.Proc. PROMECON 81, London 91-100, 1981

[65] B.E. Jones, R.C. Spooncer
NPL/Sira Ltd. Seminar on Optical Sensing Techniques
Proc SPIE, Vol.376, 29-36, 1982

[66] B.E. Jones, R.C. Spooncer
J.Phys.E: Sci.Instrum. Vol.16, 1124-26, 1983

[67] B.E. Jones, G.S. Philp,R.C. Spooncer
IMC Conf.Proc. PROMECON 84, London, 164-76, 1984

[68] B.E. Jones, R.C. Spooncer
Proc. 2nd Int.Conf. Optical Fibre Sensors, Stuttgart, 223-226, 1984

[69] L.A. Sayce
J.Phys.E: Sci.Instrum. Vol.5, 193-198, 1972

[70] R.T. Murray
First International Conference on Optical Fibre Sensors, London, 26-28 April, 114-116, 1983

[71] B.E. Jones, R.C. Spooncer, E.R. Cox, G.S. Philp
Proc SPIE Vol.545, 224-9, 1987

[72] W.B. Spillman
Applied Optics, Vol.20, No.3, 465-70, 1981

[73] B.W. Tietjen
J. Acoust. Soc. Am. 69 (4) 993-7, 1981

[74] H.Dotsch et al
First International Conference on Optical Fibre Sensors, London, 26-28 April, 67-71, 1983

[75] W.B. Spillman, D.H. McMahon
Applied Optics, Vol.19, No.1, 113-117, 1980

[76] W.B. Spliman, R.J. Gravel
Optics Letters, Vol.5, No.1, 30-1, 1980

[77] J.E. Geake
J.Phys.E: Sci. Instrum. Vol.31, 260-1, 1954

[78] W.E. Hood, E. Oldham
J.Sci.Instrum., Vol.37, 489, 1960

[79] R.J. Baumbick, J. Alexander
Control Engineering, 27 (3), 75-7, 1980

[80] J.E. Geake
J.Phys.E: Sci. Instrum. Vol.8, 860-3, 1975

[81] J.D. Place
IMC Proc.Conf. PROMECON, London, 19-22 June, 157-163, 1984

[82] A.B. Tveten, A. Dandridge, C.M. Davis, T.G. Giallorenzi
Electronics Letters, Vol.16, No.22, 854-5, 1980

[83] R.O. Miles, A. Dandridge, A.B. Tveten, T.G. Giallorenzi
Proc 29th Int Instrum. Symp. Albuquerque, 2-6 May, 1983

[84] C.M. Davis, M. Conley, E.F. Carome
IEEE Int Geoscience & Remote Sensing Symp, San Francisco, Vol.2, 3.1-4, 1983

[85] S.C. Furlong, I.J. Rush, J.M. Martin
Proc SPIE Vol.545, 352-7, 1987

[86] J.A. Bucaro, H.D. Dardy, E.F. Carome
J. Acoust. Soc. Am., Vol.62, No.5, 1302-4, 1977

[87] R.E. Jones, J.P. Willson, G.D. Pitt, R.H. Pratt
First International Conference on Optical Fibre Sensors, London, 26-28 April, 33-7, 1983

[88] A. Dandridge, A.B. Tveten, G.H. Sigel, E.J. West, T.G. Giallorenzi
Electronics Letters, Vol.16, No.11, 408-9, 1980

[89] M.M. Butusov, N.V. Ermakova, N.L. Urvantseva, V.P. Shumilin
Opt. Spectrosc. (USSR), 59 (1), 135-6, 1985

[90] A. Yariv, H.V. Windsor
Optics Letters, Vol.5, No.3, 87-9, 1980

[91] F. Parmigiani
Optical and Quantum Electronics, Vol.10, 533-5, 1978

[92] S. Ueha, N. Shibita, J. Tsujiuchi
Optics Communications, Vol.23, No.3, 407-9, 1977
[93] M. Imai
Optics Letters, Vol.5, 418-20, 1980
[94] R. Kashap, B.K. Nayar
First International Conference on Optical Fibre Sensors, London,
26-28 April, 38-42, 1983
[95] E.J. Post
Reviews of Modern Physics, Vol.39, No.2, 475-493, 1967
[96] A.B. Bukhman, E.M. Dianov, A.Y. Karasik, V.A. Kozlov, A.M. Prokhorov
Telecommun Radio Eng Part 2, Vol.37, No.4, 87-9, 1982
[97] R. Goldstein, W.C. Goss
Optical Engineering, Vol.18, No.4, 381-3, 1979
[98] E. Udd
Proc SPIE, Vol.545, 25-34, 1987
[99] G.W. Chantry
J. Phys. E: Sci Instrum., Vol.15, 3-8, 1982
[100] E.R. Cox, B.E. Jones
First International Conference on Optical Fibre Sensors, London,
26-28 April, 122-6, 1983
[101] R. Kist, S. Drope
Proc SPIE, Vol.545, 64-71, 1987
[102] D.A. Jackson, A.D. Kersey, M. Corke
Colloquium on Optical Fibre Sensors, 26 May, Digest No.1982/60
[103] B. Culshaw
Radio & Electronic Engineer, Vol.52, No.6, 283-290, 1982
[104] A.J. Rodgers
Applied Optics, Vol.20, 1403, 1981
[105] A. Papp, H. Harms
Applied Optics, Vol.19, No.22, 3729-34, 1980
[106] H. Harms, A. Papp
Applied Optics, Vol.19, No.22, 3741-5, 1980
[107] H. Aulich, W. Beck, N. Douklias, H. Harms, A. Papp, H. Schneider
Applied Optics, Vol.19, No.22, 3735-40, 1980
[108] S.R. Norman
Electronics Letters, Vol.15, 309-311, 1979
[109] A.J. Rodgers
IEE J.Electric Power Appllictions, Vol.2, No.4, 120-4, 1979
[110] S.C. Rashleigh, R. Ulrich
Applied Physics Letters, Vol.34, No.1, 768-70, 1979
[111] A.J. Barlow, J.J. Ramskov-Hansen, D.N. Payne
Applied Optics, Vol.20, No.17, 2962-8, 1981
[112] S.C. Rashleigh
Optics Letters Vol.6, No.1, 19-21, 1981
[113] K. Shibata
First International Conference on Optical Fibre Sensors, London,
26-28 April, 164-8, 1983
[114] Y. Hamasaki, T. Miyamoto, Y. Kuhara, M. Katoh, K. Tada
J. Opt. Commun, Vol.2, 7-10, 1981

[115] Y. Hamasaki, H. Gotoh, M. Katoh, S. Takeuchi
Electronics Letters, Vol.16, No.11, 406-7, 1980
[116] J.D. Beasley
Proc SPIE, Vol.544, 201-6, 1986
[117] B.E. Jones, R.C. Spooncer
First International Conference on Optical Fibre Sensors, London, 26-28 April, 173-7, 1983
[118] W.B. Spillman, D.H. McMahon
First International Conference on Optical Fibre Sensors, London, 26-28 April, 110-14, 1983
[119] J.P. Dakin
US Patent No. 4355898, 1982
[120] M.C. Hutley, R.F. Stevens, D.E. Putland
J. Opt. Sensors, Vol.1, No.2, 153-62, 1986
[121] M.C. Simon
J.Opt.Soc.Am.A., Vol.4, No.12, 2201-4, 1987
[122] E.W. Saaski, R.L. Skaugset
7th IEE/PES Trans. & Distrib Conf, 208, 1979
[123] K.A. James, W.H. Quick, V.H. Strahan
Control Engineering, No.3, 30-3, 1979
[124] N.S. Kapany
Fibre Optics: Principles and Applications, Academic Press, 1967
[125] F. Seitz
The modern theory of solids, McGraw Hill, New York, 1940
[126] R.W. Ditchburn
Light, Blackie, London, 1976
[127] H. Mueller
Physical Review, Vol.47, 947-57, 1935
[128] H. Mueller
Physical Review, Vol.47, 175-91, 1935
[129] K.S. Krishnan, S.K. Roy
Phil Mag, Vol.43, 1000-2, 1952
[130] R.M. Waxler, C.E. Weir
J.Res.Nat.Bur.Stand. Vol.69A, No.4, 325-33, 1965
[131] J.C. Maxwell
Roy Soc Edinburgh Trans, Vol.XXI, 87-120, 1853
[132] R.M. Waxler, G.W. Cleek, I.H. Malitson, M.J. Dodge
J.Res.Nat.Bur.Stand. Vol.75A, No.3, 163-174, 1971
[133] R.M. Waxler, G.W. Cleek
J.Res.Nat.Bur.Stand. Vol.77A, No.6, 755-763, 1973
[134] G.N. Ramachandran
in Progress in Crystal Physics, Vol.I, 139-167
Ed. R.S. Krishnan, Interscience, 1958
[135] E. Burnstein, P.L. Smith
Proc. Ind. Acad. Sci. A28, 377-87, 1948
[136] H.N. Ritland
J. Am. Ceram. Soc. 38, 86, 1955
[137] K. Vedam, S. Ramaseshan
in Progress in Crystal Physics, Vol.I, 102-138
Ed. R.S. Krishnan, Interscience, 1958

[162] S. Bywater, P.M. Toporowski
Polymer, Vol.13, 94-6, 1972
[163] N. Bekkedahl
J.Res.Nat.Bur.Stand. Vol.42, 145-56, 1949
[164] M. Gordon, I.A. MacNab
Trans. Faraday Soc., Vol.49, 31-9, 1953
[165] M. Serridge, T.R. Licht
Piezoelectric accelerometers and vibration preamplifiers, B & K 1987
[166] Melles Griot
Optical Components Catalogue
[167] A. Nicia
Applied Optics, Vol.20, No.18, 3136-45
[168] Spindler & Hoyer
OZ Optics Catalogue
[169] Private Communication
D.A. Rogerson
[170] Private Communication
D.A. Rogerson
[171] R.B. Heywood
Photoelasticity for Designers, Pergamon Press, 1969

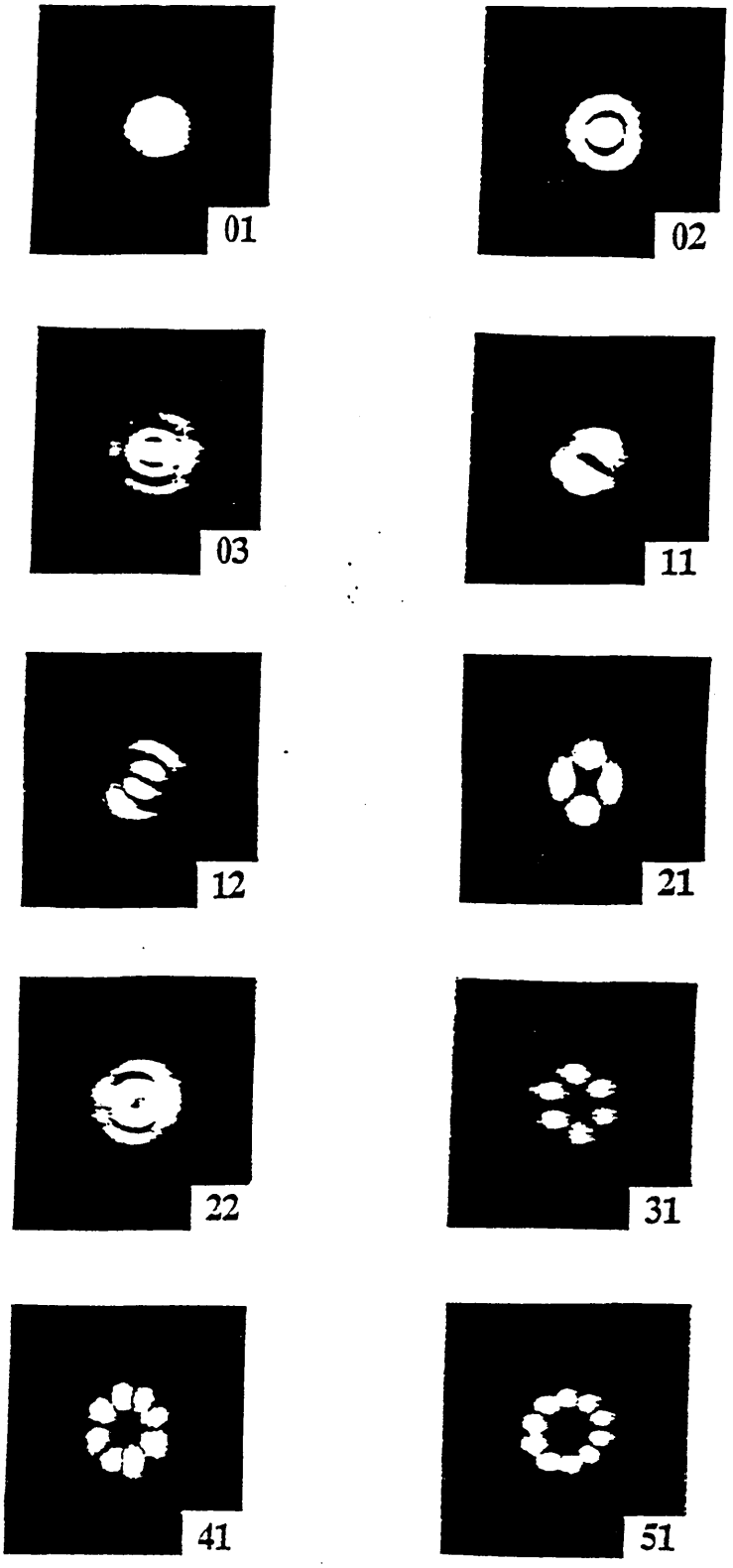

Figure 2.1 The modes of an optical waveguide with characteristic number V = 8.0. The modes are labelled using the linearly polarized (LP) mode notation [22].

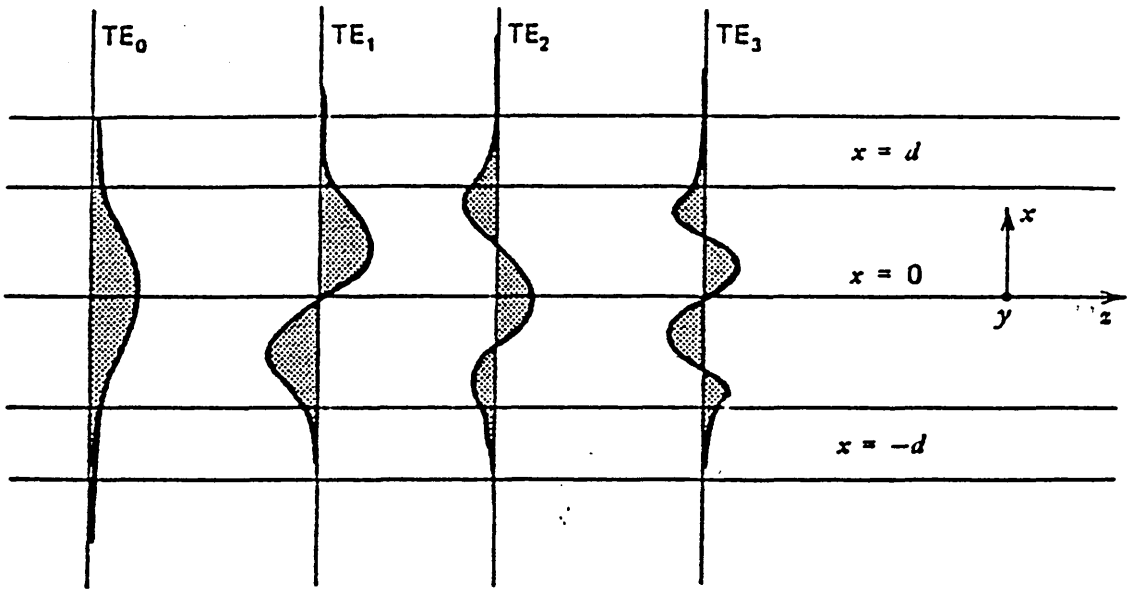

Figure 2.2 The field pattern of several low order modes in a planar dielectric slab waveguide.

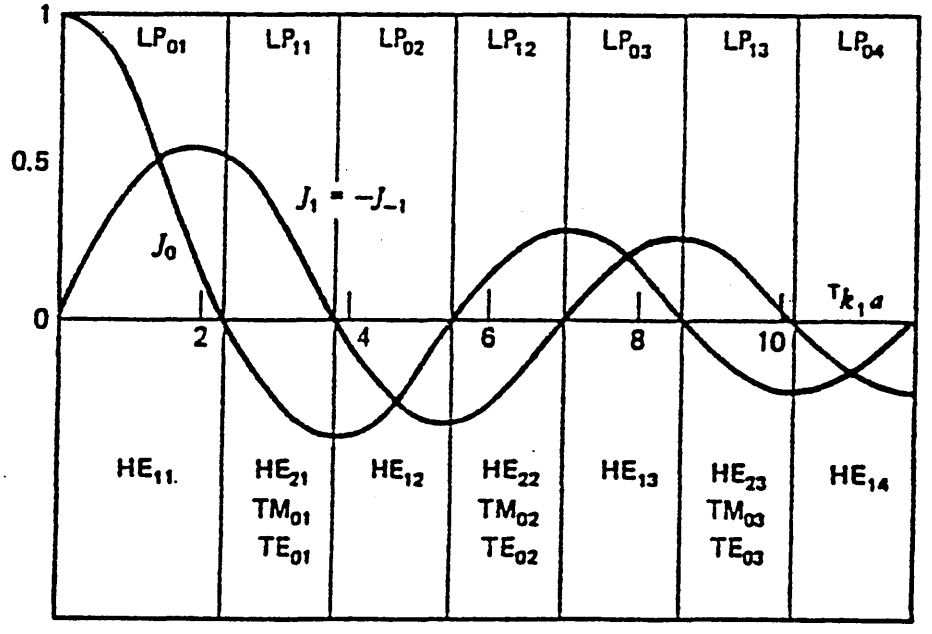

Figure 2.3 Bessel functions showing the allowed regions for various modes plotted against the V number for a step index fibre.

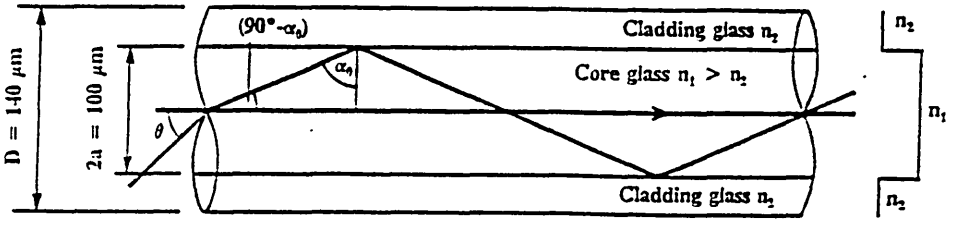

(a) A step index multimode fibre

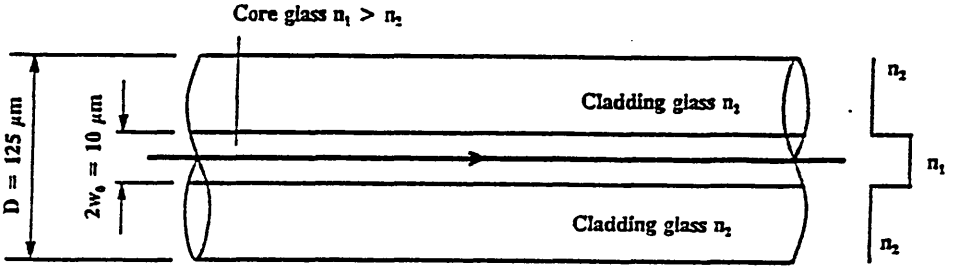

(b) A step index single mode fibre

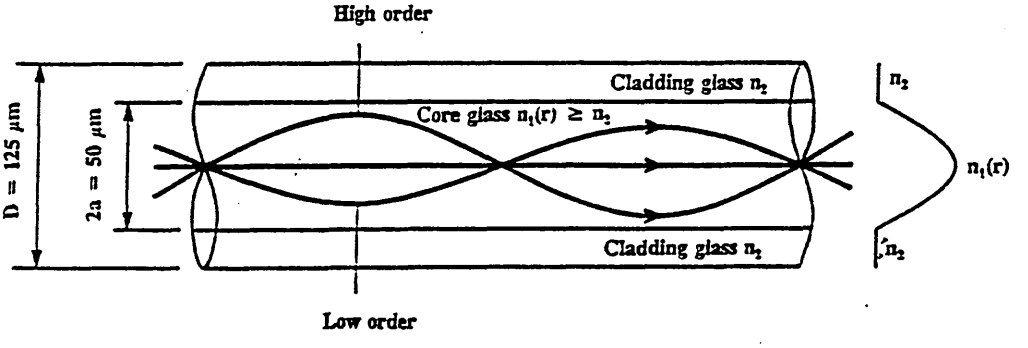

(c) A graded index fibre

Figure 2.4 Types of optical fibre showing their typical dimensions and refractive index profiles.

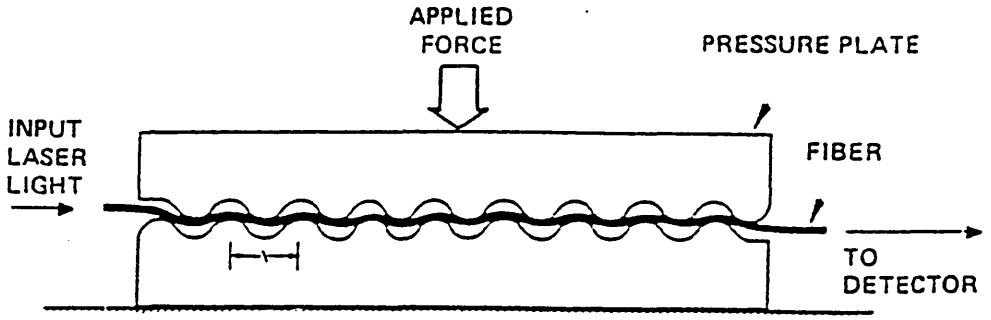

Figure 3.1 Fibre bending moss modulator [39].

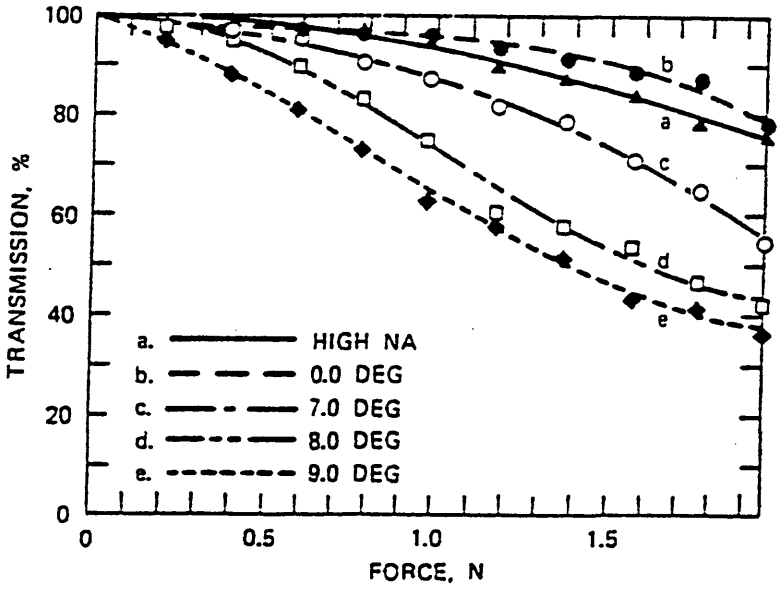

Figure 3.2 Transmission versus applied force for bending loss modulator [39].

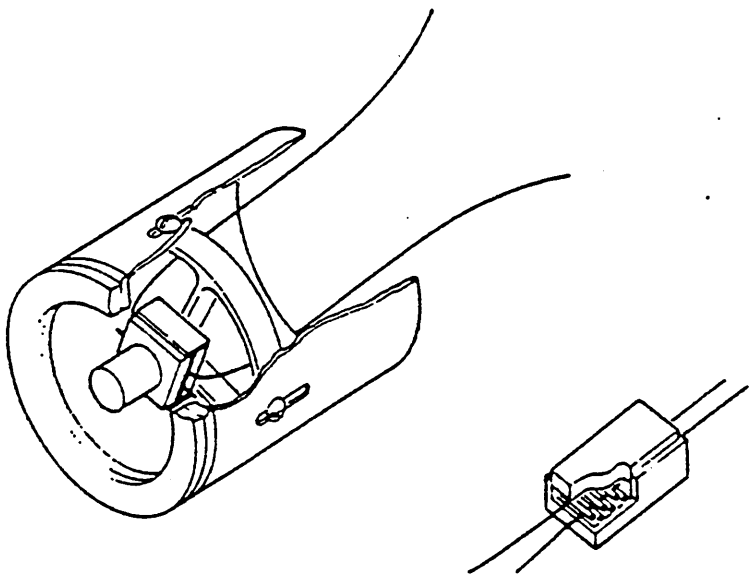

Figure 3.3 A fibre microbend acoustic sensor [41-43].

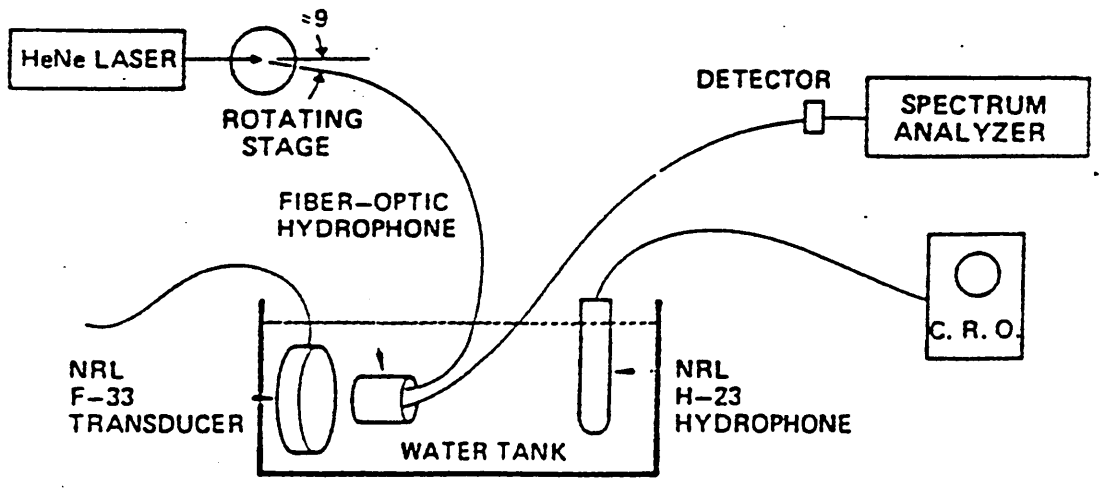

Figure 3.4 Experimental characterization equipment [41-43].

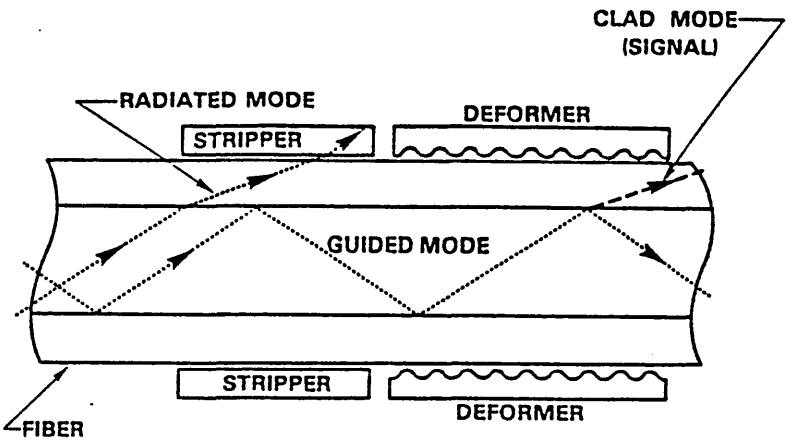

Figure 3.5 The deforming section of the displacement sensor. The light coupled from core to clad modes is detected. For higher sensitivity the light from the clad modes is stripped before the deformer [43-44].

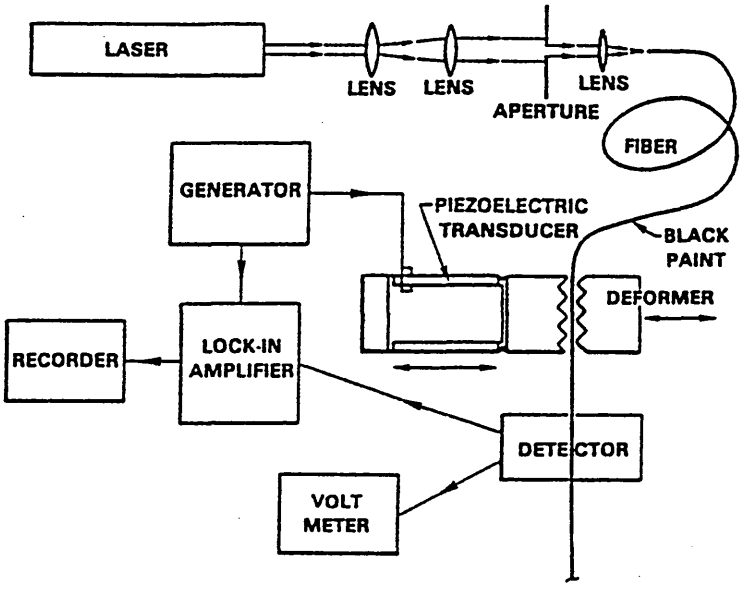

Figure 3.6 Experimental set up of the displacement microbending sensor [43-44].

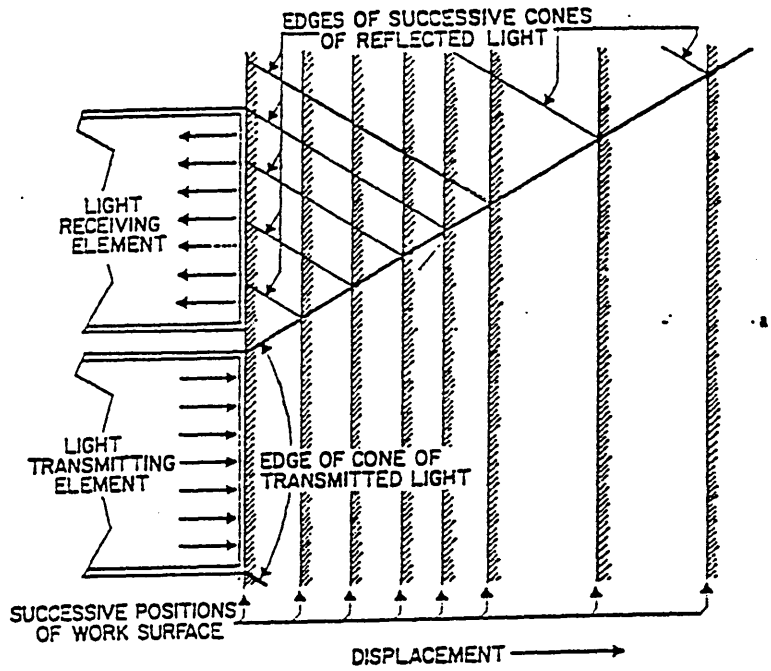

Figure 3.7 Principal of displacement sensor [49].

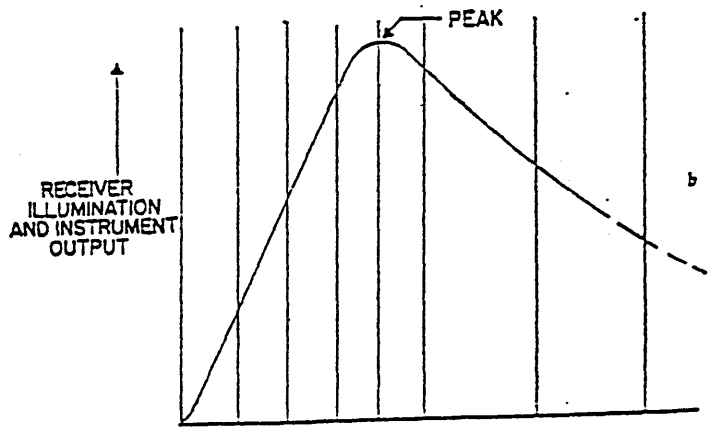

Figure 3.8 Receiver illumination as a function of displacement [49].

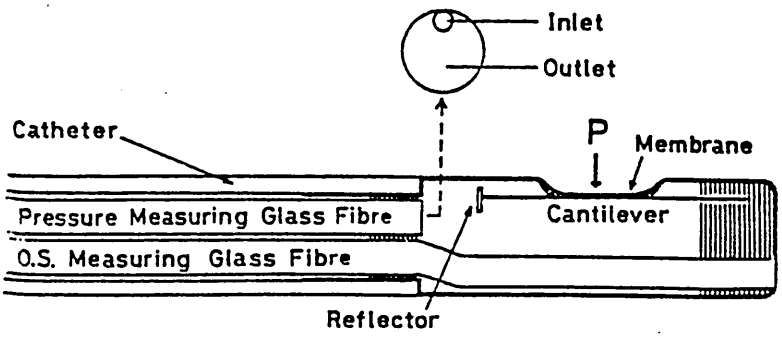

Figure 3.9 Schematic model of the fibre optic pressure catheter. The inlet section transmits light, the outer section receives signals [59].

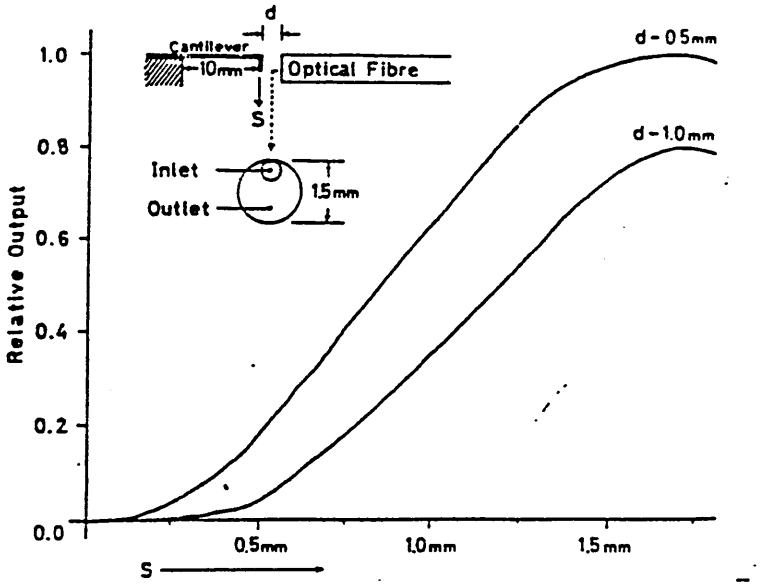

Figure 3.10 Measured output intensity for the different reflector distances d [59].

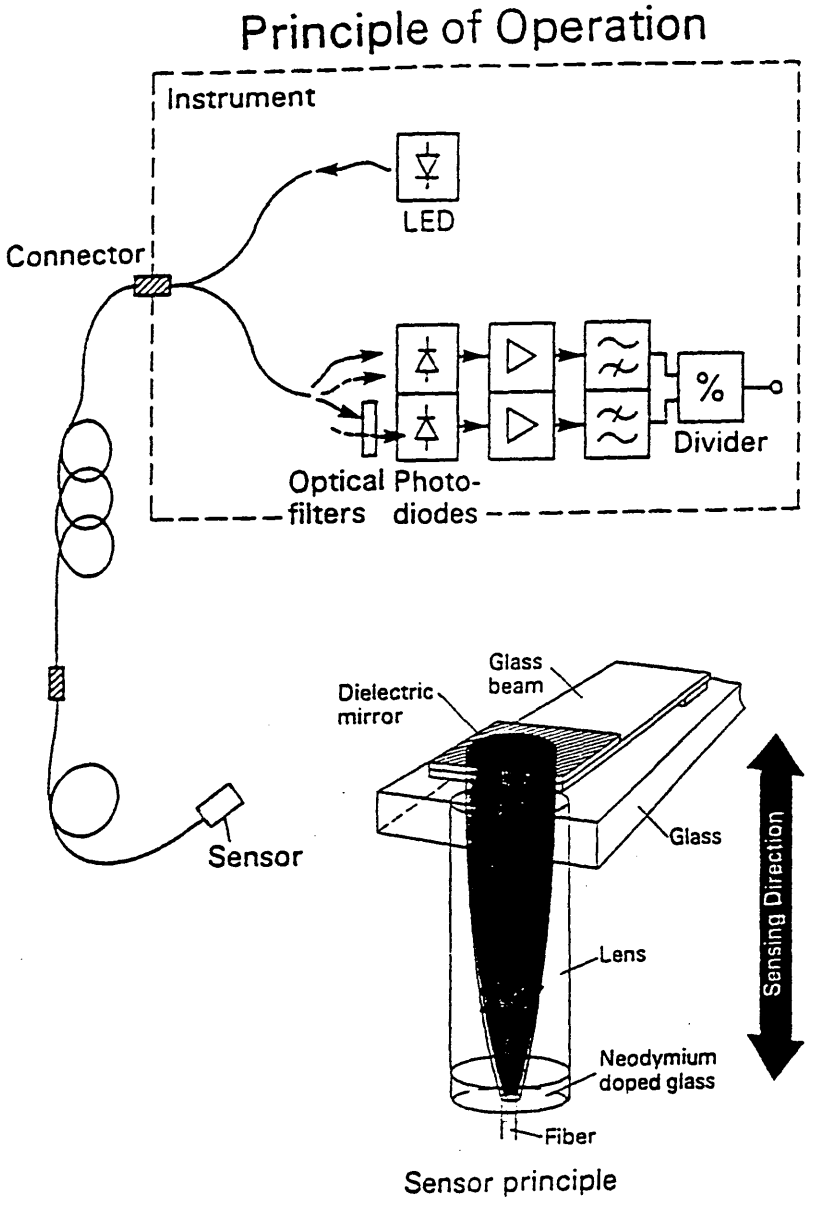

Figure 3.11 Principle of operation of Takaoka accelerometer [62]. Formerly manufactured by ASEA [61].

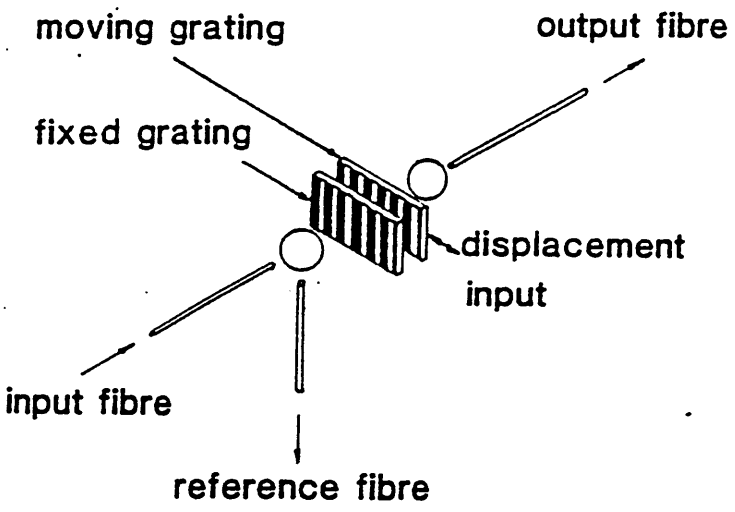

Figure 3.12 Exploded schematic of shutter modulator [65].

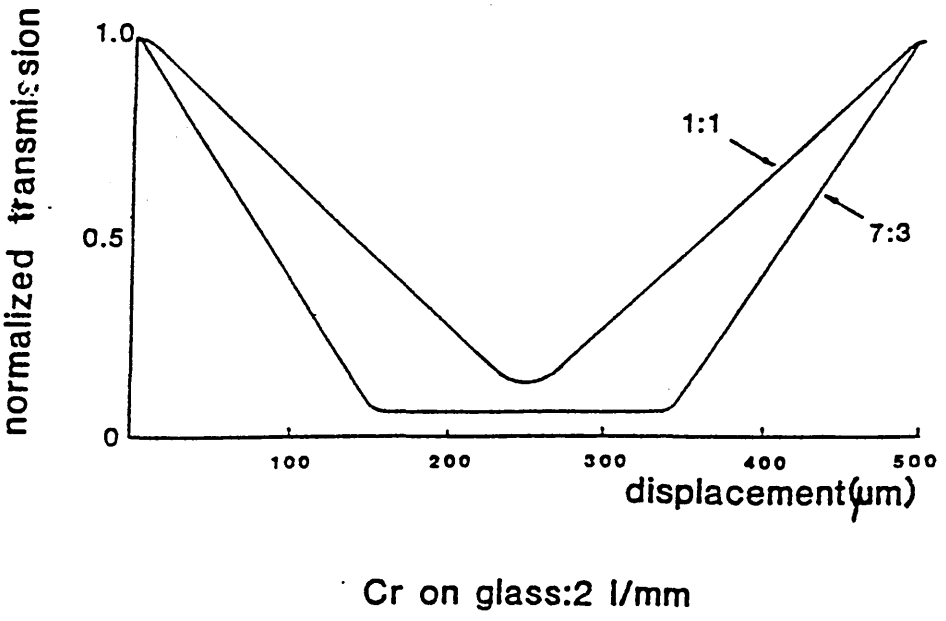

Figure 3.13 Transmission versus as a function of the displacement for the shutter modulator [65].

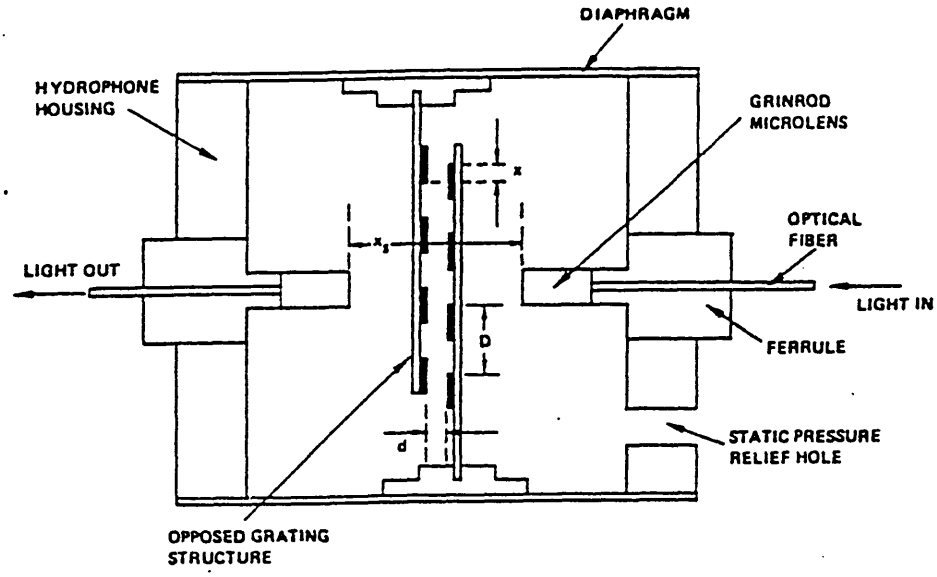

Figure 3.14 Schematic diagram of schlieren multimode fibre optic hydrophone [72].

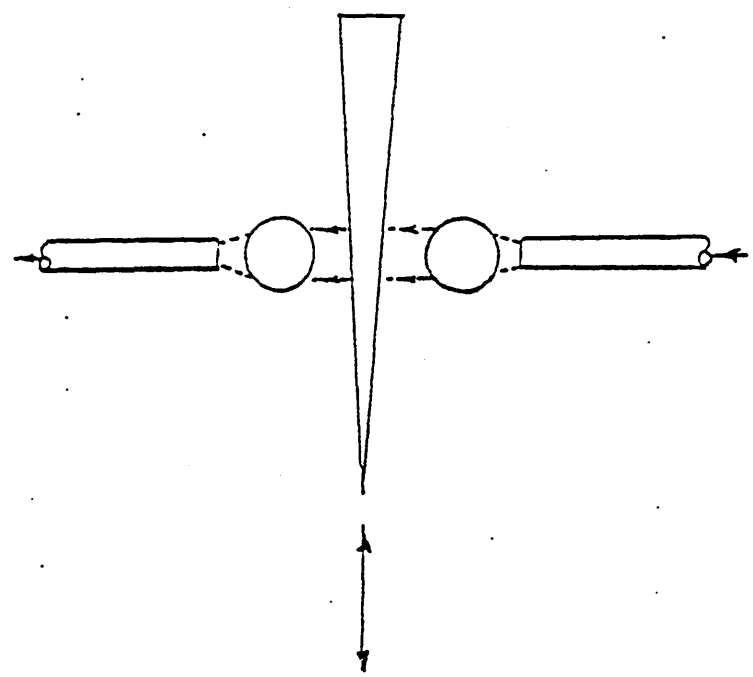

Figure 3.15 Optical wedge modulator [72].

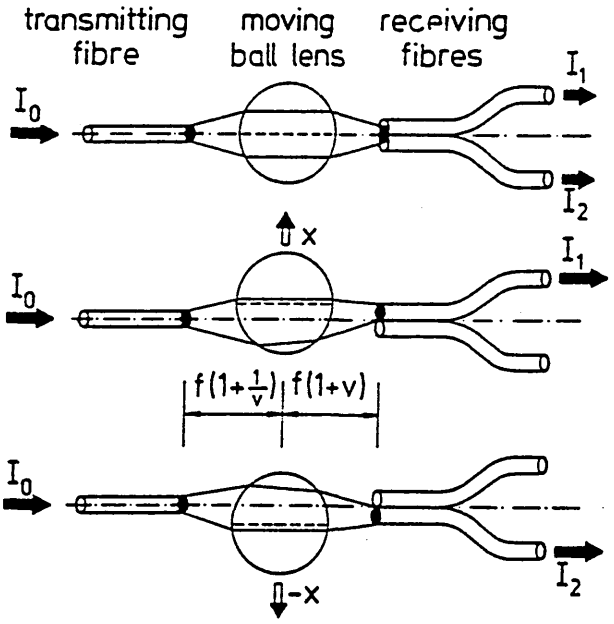

Figure 3.16 Moving ball lens principle. f is the focal length of ball lens, v is the magnification of image formation [74].

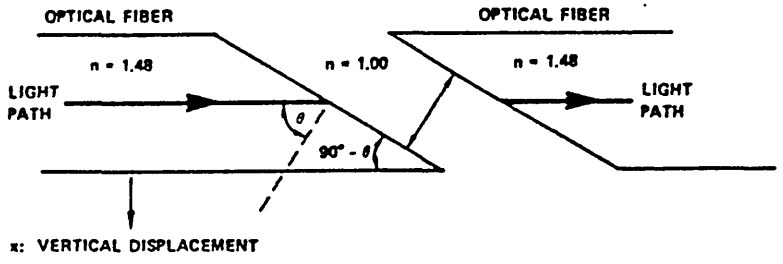

Figure 3.17 Light coupled between two multimode optical fibres via frustrated total internal reflection [75].

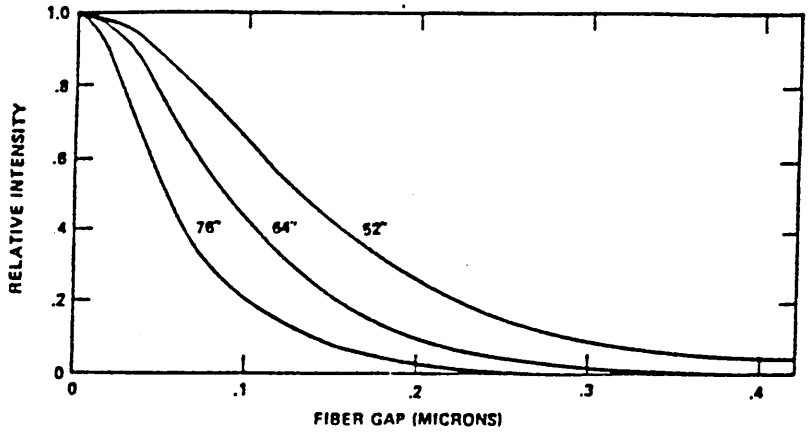

Figure 3.18 Relative intensity versus fibre gap for 85 μm core, 0.02 NA multimode optical fibre for various fibre cut angles [75].

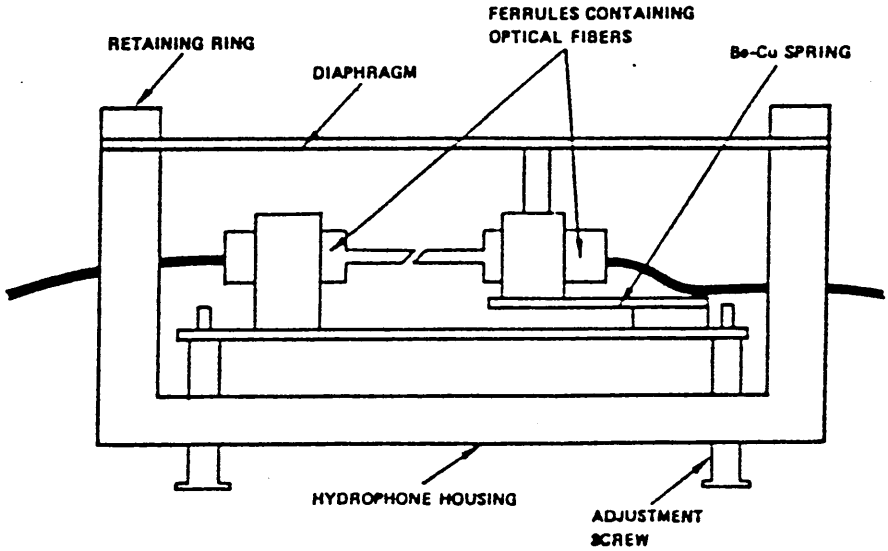

Figure 3.19 Schematic of frustrated total internal reflection optical hydrophone [75].

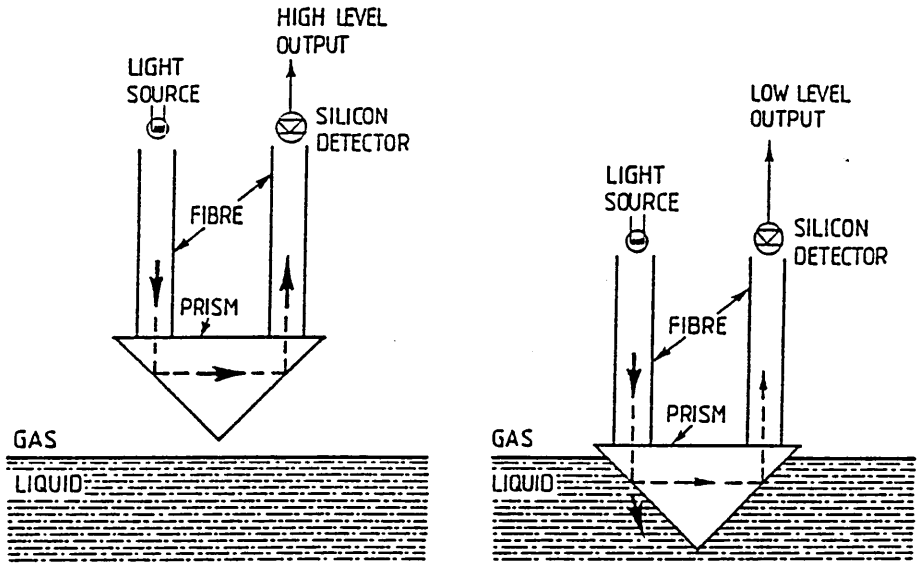

Figure 3.20 Liquid level sensor using a prism probe [81].

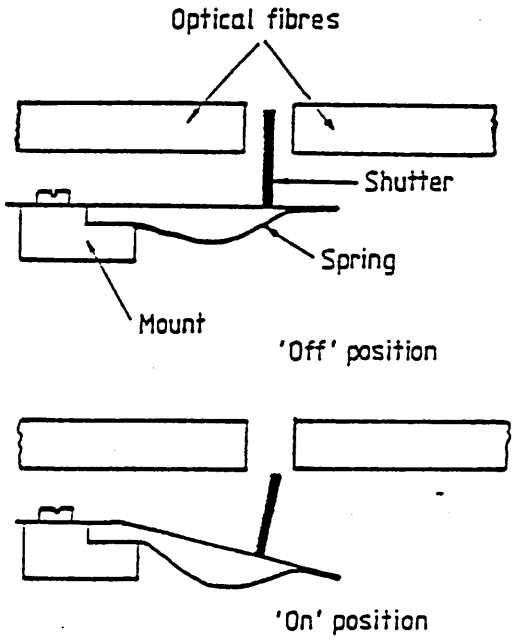

Figure 3.21 Shutter type optical microswitch [81].

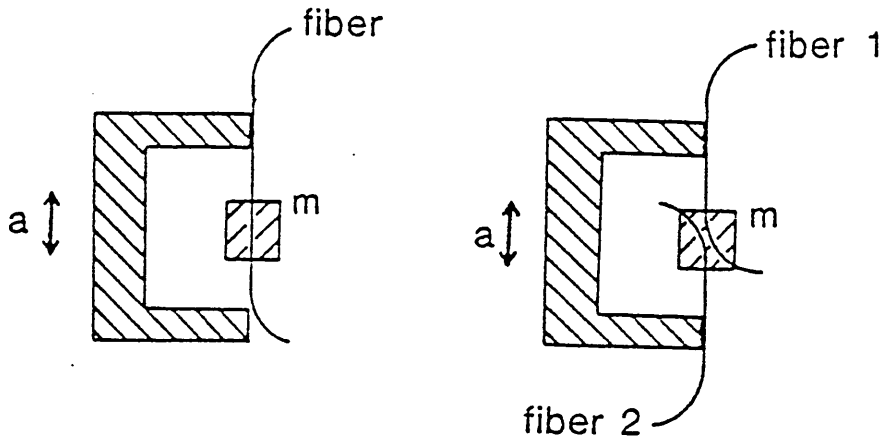

Figure 3.22 Two fibre optic accelerometer configurations [83].

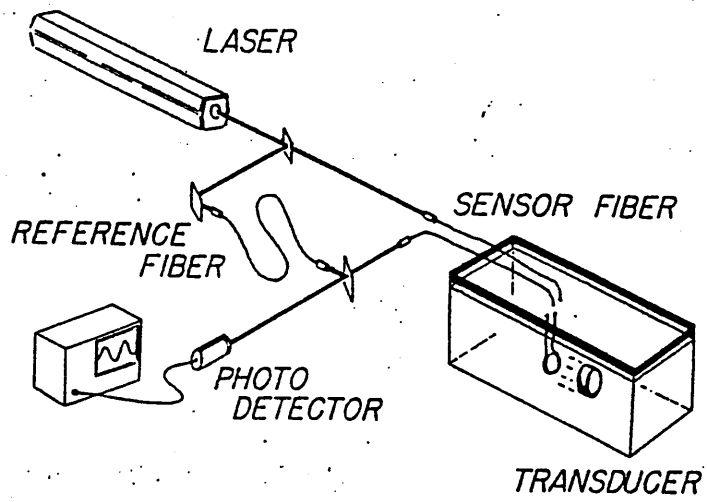

Figure 3.23 Experimental configuration of the optical fibre acoustic sensor system [86].

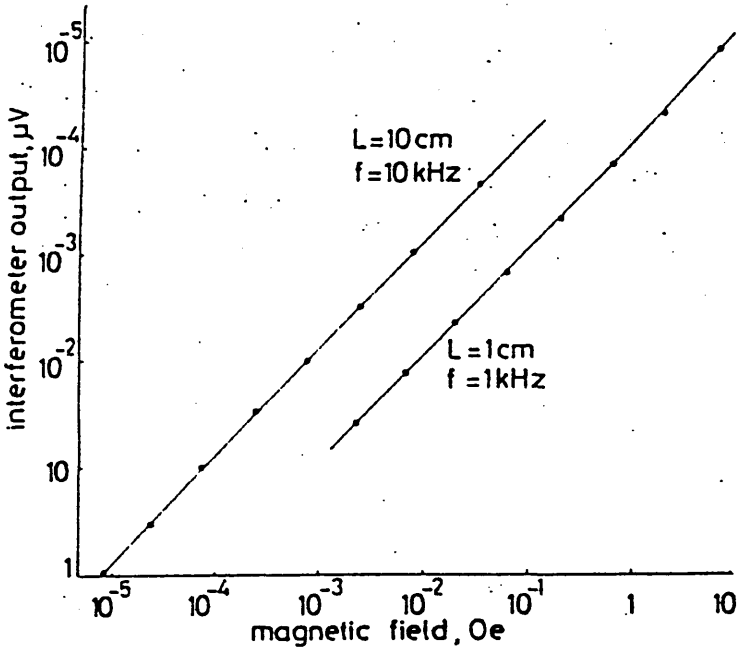

Figure 3.24 Interferometer output against applied magnetic field for two bulk nickel clad fibre devices operating at 1 kHz and 10 kHz [88].

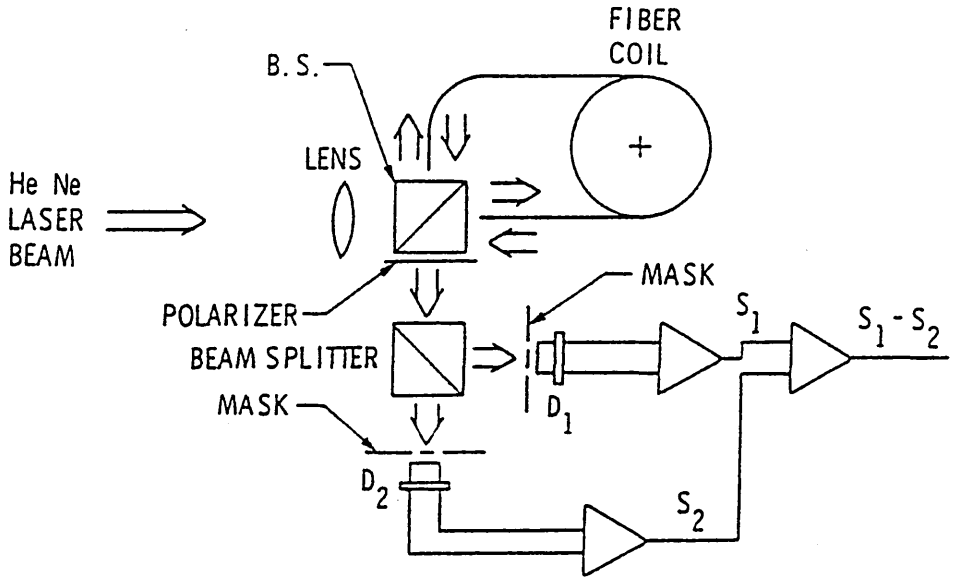

Figure 3.25 Schematic diagram of fibre optic rotation sensor [97].

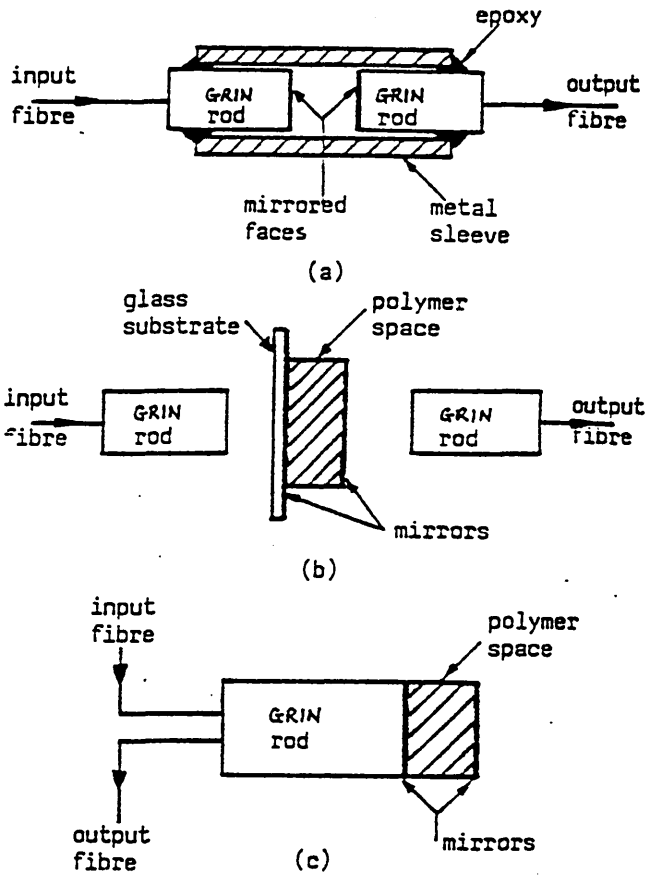

Figure 3.26 Fabry Perot sensors. (a) air spaced sensor, (b) sensor with solid spacer, (c) reflection mode sensor [100].

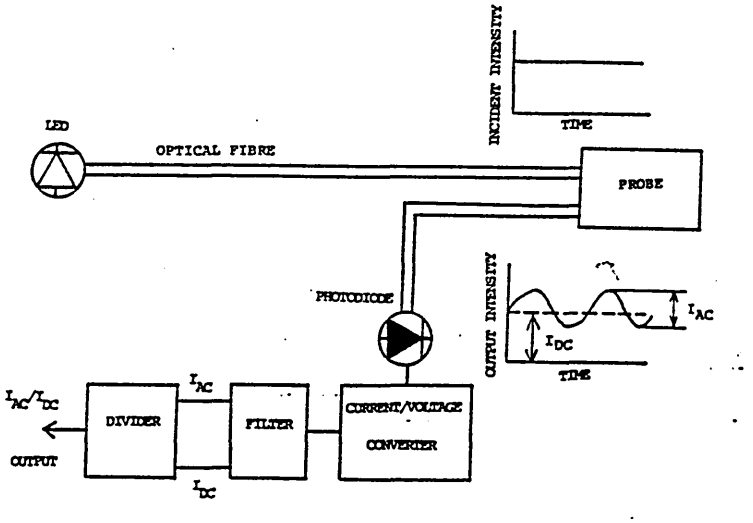

Figure 3.27 Constitution of the sensor [113].

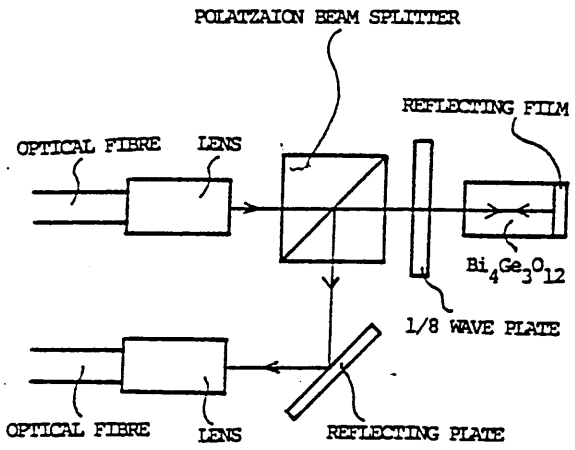

Figure 3.28 Constitution of the probe [113].

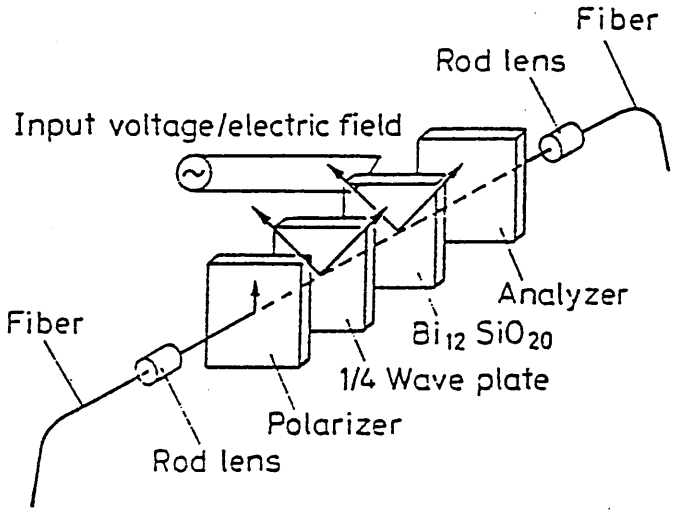

Figure 3.29 Basic structure of optical fibre sensor for the measurement of electric field intensity (OPSEF) [114].

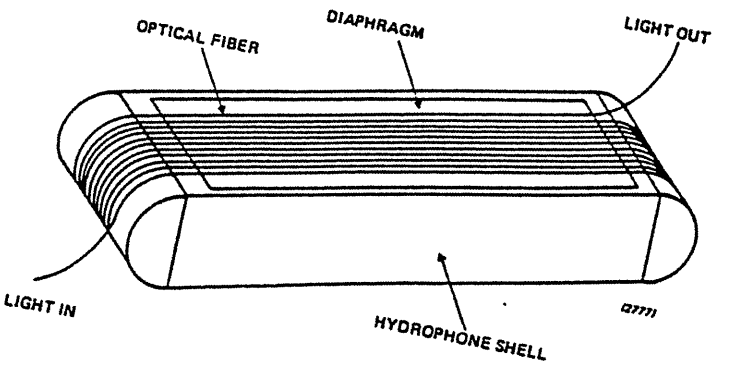

Figure 3.30 Design of optical polarisation hydrophone [116].

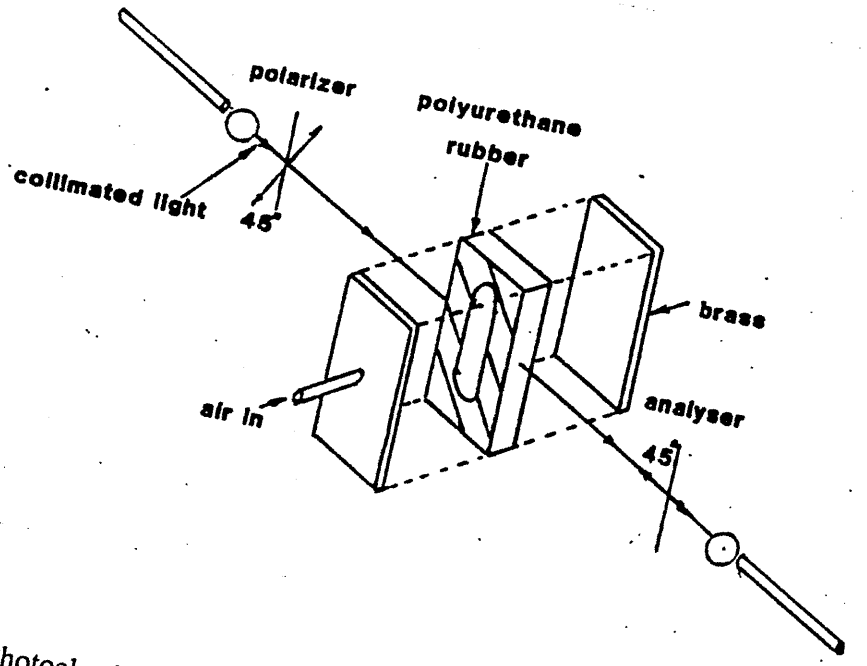

Figure 3.31 Photoelastic pressure sensor [117].

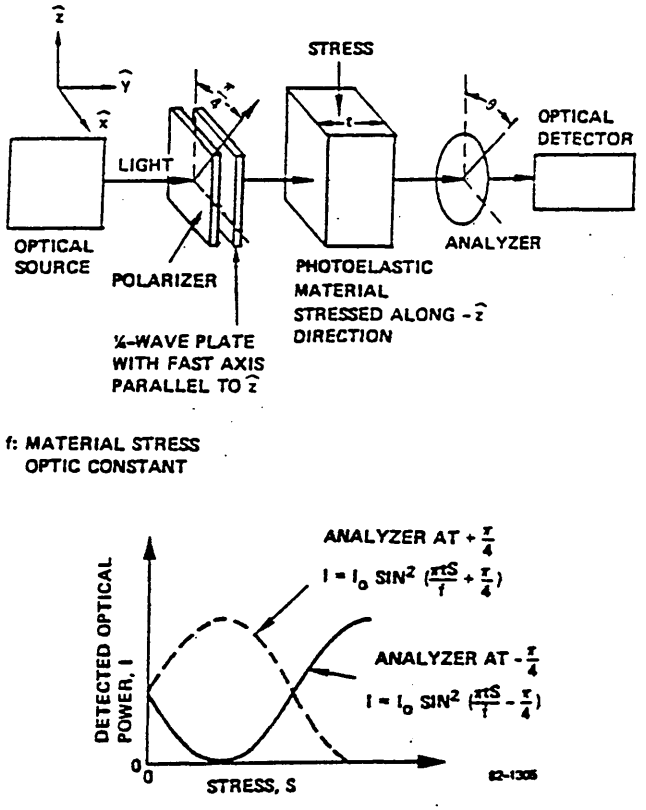

Figure 3.32 (a) structure of sensor based on photoelastic effect, (b) detected optical power plotted against stress for two analyzer orientations [118].

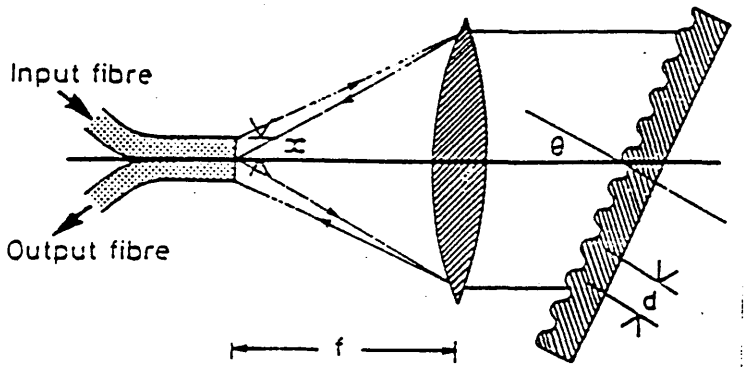

Figure 3.33 Grating monachromator [120].

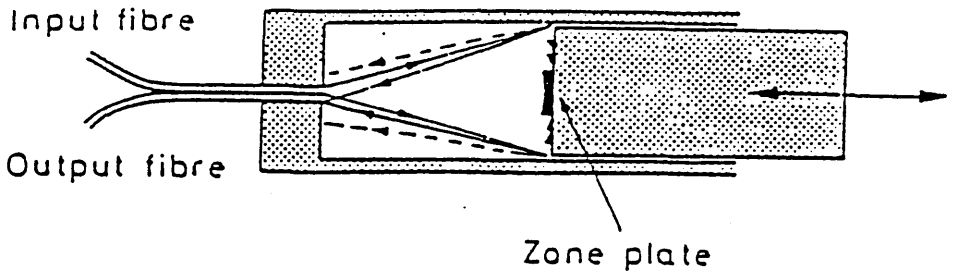

Figure 3.34 The fresnel zone plate used as a linear translational transducer [120].

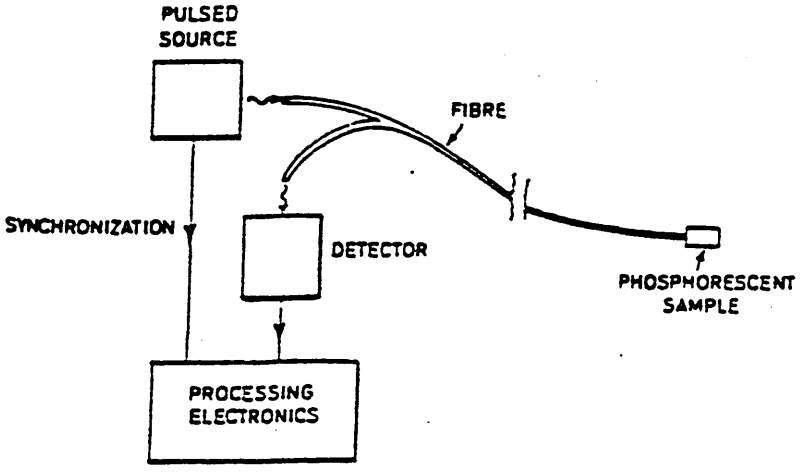

Figure 3.35 Schematic of phosphorescent sensor.

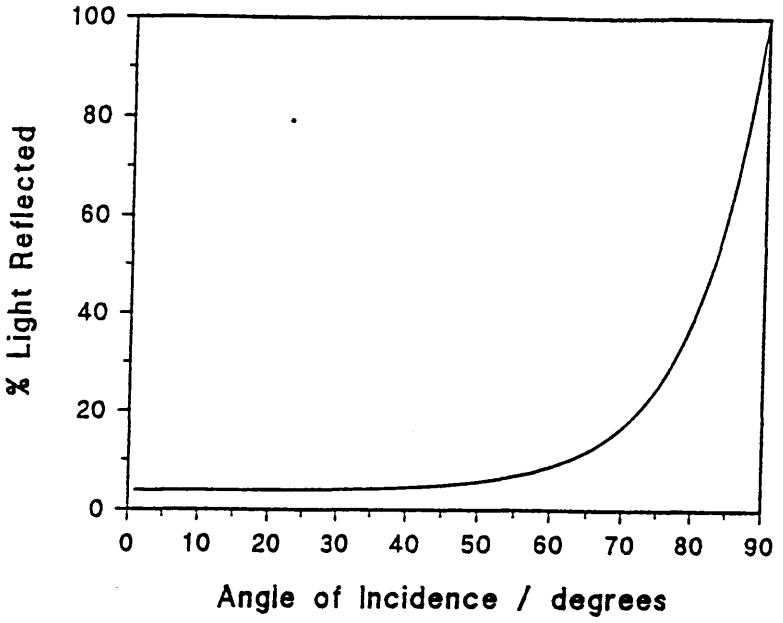

Figure 4.1 Surface reflection as function of angle of incidence α (n = 1.49) as calculated using Fresnel's equations.

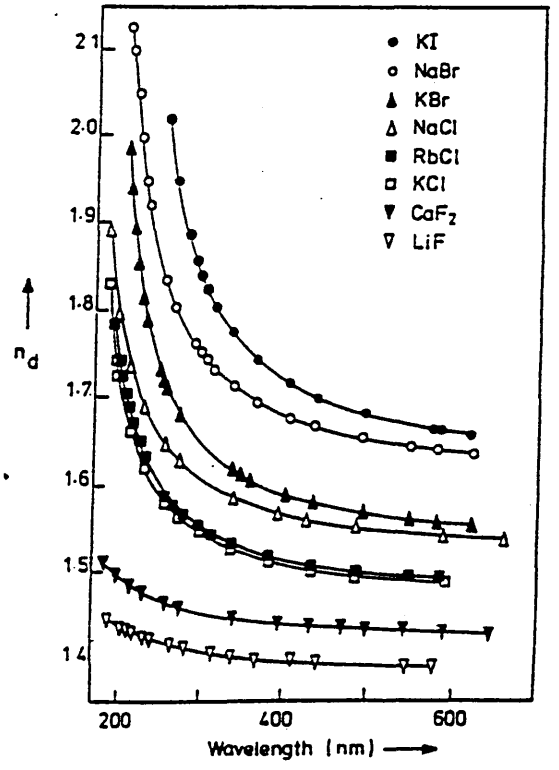

Figure 4.2 Dispersion: the variation of refractive index with wavelength in this case for varius crystalline halide glasses.

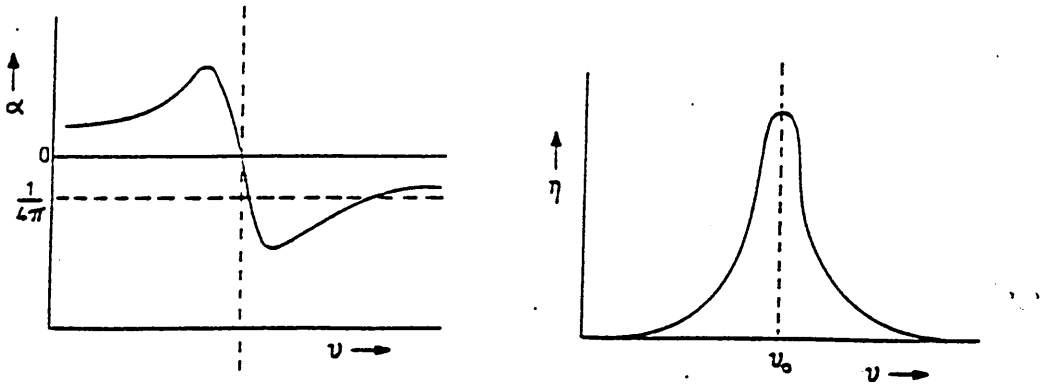

Figure 4.3 The variation of α and η with frequency (Lorentz theory).

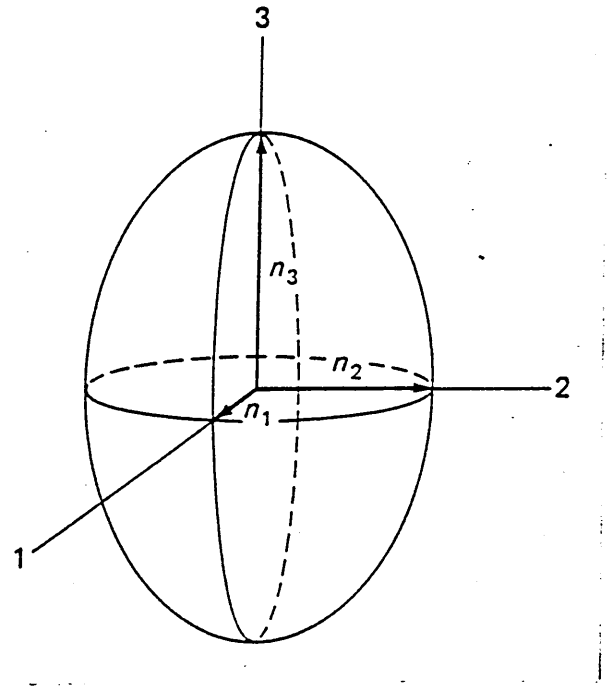

Figure 4.4 The index ellipsoid showing the three principal indices of refraction.

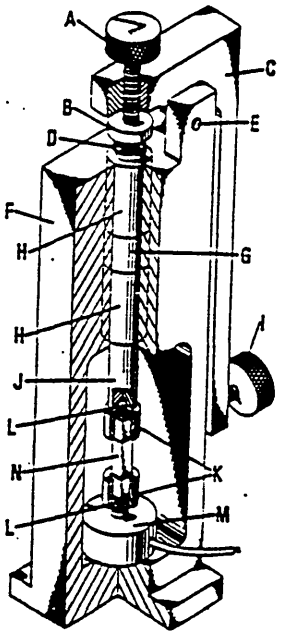

Figure 4.5 Stressing aparatus. A-adjustment screw; B-adjustment member threaded into push rod; C-lever arm; D-coil spring; E-axle; F-frame; G-spacer; H-ball bushing; I-stressing screw; J-push rod; K-specimen cup; L-steel ball; M-load cell; N-specimen.

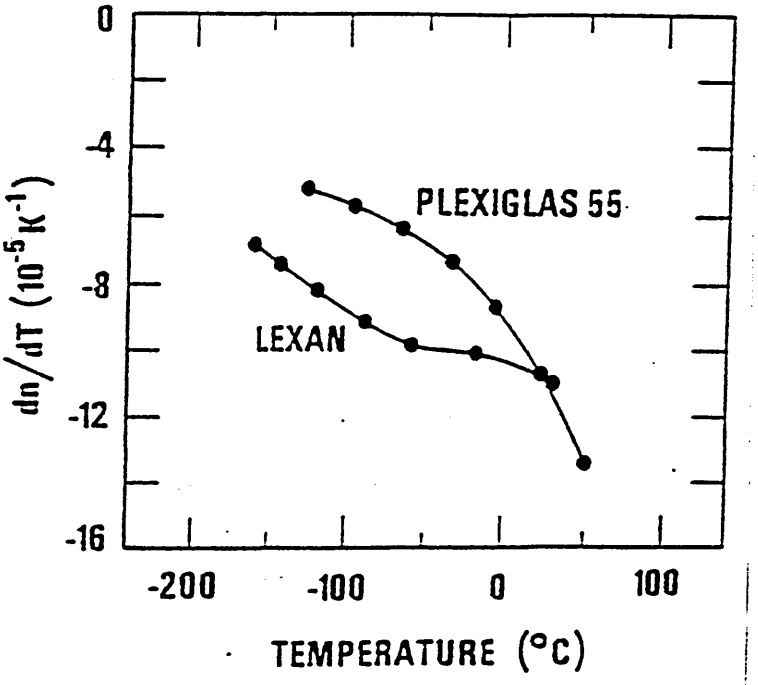

Figure 4.6 Thermo-optic coefficient as a function of temperature for Plexiglass 55 and Lexan

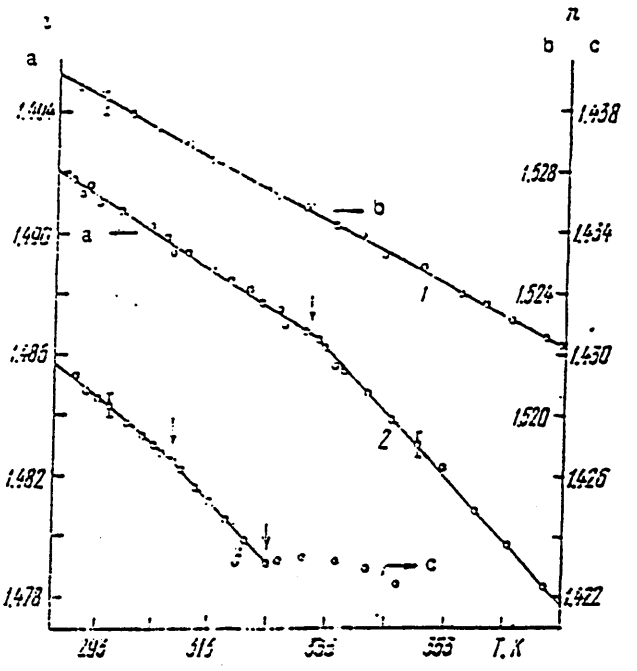

Figure 4.7 Temperature dependence of refractive index of acrylic polymers (λ=589.3 nm): 1-EA; 2-PMMA; 3-FA.

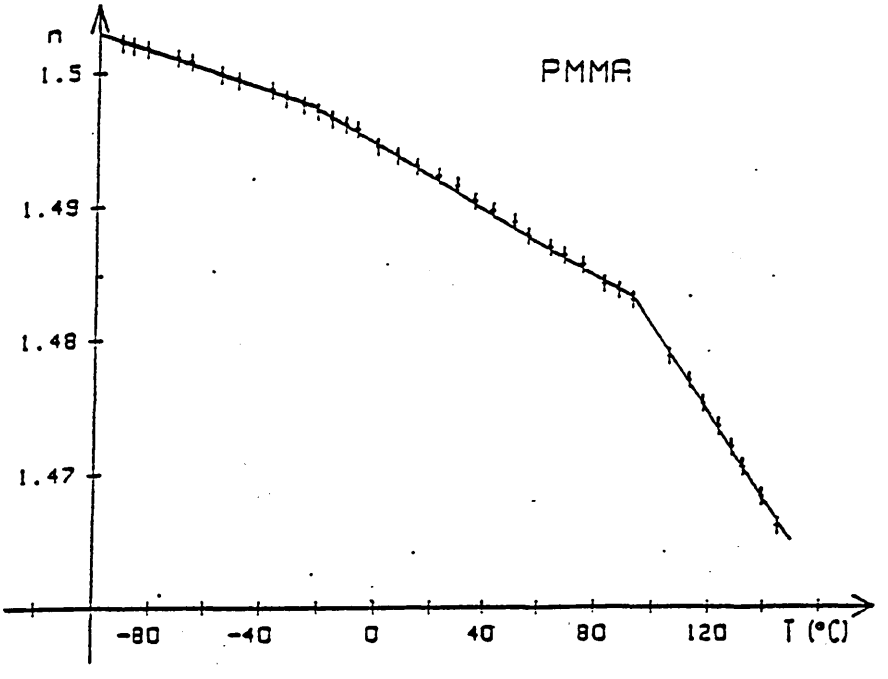

Figure 4.8 Thermal variation of refractive index of PMMA.

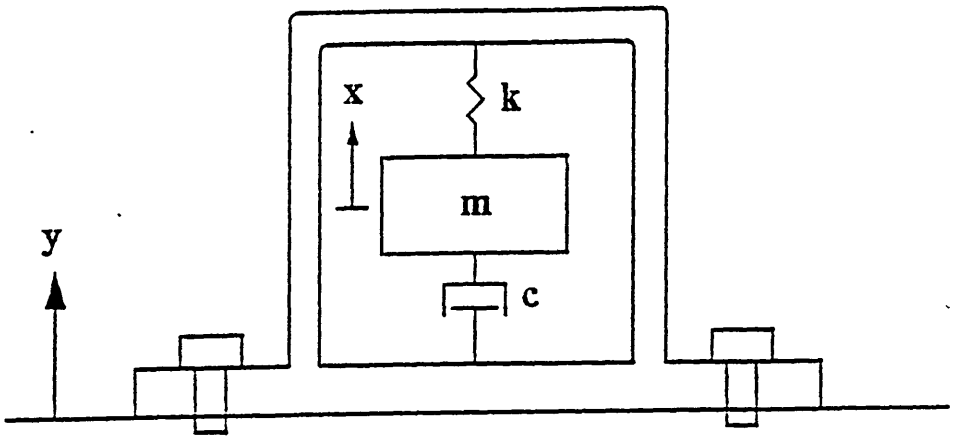

Figure 5.1 Simplified model of an accelerometer

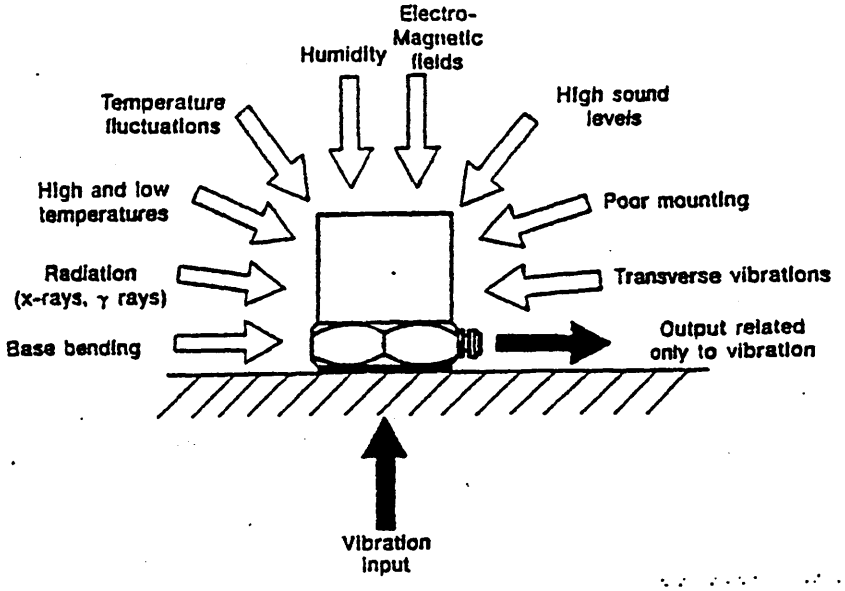

Figure 5.2 A selection of the many extraneous inputs which can result in non-vibration related outputs in a poorly designed accelerometer.

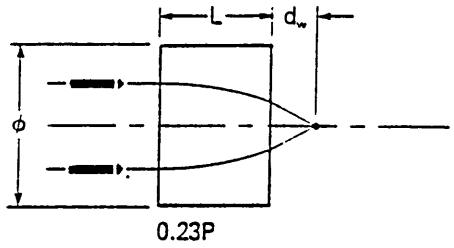

06 LGT

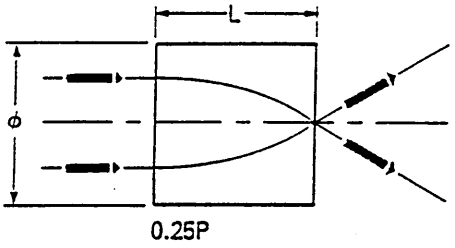

06 LGS

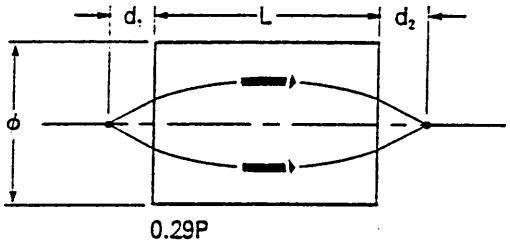

06 LGE

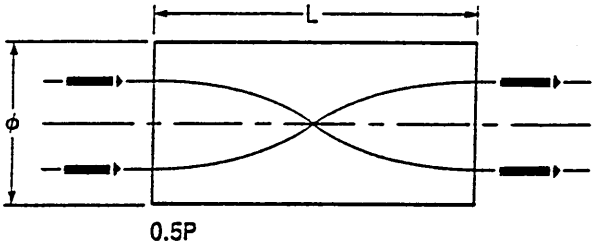

06 LGD

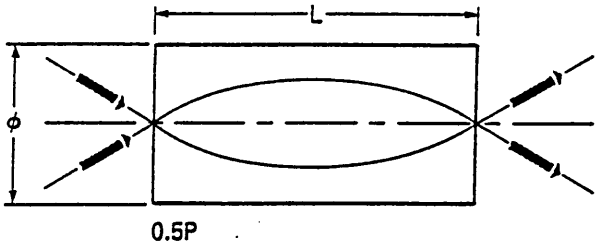

06 LGD

Figure 5.3 Imaging properties of some common fractional pitch lenses.

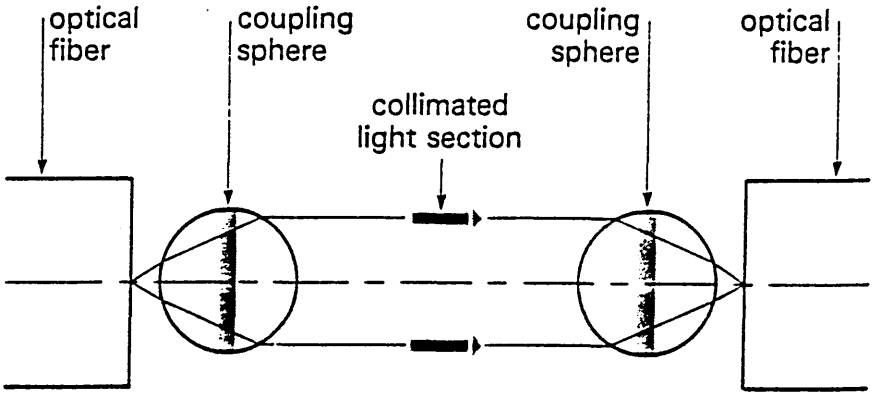

Figure 5.4 Fibre coupling using spheres.

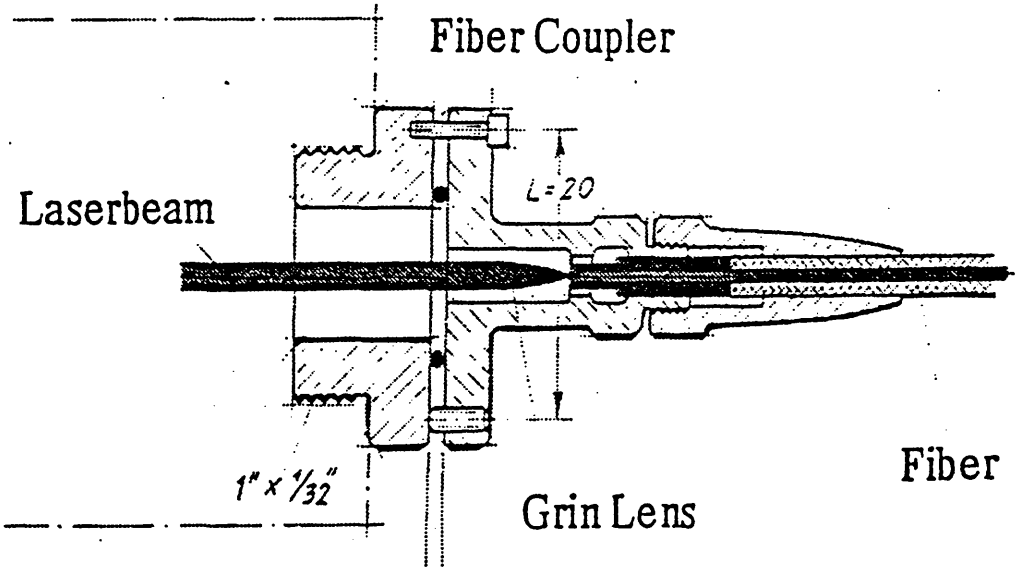

Figure 5.5 Arrangement for coupling light from a laser into an optical fibre.

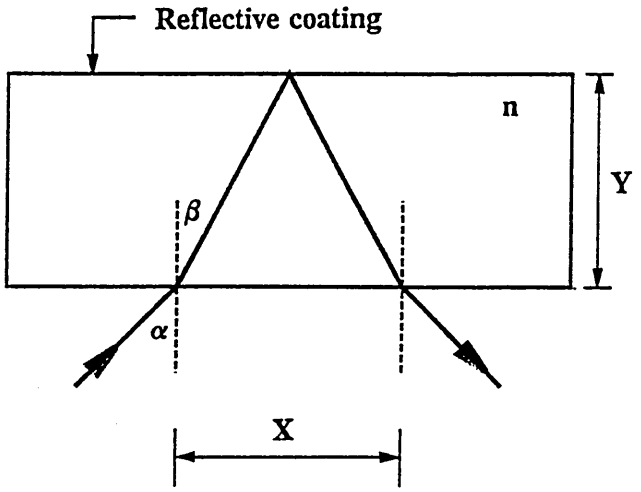

Figure 5.6 Simple reflection through a parallel sided optic medium.

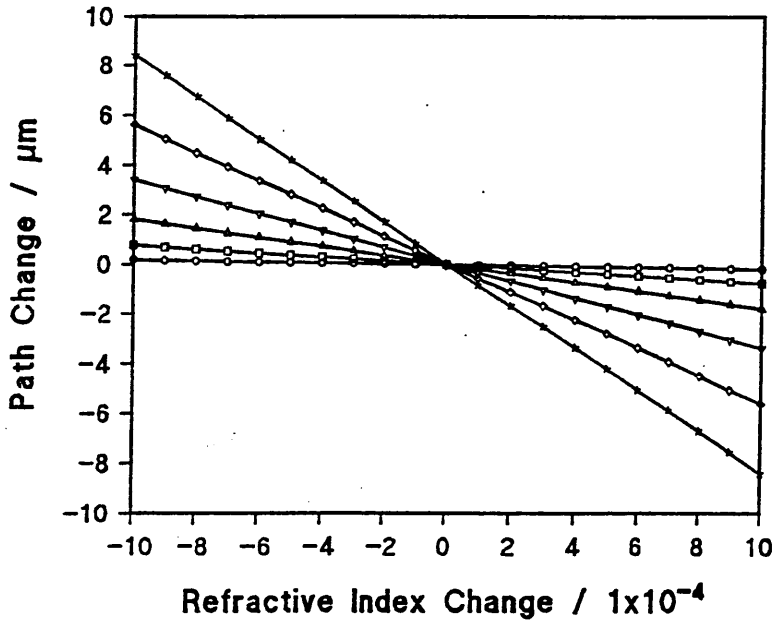

Figure 5.7 The effect of the refractive index change on the path length change for various angles of incidence in a simple reflection. (o 10°, □ 20°, ▵ 30°, ▿ 40°, ◇ 50° and ⋆ 60°)

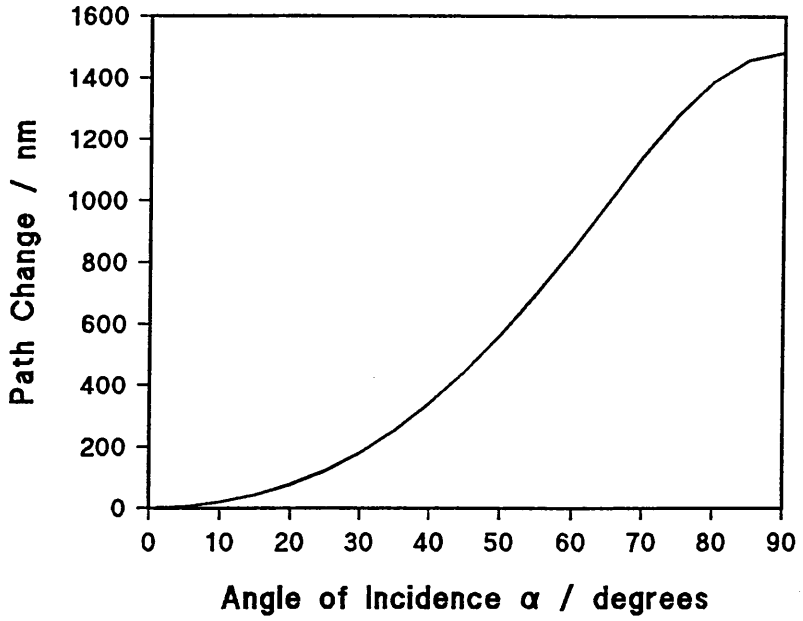

Figure 5.8 The effect of the angle of incidence on the path length change in a simple reflection

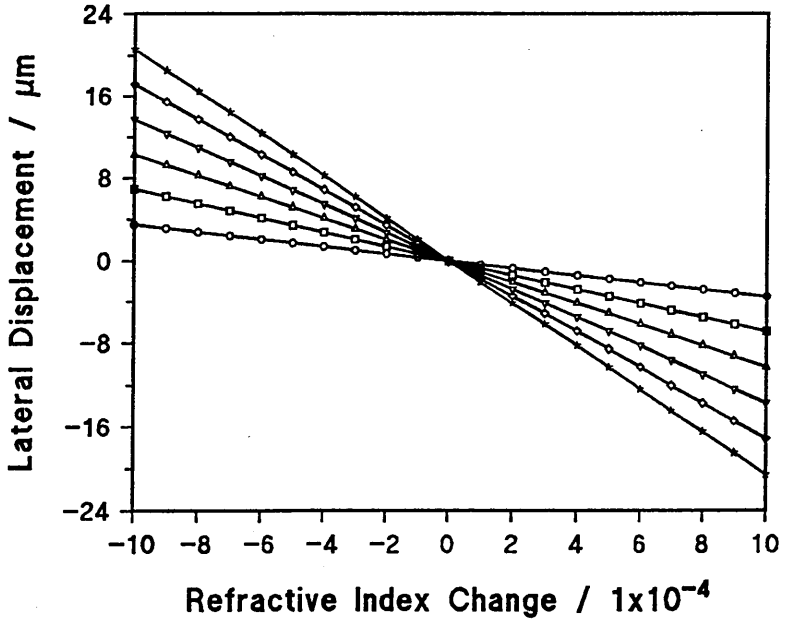

Figure 5.9 The effect of the refractive index change on the lateral displacement for various angles of incidence in a simple reflection. (o 10°, □ 20°, △ 30°, ▽ 40°, ◇ 50° and ★ 60°)

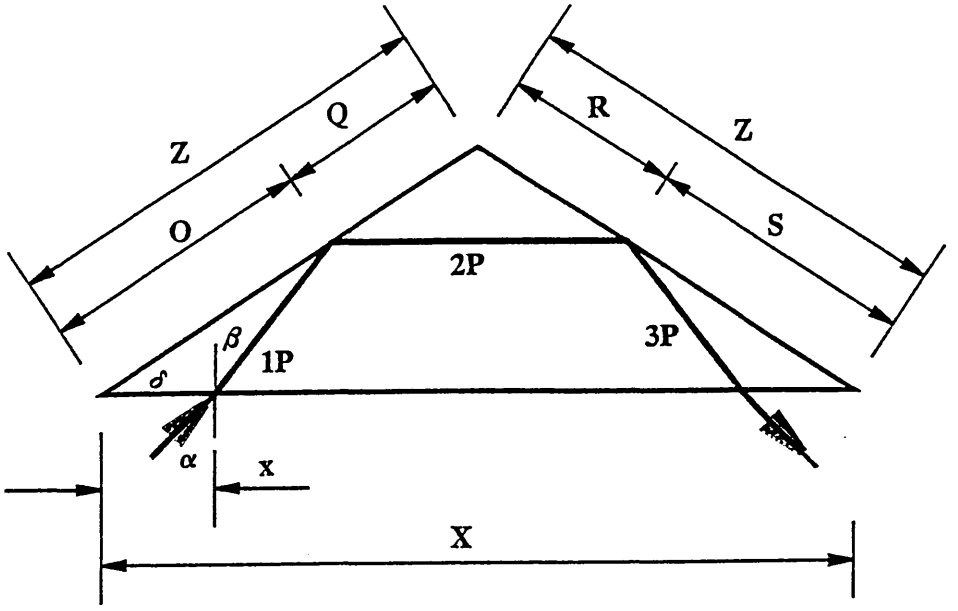

Figure 5.10 A n type reflection through an optic medium

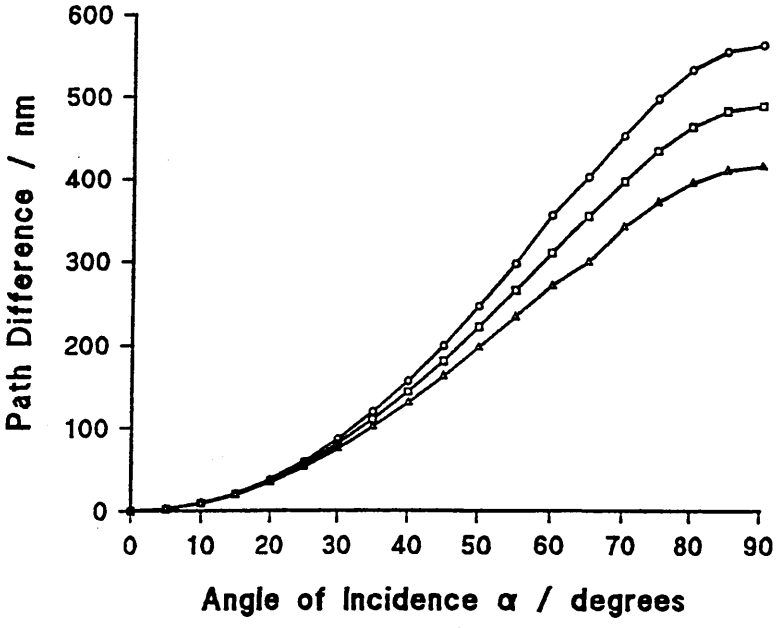

Figure 5.11 The effect of the angle of incidence on the path change for various entry point positions in a n type configuration. (o = 2mm, □ = 3mm and ▵ = 4mm)

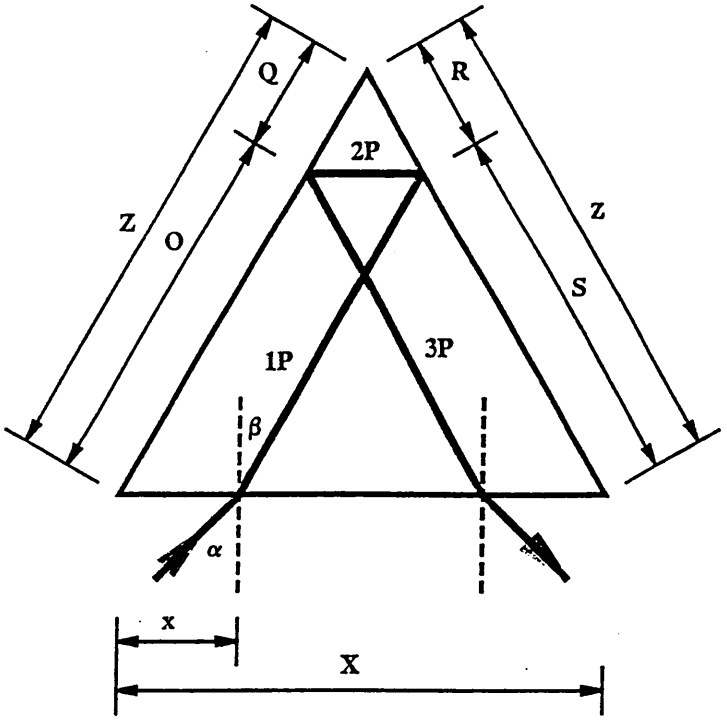

Figure 5.12 A x type reflection through an optic medium

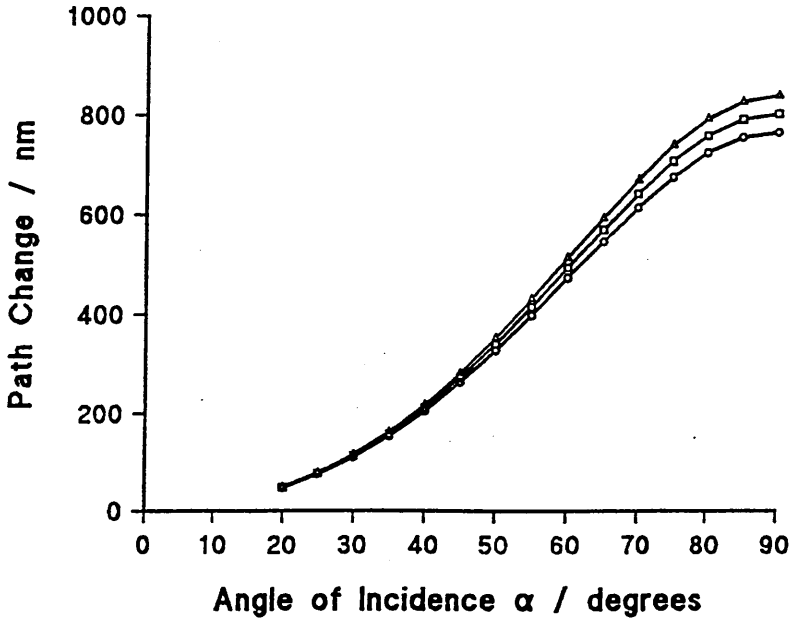

Figure 5.13 The effect of the angle of incidence on the path change for various entry point positions in a x type configuration. (Δ = 3.5mm, □ = 4mm and o = 3.5mm).

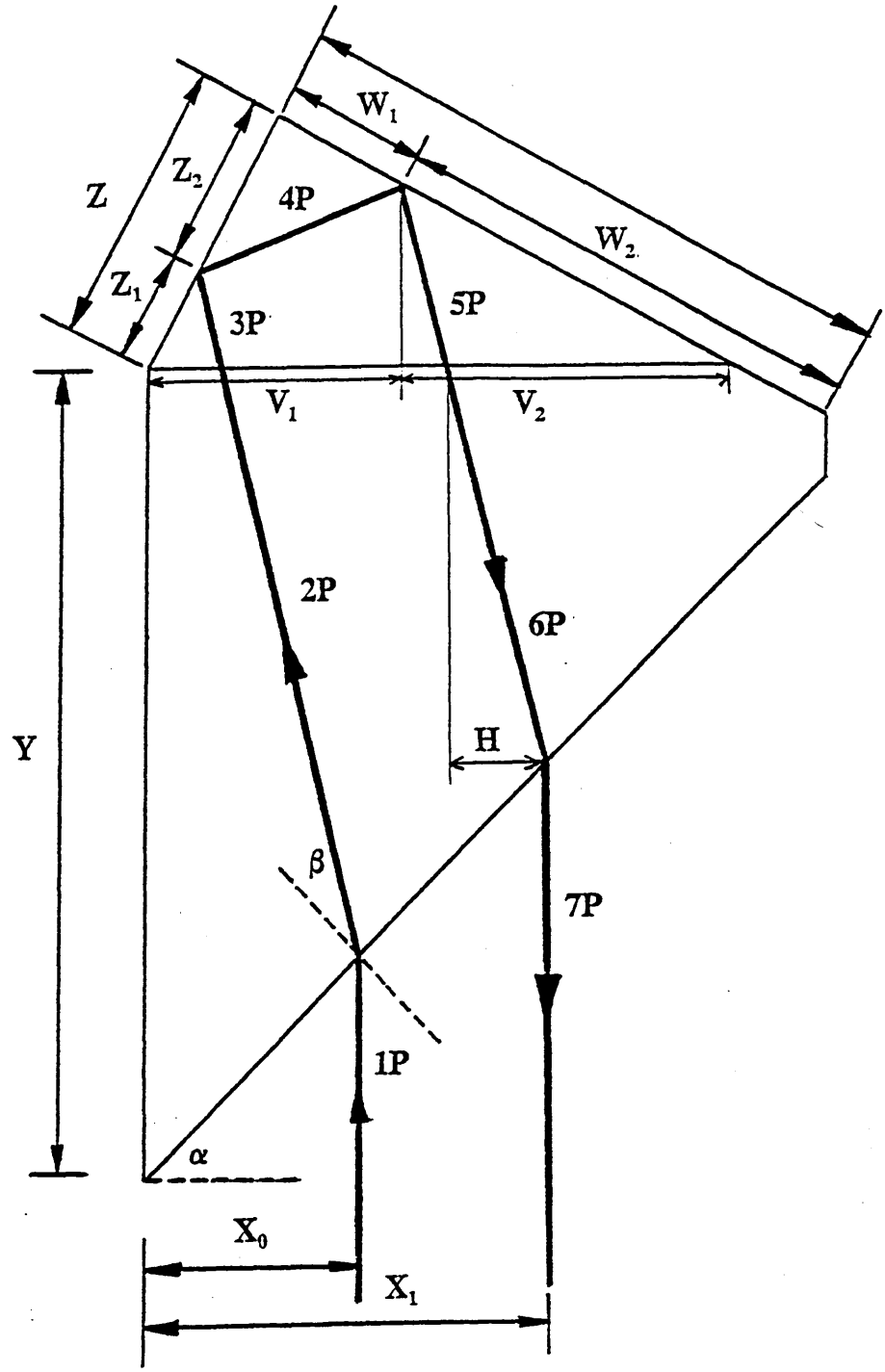

Figure 5.14 An in line reflection through a optic medium. Initially, the output beam emerges parallel to the input beam.

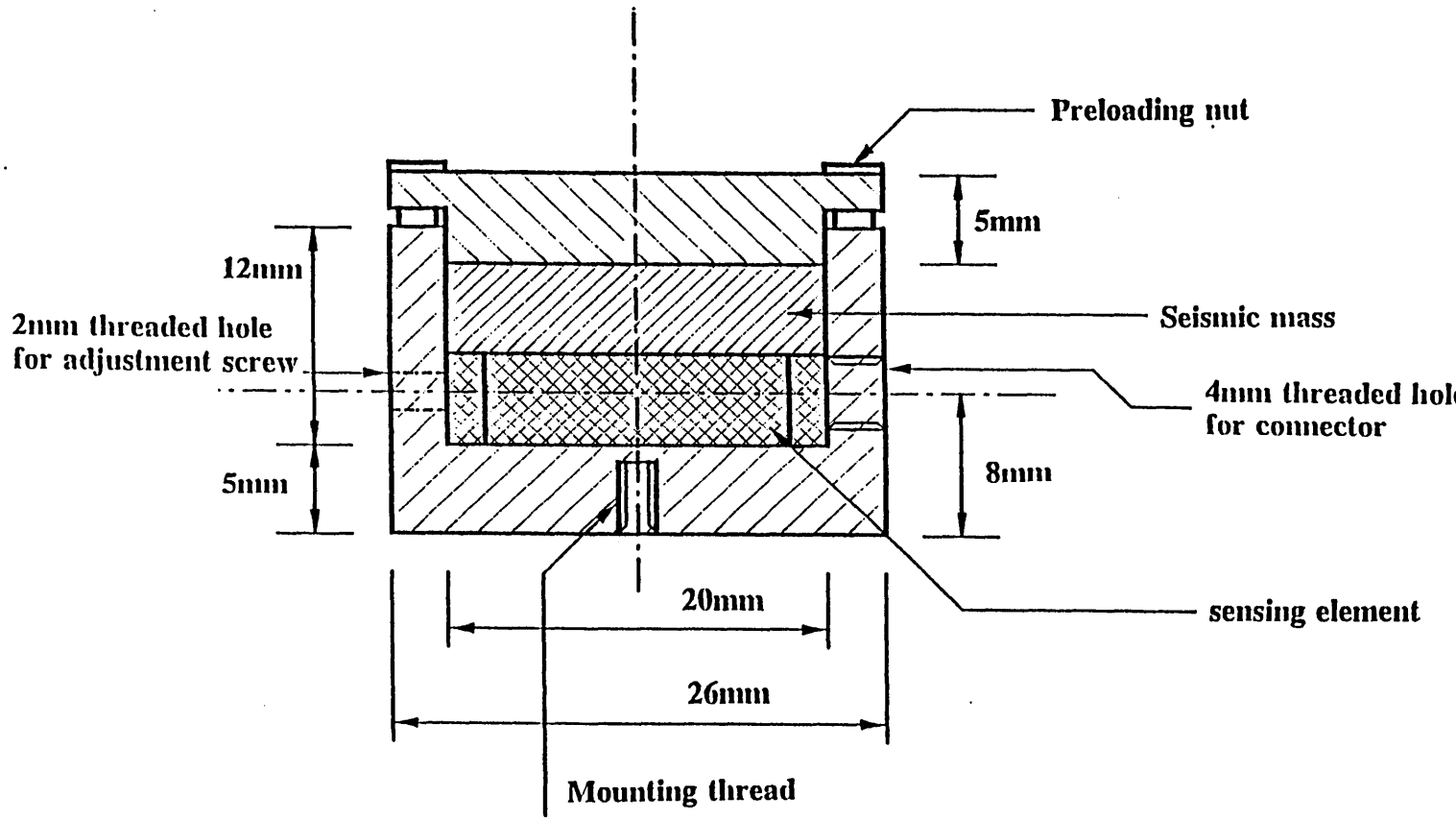

Figure 5.15.(a) A section through the prototype light modulated accelerometer.

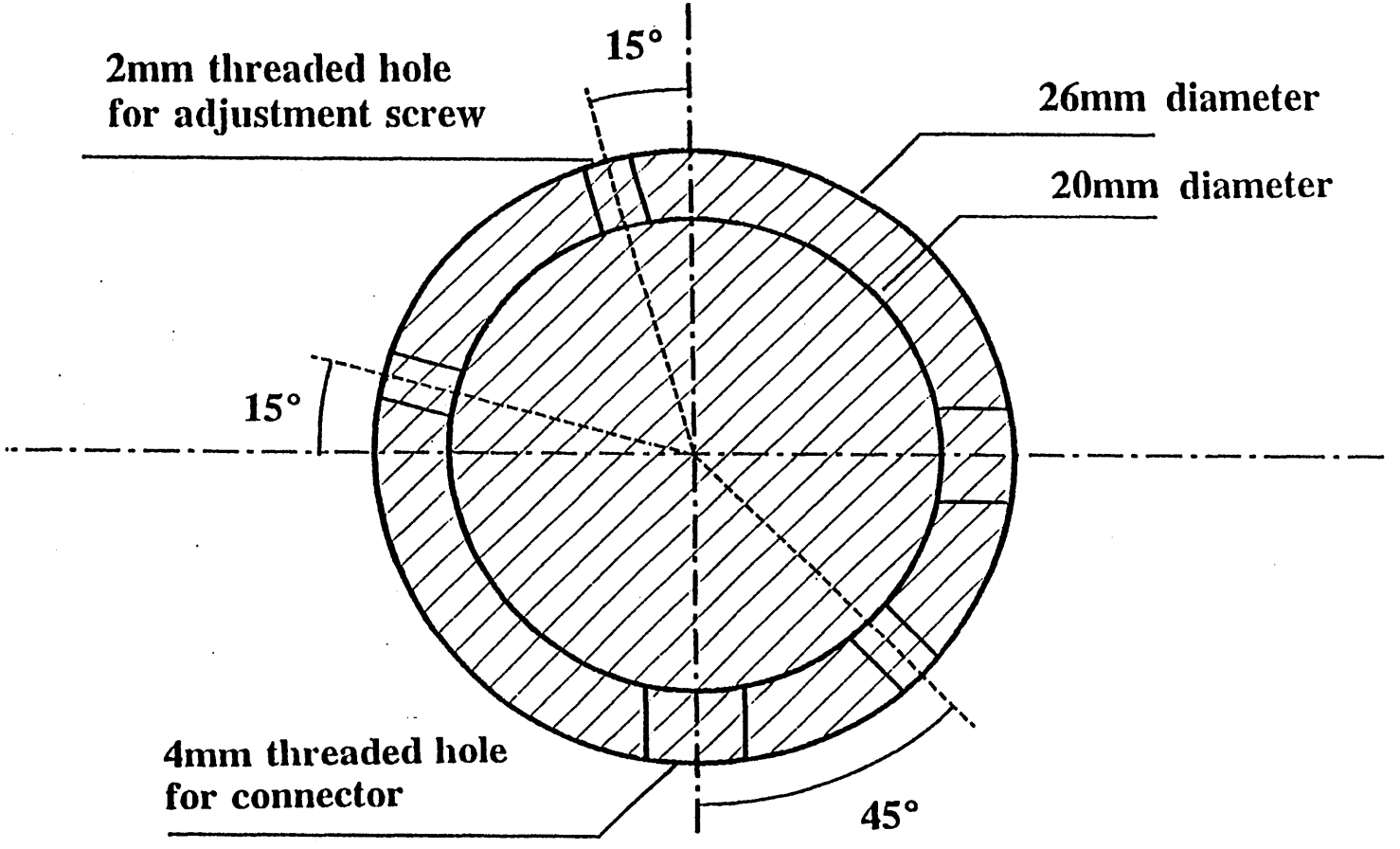

Figure 5.15.(b) A sectional plan view of the accelerometer showing the sensing element and the positioning screws.

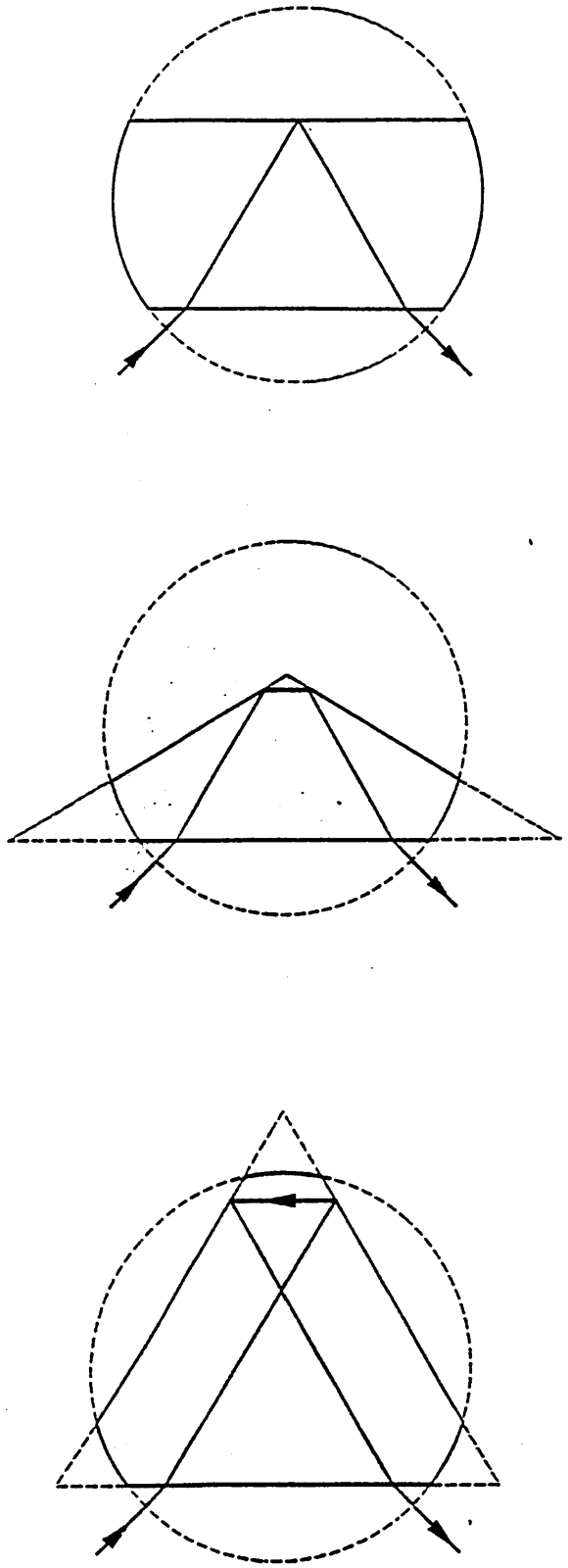

Figure 5.16 Various design configurations considered in relation to a transducer case 20 mm internal diameter.

Design Configuration	Path Change / μm
Simple	51.8
n type	36.7
x type	86.3

Table 5.1 Comparison of three design configurations with respect to the path change brought about by a given change in refractive index.

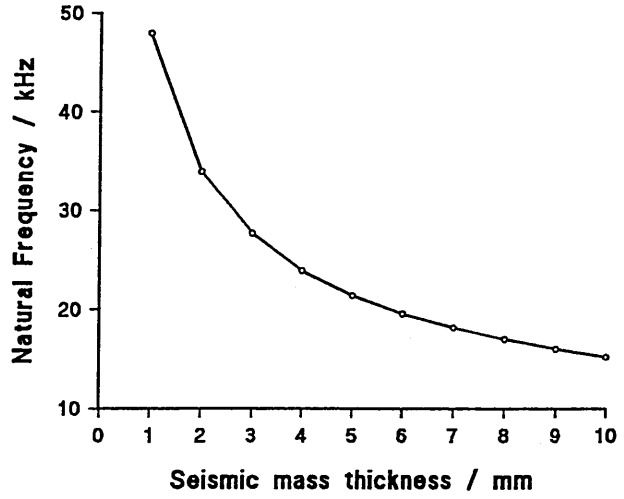

Figure 5.17 The effect of the seismic mass thickness of the natural frequency of the accelerometer.

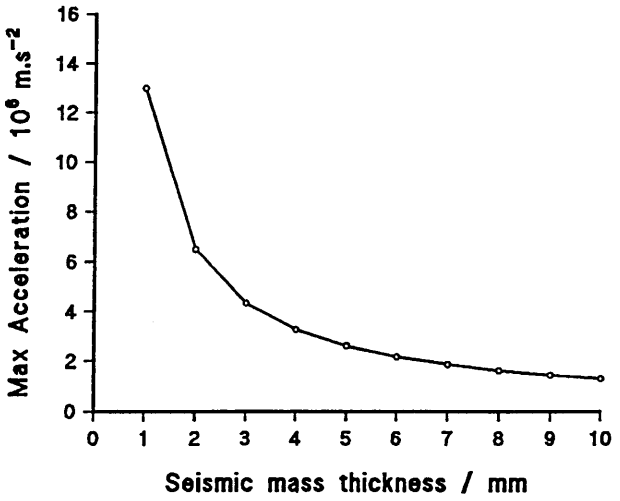

Figure 5.18 The effect of the seismic mass thickness on the maximum detectable acceleration of the transducer.

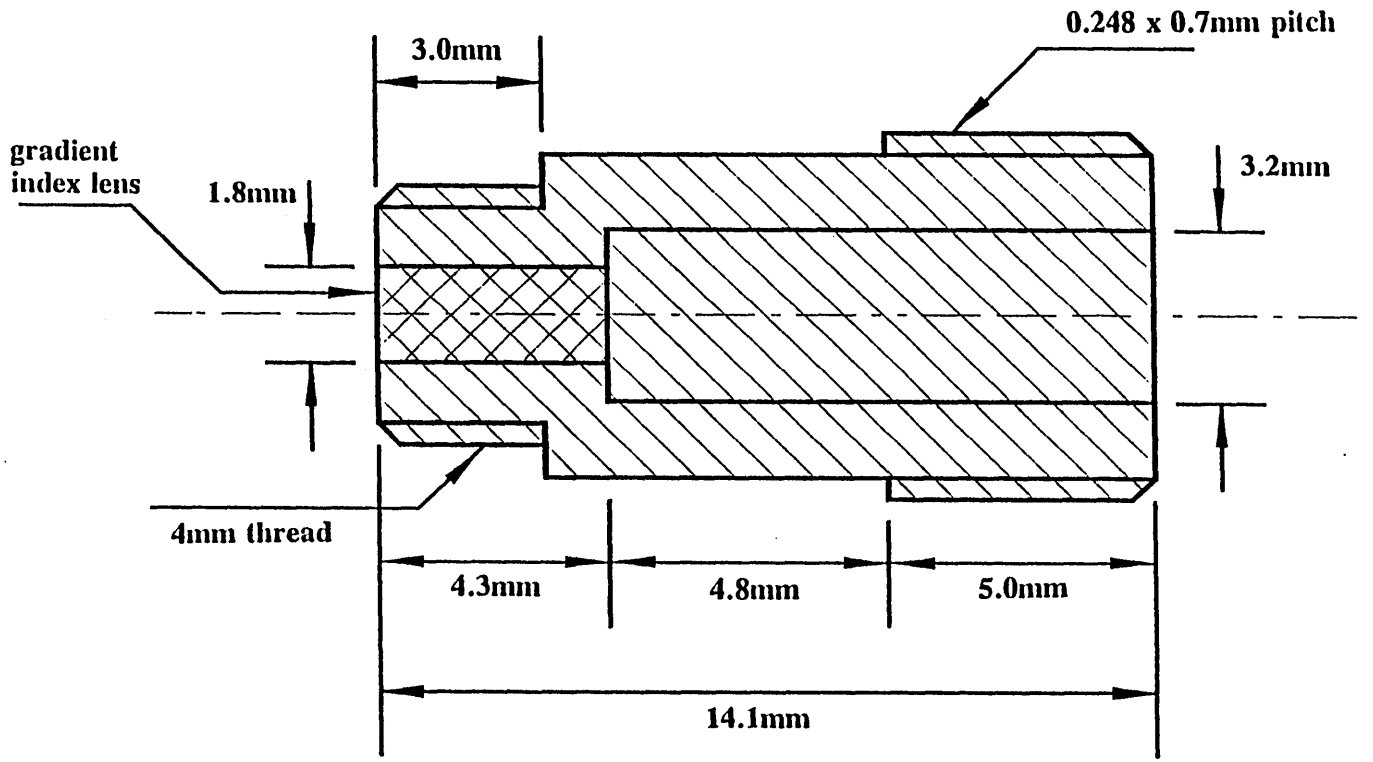

Figure 5.19 The SMA compatible connector used to couple the light from the fibre optic cables to the light modulated transducer.

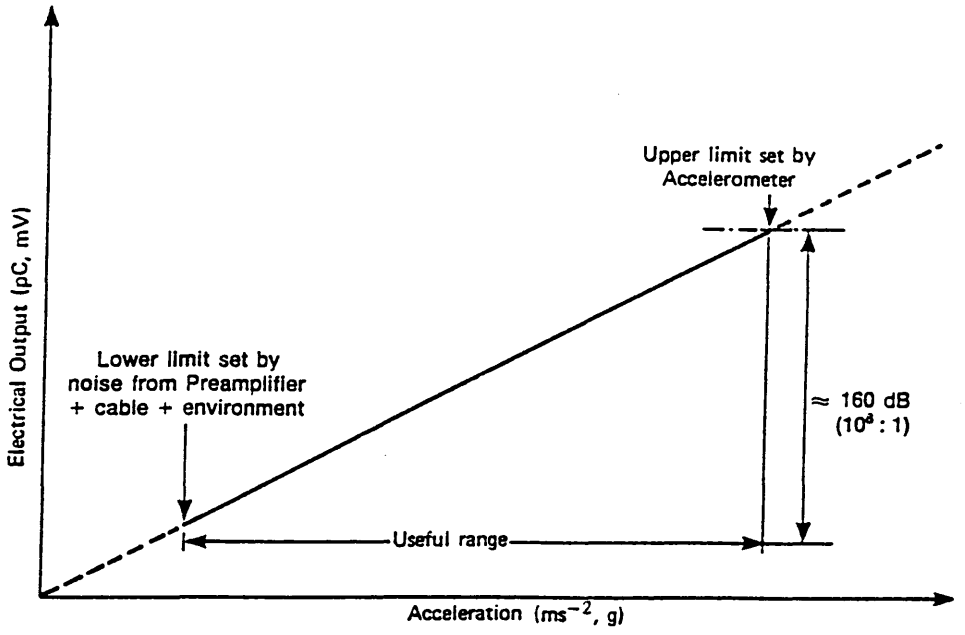

(a) Acceleration response

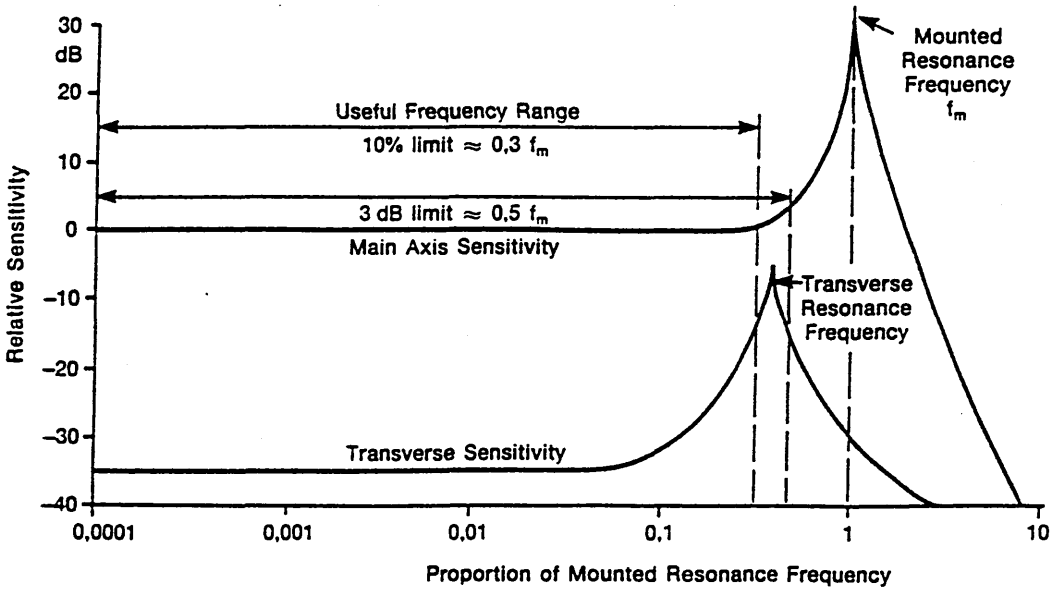

(b) Frequency response

Figure 5.20 The effects of acceleration and frequency on the electrical response of a piezoelectric accelerometer.

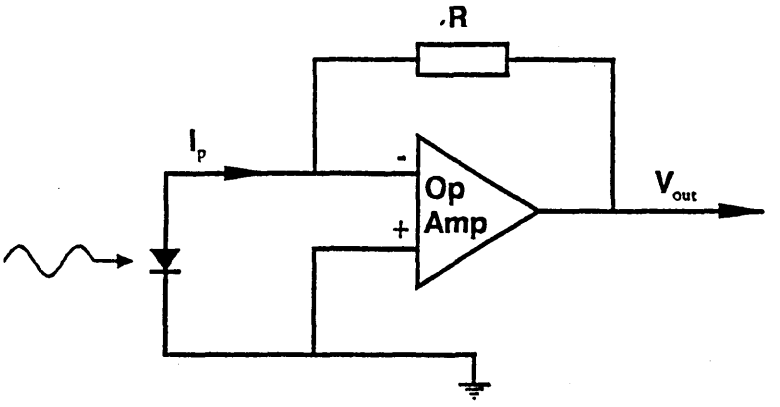

Figure 5.21 The photodetector circuit used in the experimental investigations.

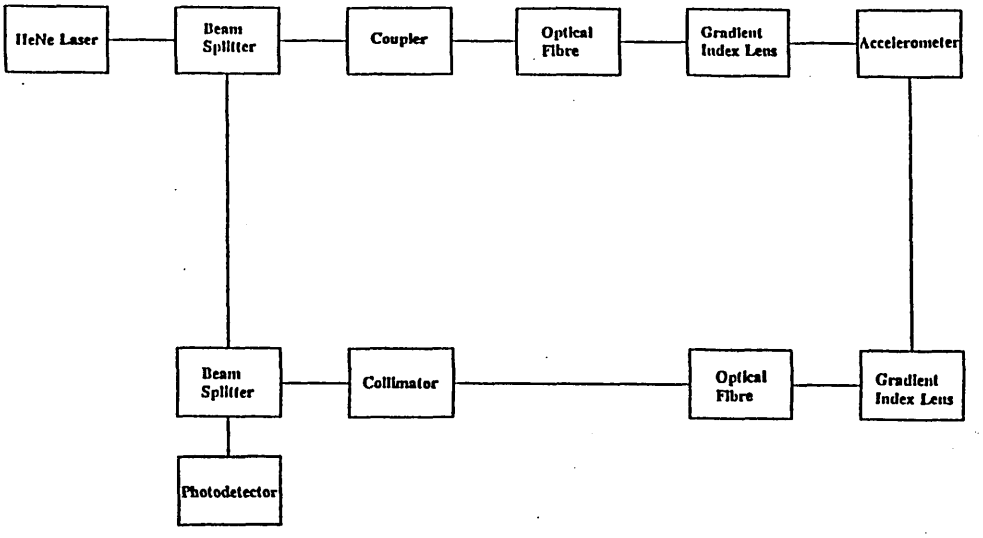

Figure 5.22 Schematic diagram of light modulated transducer system.

Component	Loss dB	No.	Cum Loss dB
Beamsplitter	3	2	6
Coupler	0.5	1	0.5
Collimator	0.6	1	0.6
Gradient Index Lens	0.5	2	1.0
Connector/fibre	1.0	2	2.0
Sensing Element	0.5[1]	1	0.5
	Total Loss		10.6

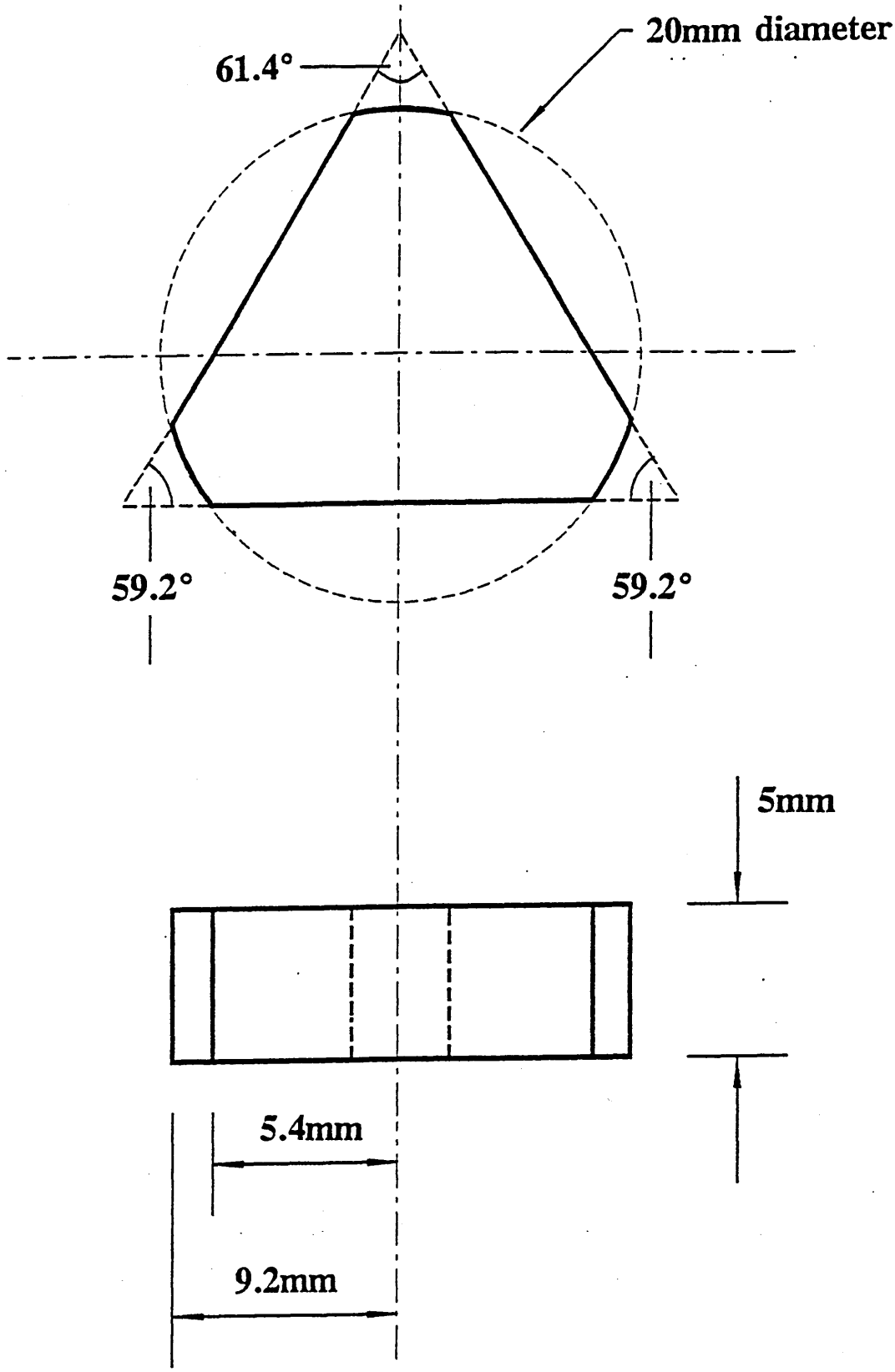

Figure 6.1 The x type sensing element manufactured for use in the prototype accelerometer

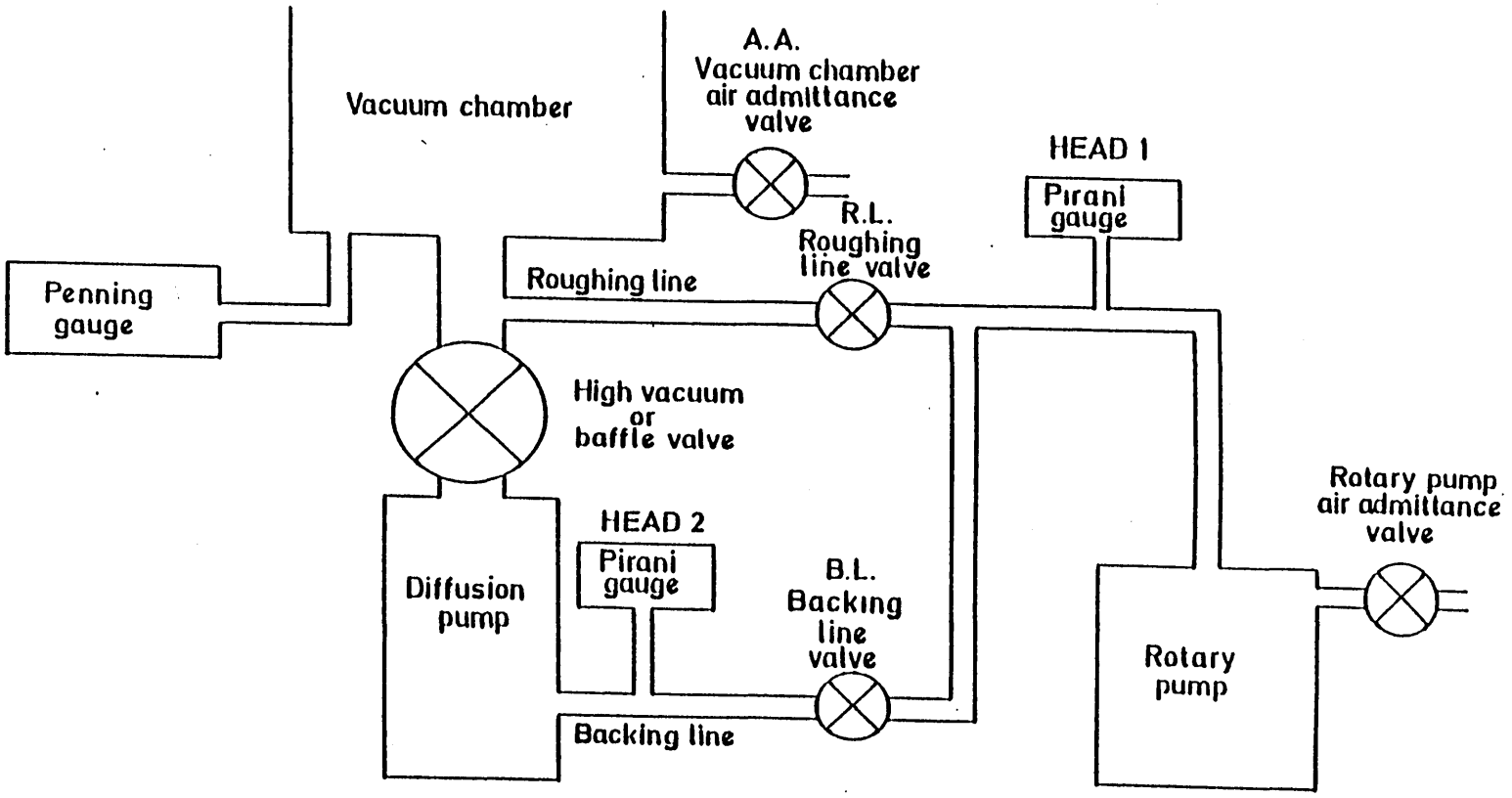

Figure 6.2 A schematic diagram of the vacuum system used for the coating the material samples used in the optical tests.

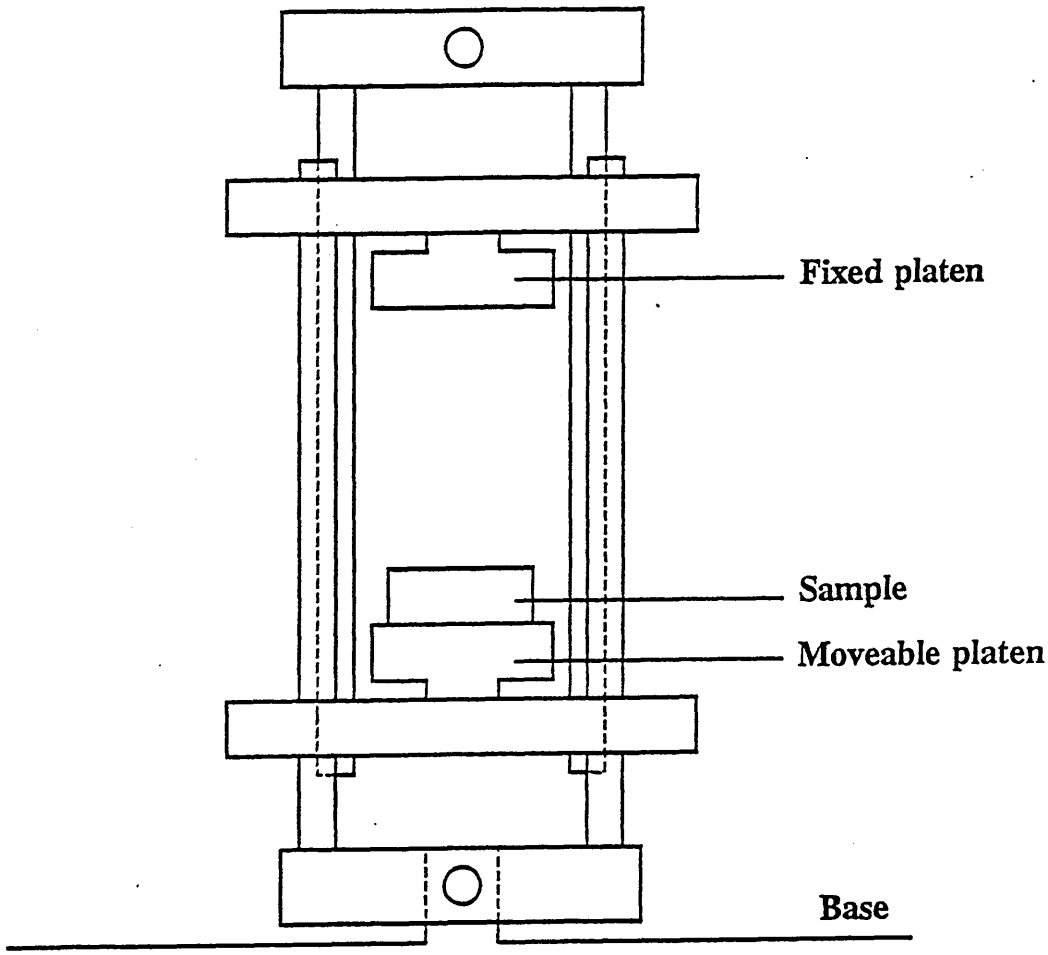

Figure 6.3 The compression rig used in conjunction with the tensile testing machine.

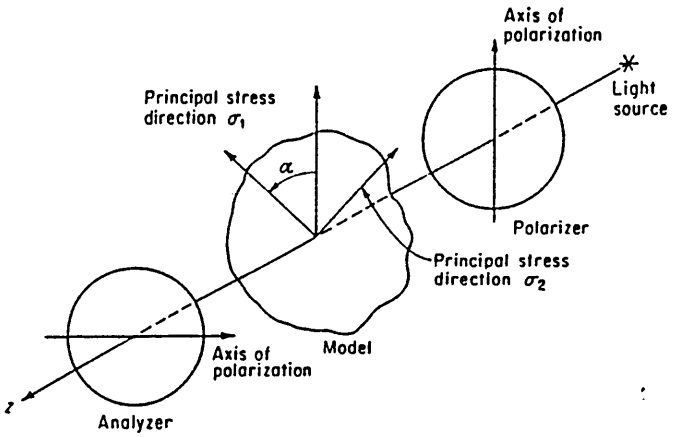

Figure 6.4 A schematic diagram of the plane polariscope

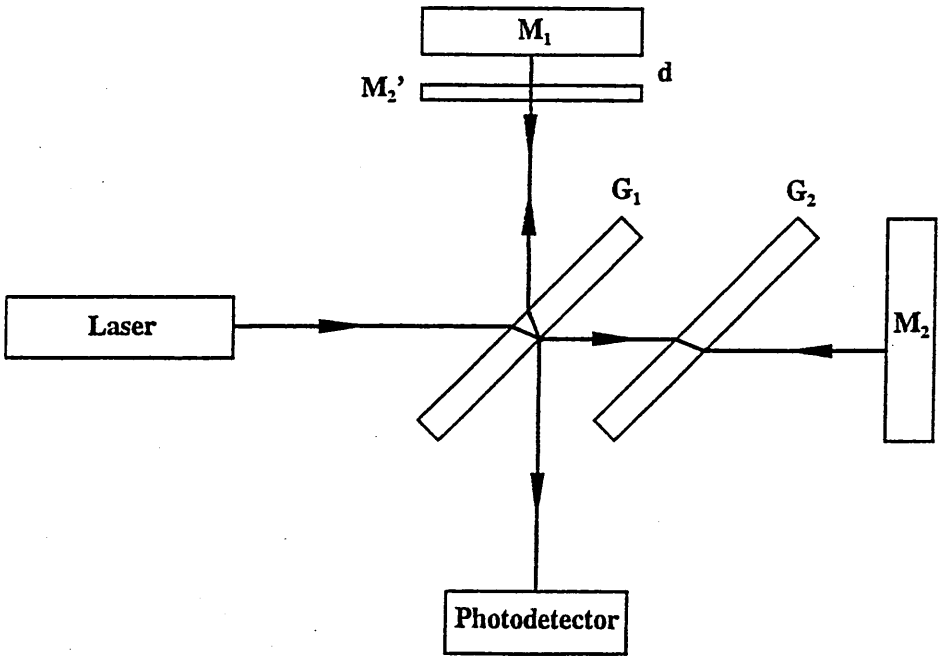

Figure 6.5 A schematic diagram of the Michelson interferometer

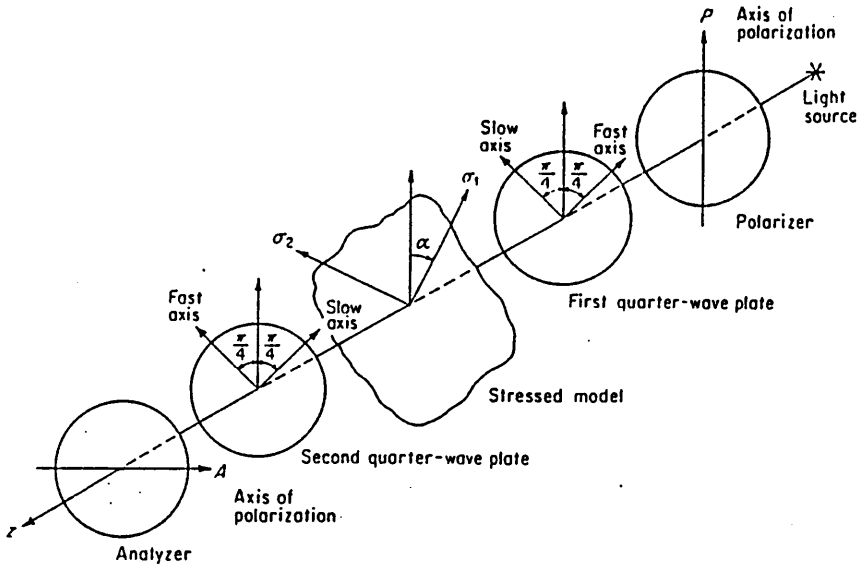

Figure 6.6 A schematic diagram of the circular polariscope

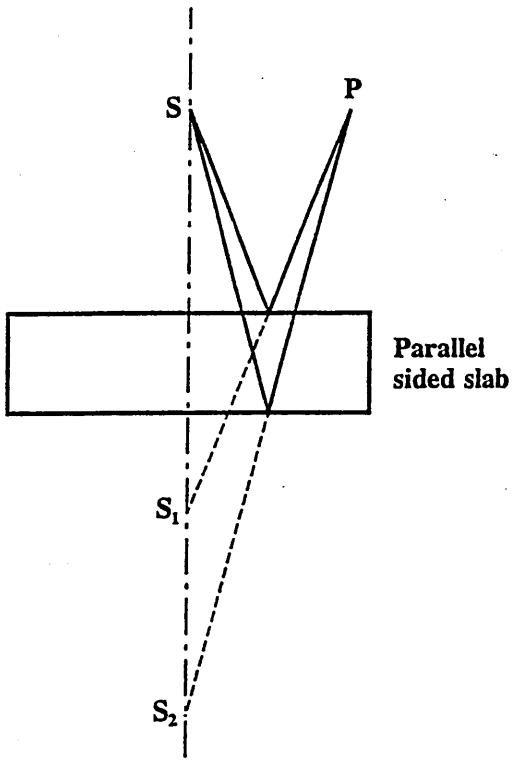

Figure 6.7 A point source S has two images S_1 and S_2 in the front and back surface of a parallel sided slab and the interference fringes produced are non-localised in space.

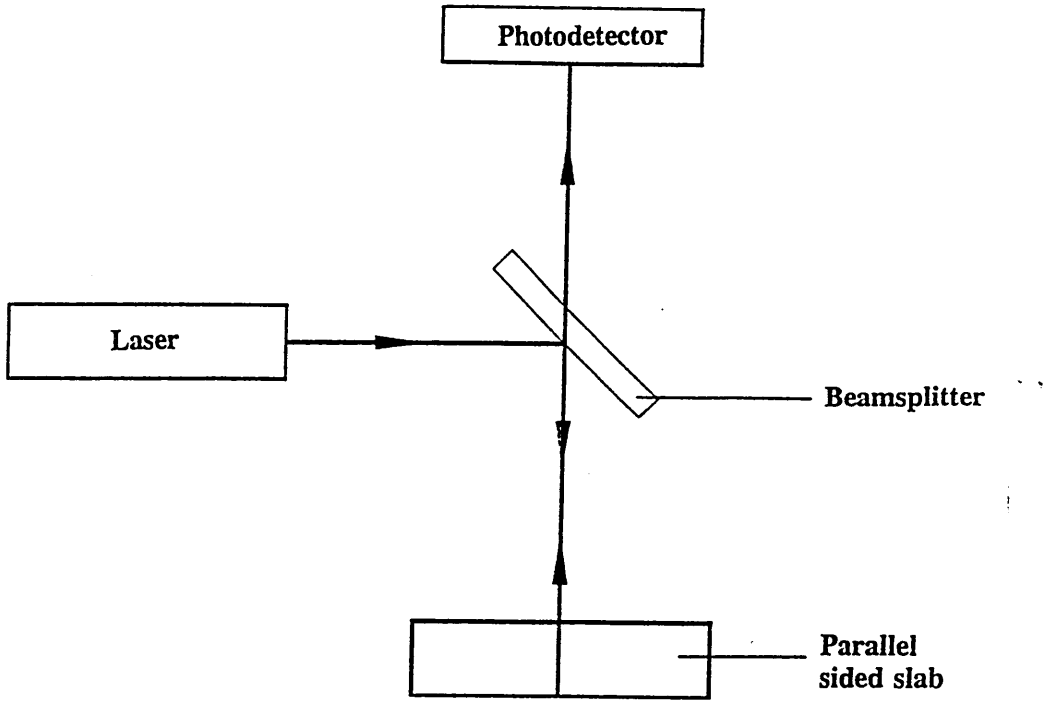

Figure 6.8 Schematic diagram showing experimental set up of the Fizeau interferometer.

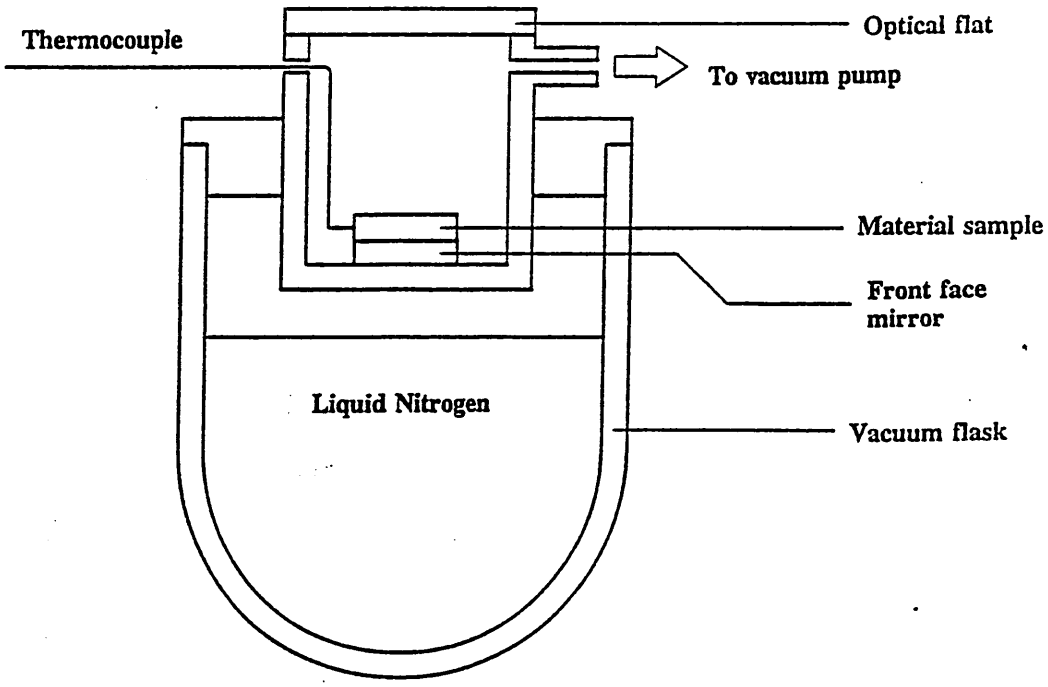

Figure 6.9 Schematic diagram of the low temperature apparatus.

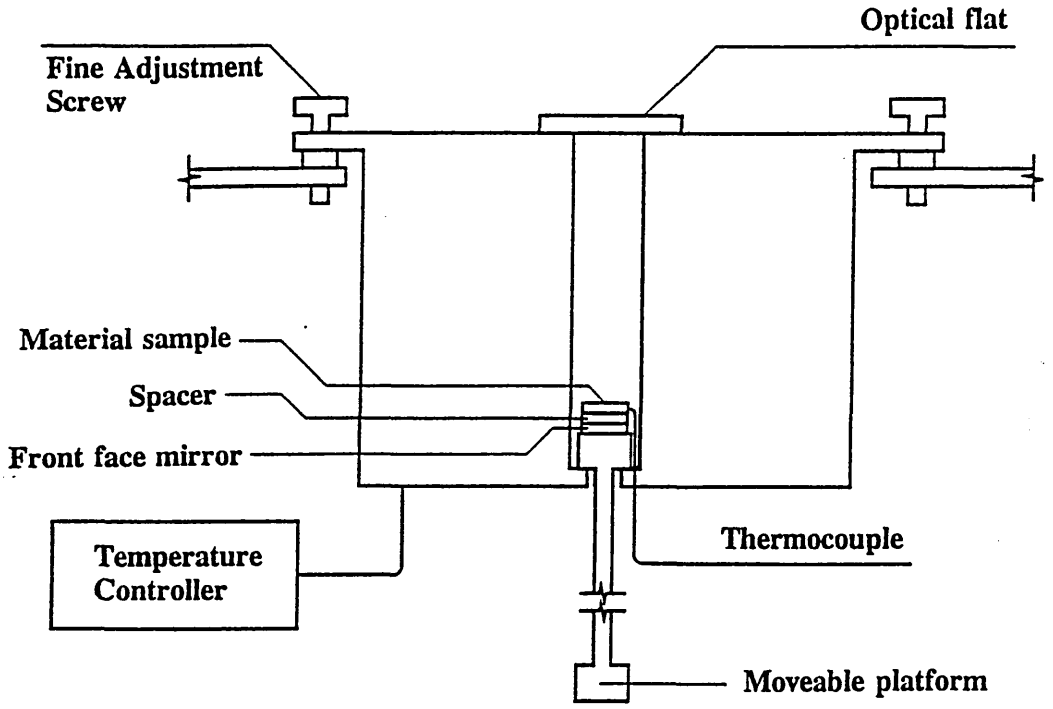

Figure 6.10 Schematic diagram of the high temperature apparatus.

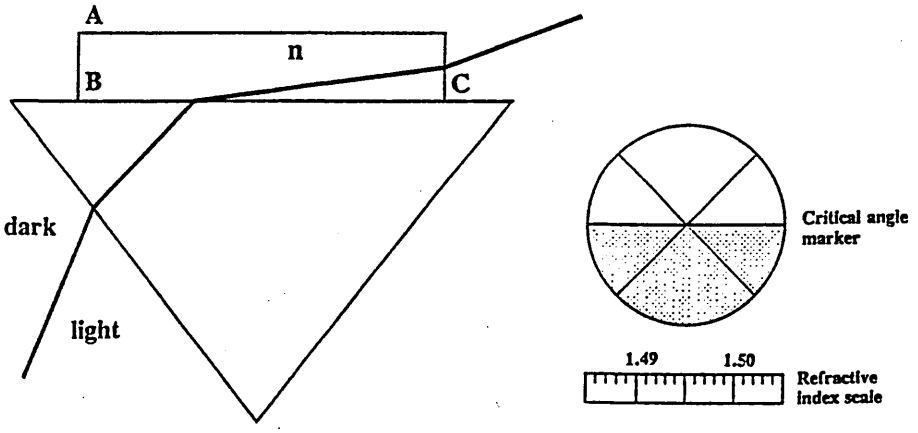

Figure 6.11 The operating principle of the Abbé refractometer

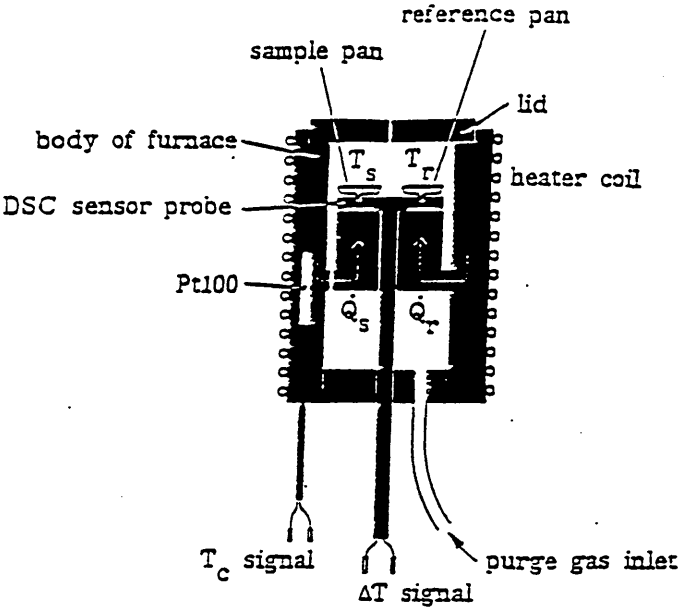

Figure 6.12 Sectional view of the differential scanning calorimeter (DSC) measuring cell.

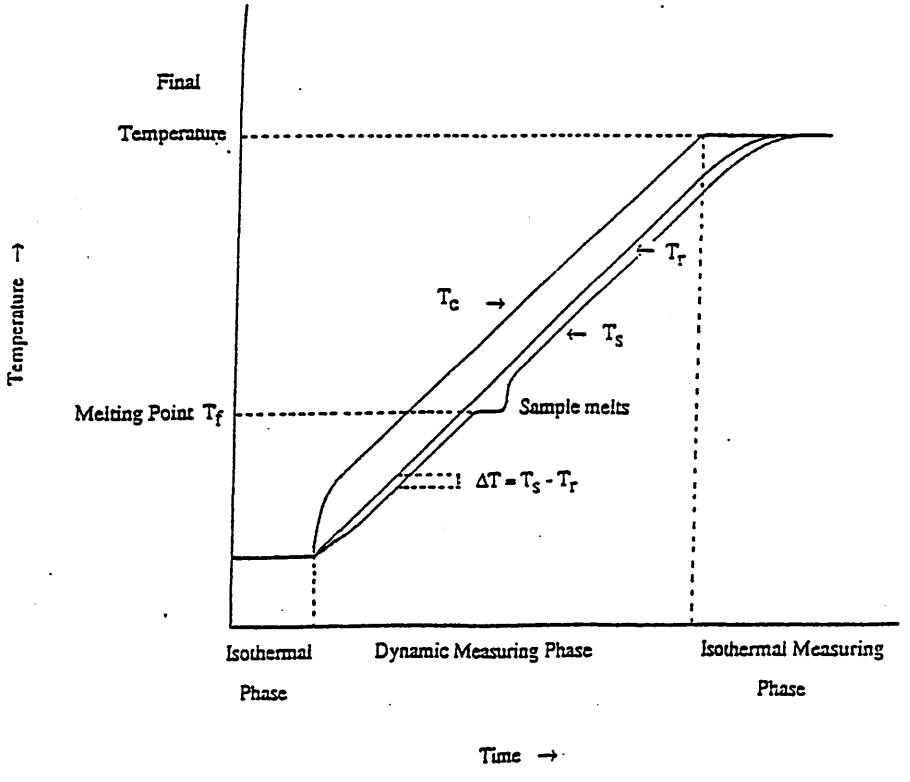

Figure 6.13 Diagram showing the temperatures in the DSC measuring cell as a function of time. T_r = displayed temperature, T_s = sample temperature and T_c = furnace temperature.

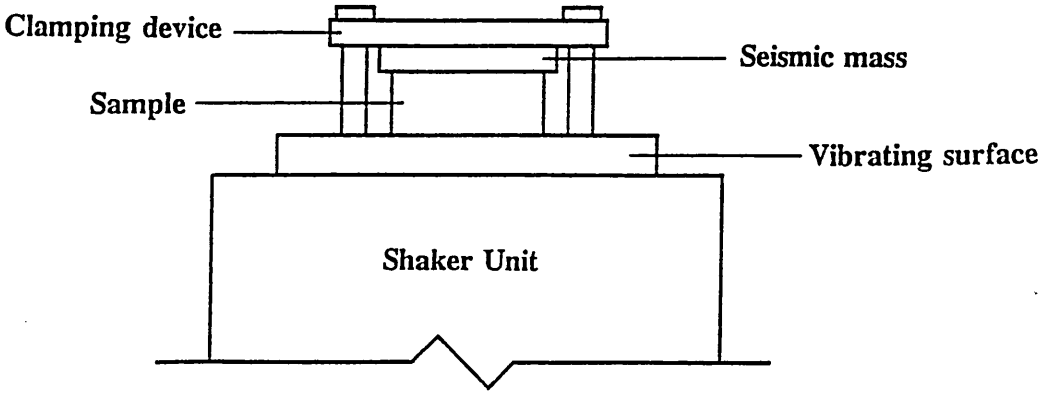

Figure 6.14 Experimental accelerometer assembled on the surface of vibration table.

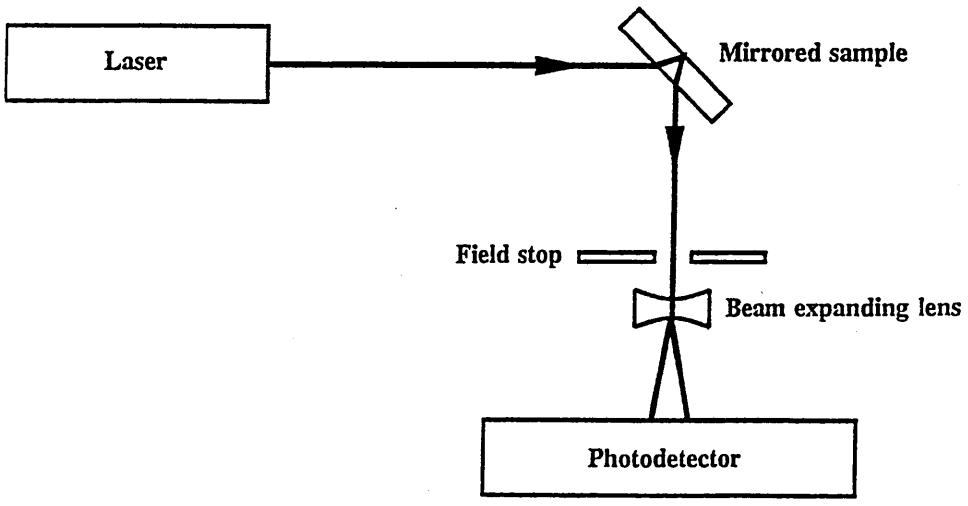

Figure 6.15 Schematic diagram of intensity modulation set up.

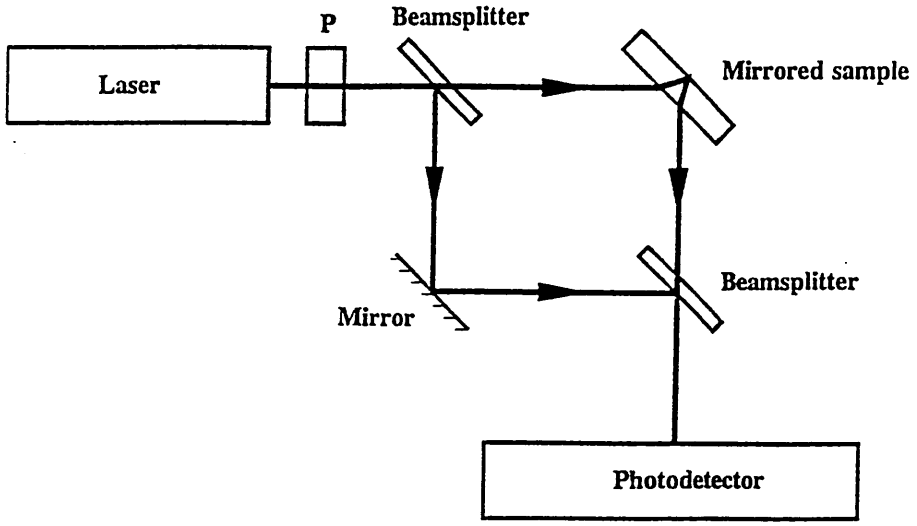

Figure 6.16 Schematic diagram of phase modulated set up.

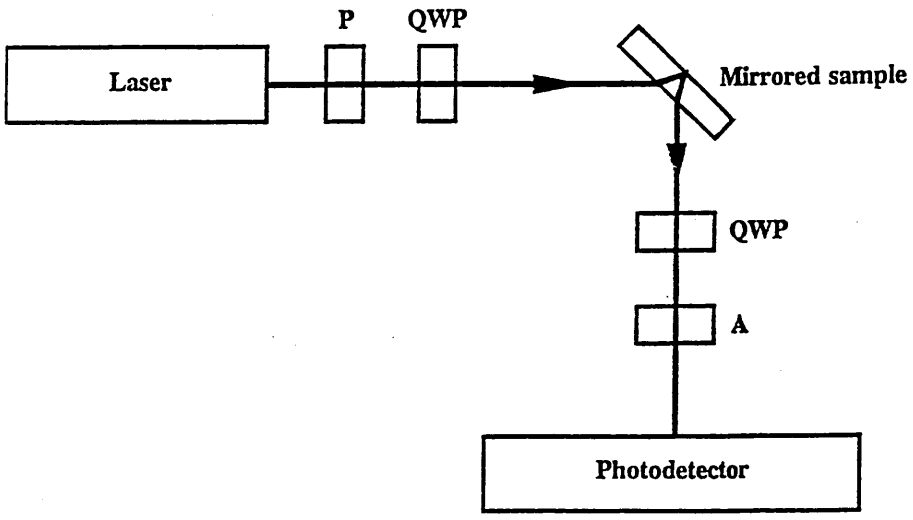

Figure 6.17 Schematic diagram of polarisation set up

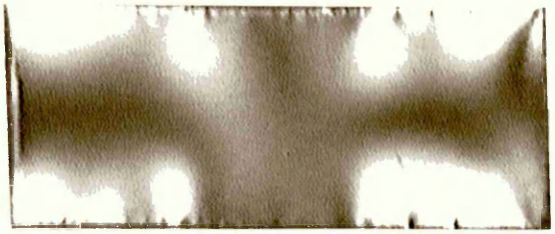

0°

5°

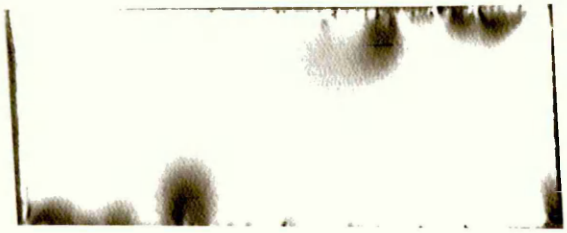

10°

15°

45°

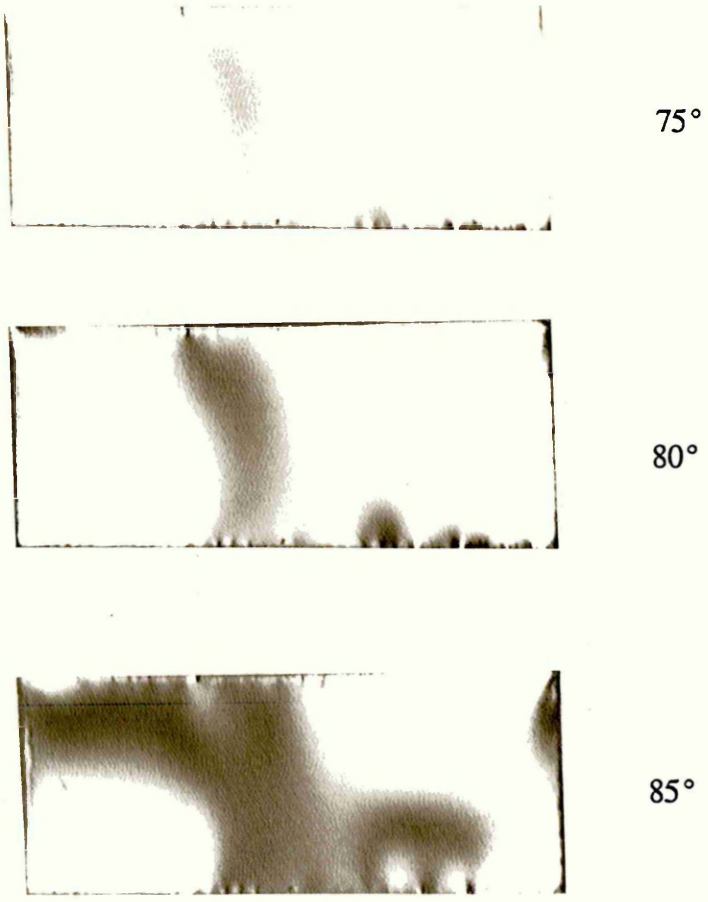

Figure 7.1 Isoclinic fringes produced in polymethyl methacrylate subjected to a compressive load for various polarizer/analyzer settings.

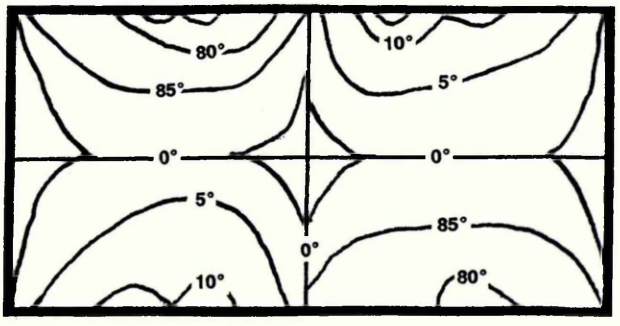

Figure 7.2 The composite isoclinic pattern obtained from a polymethyl methacrylate sample subjected to a compressive load.

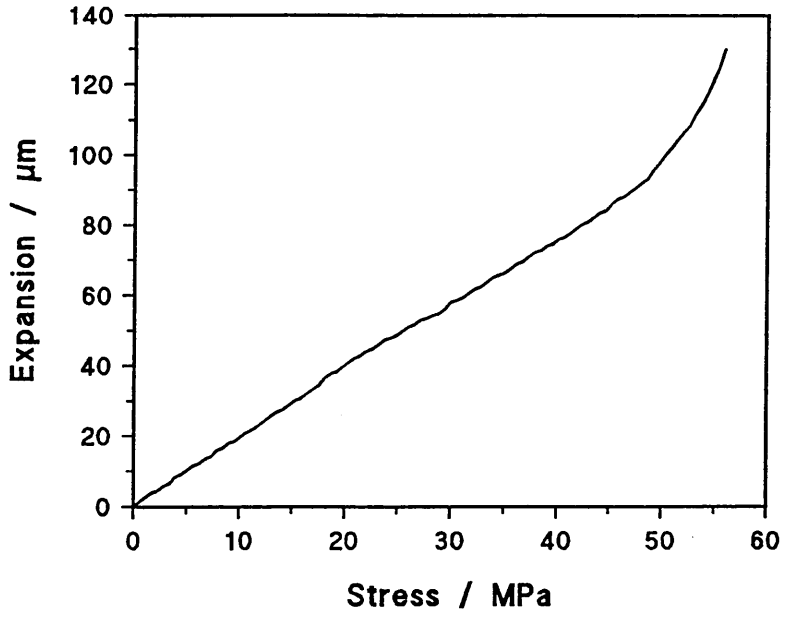

(a) Polycarbonate

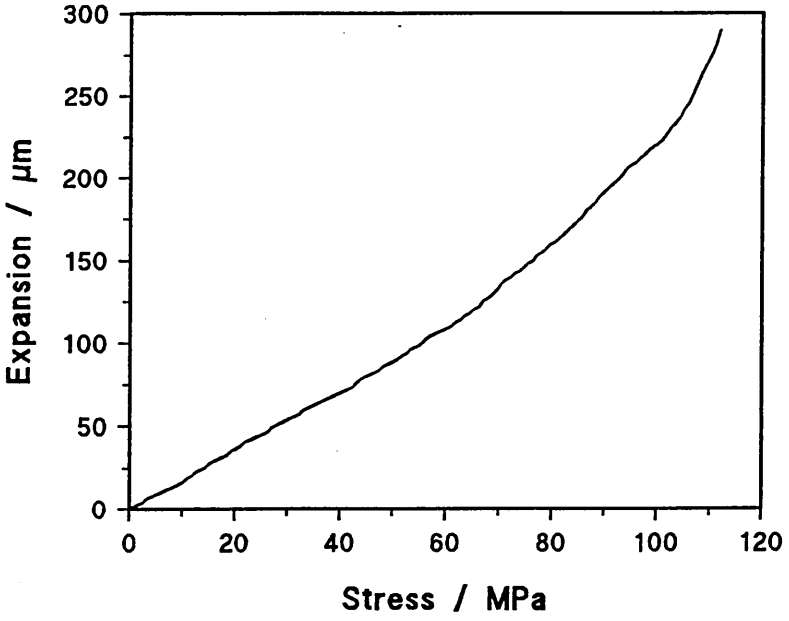

(b) Polymethyl methacrylate

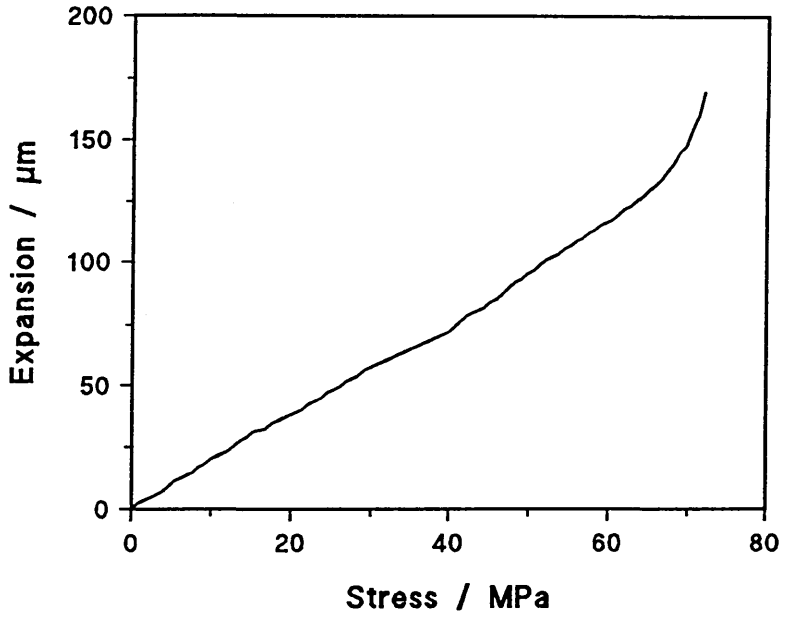

(c) Polyvinyl chloride

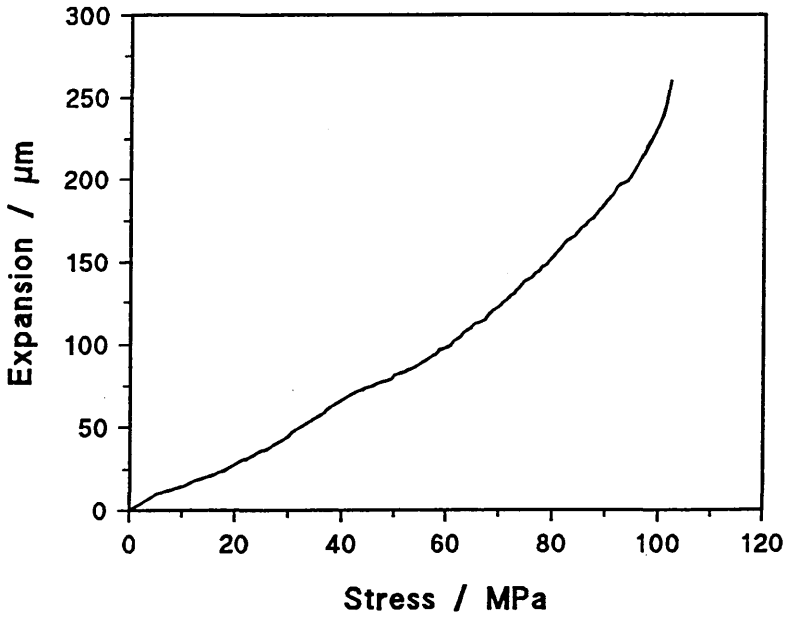

(d) Araldite epoxy resin

Figure 7.3 The expansion of the materials samples produced as a result of applied compressive stress: (a) polycarbonate; (b) polymethyl methacrylate; (c) polyvinyl chloride and (d) araldite epoxy resin.

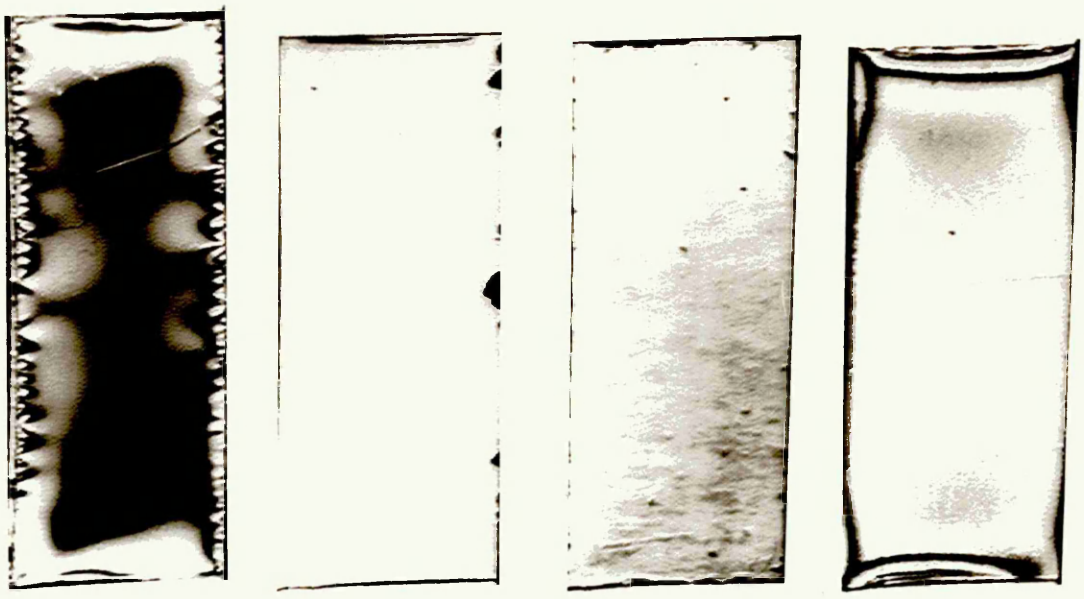

Figure 7.4 The isochromatic fringe patterns produced in each material under zero stress conditions. PC - polyvinyl chloride, PMMA - polymethyl methacrylate, PVC - polyvinyl chloride and EP - araldite epoxy resin.

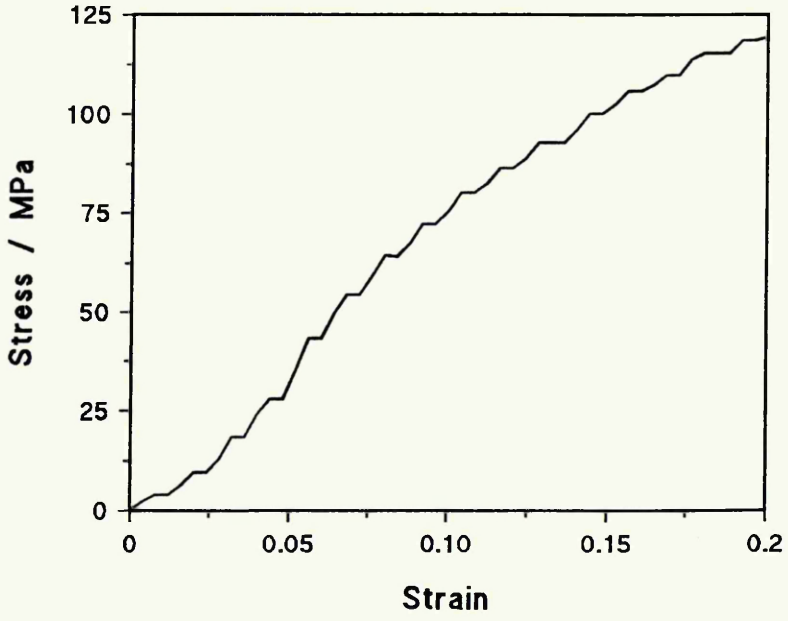

Figure 7.5 Graph illustrating the pen displacement when a fringe passed through a point viewed on the video minitor.

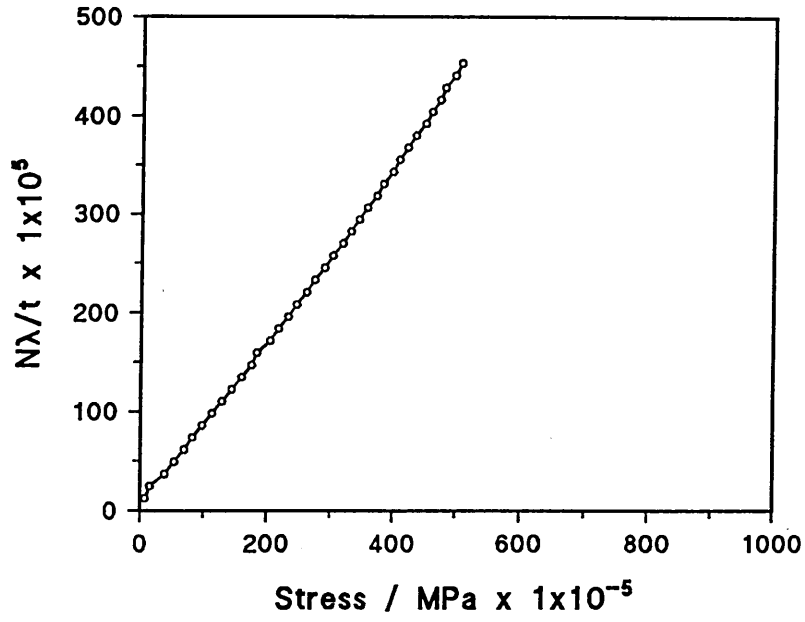

(a) Polycarbonate

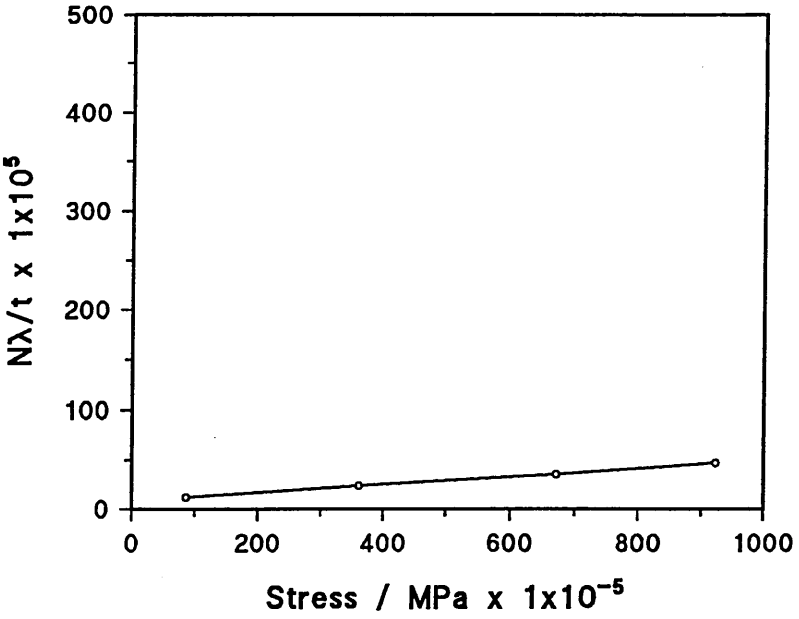

(b) Polmethyl methacrylate

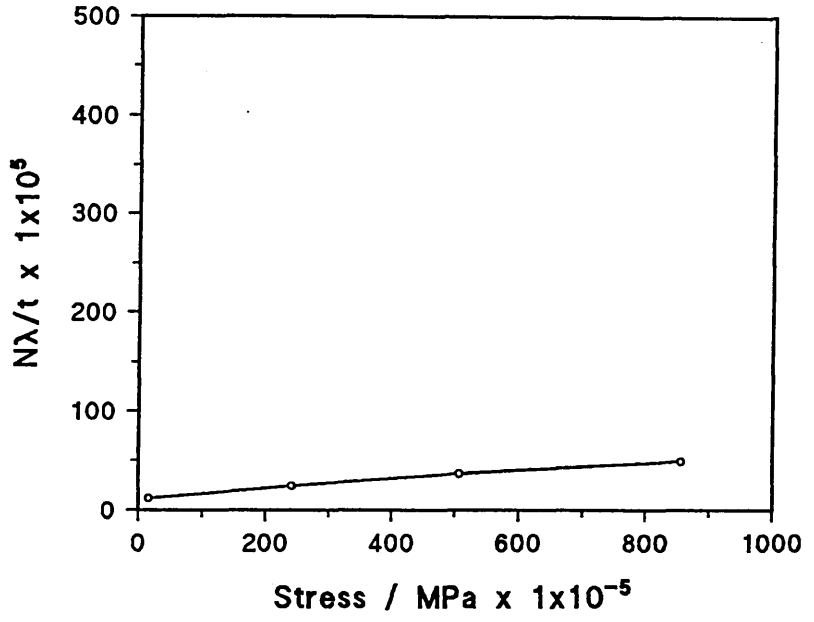

(c) Polyvinyl chloride

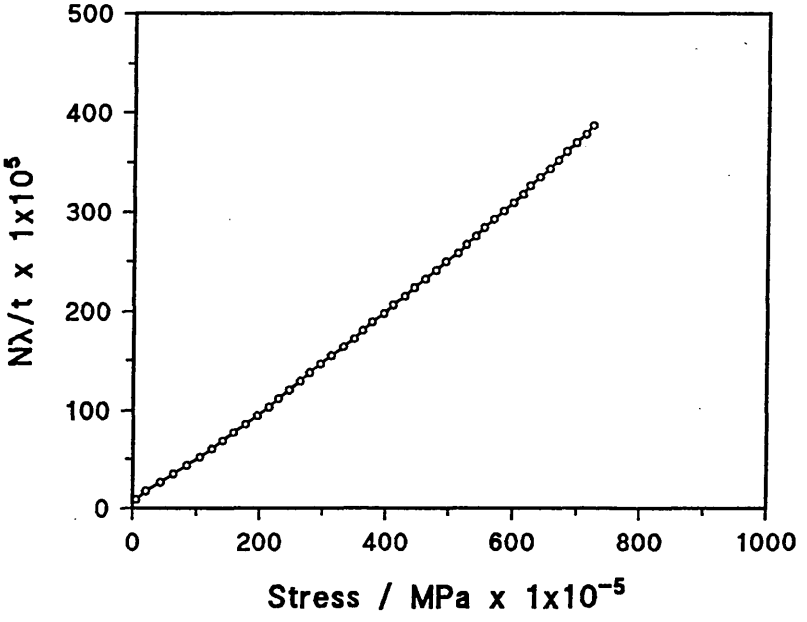

(d) Araldite epoxy resin

Figure 7.6 Nλ/t plotted against the applied compressive stress. The gradient gives the stress optic coefficient. (a) polycarbonate, (b) polymethyl methacrylate, (c) polyvinyl chloride and (d) araldite epoxy resin.

Material	C /10^{-12} Pa^{-1}	C /10^{-12} Pa^{-1}	f_σ
Polycarbonate	87.55	85.92	7228
Polymethyl methacrylate	4.13	4.10	153220
Polyvinyl chloride	4.36	4.28	145138
Araldite epoxy resin	52.73	51.83	12001

Table 7.1 - The stress optic coefficient determined, for each material, using the data plotted in figure 7.6. Also reported are the fringe stress coefficient calculated using equation 7.1 and the thickness corrected stress optic coefficient.

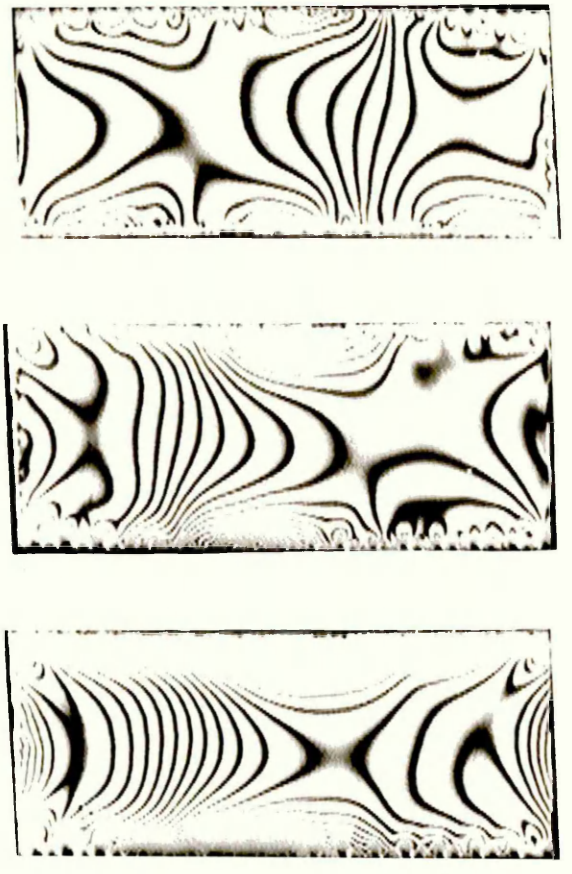

(a) Polycarbonate

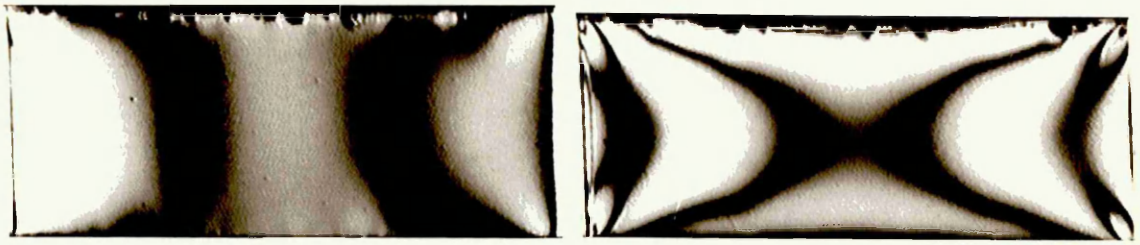

(b) Polymethyl methacrylate

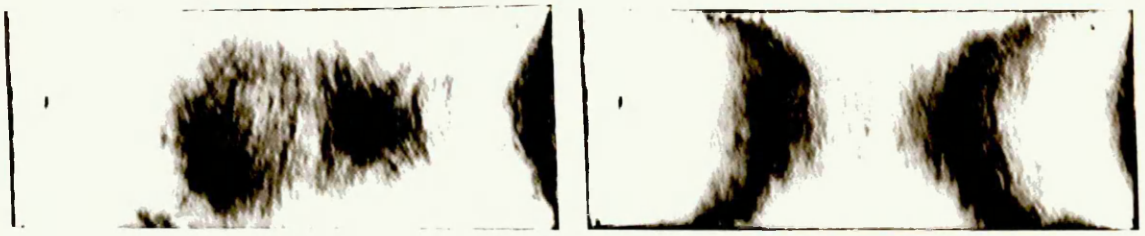

(c) Polyvinyl chloride

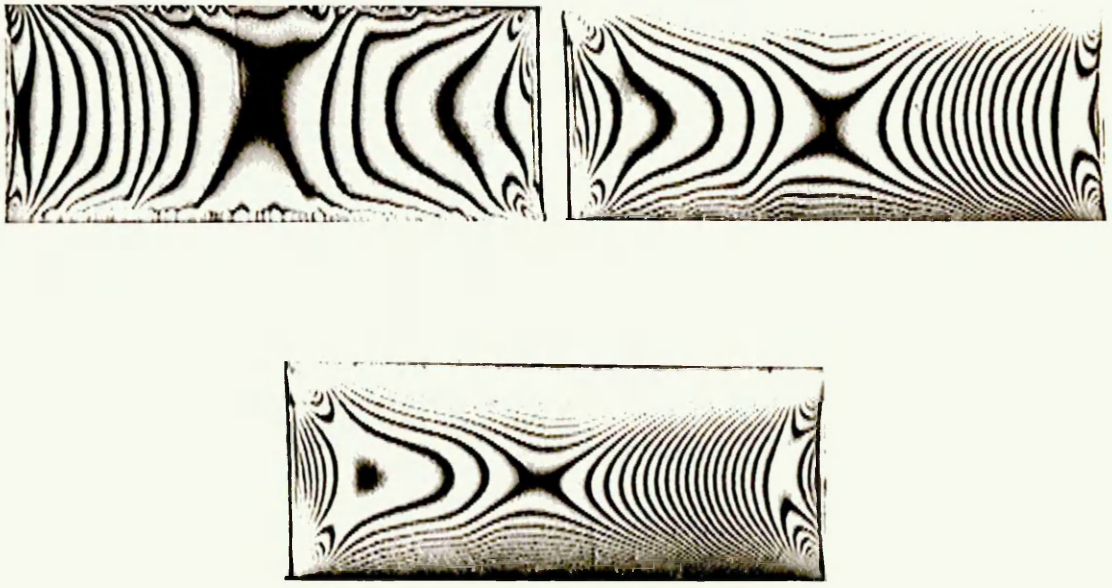

(d) Araldite epoxy resin

Figure 7.7 The isochromatic fringe pattern obtained for each material at various loads. The effect of the magnitude of the stress optic coefficent on the pattern can be observed.

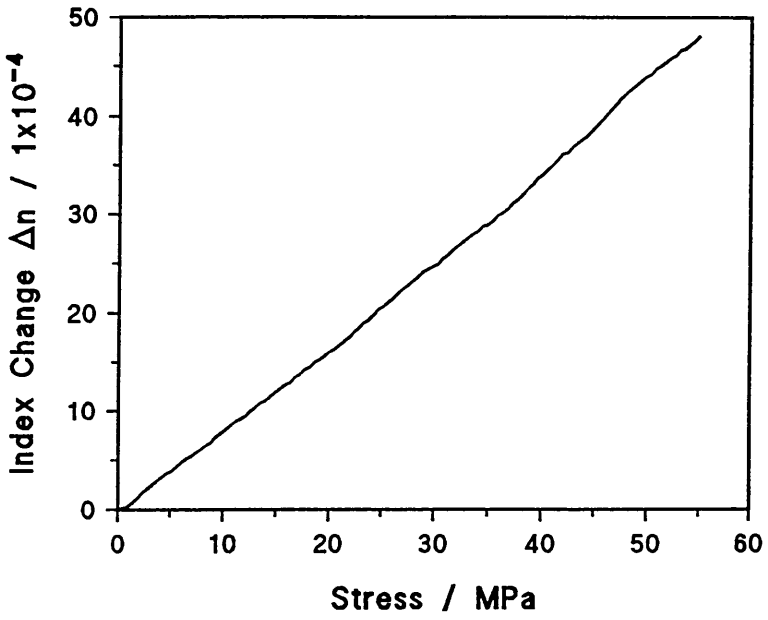

(a) Polycarbonate

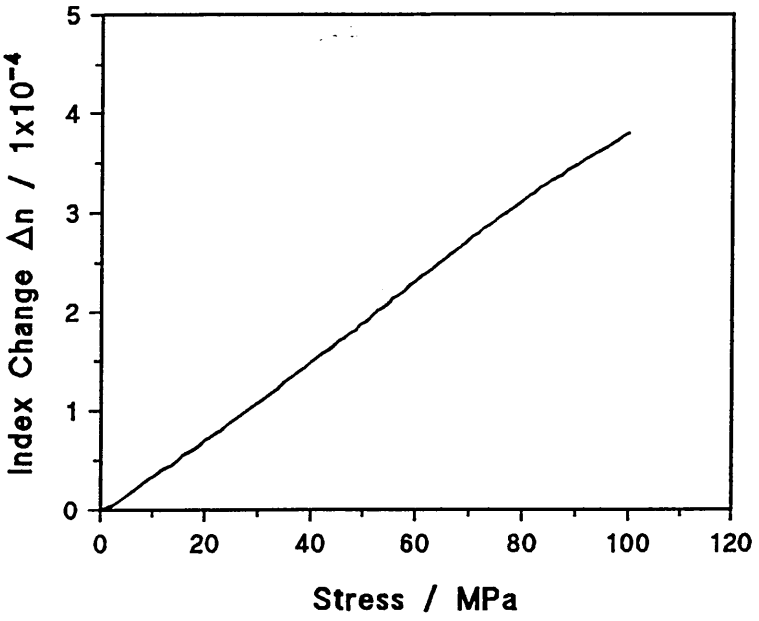

(b) Polmethyl methacrylate

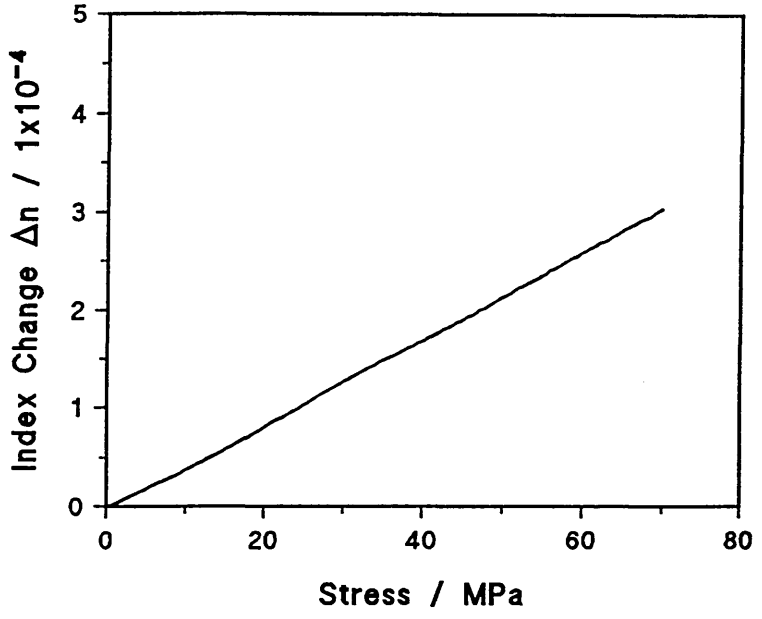

(c) Polyvinyl chloride

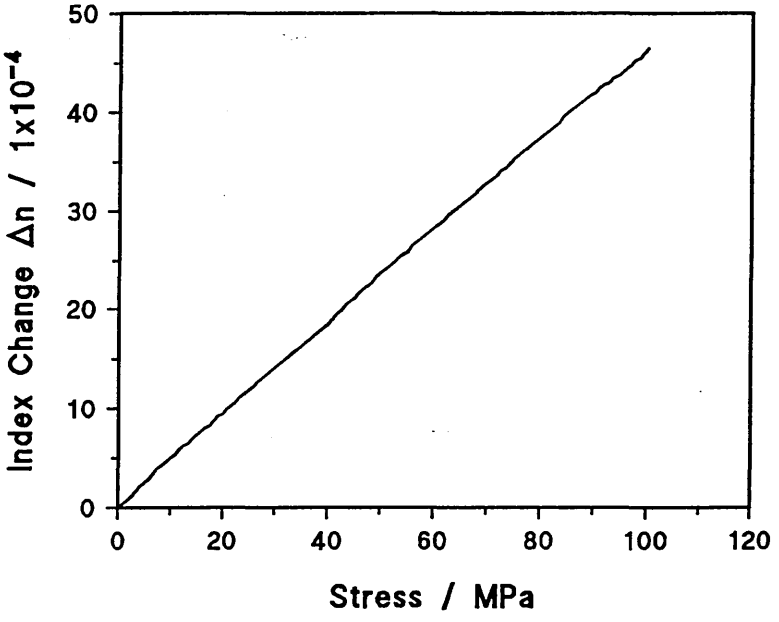

(d) Araldite epoxy resin

Figure 7.8 The change in refractive index as a result of applied compressive stress determined using the Fizeau interferometer. (a) polycarbonate, (b) polymethyl methacrylate, (c) polyvinyl chloride and (d) araldite epoxy resin.

Material	C x 10^{-12}
Polycarbonate	85.24
Polymethyl methacrylate	4.09
Polyvinyl chloride	4.24
Araldite epoxy resin	51.31

Table 7.2 The stress optic coefficient determined using the Fizeau interferometer.

Material	C x 10^{-12} /Pa	C x 10^{-12} /Pa (Lit)
Polycarbonate	84.63	90.4
Polymethyl methacrylate	4.03	4.7
Polyvinyl chloride	4.27	-
Araldite epoxy resin	50.48	62.0

Table 7.3 - The stress optic coefficient determined using the Michelson interferometer. Also shown are the values reported in the literature.

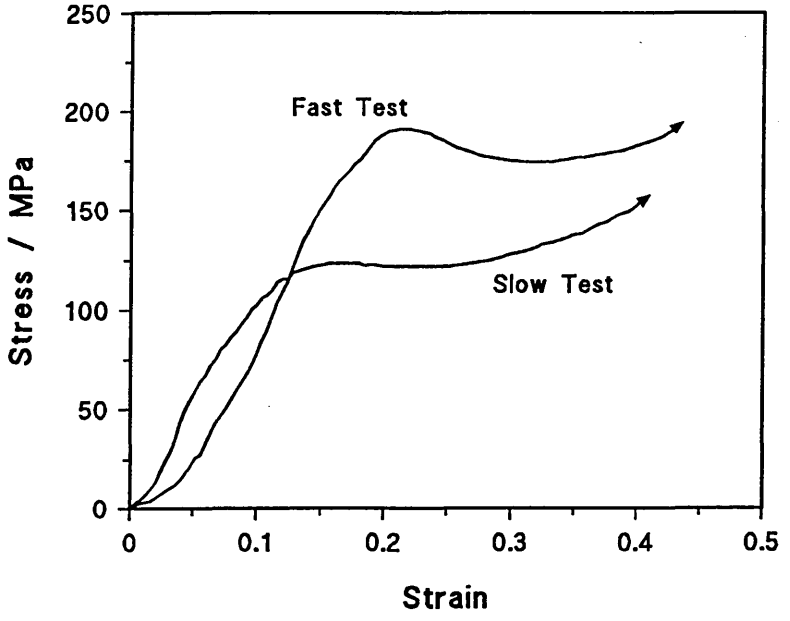

Figure 7.9 The effect of the test speed on the stress strain response of polymethyl methacrylate.

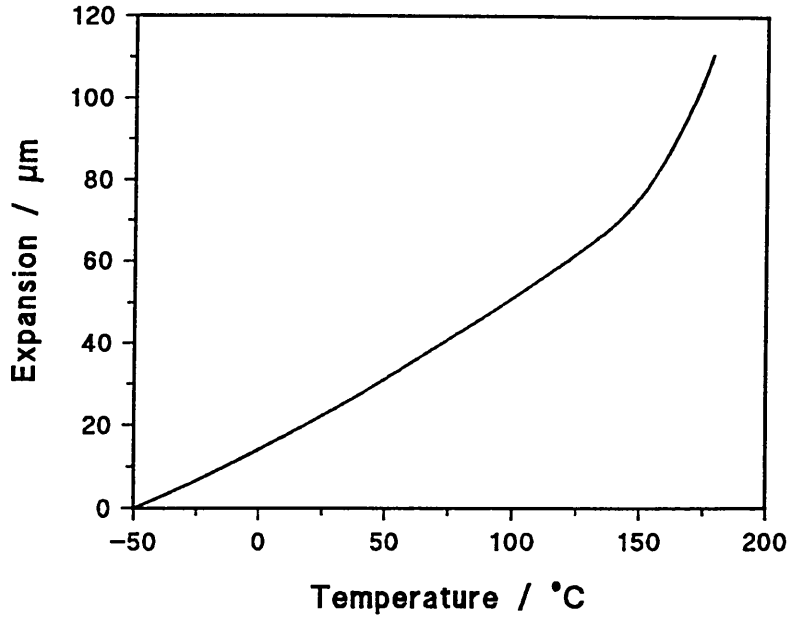

(a) Polycarbonate

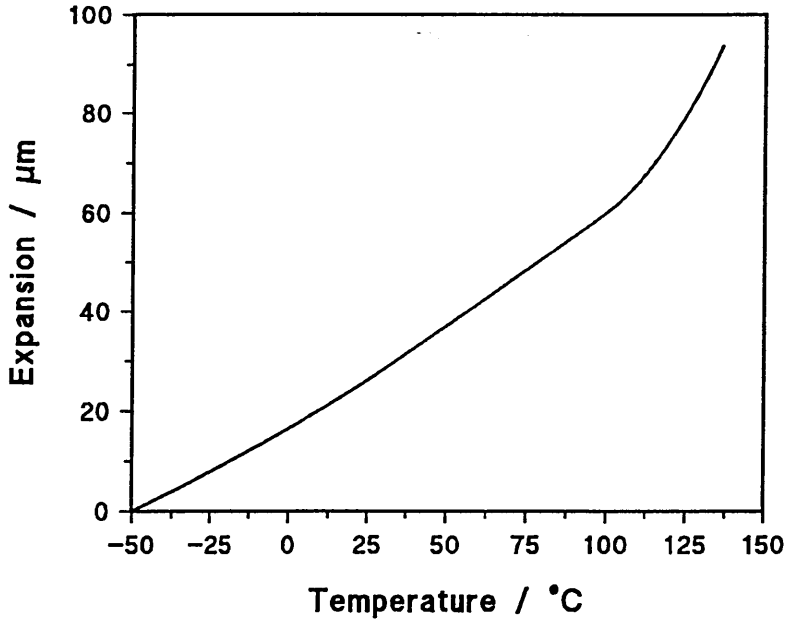

(b) Polmethyl methacrylate

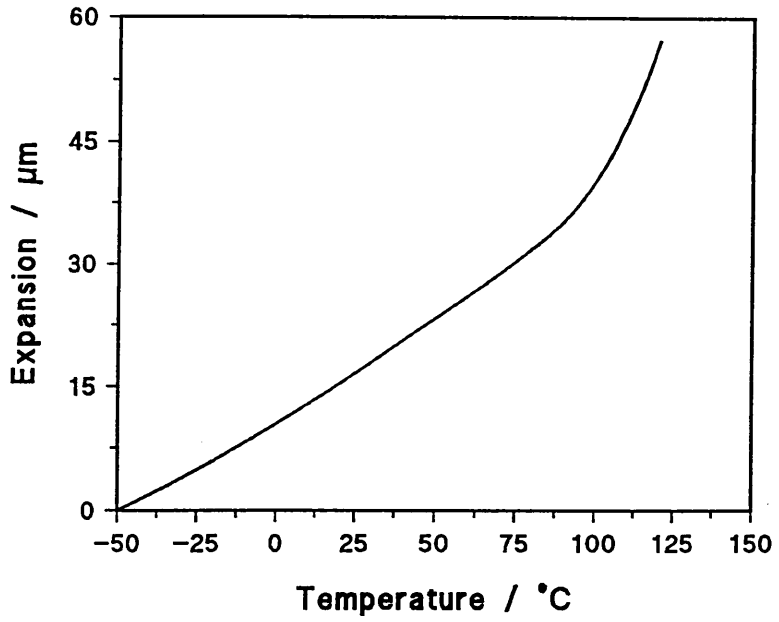

(c) Polystyrene

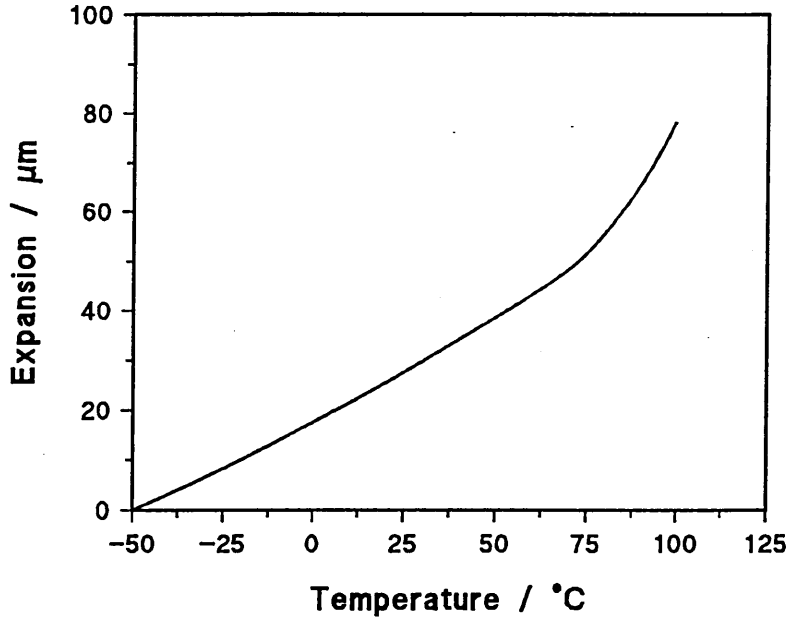

(d) Polyvinyl chloride

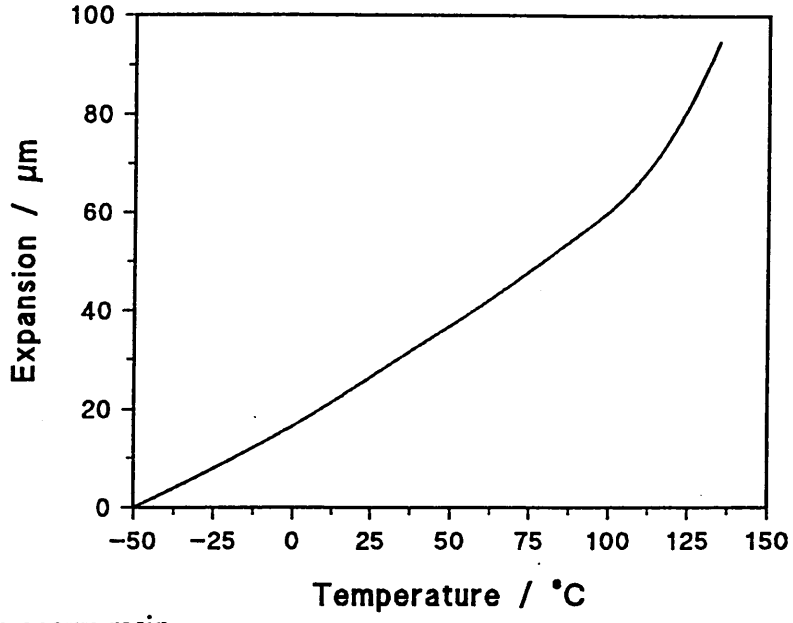

(e) Araldite epoxy resin

Figure 7.10 The thermal expansion of each material determined using the Michelson interferometer. (a) polycarbonate, (b) polymethyl methacrylate, (c) polystyrene (d) polyvinyl chloride and (e) araldite epoxy resin.

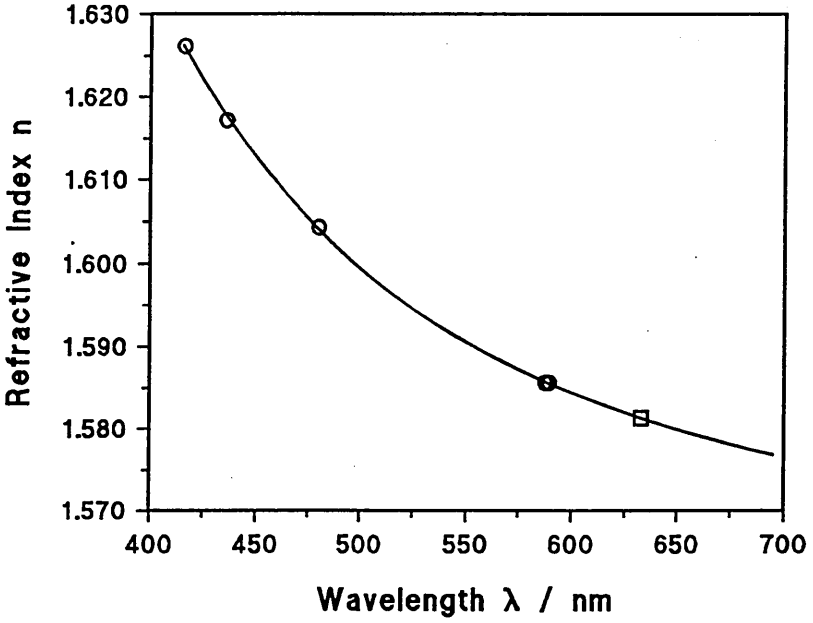

(a) Polycarbonate

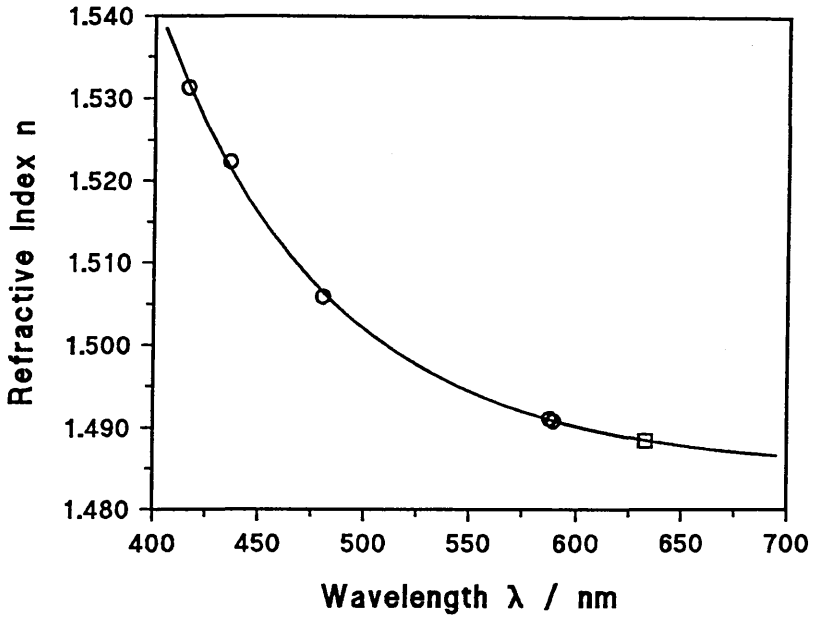

(b) Polmethyl methacrylate

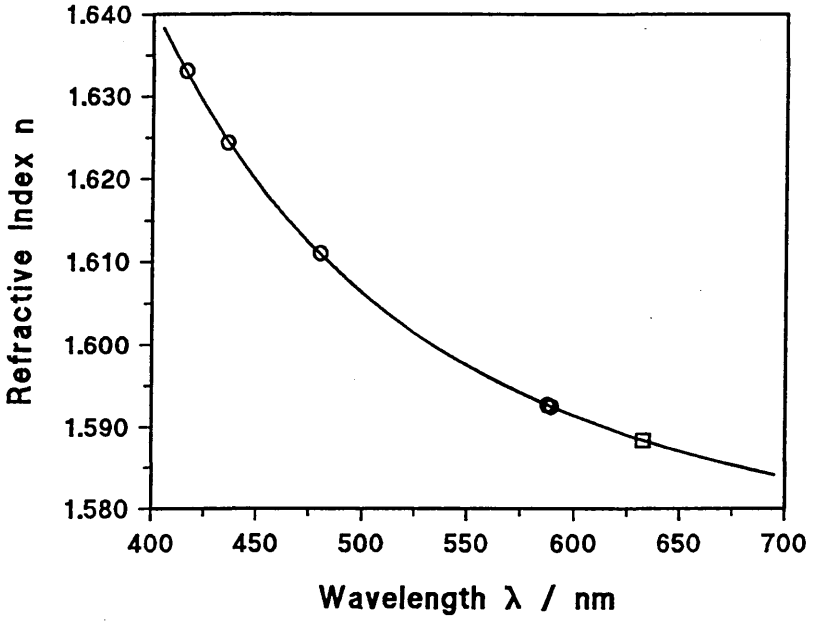

(c) Polystyrene

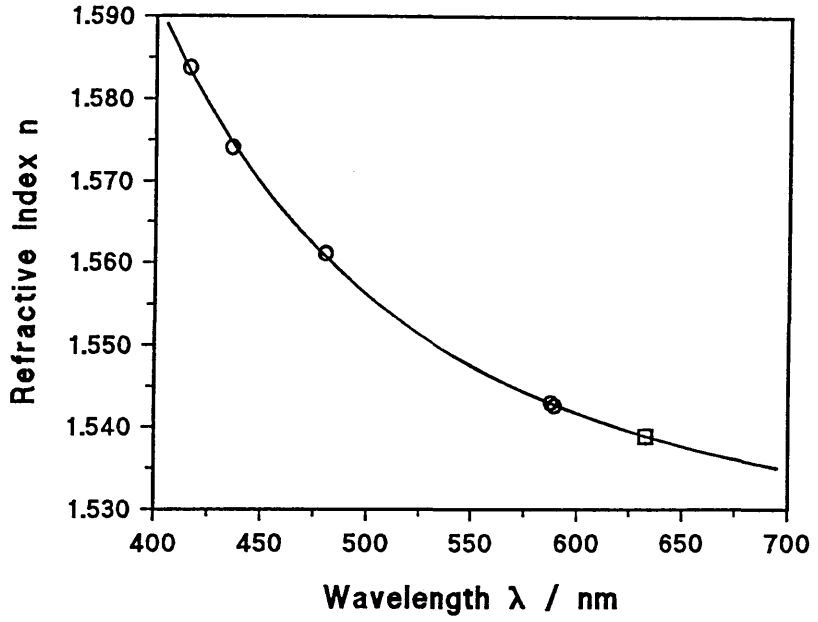

(d) Polyvinyl chloride

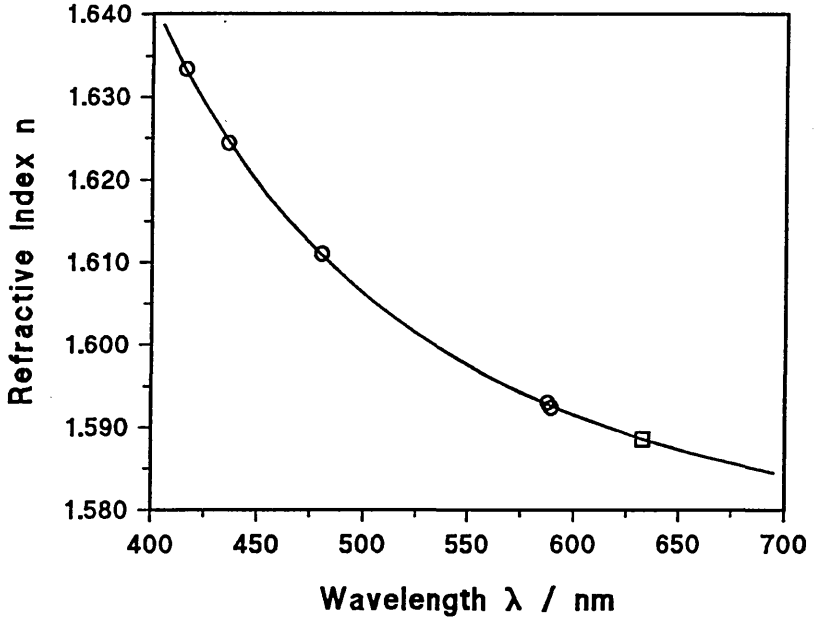

(e) Araldite epoxy resin

Figure 7.11 The refractive index variation with wavelength for each material. The graphs also show the fitted Cauchy equation along with the calculated refractive index at 632.8 nm. (a) polycarbonate, (b) polymethyl methacrylate, (c) polystyrene (d) polyvinyl chloride and (e) araldite epoxy resin.

Material	A	B	C / 10^8	n_{632}
Polycarbonate	1.5600	6326.07	8.78	1.5813
Polymethylmethacrylate	1.4897	-6368.77	23.58	1.4885
Polystyrene	1.5682	5705.76	9.51	1.5884
Polyvinylchloride	1.5222	3713.20	11.91	1.5389
Araldite epoxy resin	1.5699	4830.99	10.58	1.5886

Table 7.4 The exponents of the Cauchy equation determined for each material using the experimental values.

Material	Wavelength	Measured	Calculated	Difference
Polycarbonate	415.86	1.6262	1.6259	(0.0003)
	435.84	1.6172	1.6176	0.0004
	479.99	1.6043	1.6040	(0.0003)
	587.56	1.5856	1.5857	0.0001
	589.29	1.5856	1.5855	(0.0001)
Epoxy Resin	415.86	1.6334	1.6332	(0.0002)
	435.84	1.6244	1.6247	0.0003
	479.99	1.6110	1.6108	(0.0002)
	587.56	1.5930	1.5928	(0.0002)
	589.29	1.5924	1.5926	0.0002
Polymethyl methacrylate	415.86	1.5313	1.5317	0.0004
	435.84	1.5224	1.5215	(0.0009)
	479.99	1.5060	1.5065	0.0005
	587.56	1.4912	1.4910	(0.0002)
	589.29	1.4909	1.4909	0
Polystyrene	415.86	1.6331	1.6330	(0.0001)
	435.84	1.6244	1.6246	0.0002
	479.99	1.6110	1.6109	(0.0001)
	587.56	1.5927	1.5927	0
	589.29	1.5925	1.5925	0
Polyvinyl chloride	415.86	1.5838	1.5835	(0.0003)
	435.84	1.5741	1.5748	0.0007
	479.99	1.5611	1.5608	(0.0003)
	587.56	1.5430	1.5429	(0.0001)
	589.29	1.5426	1.5428	0.0002

Table 7.5 The experimentally determined refractive indices at each wavelength and those determined using Cauchys equation. The differences between the two are also given to illustrate the validity in the determinination of n_{632}.

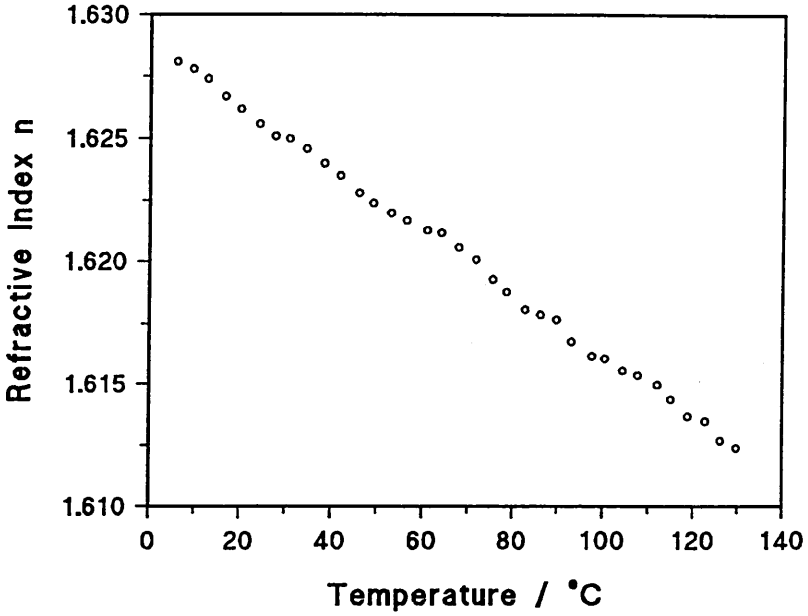

(a)

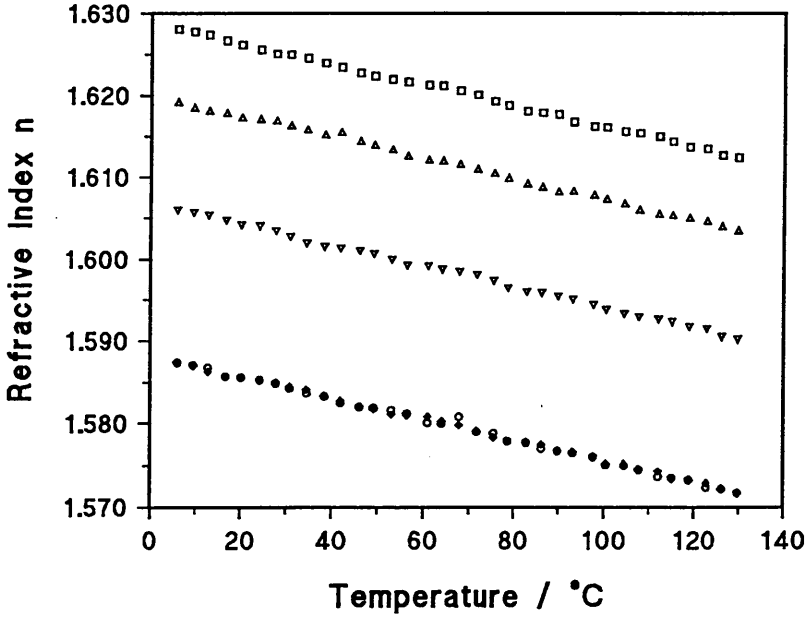

(b)

Figure 7.12 The thermal variation of refractive index for polycarbonate determined using several wavelength sources. (a) at 415.86 nm and (b) at 415.86, 435.84, 479.99, 587.56 and 589.29 nm.

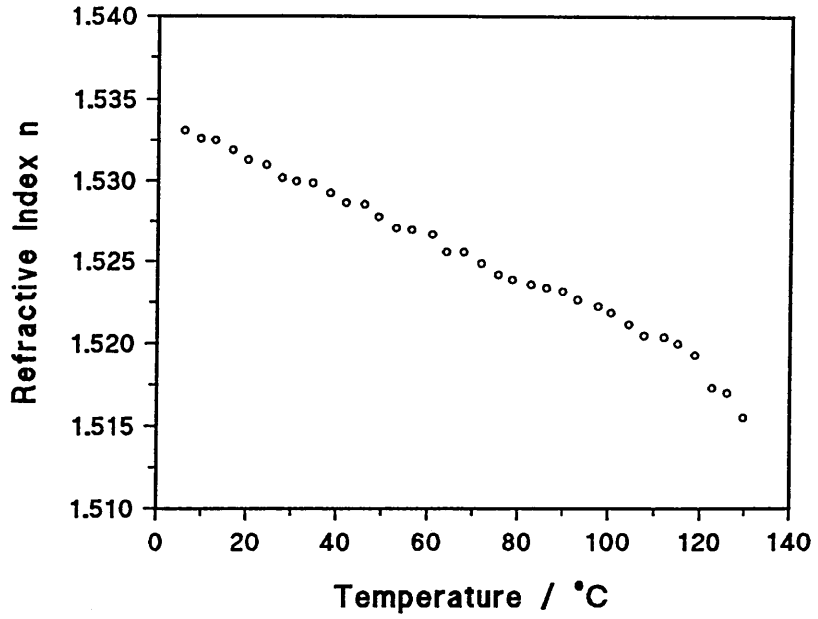

(a)

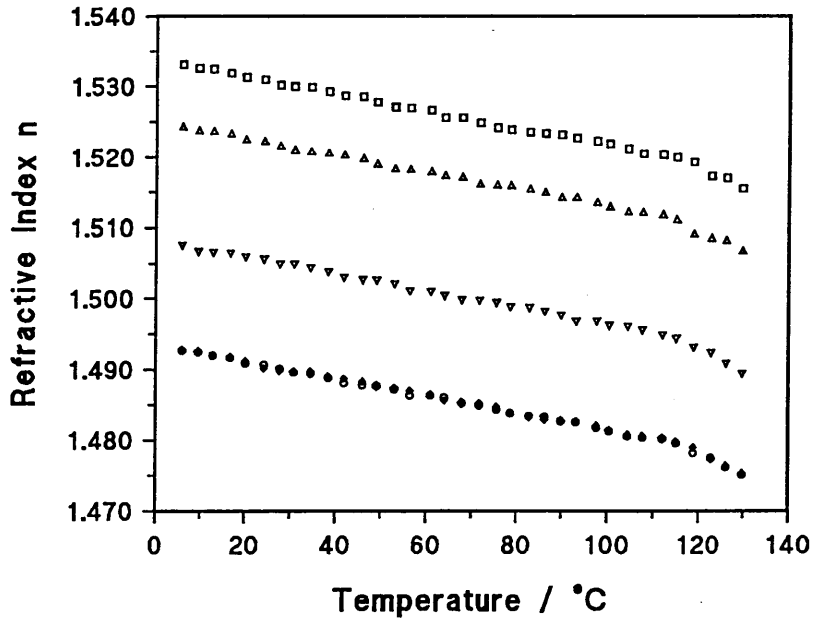

(b)

Figure 7.13 The thermal variation of refractive index for polymethyl methacrylate determined using several wavelength sources. (a) at 415.86 nm and (b) at 415.86, 435.84, 479.99, 587.56 and 589.29 nm.

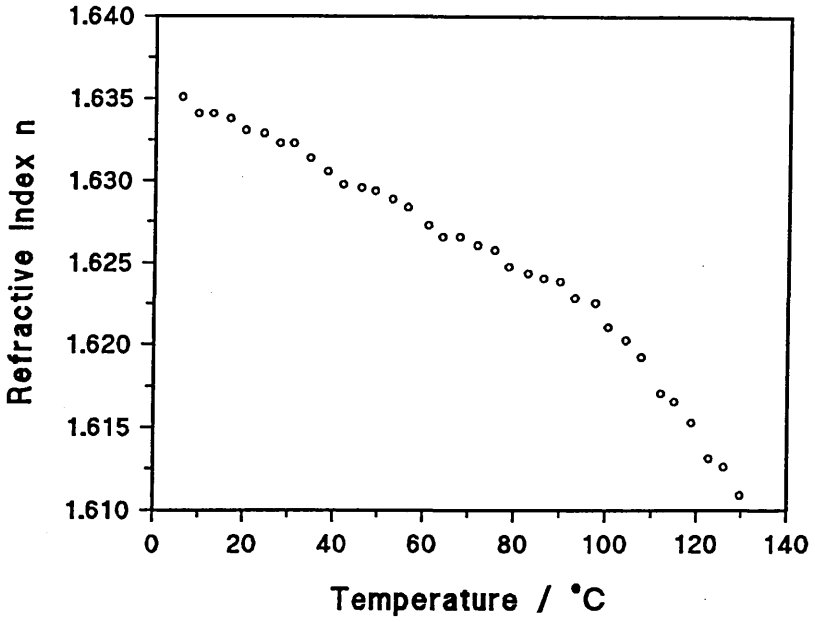

(a)

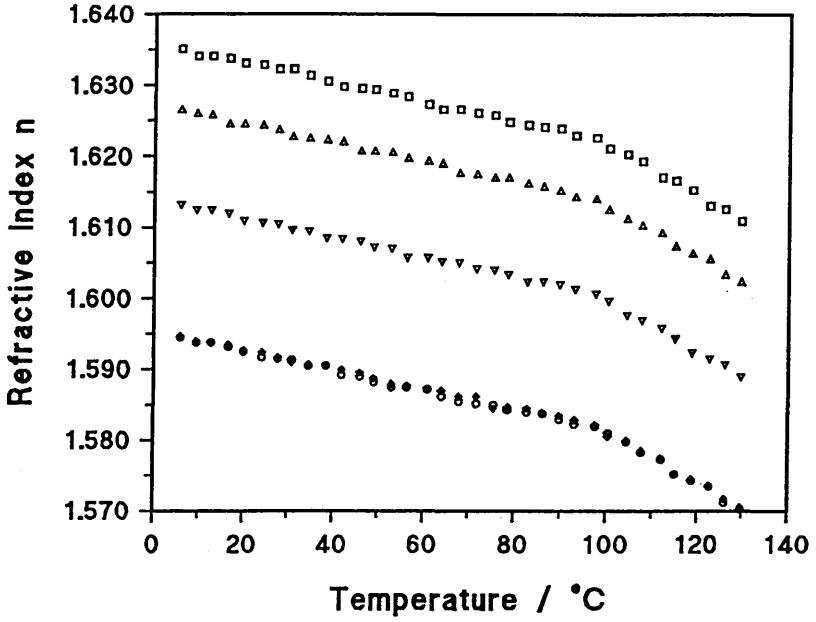

(b)

Figure 7.14 The thermal variation of refractive index for polystyrene determined using several wavelength sources. (a) at 415.86 nm and (b) at 415.86, 435.84, 479.99, 587.56 and 589.29 nm.

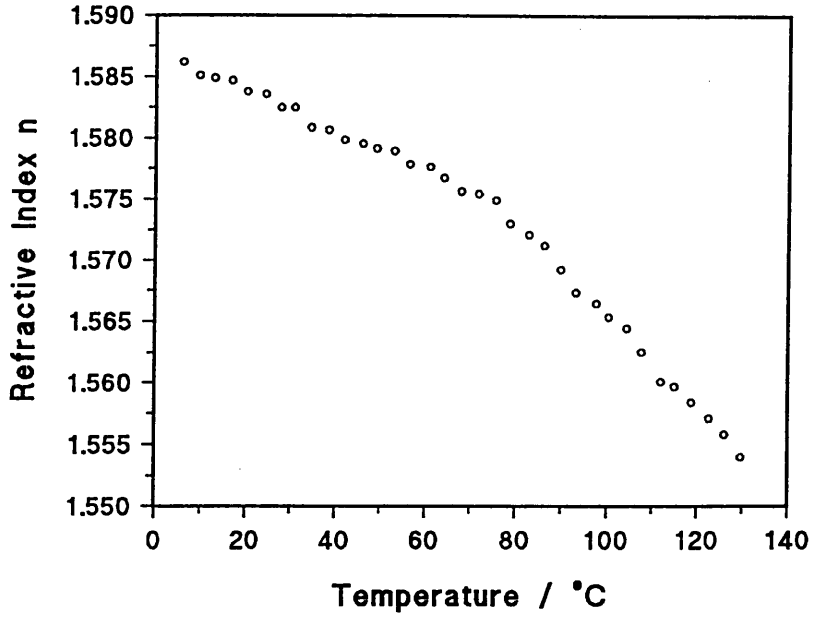

(a)

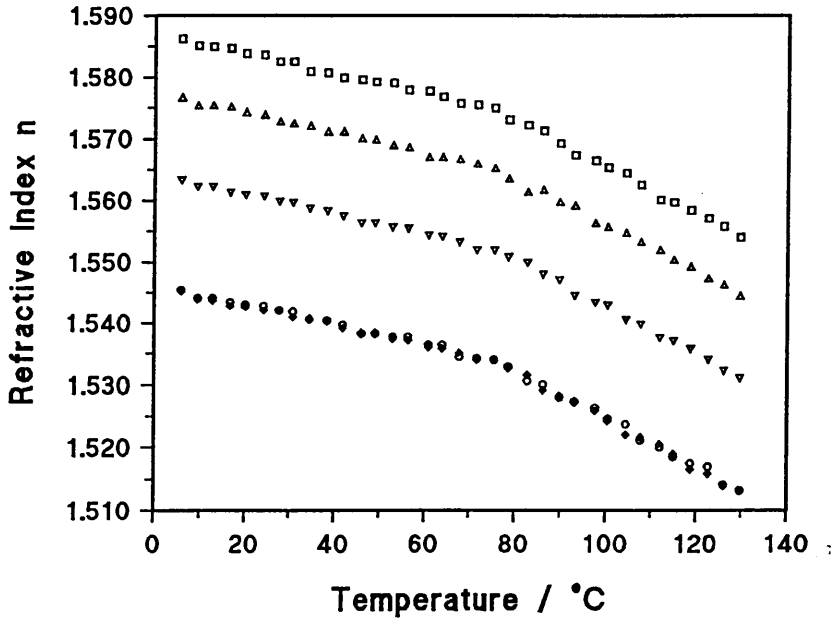

(b)

Figure 7.15 The thermal variation of refractive index for polyvinyl chloride determined using several wavelength sources. (a) at 415.86 nm and (b) at 415.86, 435.84, 479.99, 587.56 and 589.29 nm.

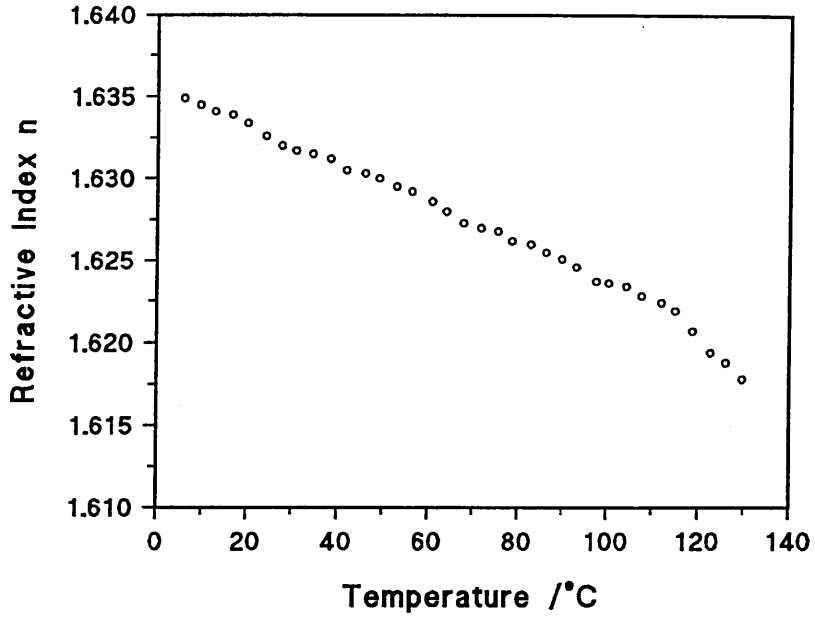

(a)

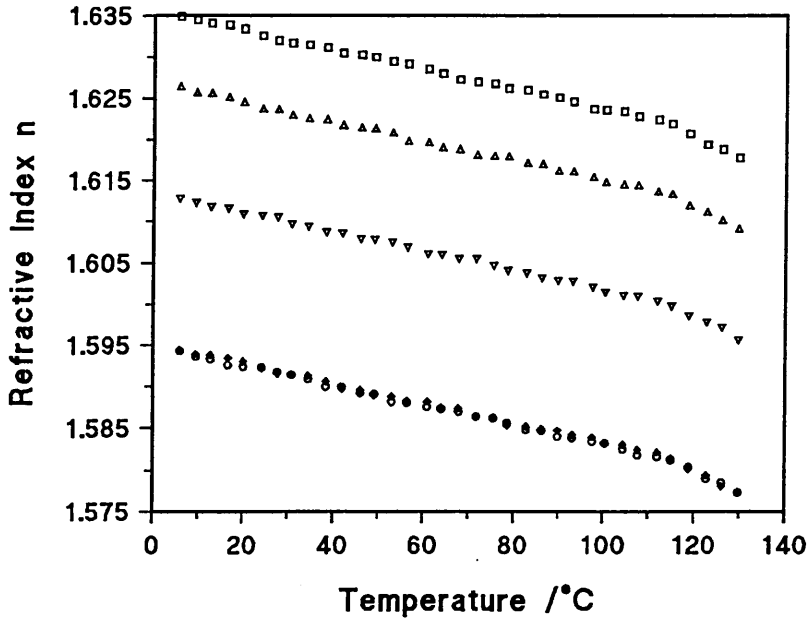

(b)

Figure 7.16 The thermal variation of refractive index for araldite epoxy resin determined using several wavelength sources. (a) at 415.86 nm and (b) at 415.86, 435.84, 479.99, 587.56 and 589.29 nm.

Material	Wavelength	dn/dT * 1x10^4	
		$<T_g$	$>T_g$
Polycarbonate	415.86	1.26	
	435.84	1.27	
	479.99	1.27	
	587.56	1.25	
	589.29	1.27	
Polymethylmethyacrylate	415.86	1.20	3.08
	435.84	1.19	2.66
	479.99	1.20	3.09
	587.56	1.21	2.87
	589.29	1.20	2.99
Polystyrene			
	415.86	1.38	3.57
	435.84	1.36	3.52
	479.99	1.37	3.60
	587.56	1.36	3.59
	589.29	1.38	3.68
Polyvinylchloride			
	415.86	1.60	3.80
	435.84	1.61	3.71
	479.99	1.62	3.88
	587.56	1.61	3.81
	589.29	1.62	3.84
Epoxy Resin	415.86	1.18	2.79
	435.84	1.19	2.73
	479.99	1.17	2.54
	587.56	1.18	2.64
	589.29	1.20	2.75

Table 7.6 The thermo-optic coefficient calculated by regression analysis on the experimental points either side of the glass transition temperature.

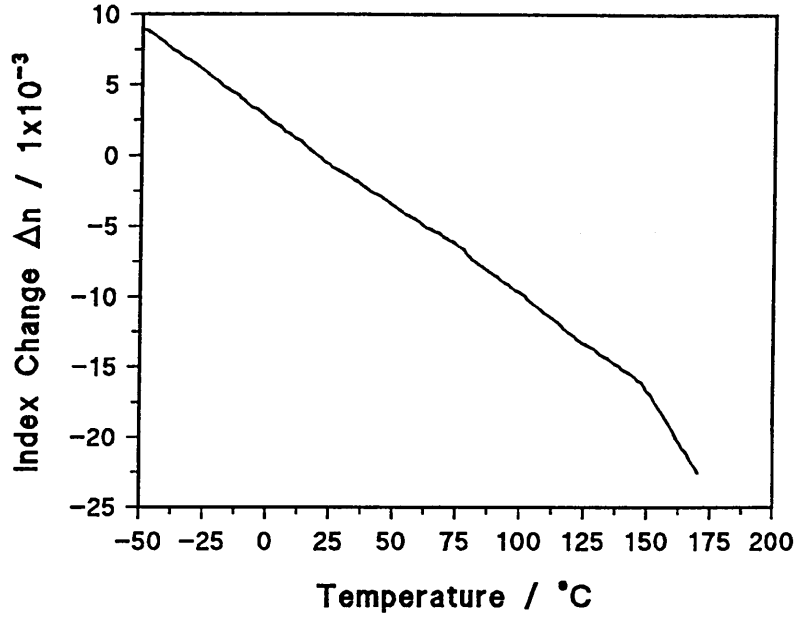

(a) Polycarbonate

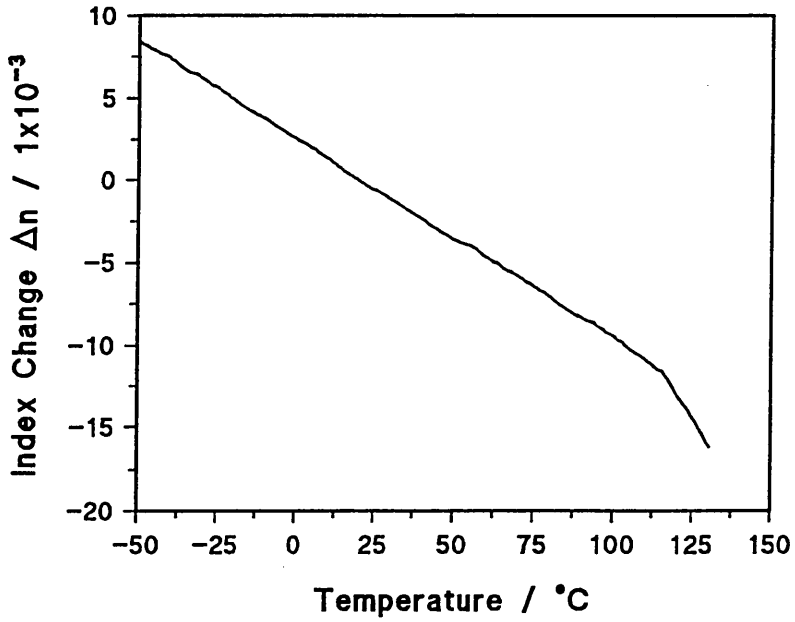

(b) Polymethyl methacrylate

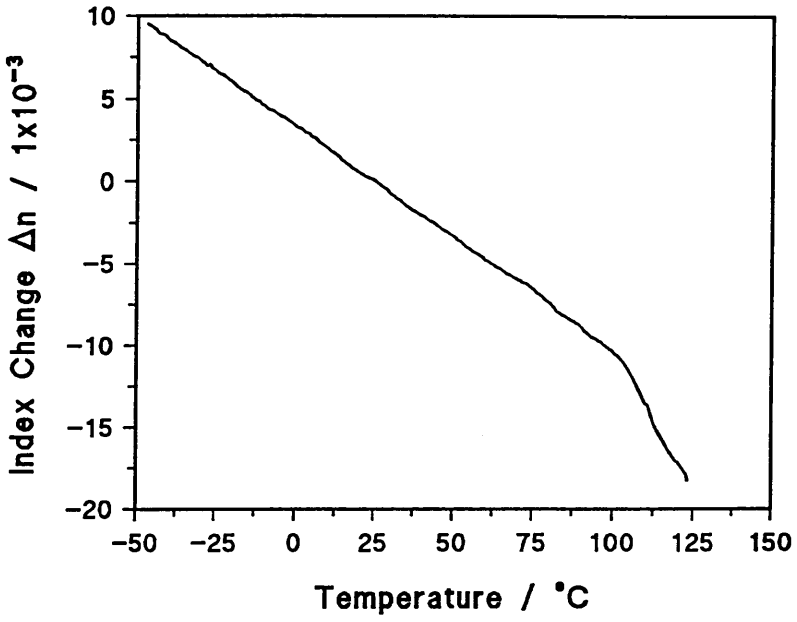

(c) Polystyrene

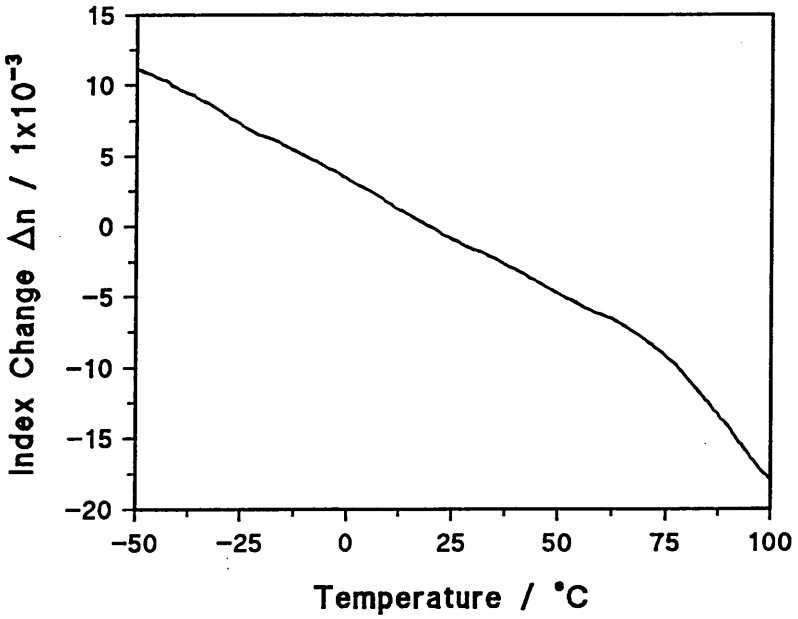

(d) Polyvinyl chloride

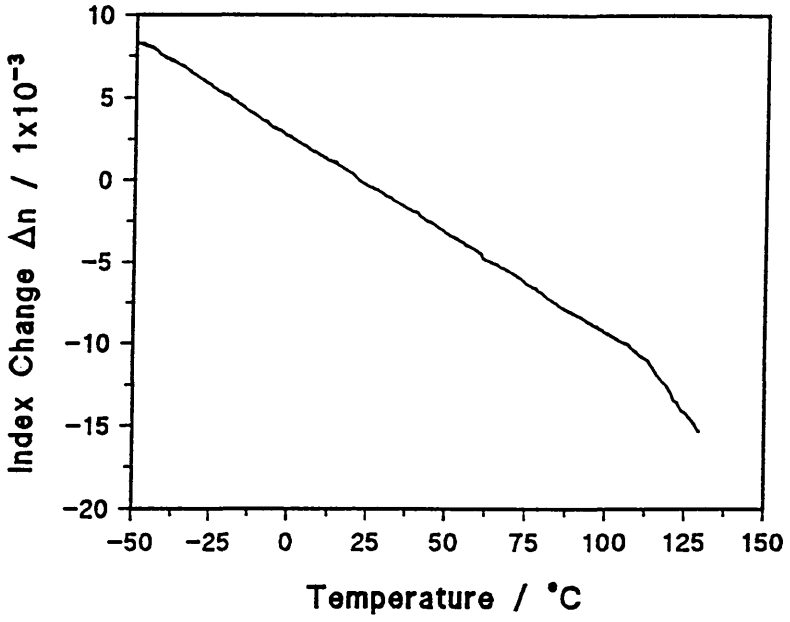

(e) Araldite epoxy resin

Figure 7.17 The change in refractive index with time determined using the Fizeau interferometer. (a) polycarbonate, (b) polymethyl methacrylate, (c) polystyrene (d) polyvinyl chloride and (e) araldite epoxy resin.

Material	dn/dT x $1x10^4$	
	$<T_g$	$>T_g$
Polycarbonate	1.28	3.03
Polymethyl methacrylate	1.20	3.02
Polstyrene	1.35	3.61
Polyvinyl chloride	1.63	3.83
Araldite epoxy resin	1.18	2.54

Table 7.7 The thermo-optic coefficient as determined using the Fizeau interferometer.

Material	dn/dT * $1x10^4$	
	$<T_g$	$>T_g$
Polycarbonate	1.26	2.97
Polymethyl methacrylate	1.21	3.06
Polstyrene	1.34	3.55
Polyvinyl chloride	1.62	3.63
Araldite epoxy resin	1.19	2.62

Table 7.8 The thermo-optic coefficient as determined using the Michelson interferometer.

Material	ρ / g.cm^{-3}	α / 1x10^{-5}	n_D
Polycarbonate	1.20	6.5	1.5856
Polymethyl methacrylate	1.18	8.0	1.4909
Polystyrene	1.05	8.0	1.5925
Polyvinyl chloride	1.39	8.0	1.5426
Araldite epoxy resin	1.23	6.2	1.5924

Table 7.9 Manufacturers property data for the materials investigated.

Material	-dn/dT / 1x10^{-4}	nα / 1x10^{-4}	-2.682$\alpha\rho$n^3/6 / 1x10^{-4}
Polycarbonate	1.26	1.03	1.16
Polymethyl methacrylate	1.20	1.19	1.18
Polystyrene	1.36	1.27	1.44
Polyvinyl chloride	1.61	1.28	1.30
Araldite epoxy resin	1.19	0.98	1.11

Table 7.10 The thermo-optic coefficient determined experimentally along with the predicted values using the two models.

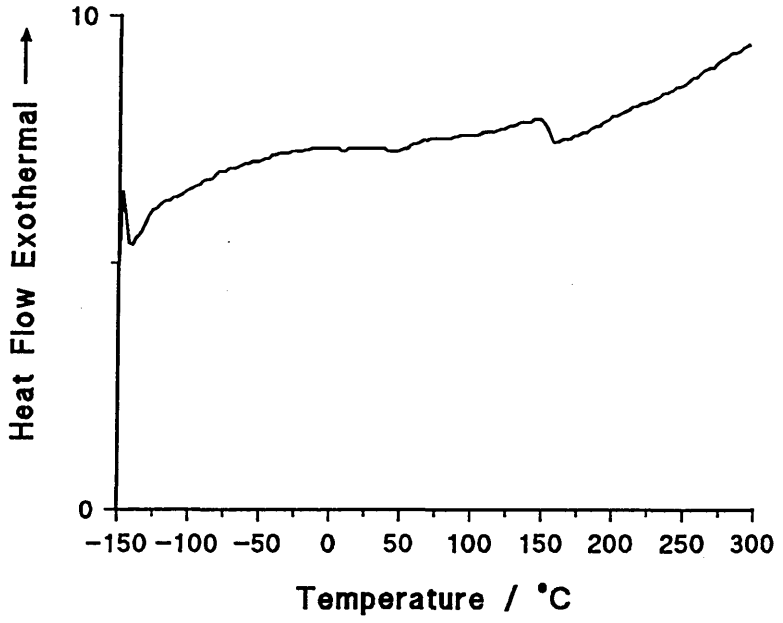

(a) Polycarbonate: -150 to 300°C

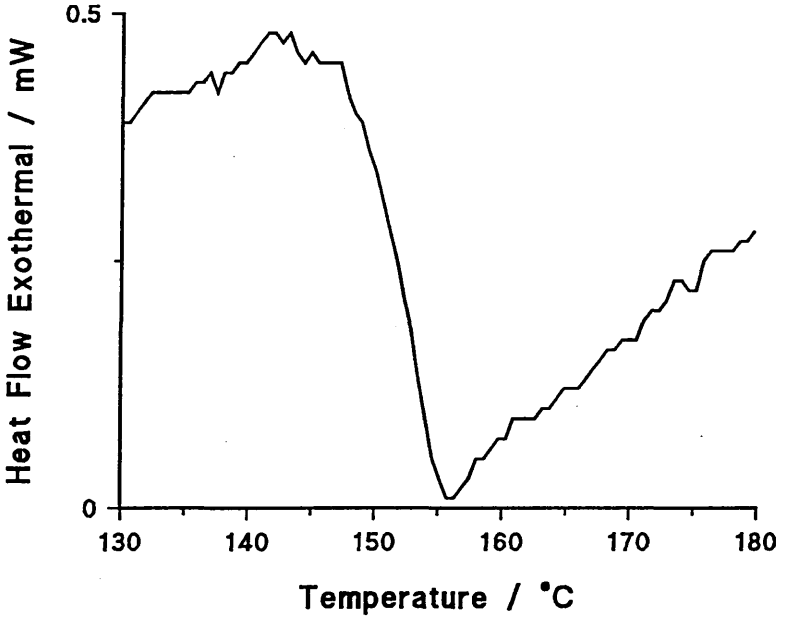

(b) Polycarbonate: 130 to 180°C.

Figure 7.18 The DSC trace for polycarbonate

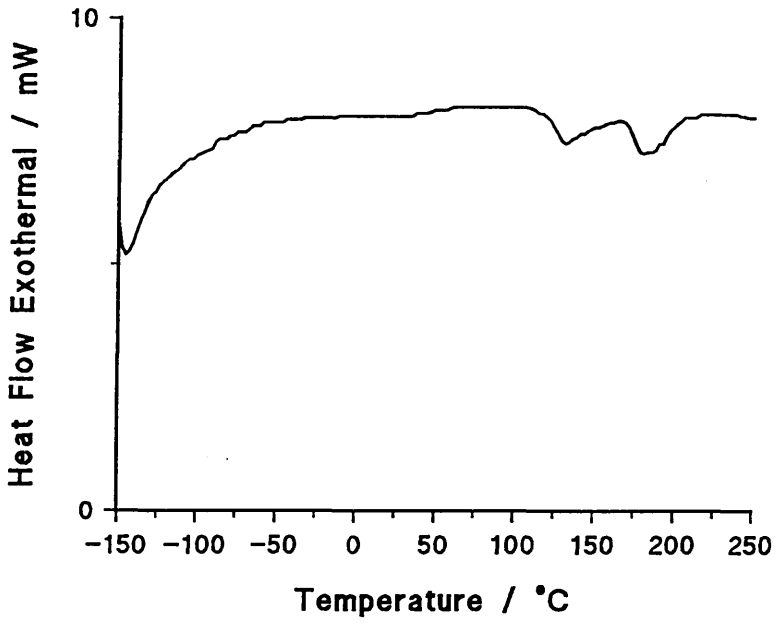

(a) Polymethyl methacrylate: -150 to 250°C

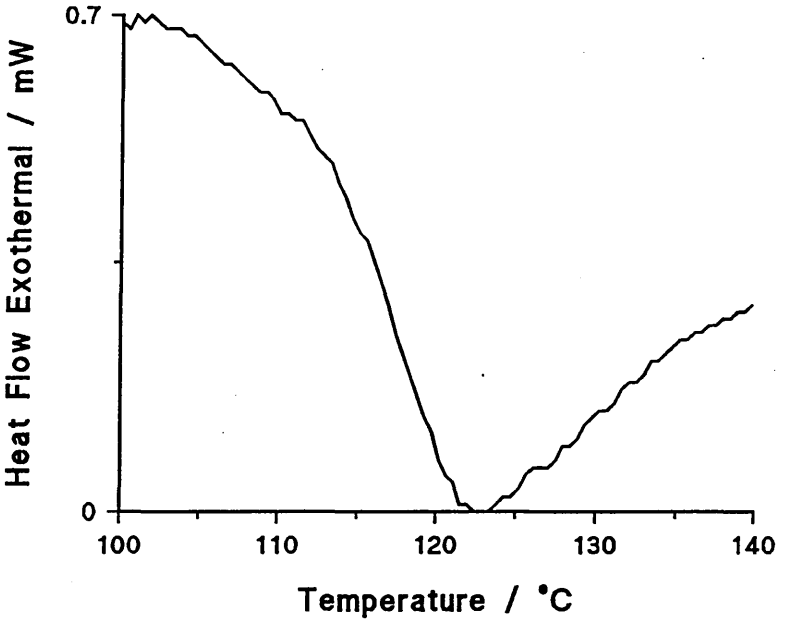

(b) Polymethy methacrylate: 100 - 140°C

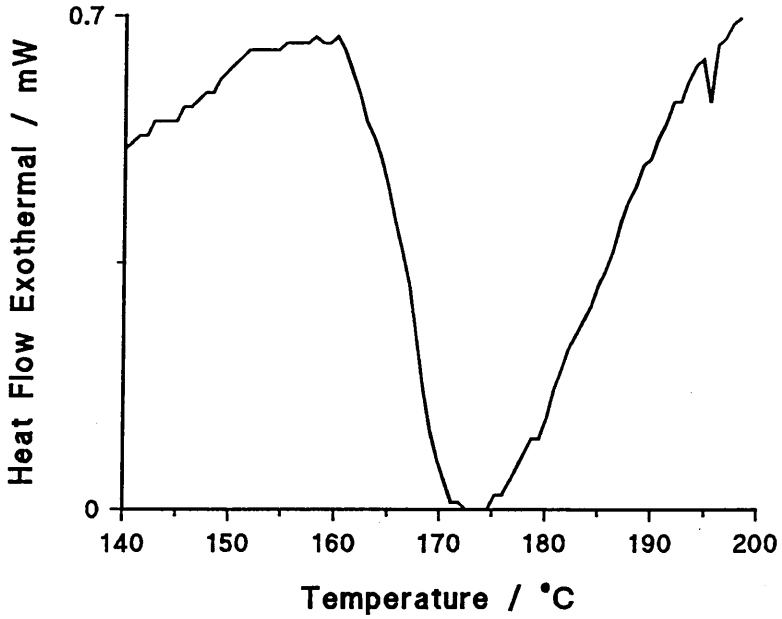

(c) Polymethyl methacrylate: 140 - 200°C

Figure 7.19 The DSC trace for polymethyl methacrylate

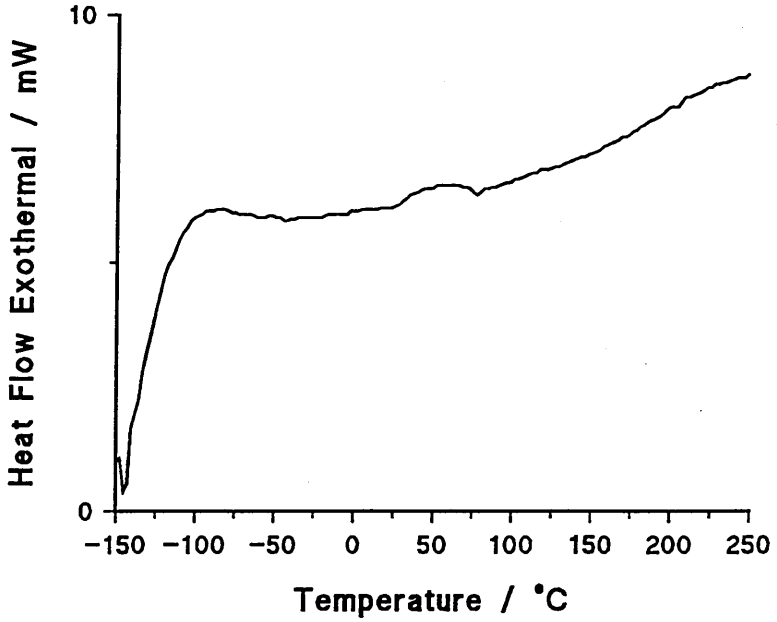

(a) Polystyrene: -150 to 250°C

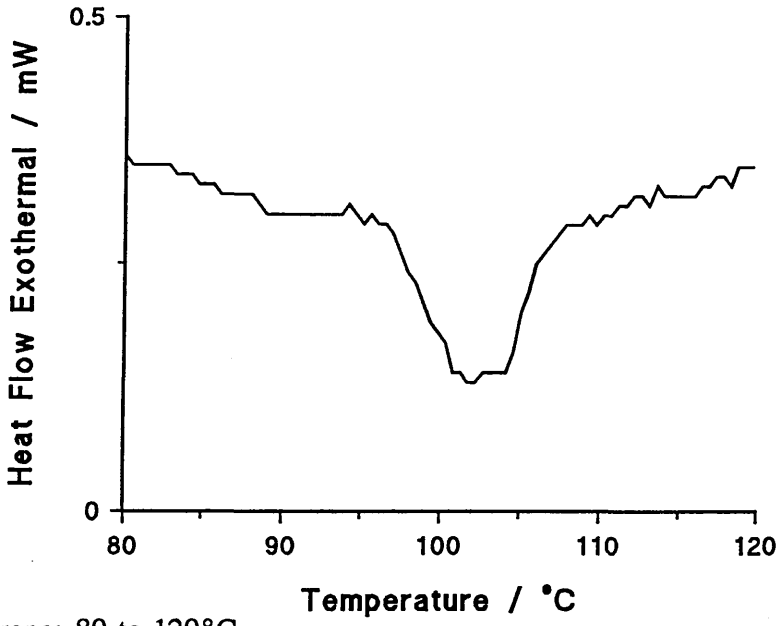

(b) Polystyrene: 80 to 120°C

Figure 7.20 The DSC trace obtained for polystyrene

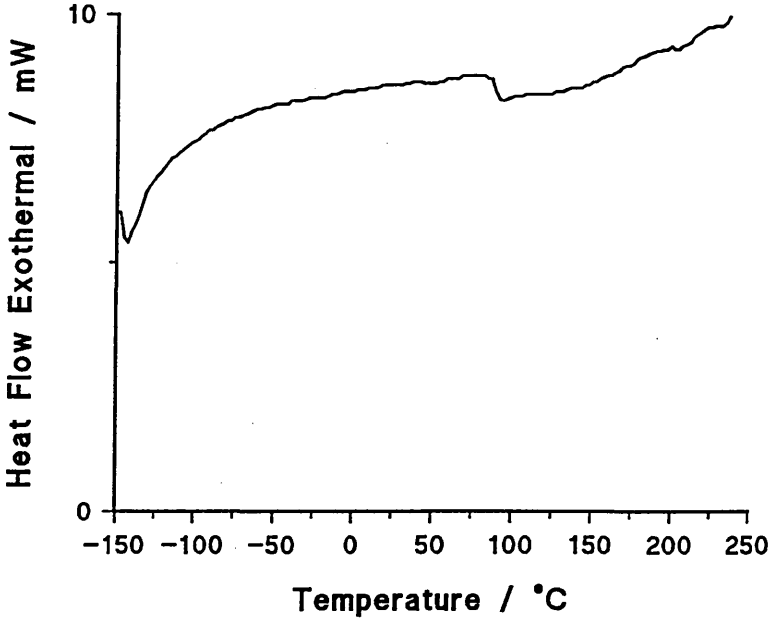

(a) Polyvinyl chloride: -150 to 250°C

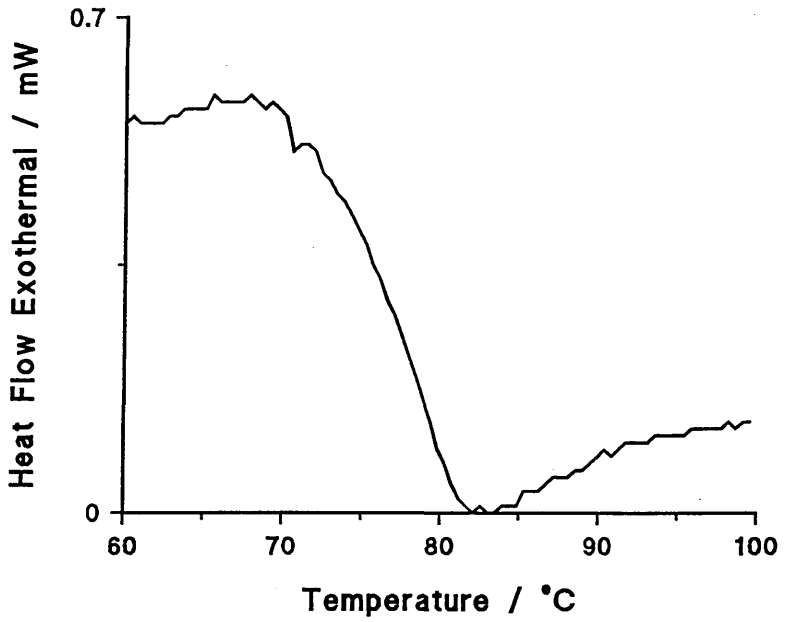

(b) Polyvinyl chloride: 60 to 100°C

Figure 7.21 The DSC trace obtained for polyvinyl chloride

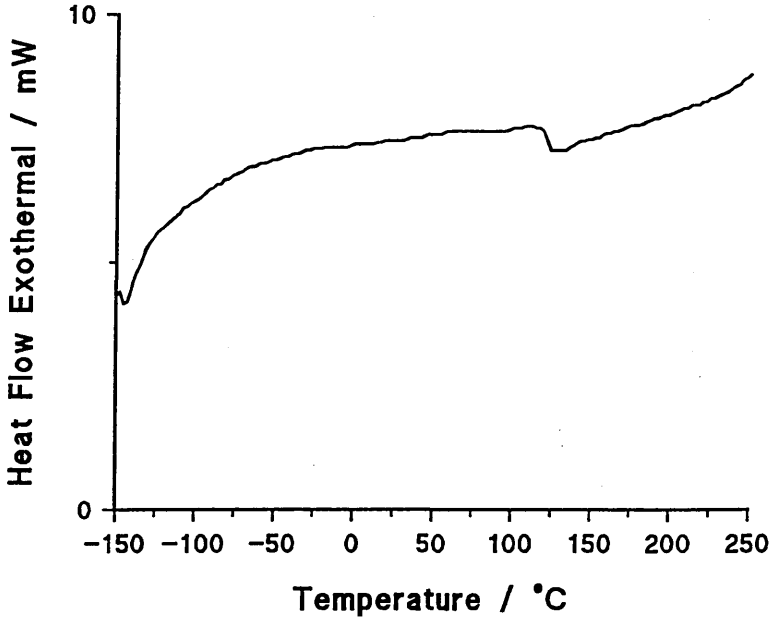

(a) Araldite epoxy resin: -150 to 250°C

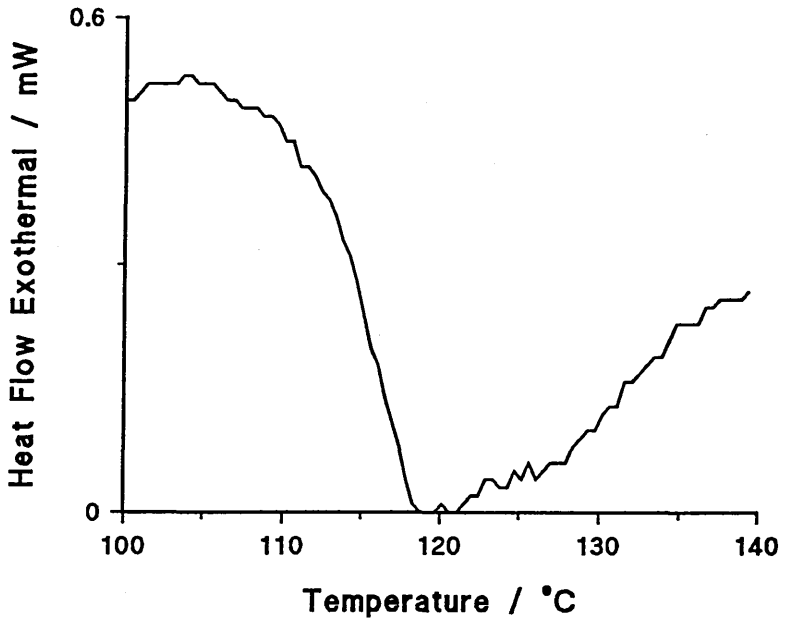

(b) Araldite epoxy resin: 100 to 140°C

Figure 7.22 The DSC trace obtained for polyvinyl chloride

Material	T_1 / °C	T_2 / °C	T_3 / °C	T Lit / °C
Polycarbonate	148.11	151.26	154.57	149
Polymethyl methacrylate	112.42	116.40	120.37	115
Polystyrene	97.59	98.09	98.59	100
Polyvinyl chloride	72.79	75.55	78.26	80
Araldite epoxy resin	111.02	114.84	118.48	115

Table 7.11 - The glass transition tempeatures determined using Differential Scanning Calorimetry. T_1 and T_3 represent the temperature at which the regression line and the inflection tangent of the 50% transition point intersect below and above the transition respectively; T_2 represents the 50% transition temperature. Also reported are the quoted literature values of the glass transition temperature.

Component	Reported Loss / dB	Measured Loss / dB
Beamsplitter	3	2.3
Coupler	<0.5	0.14
Collimator	0.6	0.2
Gradient Index Lens	0.5	0.2
Connector/fibre	1.0	11.6
Sensing element	0.5[1]	10

[1] Estimated value

Table 7.12 The losses measured for each component

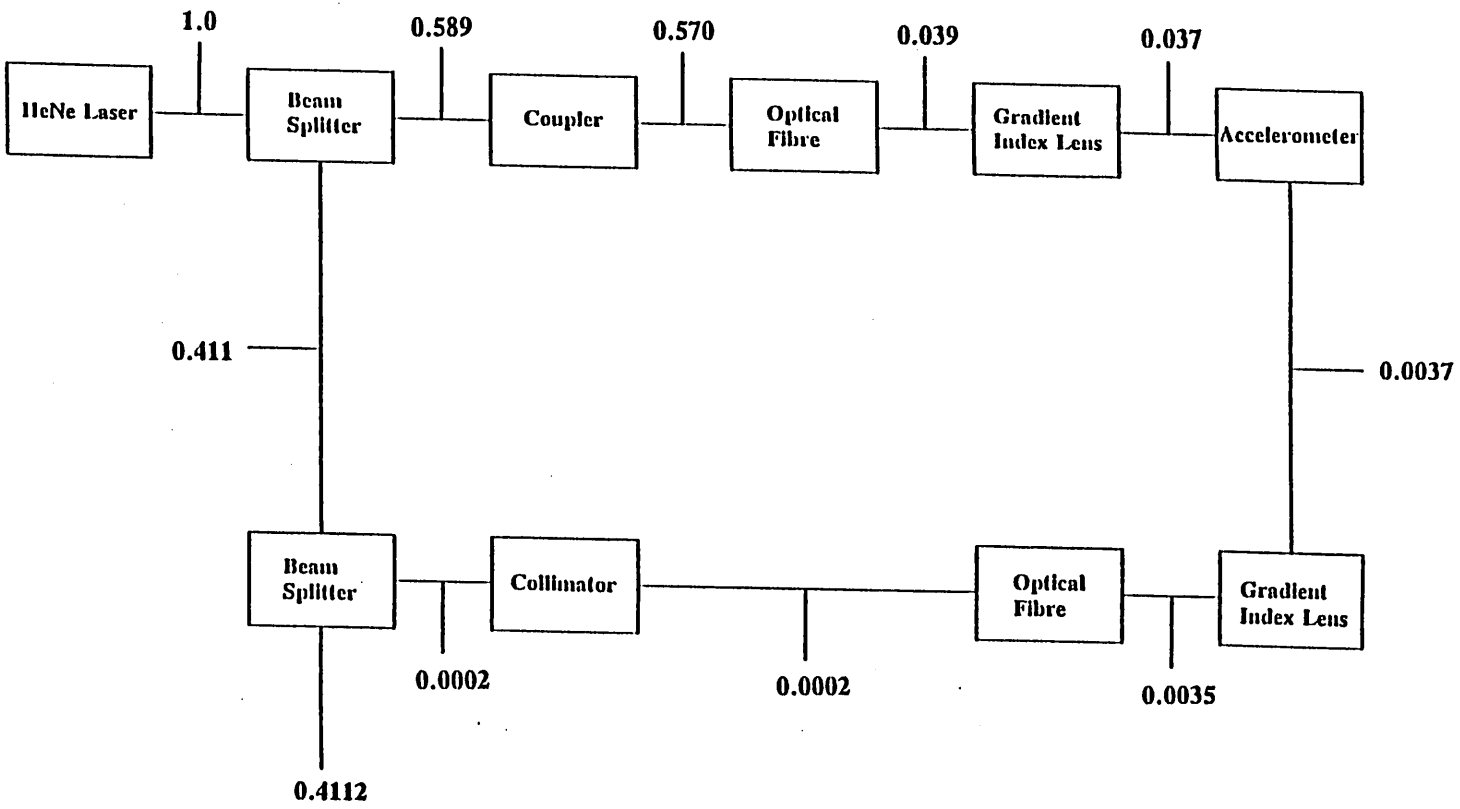

Figure 7.23 The optical circuit showing the components and the cumulative losses through the system

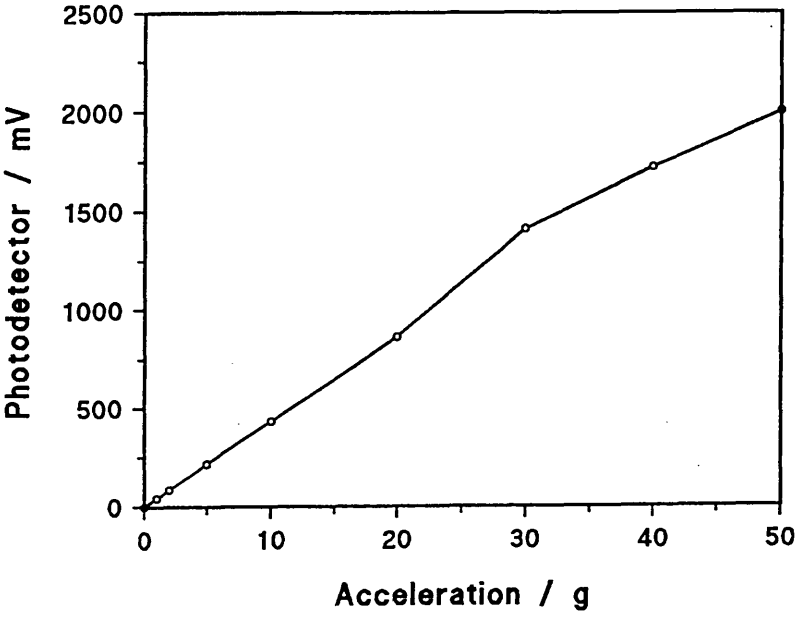

(a) Polycarbonate

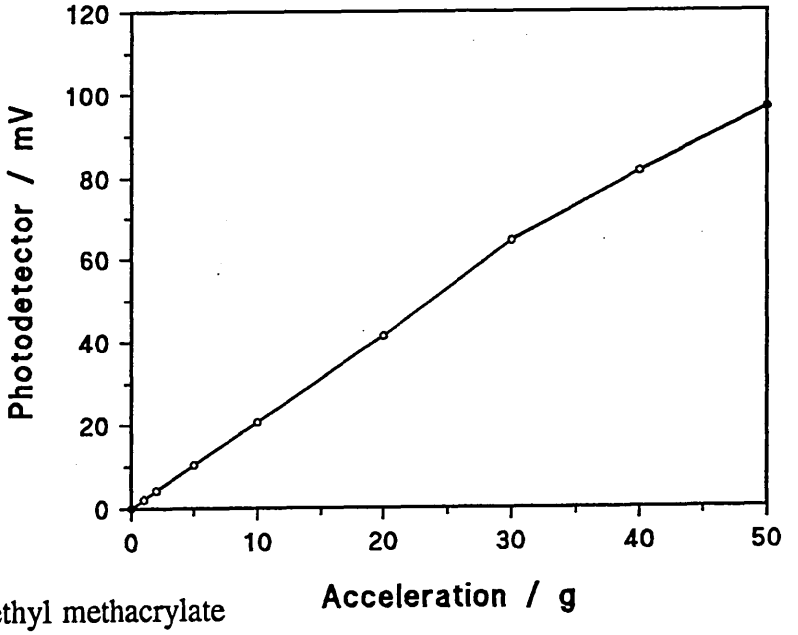

(b) Polymethyl methacrylate

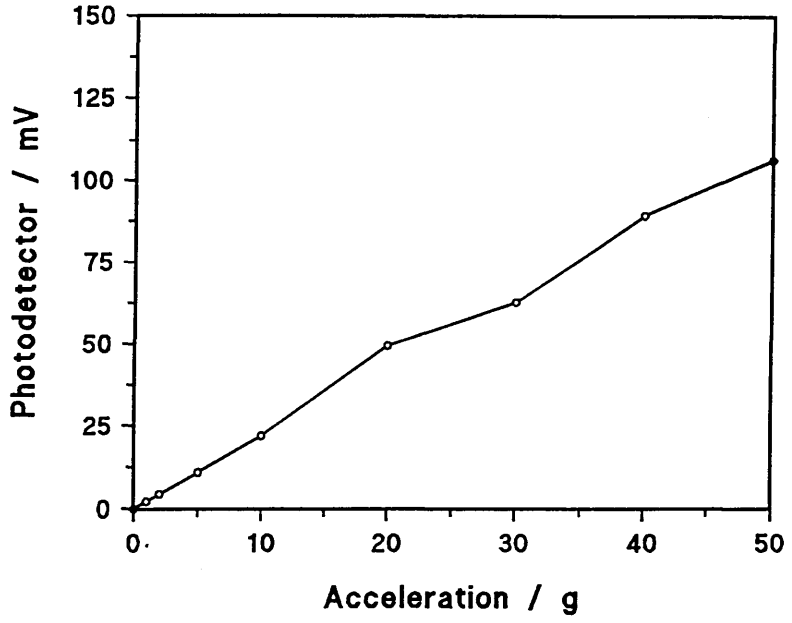

(c) Polyvinyl chloride

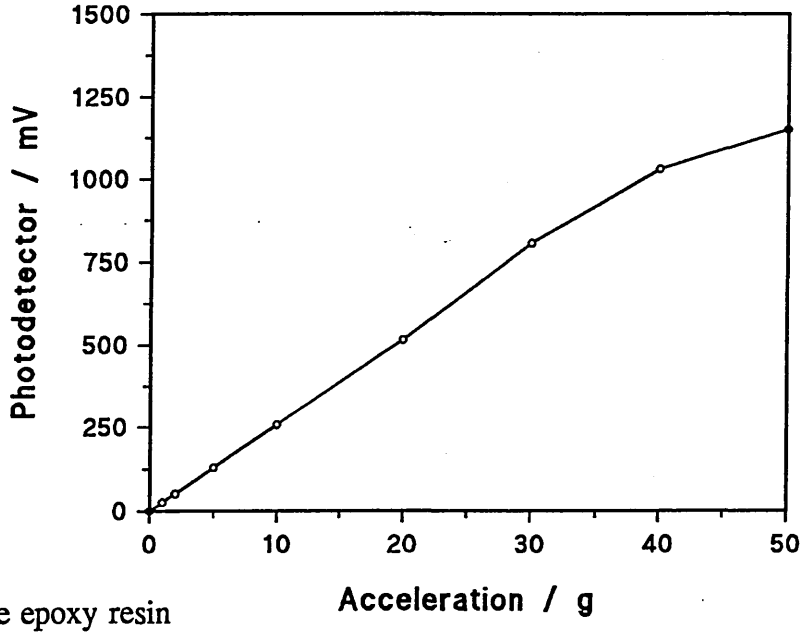

(d) Araldite epoxy resin

Figure 7.24 The photodetector response over the acceleration range tested for each material using intensity modulation. (a) Polycarbonate, (b) polymethyl methacrylate, (c) polyvinyl chloride and (d) araldite epoxy resin.

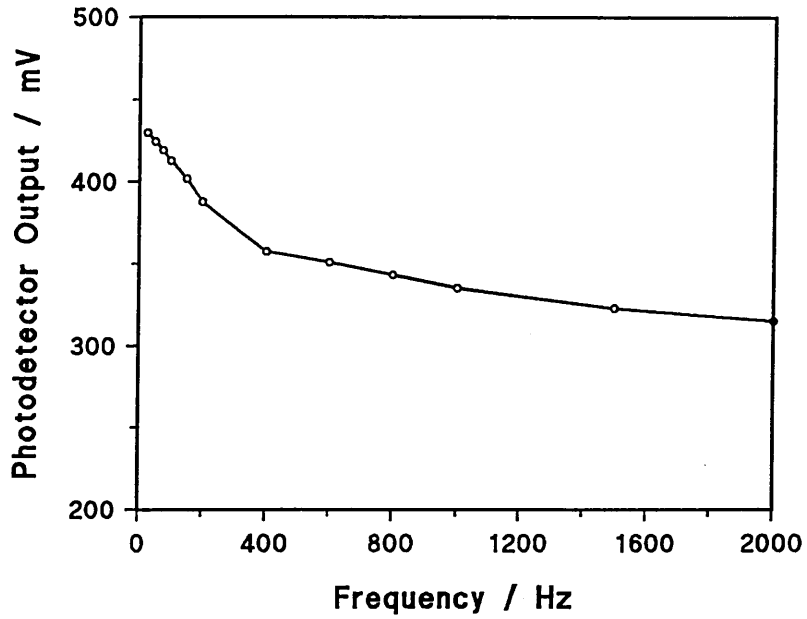

(a) Polycarbonate

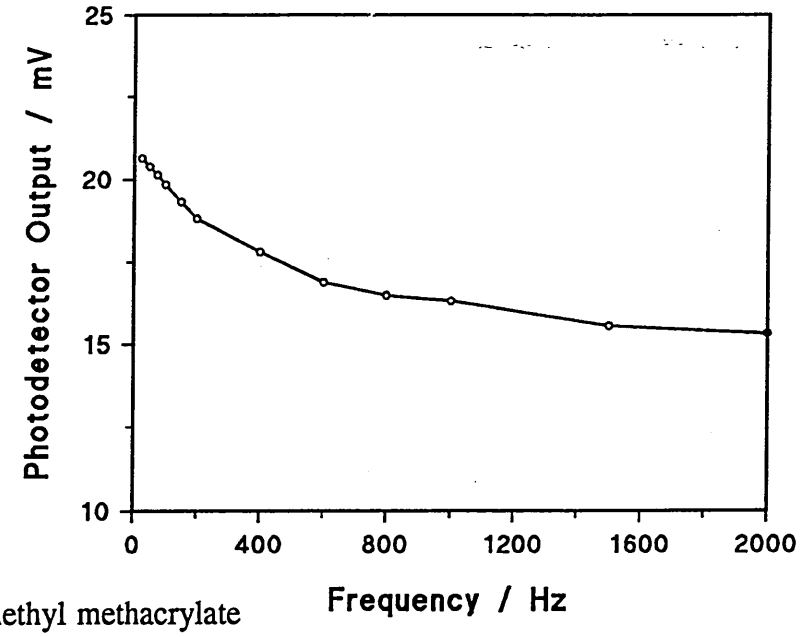

(b) Polymethyl methacrylate

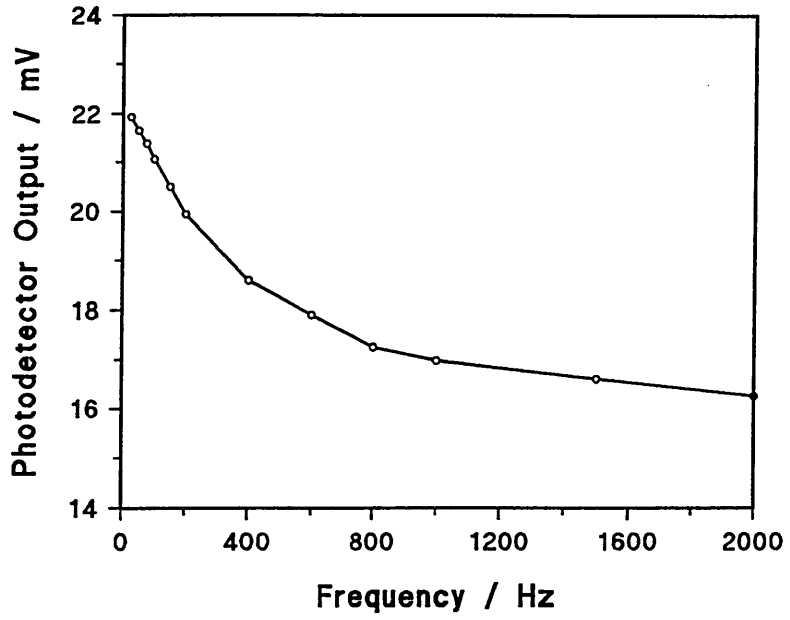

(c) Polyvinyl chloride

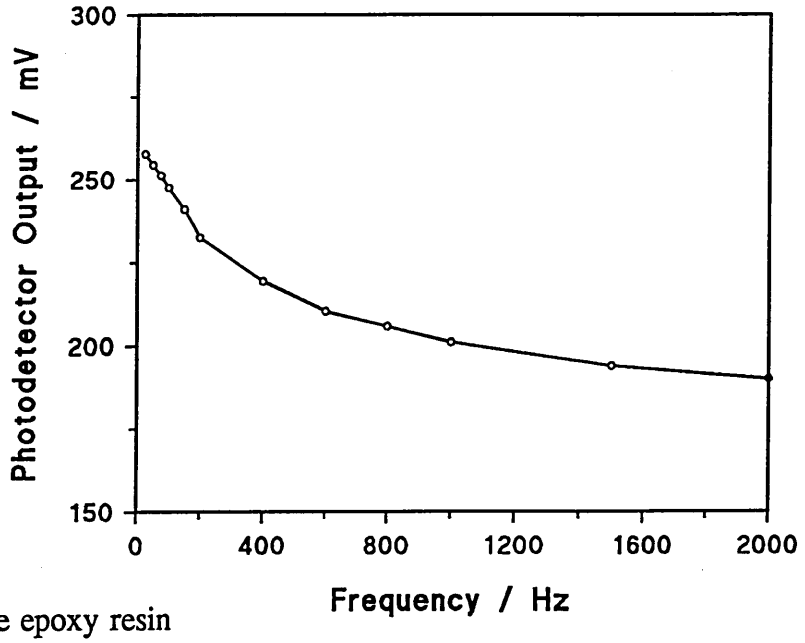

(d) Araldite epoxy resin

Figure 7.26 The photodetector response over the frequency range tested for each material using intensity modulation. (a) Polycarbonate, (b) polymethyl methacrylate, (c) polyvinyl chloride and (d) araldite epoxy resin.

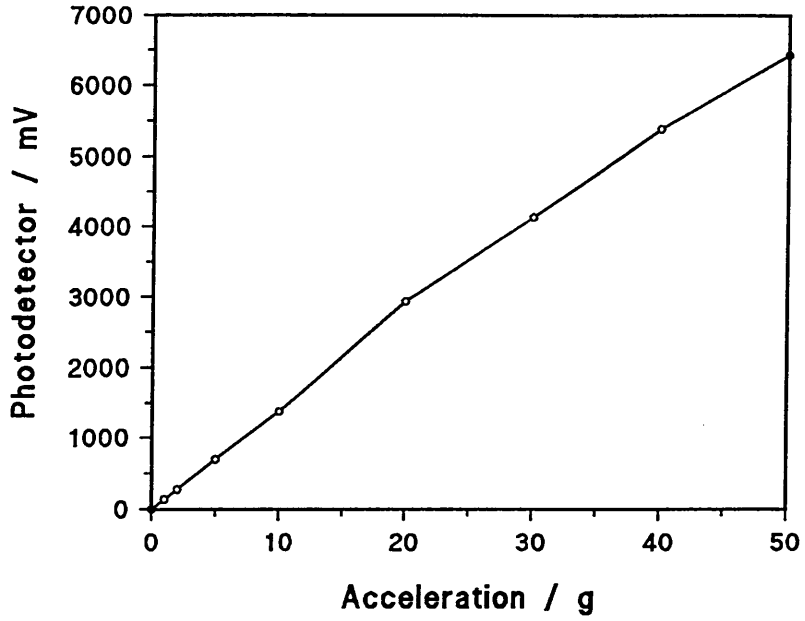

(a) Polycarbonate

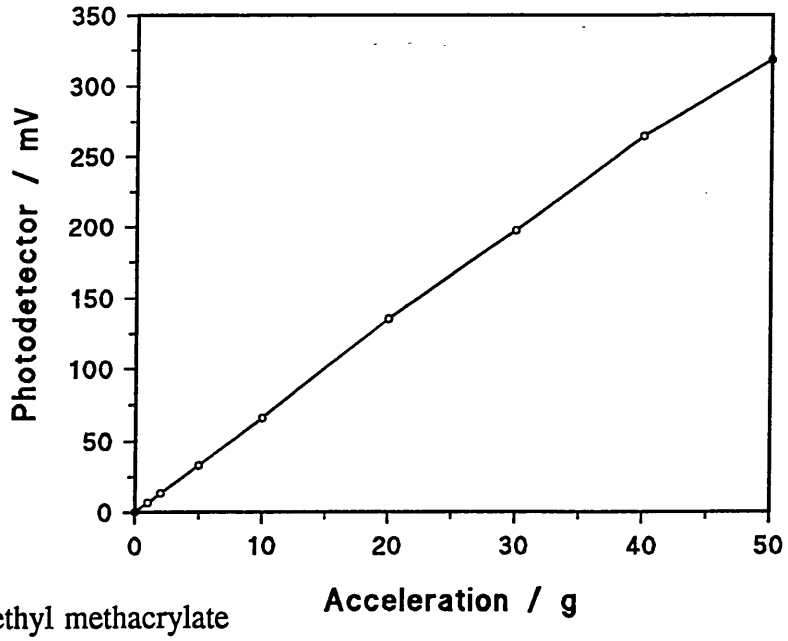

(b) Polymethyl methacrylate

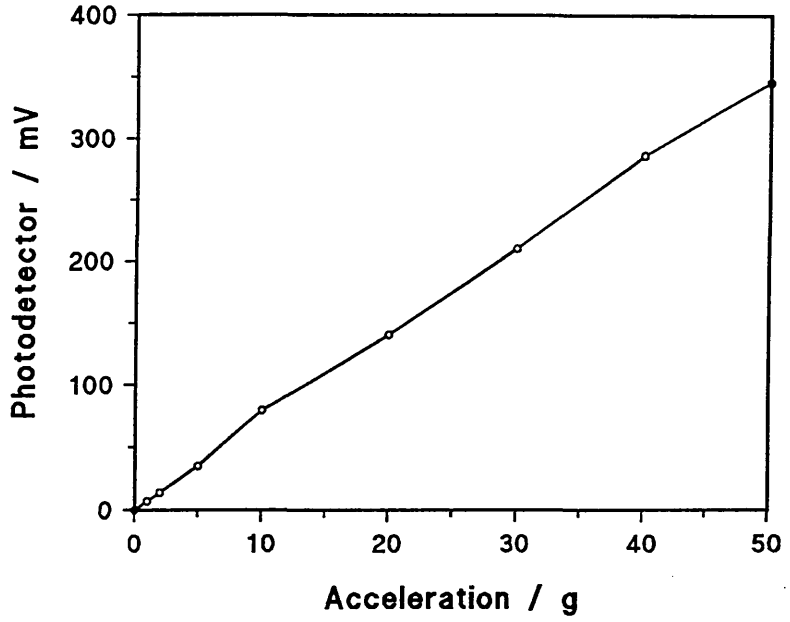

(c) Polyvinyl chloride

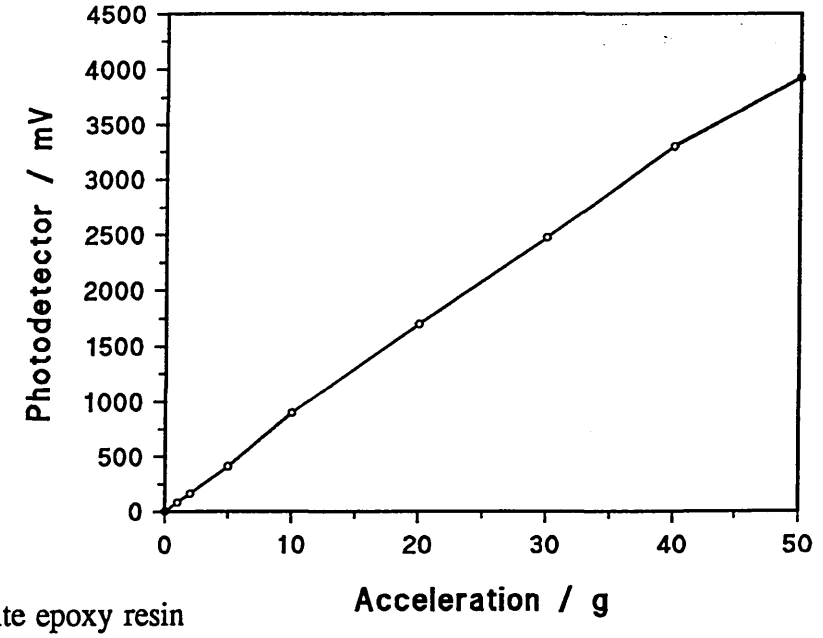

(d) Araldite epoxy resin

Figure 7.26 The photodetector response over the acceleration range tested for each material using phase modulation. (a) Polycarbonate, (b) polymethyl methacrylate, (c) polyvinyl chloride and (d) araldite epoxy resin.

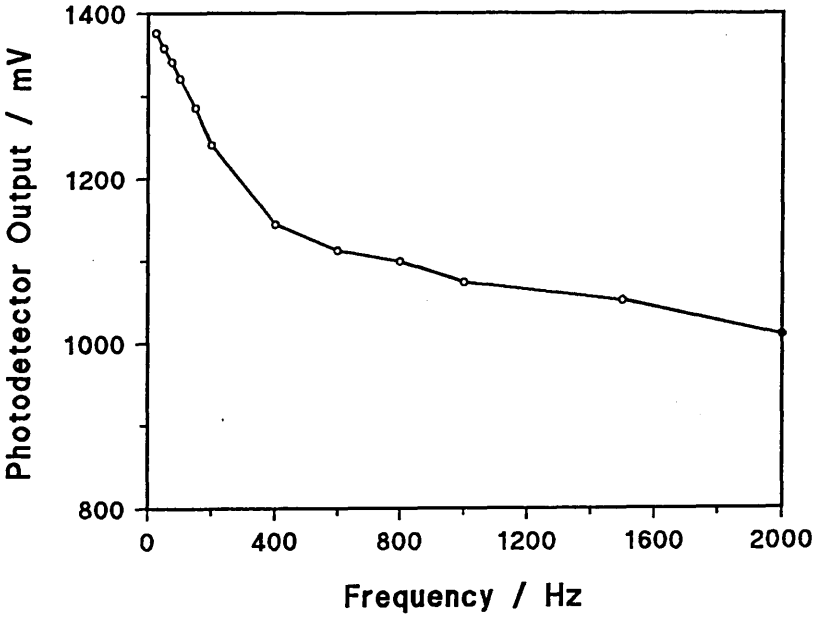

(a) Polycarbonate

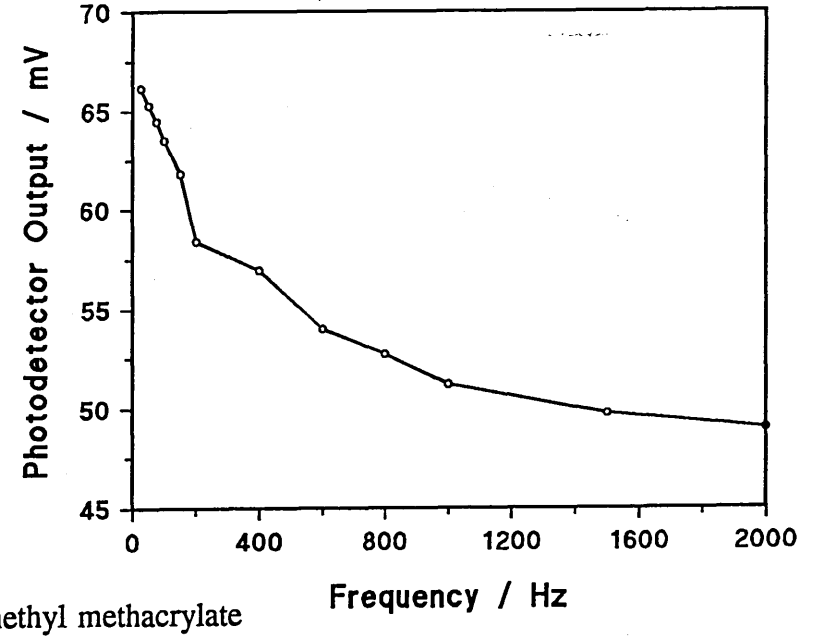

(b) Polymethyl methacrylate

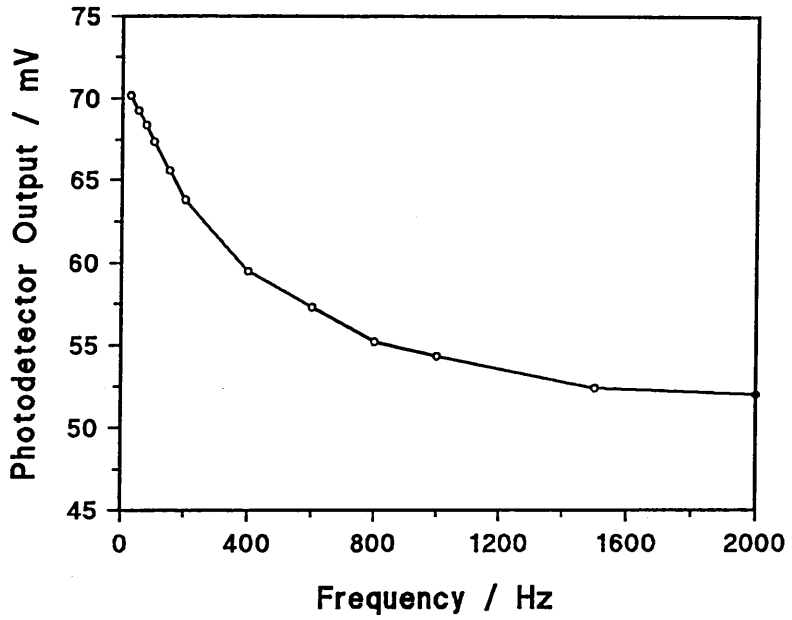

(c) Polyvinyl chloride

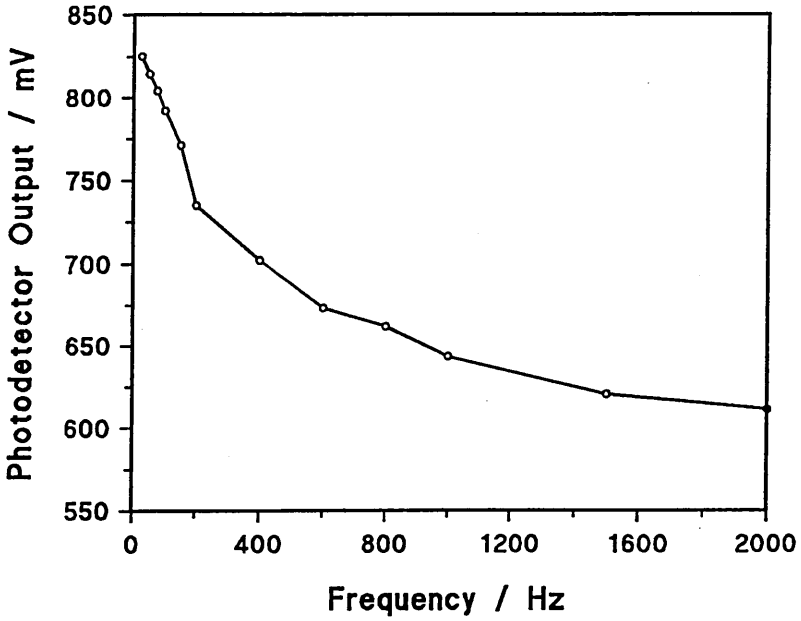

(d) Araldite epoxy resin

Figure 7.27 The photodetector response over the frequency range tested for each material using phase modulation. (a) Polycarbonate, (b) polymethyl methacrylate, (c) polyvinyl chloride and (d) araldite epoxy resin.

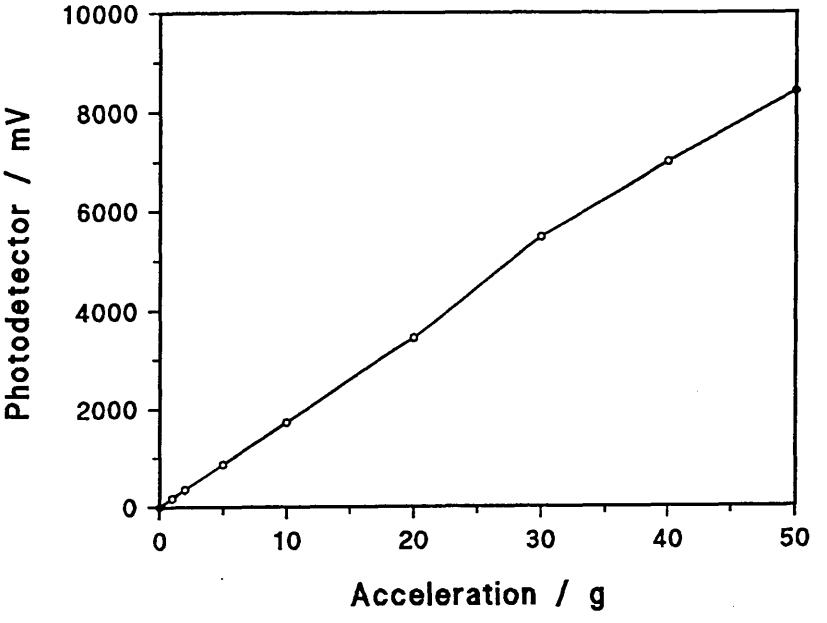

(a) Polycarbonate

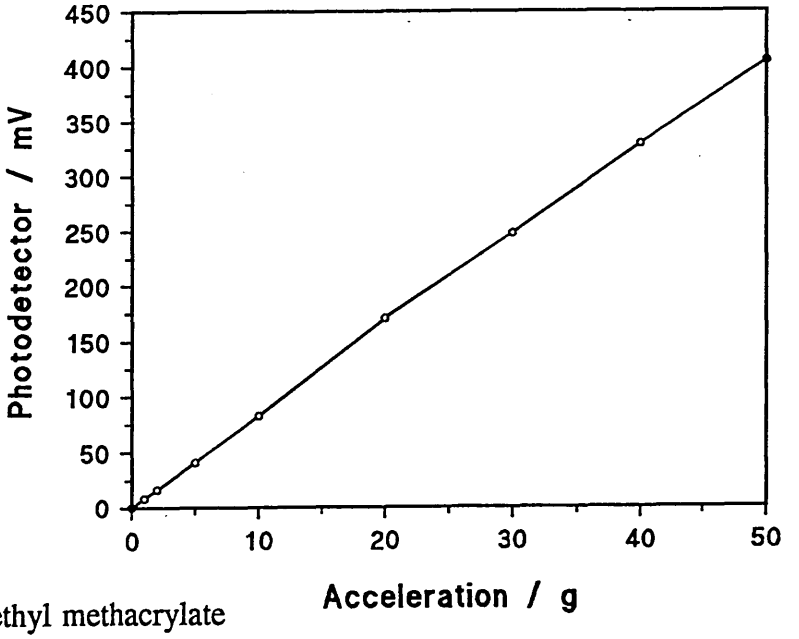

(b) Polymethyl methacrylate

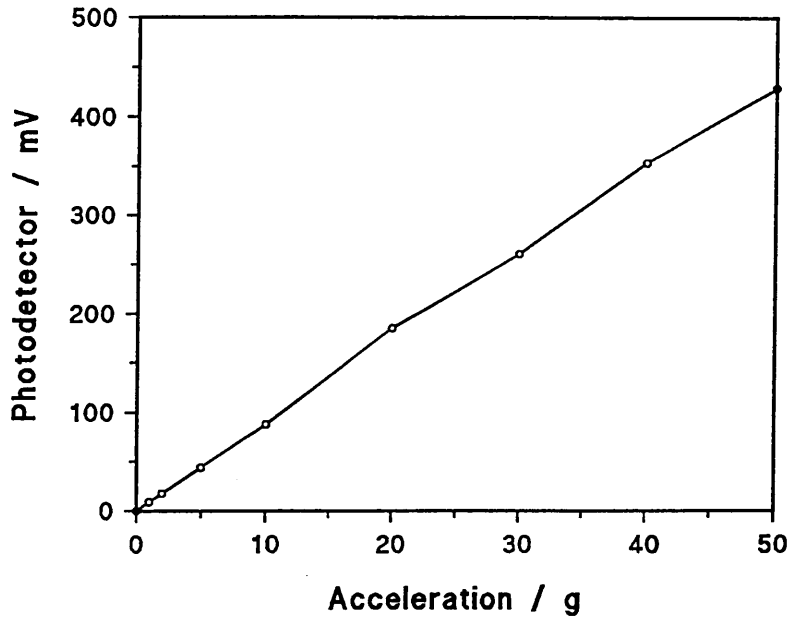

(c) Polyvinyl chloride

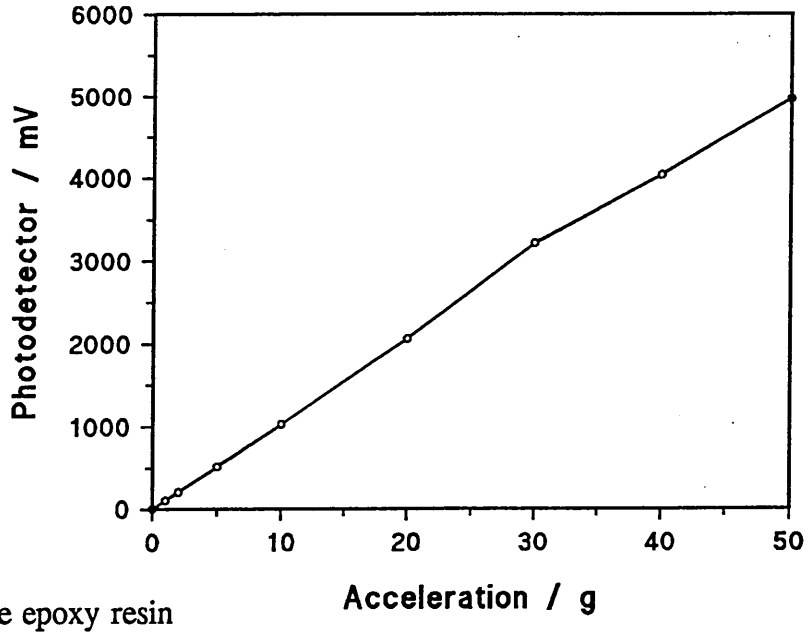

(d) Araldite epoxy resin

Figure 7.28 The photodetector response over the acceleration range tested for each material using polarisation modulation. (a) Polycarbonate, (b) polymethyl methacrylate, (c) polyvinyl chloride and (d) araldite epoxy resin.

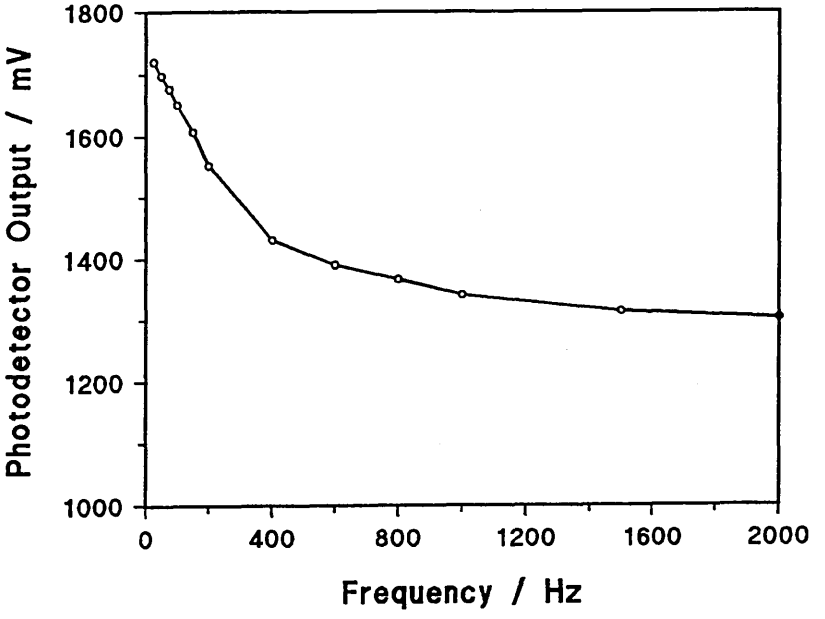

(a) Polycarbonate

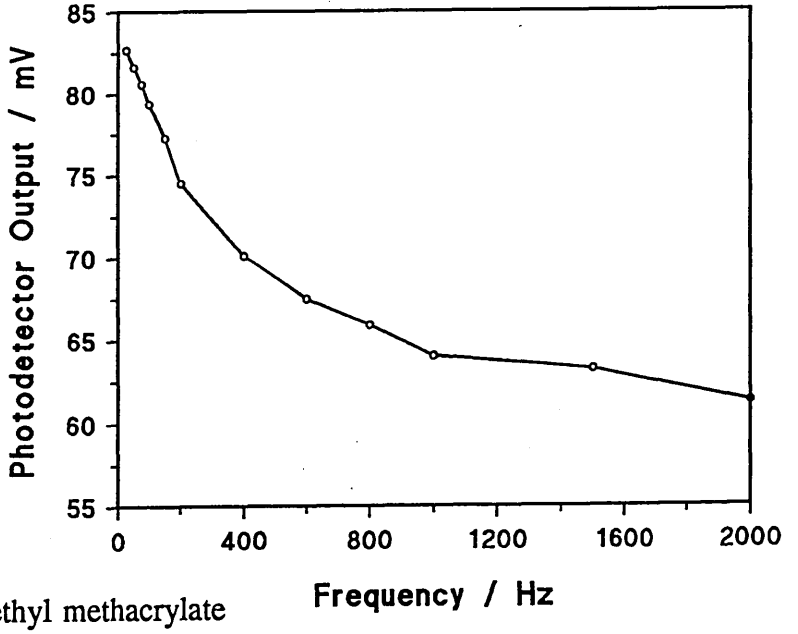

(b) Polymethyl methacrylate

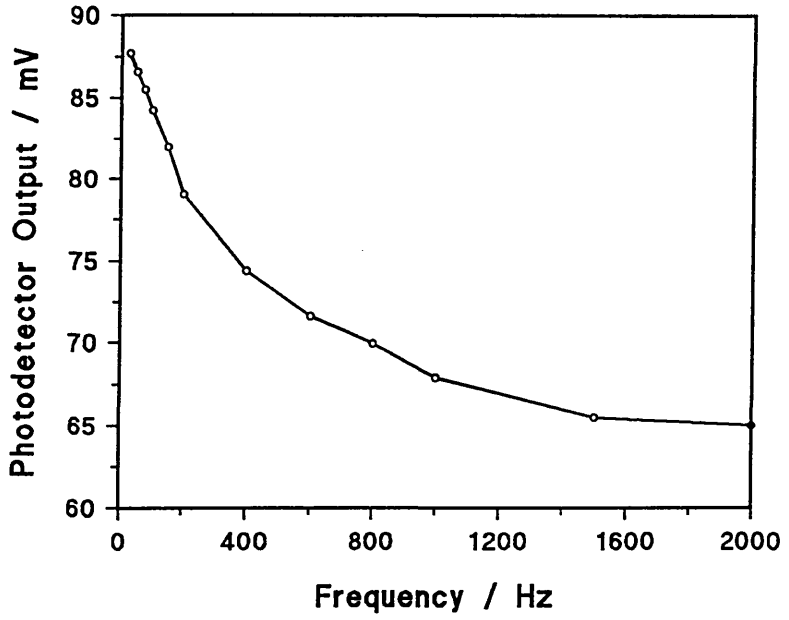

(c) Polyvinyl chloride

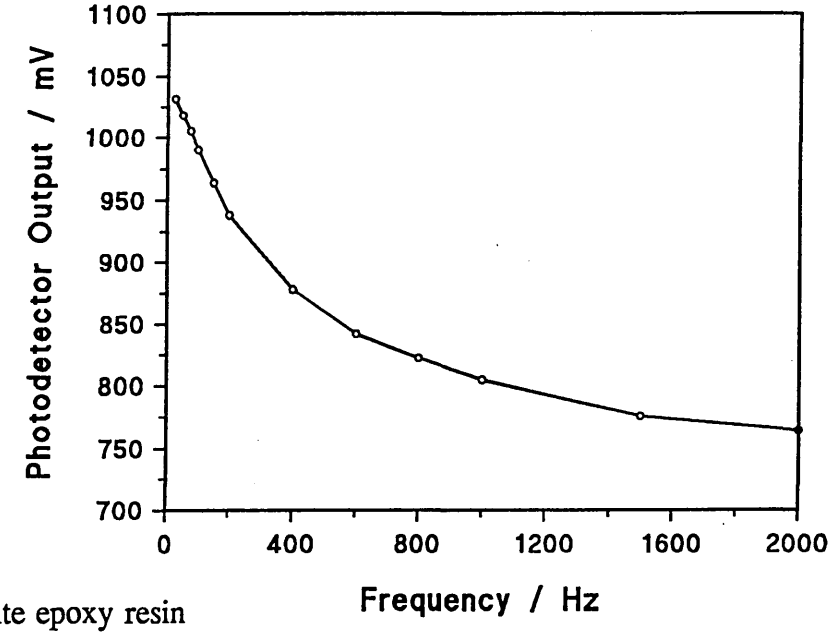

(d) Araldite epoxy resin

Figure 7.29 The photodetector response over the frequency range tested for each material using polarisation modulation. (a) Polycarbonate, (b) polymethyl methacrylate, (c) polyvinyl chloride and (d) araldite epoxy resin.

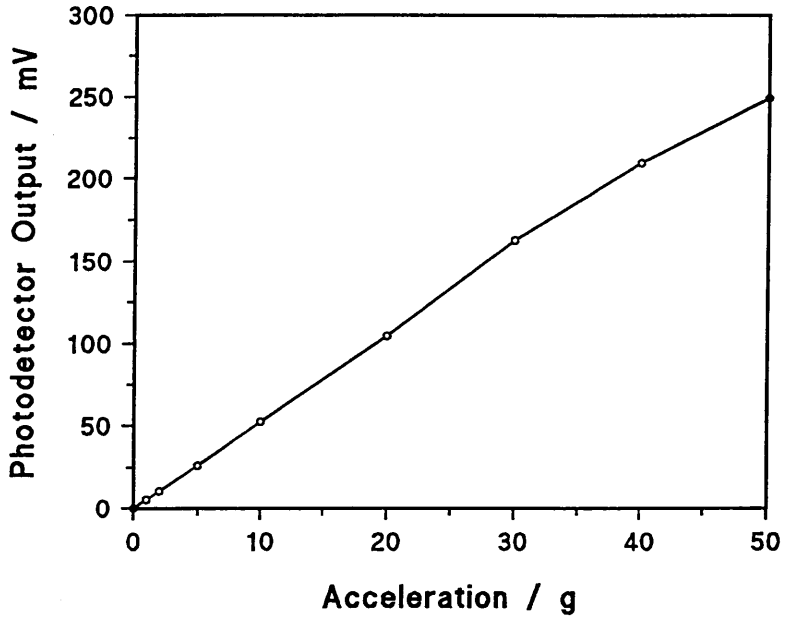

(a)

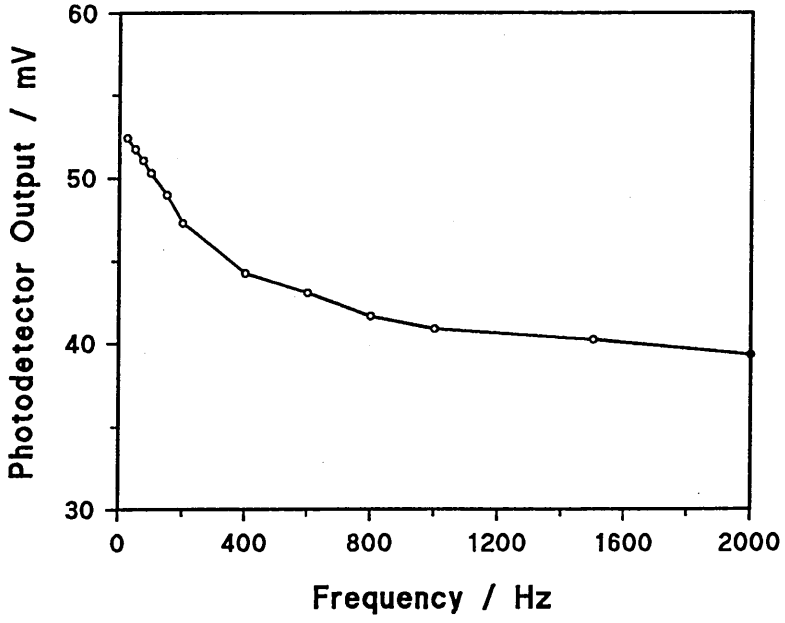

(b)

Figure 7.30 The photodetector response for the light modulated accelerometer using intensity modulation. (a) Acceleration response, (b) frequency response.

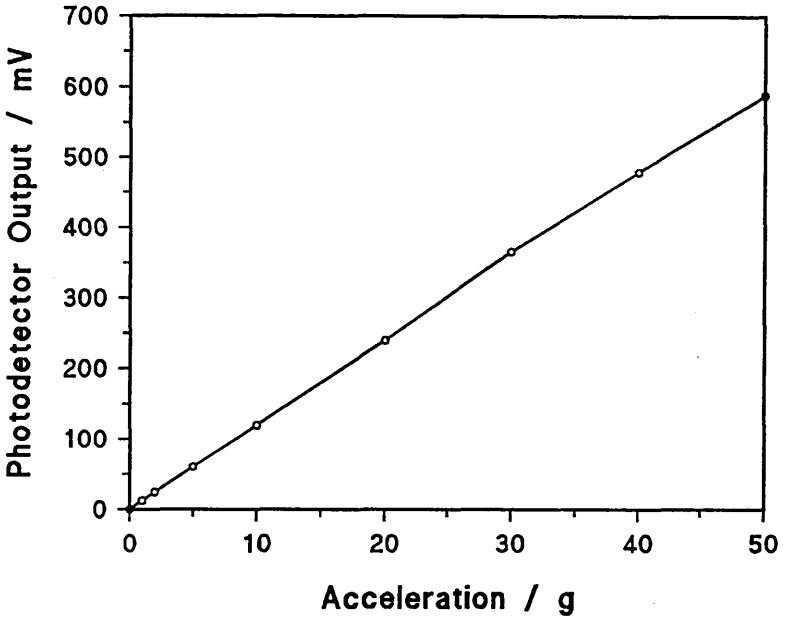

(a)

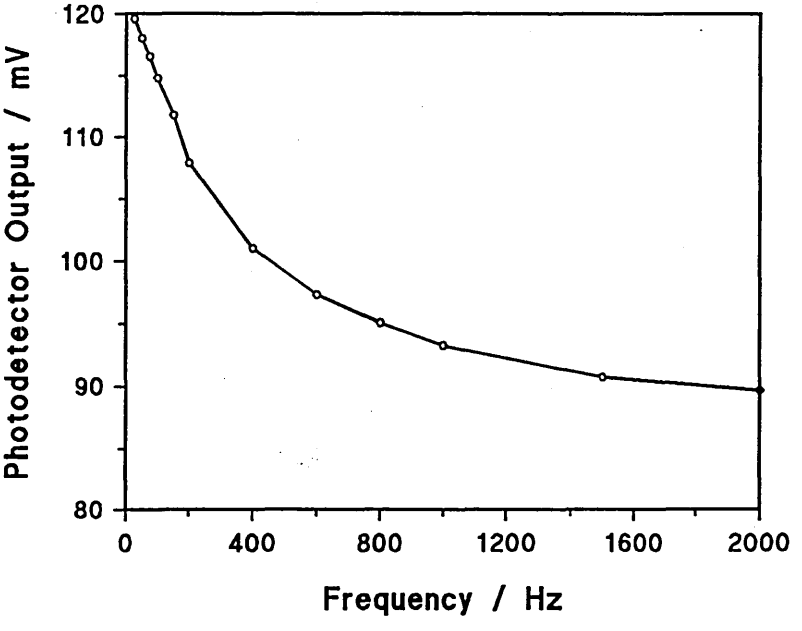

(b)

Figure 7.31 The photodetector response for the light modulated accelerometer using phase modulation. (a) Acceleration response, (b) frequency response.

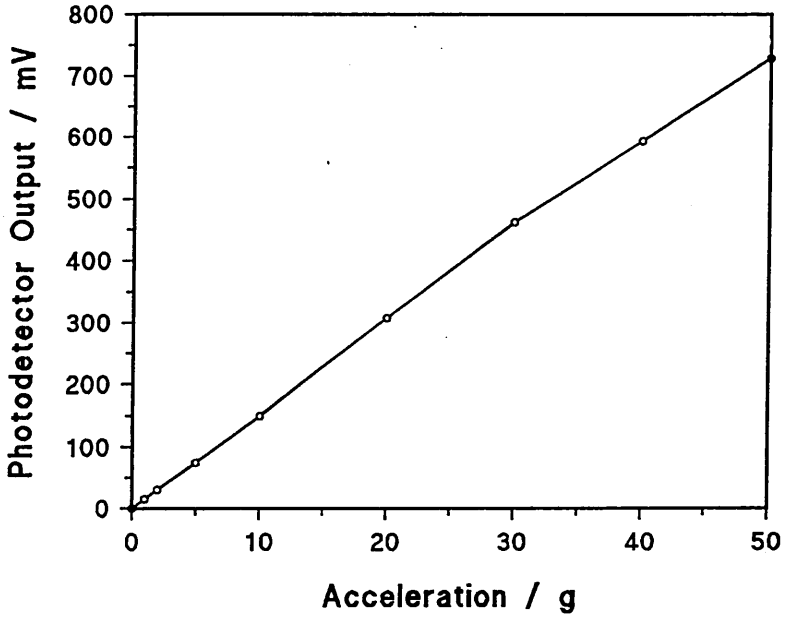

(a)

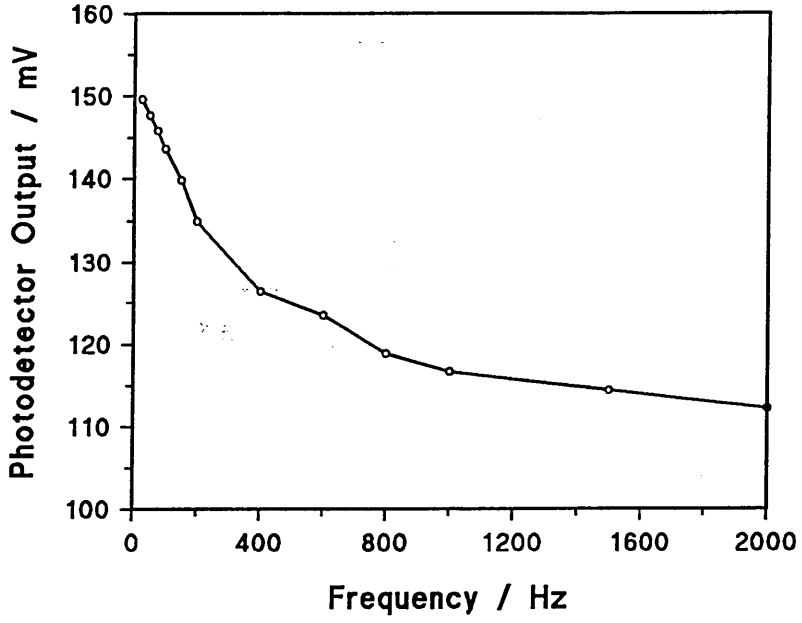

(b)

Figure 7.32 The photodetector response for the light modulated accelerometer using polarisation modulation. (a) Acceleration response, (b) frequency response.

Material	α / $1x10^{-5}$ (Exp)	α / $1x10^{-5}$ (Man)
Polycarbonate	6.6	6.5
Polymethyl methacrylate	7.6	8.0
Polystyrene	7.9	8.0
Polyvinyl chloride	8.2	8.0
Araldite epoxy resin	6.5	6.2

Table 8.1 - The thermal expansion coefficient calculated from the experimental data along with the thermal expansion coefficient reported by the manufacturers.

Appendix A - Measurement Errors

	Error	Repeatability
Stress Results		
Stress Expansion, μm	$\pm$0.4	$\pm$1
Stress optic coefficient, x10^{-12} /Pa		
Polariscope	$\pm$0.47	$\pm$1
Michelson	$\pm$0.36	$\pm$0.8
Fizeau	$\pm$0.37	$\pm$0.9
Compressive Yield strength, MPa	$\pm$0.4	$\pm$1
Thermal Results		
Thermal Expansion, μm	$\pm$0.4	$\pm$1
Thermo-optic coefficient, x10^{-4} /°C		
Abbé	$\pm$0.03	$\pm$0.02
Michelson	$\pm$0.009	$\pm$0.01
Fizeau	$\pm$0.01	$\pm$0.01
Glass Transition, T_g /°C	$\pm$2	$\pm$1
Accelerometer Results		
Acceleration, g	$\pm$0.1	$\pm$0.1
Frequency, Hz	$\pm$1	$\pm$1

Appendix B - Accelerometer Characteristics

Experimental Accelerometer

	Intensity	Phase	Polarisation
Polycarbonate			
Sensitivity, mV/g	40	130	168
Acceleration Range, g	0-50	0-50	0-50
Amplitude Nonlinearity %	<1	<1	<1
Frequency Response, Hz	0-2000	0-2000	0-2000
Resonant Frequency, Hz	27	27	27
Temperature Range, °C	-20-80	-20-80	-20-80
Weight, grams	25	25	25
Polymethyl methacrylate			
Sensitivity, mV/g	2.0	6.4	8.1
Acceleration Range, g	0-50	0-50	0-50
Amplitude Nonlinearity %	<1	<1	<1
Frequency Response, Hz	0-2000	0-2000	0-2000
Resonant Frequency, Hz	27	827	27
Temperature Range, °C	-20-80	-20-80	-20-80
Weight, grams	25	25	25
Polyvinyl chloride			
Sensitivity, mV/g	2.1	6.9	16.5
Acceleration Range, g	0-50	0-50	0-50
Amplitude Nonlinearity %	<1	<1	<1
Frequency Response, Hz	0-2000	0-2000	0-2000
Resonant Frequency, Hz	27	27	27
Temperature Range, °C	-20-80	-20-80	-20-80
Weight, grams	25	25	25
Araldite Epoxy Resin			
Sensitivity, mV/g	23	79	100
Acceleration Range, g	0-50	0-50	0-50
Amplitude Nonlinearity %	<1	<1	<1
Frequency Response, Hz	0-2000	0-2000	0-2000
Resonant Frequency, Hz	27	27	27
Temperature Range, °C	-20-80	-20-80	-20-80
Weight, grams	25	25	25

Prototype Accelerometer

Polymethyl methacrylate			
Sensitivity, mV/g	5.0	11.7	14.5
Acceleration Range, g	0-50	0-50	0-50
Amplitude Nonlinearity %	<1	<1	<1
Frequency Response, Hz	0-2000	0-2000	0-2000
Resonant Frequency, Hz	27	27	27
Temperature Range, °C	-20-80	-20-80	-20-80
Weight, grams	68	68	68